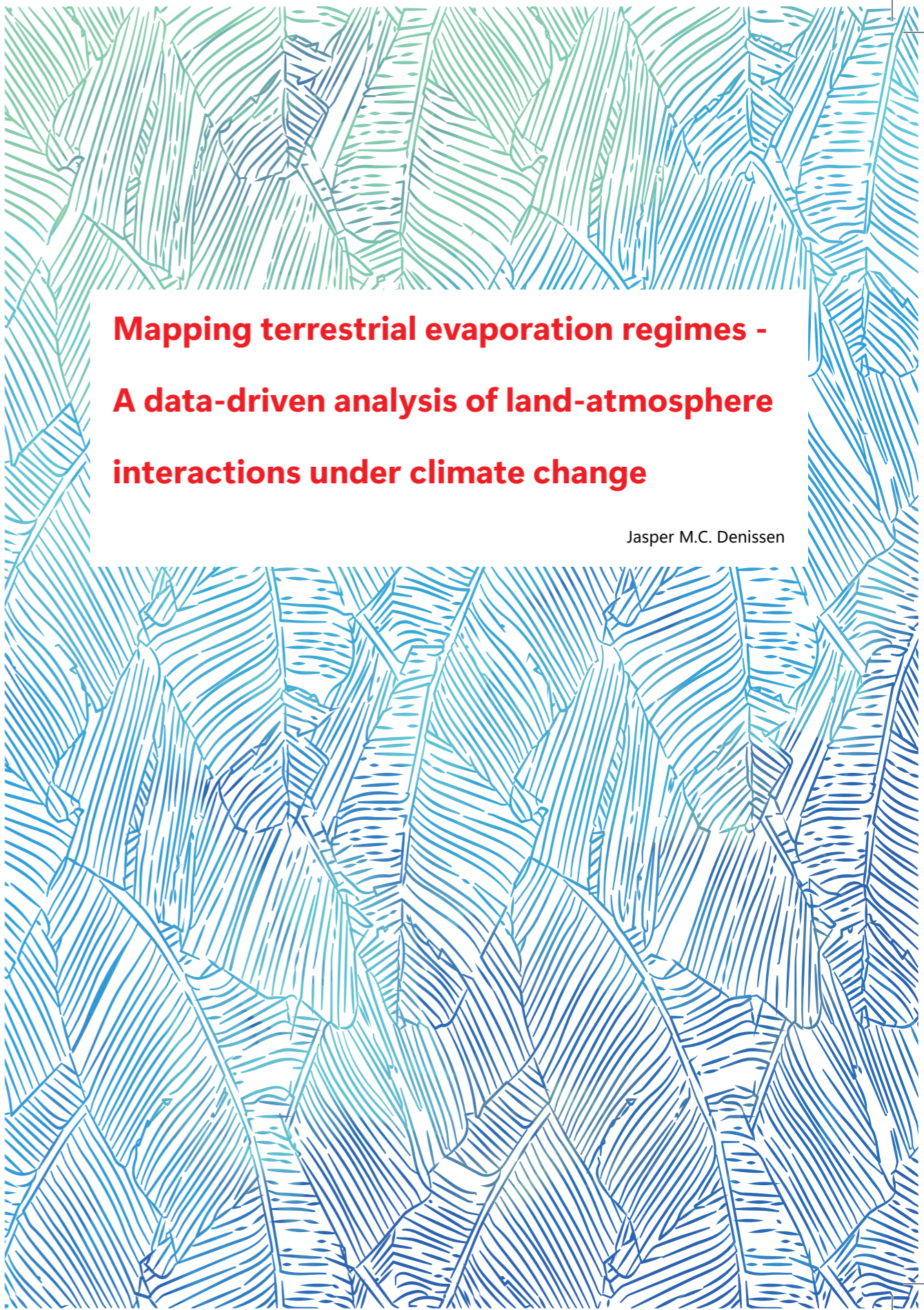


Jasper M.C. Denissen

Mapping terrestrial evaporation regimes - A data-driven analysis of land-atmosphere interactions under climate change

2022



**Mapping terrestrial evaporation regimes -
A data-driven analysis of land-atmosphere
interactions under climate change**

Jasper M.C. Denissen

Propositions

1. Temperature is a useful energy proxy for vegetation functioning.
(this thesis)
2. The Aridity Index fails to reflect the role of water availability for vegetation functioning.
(this thesis)
3. The scientific merit of a research article depends on the journals' impact factor.
4. A career in science includes working through evenings and weekends.
5. Diversity quota hamper the employment of the most excellent candidate.
6. Shunning public figures from discourse, known as cancel culture, must be possible before trial by law.

Propositions belonging to the thesis, entitled:

Mapping terrestrial evaporation regimes – A data-driven analysis of land-atmosphere interactions under climate change

Jasper M. C. Denissen
Wageningen, July 1st 2022

**Mapping terrestrial evaporation regimes –
A data-driven analysis of land-atmosphere
interactions under climate change**

Jasper M.C. Denissen

Thesis committee

Promotor:

Dr A. J. Teuling

Associate professor of Environmental Sciences

Wageningen University & Research

Co-promotors:

Dr R. Orth

Group leader of the Hydrosphere-Biosphere-Climate Interactions group

Max Planck Institute for Biogeochemistry

Prof. Dr M. Reichstein

Director of the Department of Biogeochemical Integration

Max Planck Institute for Biogeochemistry

Other members:

Prof. Dr M. Scheffer, Wageningen University & Research

Prof. Dr P. A. Dirmeyer, George Mason University

Prof. Dr P. Gentile, Columbia University

Dr K. van der Wiel, Royal Netherlands Meteorological Institute

This research was conducted under the auspices of the Graduate School for Socio-Economic and Natural Sciences of the Environment (SENSE) and the International Max Planck Research School for Global Biogeochemical Cycles (IMPRS-gBGC)

Mapping terrestrial evaporation regimes – A data-driven analysis of land-atmosphere interactions under climate change

Jasper M.C. Denissen

Thesis

submitted in fulfilment of the requirements for the degree of doctor
at Wageningen University
by the authority of the Rector Magnificus
Prof. Dr A.P.J. Mol,
in the presence of the
Thesis Committee appointed by the Academic Board
to be defended in public
on Friday 1 July, 2022
at 4 p.m. in the Omnia Auditorium.

Jasper M.C. Denissen

Mapping terrestrial evaporation regimes – A data-driven analysis of land-atmosphere interactions under climate change

222 pages.

PhD thesis, Wageningen University, Wageningen, the Netherlands (2022)

With references, with summary in English and Dutch

ISBN 978-94-6447-230-1

DOI <https://doi.org/10.18174/569775>

Contents

	Page
Contents	v
Summary	vii
Samenvatting	xi
Chapter 1 General introduction	1
Chapter 2 Terrestrial evaporation regimes from satellite observations	19
Chapter 3 Terrestrial evaporation regimes from global weather balloon soundings	41
Chapter 4 Ecosystem water limitation under climate change	63
Chapter 5 Hydrometeorological drivers of vegetation productivity extremes	101
Chapter 6 Future ecosystem water limitation and heat extremes	125
Chapter 7 Synthesis	147
References	163
Statement of authorship contributions	191
Acknowledgements	193
Curriculum Vitae	197
IMPRS certificate	203
SENSE certificate	205

Summary

Terrestrial ecosystems are essential for human life, as they provide several key services, such as food and water security, sequestration of anthropogenic carbon dioxide (CO₂) and evaporative cooling. Healthy ecosystems perform photosynthesis, during which the plants' stomata, tiny apertures on the leaf surface, are open to take up CO₂ and evaporate water into the atmosphere, thereby providing a cooling effect. At the Earth's surface, all the energy that is available from solar radiation that is not used to evaporate water, is used to heat near-surface air. Thereby, ecosystems play a key role in connecting the energy and the water balance.

In **Chapter 1**, I introduce the energy and the water balance, which are linked through the evaporation of terrestrial water by ecosystems. How much of the available energy is used to evaporate water from the land surface, the evaporative fraction (EF), depends on water supply (soil moisture); When the soil is too dry for plants to extract water from the soil, plants close their stomata to prevent water loss. As the soil moistens, plants can access this water and increase their transpiration with further soil moisture increases until the maximum EF is reached. At this point, any additional soil moisture increases will no longer affect the EF, rendering the magnitude of the evaporation of water, the terrestrial evaporation (ET), solely dependent on available energy. The soil moisture and the corresponding terrestrial evaporation regime can dampen or amplify heat waves and other extreme events. Therefore, distinguishing energy versus water-limited conditions and accurately representing in Earth system models is essential.

The aim of this thesis is to study the relevance of water versus energy limited conditions and associated regime transitions for weather, climate and related extremes under climate change. In this data-driven analysis, a multitude of data streams is used, amongst which satellite observations, in-situ observations, such as weather balloons, gridded machine-learning based data sets and heavily constrained and unconstrained model output from Earth system models. Using such a combination of data products provides a comprehensive perspective that allows to infer the role of limitations in individual data products by comparing results between them.

In addition to research focusing solely on either energy or water, I introduce a novel index in **Chapter 2** that considers the relevance of both water and energy availability for terrestrial evaporation. Using satellite observations over Europe, energy limitation is found in Northern Europe and water limitation in the Mediterranean, separated by a transitional zone across Central Europe. A soil moisture threshold, the critical soil moisture (CSM), which separates energy and

water-limited conditions, is determined at the continental and the grid cell scale. This transition matters, as it separates water-limited conditions, where soil moisture can impact the near-surface temperature through evaporation, from energy-limited conditions, where atmospheric dynamics and related temperature and solar radiation impact the evaporation of water. The CSM is sensitive to local climate, soil and vegetation characteristics, but is robust when determined using proxies from other data products for energy availability and terrestrial evaporation.

As land-atmosphere interactions work both ways, land surface conditions can also be inferred from an atmosphere perspective: In **Chapter 3**, atmospheric temperature and humidity measurements from weather balloons are translated into landscape-scale surface fluxes using a mixed-layer model. Juxtaposing these surface fluxes against satellite-observed surface soil moisture, the CSM is estimated, which is then used to separate water versus energy-limited conditions. Further, I find that afternoon atmospheric boundary layers (ABLs) are warmer, drier and deeper over water-limited as compared to energy-limited surfaces.

In **Chapter 4**, future trends ecosystem water limitation trends are studied with model output from a suite of state-of-the-art Earth system models, which (i) can complement data lacking from observations (e.g. root-zone soil moisture) and (ii) allows to infer future climate conditions. Ecosystem Limitation Index (ELI) trends based on historical simulations and future projections reveal a widespread increase in ecosystem water limitation under climate change. Although globally this is driven mostly by increasing energy availability, several hot spot regions are identified where ecosystem water limitation increases particularly rapid owing to simultaneous decreases in water availability. This shift towards ecosystem water limitation occurs in space, as transitional zones shift northwards in Canada and northern Eurasia and northeastwards in the Amazon, and in time through widespread lengthening of the water-limited season. Although net surface radiation is the most dominant driver for ELI trends, a full range of eco-climate variables is needed to understand local differences.

In previous chapters, I mainly focused on mean climate conditions, whereas the role of land-atmosphere interactions for climate extremes is even more pronounced: In **Chapter 5**, I find that in about half of the land area with active vegetation, vegetation productivity extremes jointly occur with hydrometeorological hazards. The drivers of such vegetation extremes vary in space: In the Northern Hemisphere, temperature-related hazards are found important above 50°N, whereas water-related hazards most strongly impact vegetation productivity below 50°N. Further, several key regions are identified where vegetation productivity maxima are energy-driven and minima are governed by water, which is characteristic for transitional regimes and strong land-atmosphere coupling.

In **Chapter 6**, an ensemble of Earth system models is used to find that in 77% of the vegetated land surface, maximum temperature is increasing more rapidly than mean temperatures under climate change. In several hot spot regions, such temperature divergence increases occur alongside shifts towards ecosystem water limitation and related reductions in evaporative cooling. Whereas the magnitude of temperature divergence trends is largest in initially energy-limited and

transitional regions, where ELI trends are strongest, the sensitivity is highest in initially water-limited regions, where evaporative cooling is most strongly affected by increasing ecosystem water limitation.

In **Chapter 7**, specific contributions, limitations and future research opportunities are synthesized. In conclusion, a novel index was introduced that jointly considers the relevance of energy and water availability for terrestrial evaporation. Typically, water-limited conditions are characterized by dry soils and correspondingly low terrestrial evaporation and high sensible heating of near-surface air. As such, ABLs are warmer and drier over water versus energy limitation, thereby amplifying heat extremes. Hot spot regions are found where heat extremes are amplified by reductions in evaporative cooling. Identifying such regions is essential to tailor adaptation strategies, such as irrigation or tillage practices, city greening and afforestation, to mitigate impact on human health and infrastructure. Further, these studies allow the comparison of modelled and observed land-atmosphere coupling, which could inform model development and lead to better weather and climate forecasts and accurate determination of land-atmosphere coupling hot spots and associated extreme events.

Samenvatting

Terrestrische ecosystemen zijn van essentieel belang voor mensenleven, omdat zij verschillende essentiële diensten leveren, zoals voedsel- en waterzekerheid, vastlegging van antropogene kooldioxide (CO_2) en verdampingskoeling. Gezonde ecosystemen voeren fotosynthese uit, waarbij de huidmondjes van de planten, minuscule openingen op het bladoppervlak, open staan om CO_2 op te nemen en water de atmosfeer in te verdampen, waardoor een verkoelend effect ontstaat. Aan het aardoppervlak wordt alle beschikbare energie van zonnestraling die niet wordt gebruikt om water te verdampen, gebruikt om de lucht nabij het aardoppervlak te verwarmen. Ecosystemen spelen dus een sleutelrol in de koppeling van de energie- en de waterbalans.

In **Hoofdstuk 1** introduceer ik de energie- en de waterbalans, die met elkaar verbonden zijn via de verdamping van landwater door ecosystemen. Hoeveel van de beschikbare energie wordt gebruikt om water van het landoppervlak te verdampen, de verdampingsfractie (EF), hangt af van de watertoevoer (bodemvochtigheid); wanneer de bodem te droog is voor planten om water aan de bodem te onttrekken, sluiten planten hun huidmondjes om waterverlies te voorkomen. Naarmate de bodem vochtiger wordt, krijgen planten toegang tot dit water en neemt hun transpiratie toe naarmate de bodemvochtigheid toeneemt, totdat de maximale EF is bereikt. Op dit punt heeft een verdere toename van de bodemvochtigheid geen invloed meer op de EF, zodat de grootte van de waterverdamping, de terrestrische verdamping (ET), uitsluitend afhankelijk is van de beschikbare energie. De bodemvochtigheid en het bijbehorende verdampingsregime kunnen hittegolven en andere extreme gebeurtenissen temperen of versterken. Daarom is het van essentieel belang een onderscheid te maken tussen energie- en waterbeperkte omstandigheden en deze accuraat weer te geven in aardsysteemmodellen.

Het doel van dit proefschrift is het bestuderen van de relevantie van water- versus energiebeperkte omstandigheden en de bijbehorende regime-overgangen voor weer, klimaat en gerelateerde extremen onder klimaatverandering. In deze data-gedreven analyse wordt een veelheid aan datastromen gebruikt, waaronder satellietwaarnemingen, in-situ waarnemingen, zoals weerballonnen, machine-learning gebaseerde datasets en output van zwaar begrensde en onbegrensde aardsysteemmodellen. Het gebruik van een dergelijke combinatie van gegevensproducten biedt een alomvattend perspectief dat het mogelijk maakt de rol van beperkingen in individuele gegevensproducten af te leiden door de resultaten tussen die producten te vergelijken.

Naast onderzoek dat zich uitsluitend richt op energie of water, introduceer ik in **Hoofdstuk 2** een nieuwe index die rekening houdt met de relevantie van de beschikbaarheid van zowel water als energie voor de verdamping van landwater. Op basis van satellietwaarnemingen over Europa wordt een energiebeperking aangetroffen in Noord-Europa en een waterbeperking in het Middellandse Zeegebied, gescheiden door een overgangszone in Midden-Europa. Een bodemvochtdrempel, de kritische bodemvochtigheid (CSM), die energie- en waterbeperkte omstandigheden scheidt, wordt bepaald op continentale schaal en op de schaal van rastercellen. Deze overgang is belangrijk, omdat hij een scheiding vormt tussen watergelimiteerde omstandigheden, waarbij bodemvocht de oppervlaktetemperatuur door verdamping kan beïnvloeden, en energiegelimiteerde omstandigheden, waarbij de atmosferische dynamiek en de daarmee samenhangende temperatuur en zonnestraling de verdamping van water beïnvloeden. De CSM is gevoelig voor lokale klimaat-, bodem- en vegetatiekenmerken, maar is robuust wanneer hij wordt bepaald met behulp van proxies van andere gegevensproducten voor de beschikbaarheid van energie en terrestrische verdamping.

Aangezien de interacties tussen land en atmosfeer in beide richtingen werken, kan de toestand van het landoppervlak ook worden afgeleid vanuit het perspectief van de atmosfeer: In **Hoofdstuk 3** worden metingen van de atmosferische temperatuur en vochtigheid door weerballonnen vertaald in oppervlaktefluxen op landschapsschaal met behulp van een mixed-layer model. Door deze oppervlaktefluxen af te zetten tegen het vochtgehalte van de bodem dat door satellieten is waargenomen, wordt de CSM geschat, die vervolgens wordt gebruikt om water- versus energiebeperkte omstandigheden van elkaar te scheiden. Verder ontdek ik dat de atmosferische grenslagen (ABL's) 's middags warmer, droger en dieper zijn over watergelimiteerde oppervlakken in vergelijking met energiegelimiteerde oppervlakken.

In **Hoofdstuk 4** worden toekomstige trends in de waterbeperking van ecosystemen bestudeerd aan de hand van modeloutput van een reeks geavanceerde aardsysteemmodellen, die (i) gegevens kunnen aanvullen die ontbreken in waarnemingen (bijv. bodemvocht in de wortelzone) en (ii) het mogelijk maken om toekomstige klimaatomstandigheden af te leiden. Trends in de ecosysteemlimitatie-index (ELI) op basis van historische simulaties en toekomstprojecties wijzen op een wijdverspreide toename van de waterlimitatie van ecosystemen onder invloed van de klimaatverandering. Hoewel dit wereldwijd vooral wordt aangedreven door een toenemende beschikbaarheid van energie, zijn er verschillende "hot spot"-regio's geïdentificeerd waar de waterbeperking voor ecosystemen bijzonder snel toeneemt als gevolg van een gelijktijdige afname van de beschikbaarheid van water. Deze verschuiving naar waterbeperking voor ecosystemen doet zich voor in de ruimte, aan de hand van overgangszones die naar het noorden verschuiven in Canada en noordelijk Eurazië en naar het noordoosten in het Amazonegebied, en in de tijd door een wijdverspreide verlenging van het waterbeperkte seizoen. Hoewel netto oppervlaktestraling de meest dominante drijvende kracht is achter de ELI-trends, is een volledige reeks eco-klimaatvariabelen nodig om lokale verschillen te begrijpen.

In de voorgaande hoofdstukken heb ik me vooral gericht op gemiddelde klimaatomstandigheden, terwijl de rol van land-atmosfeer interacties voor klimaatextremen nog groter is: In **Hoofdstuk 5** stel ik vast dat in ongeveer de helft van het landoppervlak met actieve vegetatie, vegetatieproductiviteitsextremen samen met hydrometeorologische ontregelingen voorkomen. De drijvende krachten achter dergelijke vegetatie-extremen variëren in de ruimte: Op het noordelijk halfrond zijn temperatuurgerelateerde risico's het belangrijkste boven 50°noorderbreedte, terwijl watergerelateerde risico's de vegetatieproductiviteit het sterkst beïnvloeden beneden 50°noorderbreedte. Voorts zijn er verschillende sleutelregio's geïdentificeerd waar de maxima van de vegetatieproductiviteit worden bepaald door energie en de minima door water, wat kenmerkend is voor overgangsregimes en een sterke koppeling land-atmosfeer.

In **Hoofdstuk 6** wordt een ensemble van aardsysteemmodellen gebruikt om te ontdekken dat in 77% van het begroeide landoppervlak de maximumtemperatuur sneller toeneemt dan de gemiddelde temperatuur onder invloed van de klimaatverandering. In verschillende hotspotregio's gaan dergelijke stijgingen van temperatuurverschillen gepaard met verschuivingen in de richting van waterbeperking voor ecosystemen en daarmee samenhangende verminderingen van verdampingskoeling. Terwijl de grootte van temperatuur divergentie trends het grootst is in aanvankelijk energie-beperkte en overgangsregio's, waar de ELI trends het sterkst zijn, is de gevoeligheid het hoogst in aanvankelijk waterarme regio's, waar de verdampingskoeling het sterkst wordt beïnvloed door de toenemende waterbeperking van het ecosysteem.

In **Hoofdstuk 7** worden specifieke bijdragen, beperkingen en toekomstige onderzoeksmogelijkheden samengevat. Tot slot werd een nieuwe index geïntroduceerd die de relevantie van de beschikbaarheid van energie en water voor de verdamping van land in beschouwing neemt. Typisch worden waterarme omstandigheden gekenmerkt door droge bodems en een overeenkomstige lage verdamping en hoge voelbare opwarming van de lucht aan het aardoppervlak. Als zodanig zijn ABL's warmer en droger bij water- versus energiebeperking, waardoor hitte-extremen worden versterkt. Hotspotregio's worden gevonden waar hitte-extremen worden versterkt door verminderde verdampingskoeling. Het identificeren van dergelijke gebieden is essentieel om aanpassingsstrategieën, zoals irrigatie- of grondbewerkingspraktijken, stadsvergroening en bossing, op maat te maken om de gevolgen voor de menselijke gezondheid en de infrastructuur te beperken. Bovendien maken deze studies een vergelijking mogelijk van de gemodelleerde en waargenomen koppeling tussen land en atmosfeer, hetgeen modelontwikkeling ten goede kan komen en kan leiden tot betere weer- en klimaatvoorspellingen en een nauwkeurige bepaling van de hot spots van de koppeling tussen land en atmosfeer en de bijbehorende extreme gebeurtenissen.

Chapter 1

General introduction

1.1 Background: Land-atmosphere interactions

The Earth system can be subdivided in several spheres: the lithosphere, hydrosphere, atmosphere and the biosphere. Whereas this distinction is useful for classification purposes, the Earth system can only be understood through the interactions between those spheres. Many of these interactions occur at the Earth's surface, where solar radiation provides the energy that is at the base of a myriad processes that shape the weather we experience every day and that on rare occasions result in extremes that can crucially impact life. How the weather is affected by the Earth's surface depends on its properties, including vegetation coverage and soil properties, which in turn are influenced by the prevalent local climate. This thesis presents a study of the Earth's surface and how it modulates flows of energy and water between the land and the atmosphere.

1.1.1 Surface water & energy balance

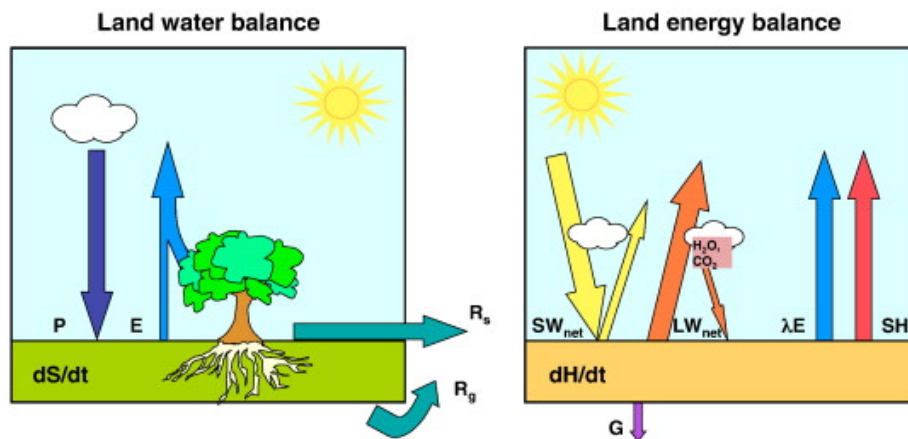


Figure 1.1: Schematic representation of the energy and water cycles. The land water balance is depicted in the left panel and the energy balance in the right panel. The arrows represent fluxes of water and energy. The meaning of the abbreviations is elaborated on in the text. Throughout this thesis, I will refer to the total sum of evaporative processes at the land surface as terrestrial evaporation (ET) (E, left panel) in mm d^{-1} or latent heat flux (LE) in W m^{-2} . ET can be converted to the LE (or λE , right panel) with the use of the latent heat of vaporization (λ). Figure from Seneviratne et al. (2010).

Water and energy availability at the land surface are vital for fresh water reserves and healthy ecosystems that provide food and evaporative cooling and sequester atmospheric carbon dioxide (CO_2) (Mekonnen and Hoekstra, 2016; Piao et al., 2010). To this end, taking stock of water and energy fluxes is essential. Figure 1.1 schematically describes the most important processes for the land water and energy balance occurring at the land surface. The land water and energy balance (left), excluding the lateral sub-surface exchange of water to adjacent soils, can be described in Eq. 1.1:

$$\frac{dS}{dt} = P - ET - R_n - R_g \quad (1.1)$$

Where the water storage (dS/dt) in the considered soil layer (in mm d^{-1}) results from the difference between precipitation (P) and terrestrial evaporation (ET), drainage (R_g) and surface runoff (R_s). Depending on the depth of the considered soil layer, dS/dt might encompass surface and root-zone soil moisture or moisture stored in deeper layers that is unavailable to vegetation. As it costs energy to evaporate water, ET is also present in the surface energy balance, as proposed in Eq. 1.2:

$$\frac{dH}{dt} = R_n - H - LE + G \quad (1.2)$$

where dH/dt denotes the heat storage in the considered soil layer and the vegetation and R_n is the surface net radiation in W m^{-2} , or the amount of energy at the land surface that is available for the sensible heat flux (H) and latent heat flux (LE) and the ground heat flux (G). As the land surface is considered solely as the interface (an infinitesimally thin layer), dH/dt can be omitted from the equation. On time scales longer than days, G averages out and is usually neglected. What remains is that R_n either partitions into the sensible or latent heat flux. Further, the R_n also results from the budget of all radiative components:

$$R_n = SW_{net} + LW_{net} \quad (1.3)$$

Where SW_{net} and LW_{net} are the sum of incoming and outgoing shortwave and longwave radiation, respectively. Whereas all fluxes in Figure 1.1 are important solely for their own respective balance, ET (or LE) effectively links the energy and the water balance together, therefore exerting influence both on heat and moisture input into the atmosphere. As such, ET is a crucial variable to understand within climate sciences.

1.1.2 Evaporative processes

I discuss two perspectives that are relevant for quantifying the magnitude of ET and its drivers: An atmospheric perspective and a land surface perspective.

An atmospheric perspective

Evaporation of water is only possible when sufficient energy is available for the phase transition of water from liquid to vapor. Furthermore ET is driven by vapor pressure gradients, as all turbulent transfer processes that transport a physical quantity are driven by their respective gradients. More specifically for ET at the land surface, the vapor pressure gradient denotes

the difference between surface and atmospheric vapor pressure. Provided that sufficient energy is readily available for evaporation, the highest evaporative rates are achieved with the largest gradients between surface and atmospheric vapor pressures. The atmospheric vapor pressure can be expressed as vapor pressure deficit (VPD), as follows:

$$VPD = e_{sat} \left(1 - \frac{RH}{100}\right) \quad (1.4)$$

The VPD denotes the difference between vapor pressure (e) and saturated vapor pressure (e_{sat}) in kPa. The RH denotes the relative humidity (RH), which is a relative measure atmospheric water vapor content, expressed as e over e_{sat} in % and therefore directly depends on specific humidity (q). The e_{sat} has been derived empirically as proposed by the World Meteorological Organization (WMO), as follows:

$$e_{sat} = 610.7 \frac{10(7.5T_a)/(237.3 + T_a)}{1000} \quad (1.5)$$

Where air temperature (T_a) is in °C. From Eqs. 1.4 and 1.5 can be deduced that, from an atmospheric perspective, any evaporative process at the land surface is tightly coupled to T_a , as higher temperatures entail a larger atmospheric capacity to hold water vapor (e_{sat}), and to the RH, which reflects the actual atmospheric water vapor content.

A land surface perspective

Evaporation of water from the land surface can be described using a conceptual piecewise-linear framework, where the evaporative fraction (EF), which denotes ET that is normalized by R_n to exclude (diurnal) radiation variability effects, is driven primarily by soil moisture (Budyko, 1974; Koster et al., 2009; Seneviratne et al., 2010), in Figure 1.2.

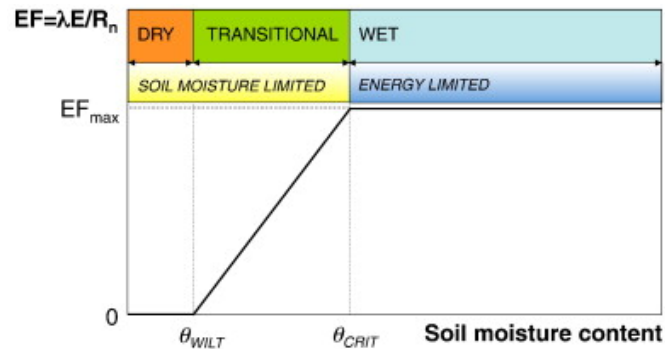


Figure 1.2: Conceptual framework showing the response of the evaporative fraction (EF) to soil moisture, divided into regimes that express typical relationships. EF_{max} is the maximum capacity of EF. Figure from Seneviratne et al. (2010).

Conceptually, a piece-wise linear relationship between EF and soil moisture with two characteristic terrestrial evaporation regimes can be distinguished: (i) the soil moisture-limited, or water-limited, regime, where EF and ET are assumed to be limited by soil moisture, and (ii) the energy-limited regime, where EF is at its maximum capacity (EF_{\max}). The water-limited regime can be subdivided into the dry and transitional regime. In the dry regime, where the soil moisture content is below wilting point (θ_{wilt}), the soil is too dry, such that no moisture can be extracted for evaporation. In the transitional regime, whenever soil moisture would exceed the θ_{wilt} , water can be extracted from the soil and EF increases alongside soil moisture increases until the EF_{\max} is reached at the critical soil moisture (θ_{wilt}), or the CSM. The θ_{wilt} denotes the transition between water- and energy-limited conditions. As the EF is already at its maximum capacity, further increases in soil moisture are assumed to no longer increase EF, but ET is now directly governed by R_n . As such, the value of EF does not necessarily reflect whether any evaporation is actually occurring or not, as EF might be larger than zero, but no evaporation will happen without surface available energy. This dictates that the ET always depends on both water and energy availability. Within this context, the CSM is a crucial parameter; Whenever the soil moisture is below the CSM, ET is mostly governed by the land surface (soil moisture), whereas soil moistures above the CSM dictate that ET is limited by the atmosphere (R_n). Next to figure 1.2, there are other frameworks that can distinguish terrestrial evaporation regimes, such as a soil water loss function supported by surface soil moisture observations (Akbar et al., 2018), as the sensitivity of surface fluxes to soil moisture variability (Dirmeyer, 2011) or as a function of soil moisture and atmospheric stability (Santanello et al., 2007).

Components

Up until this point, the bulk flux of all evaporative processes has been referred to as ET. However, to understand spatiotemporal variability in ET, I should discuss the different components that ET comprises, which includes (i) *plant transpiration*, (ii) *bare soil evaporation* and (iii) *canopy interception*. As stated in equations 1.4 and 1.5, sufficient water and energy should be available for the evaporation of water. However, different constraints apply to different evaporative components.

Bare soil evaporation is the evaporation of water directly from the soil matrix of the surface soil layer (top few cm). The soil moisture in the surface layer is generally available after precipitation events and can be stored before it either evaporates or percolates to deeper layers. Whether water can be extracted from the soil matrix depends on local soil characteristics, such as the soil texture. Generally, the finer grained the soil is, the stronger the water can be held by the soil matrix, thereby affecting the θ_{wilt} and the θ_{wilt} .

Plant transpiration, which is globally the largest component of ET (Berg and Sheffield, 2019b; Good et al., 2015; Lawrence et al., 2007; Schlesinger and Jasechko, 2014), is also affected by soil characteristics, as the maximum potential with which plants can extract soil moisture differs

between vegetation types (Novák and Havrila, 2006; Teuling et al., 2009b), which also affects the θ_{wilt} and the θ_{wilt} . Plant transpiration occurs as water vapor leaves the plants through stomatal apertures, which are open when plants are photosynthetically active. Moreover, the processes of photosynthesis and plant transpiration are tightly linked, effectively connecting the carbon and the water cycles (Gentine et al., 2019; Humphrey et al., 2021). This coupling occurs through the stomatal conductance (g_s), which reflects the ease with which plants exchange water vapor with the atmosphere, as g_s tries to optimize photosynthetic activity given the apparent environmental conditions:

- (i) Photosynthetically Active Radiation (PAR); the light that is used by plants for photosynthesis in the wavelengths between 0.4 and 0.7 μm , should be sufficiently available for plants to open their stomata.
- (ii) Leaf temperature; excessively low or high temperatures might lead to lower RuBisCO enzyme activity (Busch and Sage, 2017; Perdomo et al., 2017), which affects photosynthetic activity and therefore g_s .
- (iii) VPD; The atmospheric water demand should not be too high, as high VPD related hot and dry days lead to stomatal closure to prevent excessive water loss (Fu et al., 2022b; Novick et al., 2016; Oren et al., 1999; Yuan et al., 2019)
- (iv) Leaf water potential; The leaf water potential is governed by the influx and outflux of water in the plant. The influx is related to soil moisture; when insufficient water is available to maintain EF_{max} (soil moisture $< \theta_{\text{wilt}}$), plants can close their stomatal apertures to prevent excessive water loss and to maintain turgor. The outflux is governed by the VPD and corresponding atmospheric demand of water. High VPDs and associated plant transpiration (outflux) poses additional difficulties for plants to maintain turgor, which leads to closing stomatal apertures.
- (v) Atmospheric CO_2 concentration; Plants need CO_2 for photosynthesis. Higher atmospheric CO_2 concentrations increase the influx of CO_2 and the photosynthetic activity. However, if the concentration and related influx of CO_2 is higher than what is used for photosynthesis, the plants' internal CO_2 concentration increases, which leads to closing of stomatal apertures.

In response to physiological effects of rising atmospheric CO_2 that testify beneficial conditions (e.g. higher stomatal conductance), plants function more efficiently and consequently undergo structural changes to keep up heightened photosynthetic activity. This so-called CO_2 fertilization tends to increase the leaf area index (LAI) and related proxies (Donohue et al., 2013; Ukkola et al., 2016; Zhu et al., 2016), which reflects the area of leaves per unit area soil, in turn increasing the surface area from which plants can transpire water (Wei et al., 2017). As LAI and related proxies are projected to increase in the future alongside CO_2 fertilization (Piao et al., 2020), albeit with differences between natural and managed vegetation (Winkler et al., 2021). This could hint at an increasingly important role for vegetation in the global carbon and water cycles. Due to the

tight coupling between the carbon and the water balances (Gentine et al., 2019; Humphrey et al., 2021) and plant transpiration being the dominant evaporative component globally, vegetation indices such as gross primary productivity (GPP), sun-induced chlorophyll fluorescence (SIF), Normalized Difference Vegetation Index (NDVI), LAI and enhanced vegetation index (EVI) can be used as proxies for ET.

Canopy interception denotes the evaporation of water from plants' leaves and therefore directly depends on rainfall and LAI.

When considering the bulk of all evaporative components (ET), several factors should be kept in mind: (i) The individual evaporative components might be governed by different environmental drivers. (ii) Some of the drivers are connected: T_a and VPD, for example (through Eqs. 1.4 and 1.5). Also, R_n is connected to T_a , because T_a responds directly to sensible heating, which is radiation driven through Eq. 1.2. (iii) The compound effect that environmental drivers might have on separate evaporative components is difficult to disentangle; a higher VPD in principle leads to higher evaporative rates, but it also leads to stomatal closure, which might restrain plant transpiration.

Despite these complexities, it is still useful to look at the bulk of all evaporative processes, because of the common denominators that are relevant for all evaporative processes: water (soil moisture, precipitation) and energy (air temperature, surface net radiation) availability. Making sense of spatiotemporal variability in ET is possible by considering different climate, soil and vegetation characteristics.

1.1.3 The Atmospheric Boundary Layer ABL

ET has been established as the link between the energy and water cycles in Figure 1.1 and Eq. 1.1 and 1.2. As such, ET couples the land surface to the atmosphere, as ET plays a key role for the heat and moisture input into the atmospheric boundary layer (ABL). In this context, the ABL is lowest layer of the atmosphere and with a depth of usually a few meters to 1-3km it is directly influenced both from the land surface and from upper-air processes in the troposphere. Hence, the weather we experience at the land surface and which is introduced by large-scale circulation patterns that affect the ABL from the top, is modulated by surface fluxes.

Land surface - ABL interactions

Figure 1.3 schematically depicts how surface and entrainment fluxes of heat and moisture affect the temperature, humidity and depth of the ABL. Within the ABL, the LE is involved in multiple feedback loops, of which three key components are water availability (soil moisture) and atmospheric demand of water (VPD), which next to direct controls on LE, exert indirect influence via the g_s . The direct effects dictate that sufficient soil moisture should be available (soil moisture $> \theta_{wilt}$, see Figure 1.2), such that water can be extracted from the soil. If ample soil moisture is

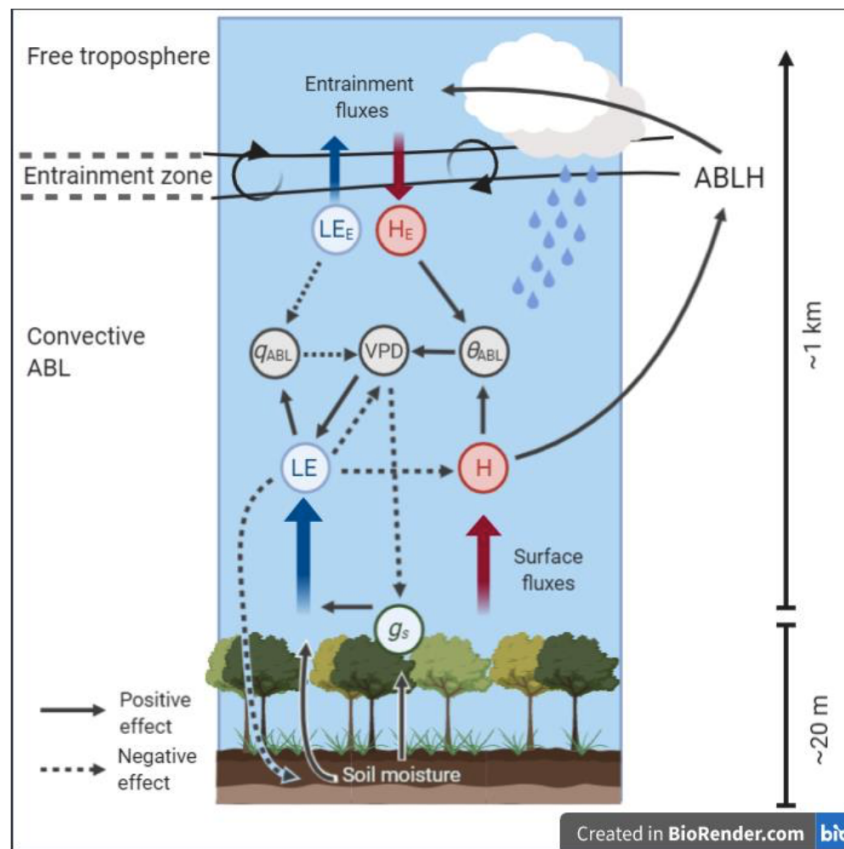


Figure 1.3: Schematic depiction of how the land surface affects ABL quantities and vice-versa. The relevant quantities in this figure are described in the text, between which there are either positive (solid arrows) or negative (dashed arrows) effects. Figure from Helbig et al. (2020).

available, leaf water potential and turgor can be maintained, rendering the stomatal apertures open ($\uparrow g_s$). Next to that, a higher atmospheric demand of water (VPD) involves higher LE, but at the same stomatal apertures close in response to high VPDs, decreasing g_s and limiting LE. All the surface available energy that is not used to evaporate water LE, is used for sensible heating H. This partitioning of surface fluxes determines the heat and moisture input into the ABL, and therefore exert great influence on the q_{ABL} and potential temperature $(\theta)_{ABL}$, that together determine the VPD through Eqs. 1.4 and 1.5.

Further, H heats up near-surface air parcels, that become warmer and therefore more buoyant than their surroundings and rise throughout the ABL, effectively mixing heat and moisture from the land surface through the ABL, until they hit the top of the ABL: the atmospheric boundary layer height (ABLH). From there, temperature increases with height, which prevents air parcels to rise higher, effectively acting as a lid on top of the ABL. However, air parcels overshoot this temperature inversion, thereby entraining warm and dry tropospheric air into the ABL (Vilà-Guerau de Arellano et al., 2015), which are expressed as the entrainment latent heat flux (LE_E) and the entrainment sensible heat flux (H_E), which in turn affect also affect q_{ABL} and θ_{ABL} .

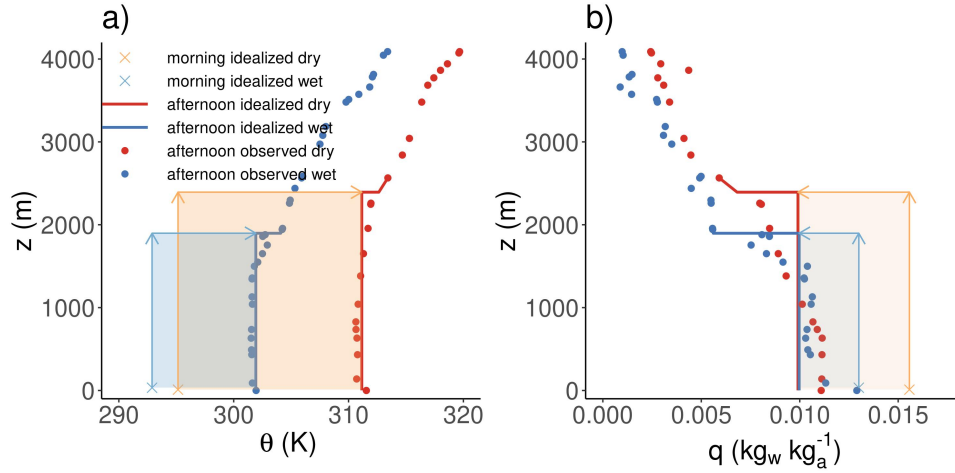
Diurnal evolution of the ABL

Figure 1.4: Typical diurnal evolution of ABL properties over dry and wet land surfaces. θ (a, in K) and q (b, in kg kg^{-1}) with respect to height (z , in m) on example wet (25-06-2014) and dry (07-07-2012) days in Lincoln, IL, U.S. (89.33 W, 40.15 N). The crosses and stippling depict atmospheric measurements from weather balloons from the IGRA data set (Durre et al., 2006). The colored lines depict idealized profiles as computed by a mixed-layer model: CLASS4GL (Wouters et al., 2019). Figure from Denissen et al. (2021).

It is clear from Figure 1.3 that soil moisture both directly and indirectly modulates heat and moisture input into the ABL through the partitioning of surface heat fluxes and therefore exert a great influence on ABL dynamics. Further, the role of dry and wet land surfaces for the diurnal evolution of the ABL in terms of θ , q and the ABL depth is explored in Figure 1.4. The evolution of the ABL starts at sunrise; At that time, the land surface starts warming due to incoming radiation and sensible heating creates rising air parcels, deepening the ABL and thereby mixing air above the land surface, which carries characteristics from the day(s) before. The θ and q of the parcels originating from the land surface depend directly on the surface flux partitioning: over dry land surfaces EF is low because of water limitation (Figure 1.2), which elevates H and related θ and limits LE and q , leading to substantial warming (Figure 1.4a), drying (Figure 1.4b) and deepening of the ABL from morning to the afternoon. Over wet land surfaces and corresponding energy limited conditions, the EF is generally higher, which involves less sensible heating and more moisture input into the ABL through air parcels originating at the land surface, which consequently heats (Figure 1.4a), dries (Figure 1.4b) and deepens less during daytime. Interestingly, the ABL is drying during the daytime, despite relevant moisture input from the land surface. This relates, next to the entrainment of dry free-tropospheric air (Vilà-Guerau de Arellano et al., 2015), to the so-called moisture capacity of the ABL: As during the daytime the volume in which air parcels that originate from the land surface are mixed is increasing, this leads to a net drying effect (Panwar et al., 2019). The same concept applies to the heat capacity of the ABL, but effects are typically less pronounced, as the ABL is heated from the top

and bottom, whereas the only moisture input is LE at the land surface, leading often to a more skewed vertical profile in terms of q than in terms of θ (Mahrt, 1991). In spite of such feedback processes, the evolution of the ABL is characteristically different through typical surface flux partitioning related to wet (energy limited) versus dry (water limited) land surfaces.

Implications on extreme events

Through modulating the surface flux partitioning and corresponding diurnal ABL evolution, the prevailing evaporative regime can impact weather and climate, particularly so during extreme events like heat waves and droughts (Guillod et al., 2015; Hirschi et al., 2011; Koster et al., 2016; Koster et al., 2004; Taylor et al., 2012), which have severe implications for human health (Bogdanovich et al., 2022; Wouters et al., 2022). The other way around, the impact of extreme events on the land surface can also be modulated by the evaporative regime at hand (Hauser et al., 2016; Hirschi et al., 2011; Miralles et al., 2014b), such that a heat wave and a corresponding drought over water-limited land surfaces might reduce ET or other proxies related to vegetation functioning, but can be beneficial for energy-limited land surfaces (Flach et al., 2018; Zscheischler et al., 2014a). As such, determining the evaporative regime is key to our ability to estimate the impacts of extreme events.

1.1.4 Water versus energy-limited conditions

So far, I have established that (i) ET plays a key role in both energy and water balances (Figure 1.1), (ii) ET is critically governed by wet versus dry land surface conditions and can be separated into water- and energy-limited regimes (Figure 1.2) and (iii) near-surface weather and respective diurnal evolution (Figure 1.3 and 1.4) are affected by wet versus dry land surface conditions. The question that remains unanswered is what water and energy limited conditions and the regime transitions between them entail.

In water-limited conditions, the land surface (soil moisture) and related water availability exert great influence on ET and therefore on near-surface weather. In energy-limited conditions, it is the near-surface weather and related energy availability that can limit ET. Therefore, the apparent evaporative regime denotes whether the land surface is driving the near-surface weather or vice-versa (Orth, 2021). Subsequently, the transition between these regimes matters, because it entails a change of causal direction (Santanello et al., 2018).

Regime shifts and the critical soil moisture

As the transition between terrestrial evaporation regimes denotes a switch in causal direction between the land surface and the atmosphere, it is key to pinpoint when and where these transitions occur. To this end, traditional pot experiments have been successful at relating soil-

and vegetation-specific CSMs to characteristic matrix potentials (Genuchten, 1987). However, these retrieved CSMs are difficult to apply in large-scale modelling practices, as grid cells are composites of various soil and vegetation types and upscaling small-scale estimates of the CSM is complicated due to non-linear relationships between soil moisture and matrix potentials. To this end, the conceptual framework put forward by Seneviratne et al. (2010) in Figure 1.2 has been applied to derive large-scale CSM estimates (Haghighi et al., 2018; Schwingshackl et al., 2017; Schwingshackl et al., 2018). Next to that, the CSM has been determined based on satellite-observed diurnal temperature amplitudes (Feldman et al., 2019) or even based on satellite-observed soil moisture drydowns (Akbar et al., 2018).

Spatiotemporal variability of terrestrial evaporation regimes

Variability with regards to the occurrence of terrestrial evaporation regimes exist both in space and in time. Water-limited conditions apply where energy is abundant, which generally includes areas with considerable solar radiation due to infrequently occurring cloud cover and related precipitation. Energy-limited conditions prevail where ample water is available, but either cold temperatures or frequent cloud cover limits terrestrial evaporation. However, the prevailing evaporative regime is seldom stationary in time, as transitions between them can occur. Such transitions can be induced seasonally, for example due to the strong seasonal cycle in incoming radiation in the mid to high latitudes, or in water availability, due to rain seasons in the tropics. In addition to seasonal changes, weather and climate extremes might introduce shifts in energy or water limitation; A wet spell could temporally shift water-limited regions into energy limitation, whereas a drought due to a lack of rainfall and accompanying clear skies in generally energy-limited has the opposite effect (Hauser et al., 2016; Koster et al., 2009; Zscheischler et al., 2015). Next to such (intra-)seasonal regime shifts, they can also be subject to long-term trends spanning multiple decades, resulting from changes in water and/or energy availability due to climate change (Berg and McColl, 2021; Greve et al., 2019). Such long-term trends are challenging to disentangle, because they are complicated (i) by CO₂ fertilization effects on ET (Piao et al., 2020; Winkler et al., 2021), (ii) nutrient availability (Peñuelas et al., 2017) and (iii) land use changes (Tollerud et al., 2020). Within this context, it is paramount to find a robust way to reveal the complex spatiotemporal dynamics of terrestrial evaporation regimes and its drivers.

1.1.5 Relevant physical quantities within land-atmosphere interactions

The connection between the land surface and the atmosphere is shaped by the relations between physical quantities indicated in Figure 1.2 and 1.3, which can vary between underlying terrestrial evaporation regimes. Typically, these relations express the relevance of water availability (soil moisture, precipitation) or energy availability (temperature, surface net radiation) for evaporative processes (terrestrial evaporation, evaporative fraction) and related vegetation functioning proxies (GPP, SIF, NDVI, LAI, EVI) (Akbar et al., 2018; Berg and McColl, 2021; Humphrey et al., 2021;

Koster et al., 2009; Novick et al., 2016; Schwingshackl et al., 2018; Seneviratne et al., 2006; Teuling et al., 2009a; Yuan et al., 2019; Zscheischler et al., 2015) or second-order conditions that (in)directly relate to surface heat flux partitioning (temperature, precipitation) (Guilod et al., 2015; Koster et al., 2004; Taylor et al., 2012; Vogel et al., 2018; Zhou et al., 2021). Understanding interactions between those physical quantities can be achieved by implementing them in Earth system models and trying to reproduce what is observed in the natural world. A glimpse of the future might be obtained by subjecting these models to possible future scenarios. This means that (i) we depend crucially on the quality of observations, as we rely on those for model initialization and calibration and (ii) we need both observations and models to understand the entirety of these interactions.

Observations

Observational data from different sources is available, ranging from satellite observations and networks of in-situ observations, including eddy covariance (EC) measurements, weather balloons and station soil moisture observations, to observation-based machine-learning products.

Many vital physical quantities can be observed from space by *satellites*, amongst which: soil moisture from the European Space Agency (ESA) Climate Change Initiative (CCI) (Dorigo et al., 2017; Gruber et al., 2017; Liu et al., 2012) and the Soil Moisture Active Passive (SMAP) mission (Entekhabi et al., 2010), NDVI, LAI and EVI from the Advanced Very High Resolution Radiometer (AVHRR), which is part of the third generation Global Inventory Monitoring and Modeling System (GIMMS) project (Zhu et al., 2013), SIF from Global Ozone Monitoring Experiment-2 (GOME-2) (Köhler et al., 2015) or Tropospheric Monitoring Instrument (TROPOMI) (Köhler et al., 2018). While providing unprecedented spatial coverages and an abundance of observations, there are some common issues with satellite observations that should be considered. Satellite observations of surface soil moisture can be used as a proxy for plant available water. However, one would ideally consider root-zone soil moisture. This is problematic, as there is no such observational data set, let alone one with global coverage. Moreover, one should consider the rooting depth for root-zone soil moisture estimates, which differs across vegetation types and is difficult to observe (Canadell et al., 1996; Fan et al., 2017; Jackson et al., 1996). As satellite microwave measurements only penetrate the top few cm of the soil (Ulaby, 1982), they only fully represent the root-zone for plants with shallow root systems. Further, these microwave measurements can be erroneous over organic soils and/or densely vegetated land surfaces (Dorigo et al., 2017; Ulaby, 1982). However, surface soil moisture is shown to be a reasonably proxy for root-zone soil moisture (Ford et al., 2014; Qiu et al., 2014), notwithstanding substantial seasonal variability, for example during dry-downs (Hirschi et al., 2014; Qiu et al., 2016). Another relevant proxy is available from satellite observations: SIF reflects plant photosynthetic activity, as it closely links to stomatal regulation and consequently to plant transpiration (Maes et al., 2020). However, the GOME-2 SIF should be used with care, as (i) the early equator overpass time of the satellite is 10:00 local solar time, which is well before vegetation reaches maximum

daily photosynthetic activity (Köhler et al., 2015), (ii) SIF measurements are vulnerable to excess cloudiness, inducing noise especially above the Amazon (Joiner et al., 2013; Köhler et al., 2015) and (iii) satellites might drift and/or sensors might damage over time, which further deteriorates the quality of the observations (EUMETSAT, 2017). Although satellite observations are subject to numerous measurement errors, they are not biased by model assumptions and therefore serve as an independent reference of the state of the land surface.

In-situ observations: (i) Surface carbon, energy and water fluxes can be measured at the ecosystem scale with *EC towers* and have been collected in the FLUXNET2015 dataset (Pastorello et al., 2020). (ii) *Soil moisture station measurements* are available from International Soil Moisture Network (ISMN) (Dorigo et al., 2021). (iii) Atmospheric wind speed, temperature and humidity measurements at the landscape scale are available from *weather balloons* and are organized in the IGRA dataset (Durre et al., 2006). (iv) Station-observed daily climate variables at the land surface are collected in the Global Historical Climatology Network (GHCN)-Daily dataset (Menne et al., 2012), where precipitation is the variable that is most widely available across stations. Although such measurements are distributed across the globe and therefore cover a range of climate, soil and vegetation types, they are not evenly distributed, as the coverage of most measurement networks is most dense in North America, Europe and Australia. To compensate the uneven distribution of in-situ observations and to accomplish ground-breaking global coverage, machine learning methods have been deployed successfully to exploit the wealth of in-situ observations (Ghiggi et al., 2019; Jung et al., 2019; O and Orth, 2021). Even if these datasets are observation-based, they should be applied carefully, as the performance of these data sets is typically poorer in areas (the tropics/arctics and desert regions) or during times that are undersampled (weather extremes) (Jung et al., 2020). However, these datasets prove essential for climate research as they exploit in-situ measurements by learning relations between physical quantities used as predictors.

Earth system models

Observations are vital for the initialization and validation and parameter calibration of an array of different models, including *Reanalysis models*, *Earth system models* and, for example, *mixed-layer models that simulate the evolution of the ABL*. Within this context, there are coupled and uncoupled models. Whereas uncoupled models rely on observation-based external forcing that elicits a response of a respective model diagnostic (ET response to air temperature), coupled models allow for interactions in both directions (ET response to air temperature, which consequently affects air temperature through changes in surface flux partitioning). Moreover, coupled models can be heavily constrained by historical observations, whereas unconstrained models can be used to project future climate conditions.

Uncoupled models can provide a great service in reducing the difficulty of model tasks by computing only the interactions that are of interest and considering the other relevant physical

quantities as external forcing. One example of this is Global Land Evaporation Amsterdam Model (GLEAM), which estimates evaporative components and surface and root-zone soil moisture relying solely on satellite observed data (Martens et al., 2017). Another example is CLASS4GL, which uses weather balloons and other observation-based ancillary data to compute the diurnal evolution of the ABL (Wouters et al., 2019). Although these models are extremely useful to study how external forcing (climate) affects the model output, they do not capture how, in turn, the model output affects the climate.

Numerous physical quantities are available from model output by coupled and heavily constrained models like ERA5 and ERA5-Land (Hersbach et al., 2020; Muñoz-Sabater et al., 2021). These models maximize their performance by constraining the model by assimilating any observation that proves useful for historical simulations. Therefore, the variable-specific model performance depends directly on the quality of the observations, which makes variables like air temperature and net surface radiation better constrained than, for example, ET and GPP. Due to these historical data assimilation techniques, such models can only provide historical simulations. Unconstrained Earth system models, for example from the Coupled Model Intercomparison Project Phase 6 (CMIP6) ensemble (Eyring et al., 2016), are more flexible and can be used both to simulate historical and to project future climate conditions (O'Neill et al., 2016). In order to do this, assumptions are necessary on, amongst others, land use change, (anthropogenic) CO₂ emissions and plant nutrient availability. Earth system models are the best tools currently at our disposal to learn about and try to anticipate possible future climate conditions and related extremes. As such, an accurate representation of the apparent evaporative regime in Earth system models can aid weather and climate forecasts, such that future agricultural practices can be tailor made, as well as, city greening, land cover management and afforestation to dampen the intensity of future weather and climate extremes (Schwaab et al., 2021; Sillmann et al., 2017).

Dryness indices

A myriad of dryness indices, such as the Aridity Index (AI) (Transeau, 1905), Palmer Drought Severity Index (PDSI) (Palmer, 1965) and the Standardized Precipitation Evapotranspiration Index (SPEI) (Vicente-Serrano et al., 2010), have been developed to specifically reflect aspects of the climate system, amongst which land-atmosphere coupling and corresponding terrestrial evaporation regimes, atmospheric and hydrologic dryness. These indices are being applied to reflect water availability for terrestrial evaporation or ecosystem functioning (Greve et al., 2017; Scheff et al., 2021; Scheff et al., 2017), but recently aroused suspicion with respect to their capability to do so (Scheff et al., 2021); As models consistently project decreases in these indices (Feng and Fu, 2013; Naumann et al., 2018; Zhao and Dai, 2017), which would indicate increasing water limitation, changes in plant available water (root-zone soil moisture) are ambiguous (Berg and Sheffield, 2019b; Berg et al., 2017; Greve et al., 2019), while photosynthesis is even projected to increase (Greve et al., 2017; Scheff et al., 2017). Evidently, these indices fail to accurately estimate the water availability that is relevant for ecosystem functioning, which

elicits the need for a more capable index. Currently, the way is being paved by indices that evaluate the importance of either energy or water availability for vegetation functioning (Berg and McColl, 2021; Zscheischler et al., 2015), but simultaneous evaluations of both energy and water availability are lacking.

1.2 Principal research questions

The aim of this thesis is to determine how water versus energy limited vegetation modulates climate climate and related extremes. Thereby, I optimally make use of a plethora of data from different data streams, ranging from satellite and weather balloon observations, to heavily constrained and unconstrained Earth system models, in order to compensate for shortcomings in individual data products. More specifically, the following three research questions crystallized that will be investigated and answered:

1. What is the role of soil moisture for terrestrial evaporation regimes?
2. How do terrestrial evaporation regimes vary regionally, across seasons and with climate change?
3. How do terrestrial evaporation regimes affect climate extremes?

1.3 Thesis Overview

This thesis consists of 7 chapters, including the general introduction. The research questions posed in the preceding section are investigated and answered in Chapter 2 through 6, as summarized in Figure 1.5. These chapters have been published (2, 3 and 5), are in revision (4) or are submitted (6) to peer-reviewed journals.

In **Chapter 2**, I introduce the Ecosystem Limitation Index (ELI): a novel correlative index that can distinguish energy versus water-limited conditions and related transitions (CSM). I do so by using (proxies for) energy and water availability and vegetation functioning from satellite observations over Europe. The CSM is determined at the continental and grid-based spatial scale. Further, the respective roles of various climate, soil and vegetation characteristics for the CSM are tested, as well as its robustness when determined using different data sets and proxies for energy and water availability.

In **Chapter 3**, I show that the influence of soil moisture on surface flux partitioning can be measured in the ABL. Atmospheric temperature and humidity measurements from weather balloons are translated at the hand of a mixed-layer model to estimate surface fluxes at the landscape scale. Further, I distinguish differing diurnal evolution of the ABL over energy- versus water-limited conditions.

In **Chapter 4**, I show a widespread shift from ecosystem energy to water limitation with climate change. To this end, the ELI is computed using data from a suite of state-of-the-art Earth system models. I show shifts towards ecosystem water limitation and related regime shifts both in space and in time. Further, I attribute these trends to trends of related eco-climate variables.

In **Chapter 5**, I analyze the spatially varying relevance of hydrometeorological hazards for vegetation productivity extremes. I compare concurrent anomalies and respective extremeness of hydrometeorological variables during SIF maxima and minima. In addition, I study the timing of such extremes. An attribution analysis reveals the respective drivers and the influence of underlying evaporative and related climate regimes. Finally, I investigate transitional areas where between vegetation productivity controls shift between water and energy variables.

In **Chapter 6**, I show that increasing ecosystem water limitation fuels future heat extremes. In this study, I use an ensemble of state-of-the-art Earth system models to compute ELI trends and assess their relevance for mean versus maximum temperature trends. I define numerous hot spots where heat extremes are amplified alongside shifts towards ecosystem water limitation and investigate how this relation is modulated by the initial evaporative regime.

In **Chapter 7**, I conclude the main findings of the chapters by answering the research questions. I discuss any overarching shortcomings of the analyses presented in the chapters and ideas for analyses to overcome them. Finally, I elaborate on additional avenues that have emerged from executing and discussing the analyses.

Overarching question: How does **water** versus **energy** limited vegetation modulate climate and related extremes?

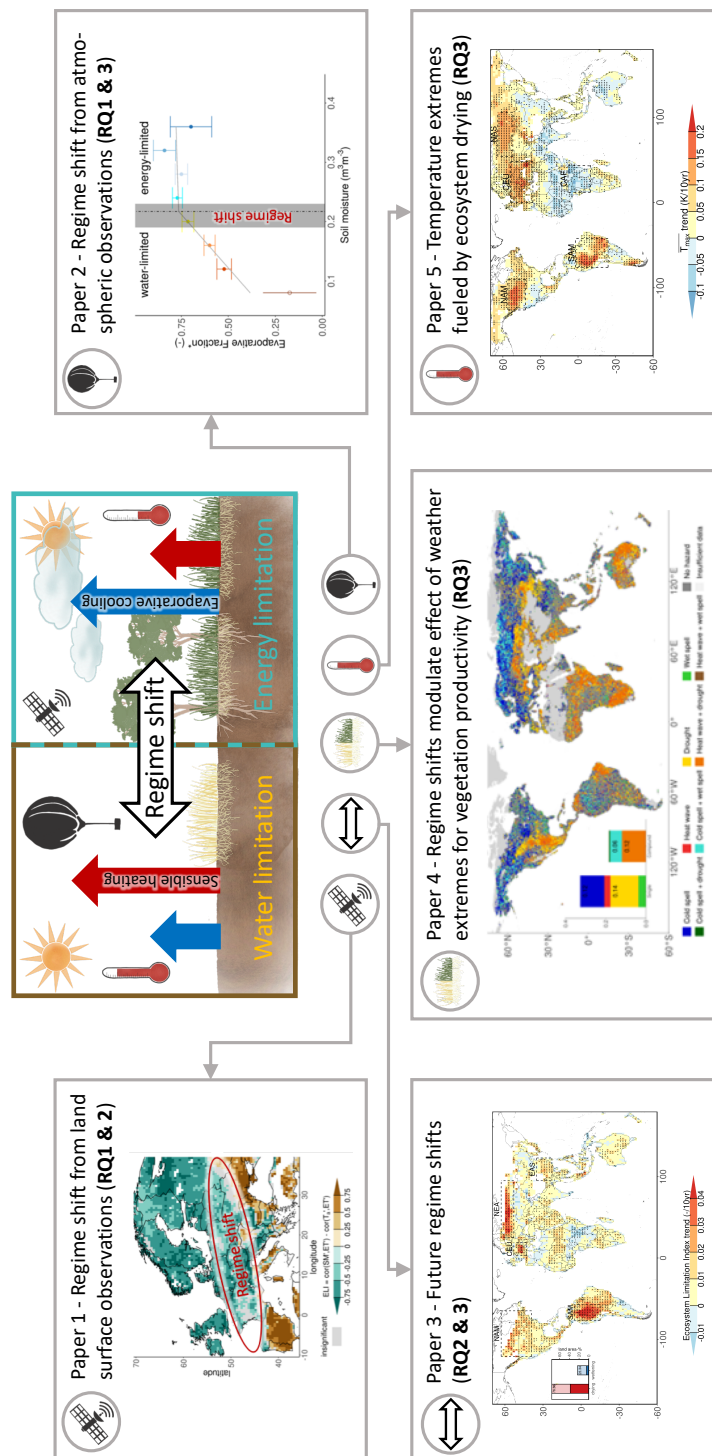


Figure 1.5: Visual representation of the thesis. The left-middle panel describes the differences between vegetation states in water- and energy-limited conditions, thereby affecting sensible heating and evaporative cooling and consequently climate extremes. All surrounding panels depict the (shared) first-author articles written during the thesis in Chapters 2 – 6 and which RQs they address, respectively.

Chapter 2

Terrestrial evaporation regimes from satellite observations

This chapter is based on:

J. M. C. Denissen, A. J. Teuling, M. Reichstein, and R. Orth (2020). “Critical Soil Moisture Derived From Satellite Observations Over Europe”. *Journal of Geophysical Research: Atmospheres* 125.6, e2019JD031672

Abstract

Terrestrial evaporation (ET) is a crucial quantity through which land surface conditions can impact near-surface weather and vice versa. ET can be limited by energy or water availability. The transition between water- and energy-limited regimes is marked by the critical soil moisture (CSM), which is traditionally derived from small-sample laboratory analysis. Here, we aim to determine the CSM at a larger spatial scale relevant for climate modeling, using state-of-the-art gridded data sets. For this purpose, we introduce a new correlation-difference metric with which the CSM can be accurately inferred using multiple data streams. We perform such an analysis at the continental scale and determine a large-scale CSM as an emergent property. In addition, we determine small-scale CSMs at the grid cell scale and find substantial spatial variability. Consistently from both analyses we find that soil texture, climate conditions, and vegetation characteristics are influencing the CSM, with similar respective importance. In contrast, comparable CSMs are found when applying alternative large-scale energy and vegetation data sets, highlighting the robustness of our results. Based on our findings, the state of the vegetation and corresponding land-atmosphere coupling can be inferred, to first order, from easily accessible satellite observations of surface soil moisture.

2.1 Introduction

Terrestrial evaporation (ET) is a crucial variable in land-atmosphere interactions, since it affects the carbon, energy, and water balances. Therefore, ET can potentially impact weather and climate, especially during extreme events such as droughts and heat waves (Guillod et al., 2015; Hirschi et al., 2011; Koster et al., 2016; Koster et al., 2004; Taylor et al., 2012). Conceptually, we distinguish two evaporative regimes: (i) the water-limited regime, where ET is mainly controlled by soil moisture availability, and (ii) the energy-limited regime, where ET is mostly governed by energy (temperature and radiation) supply (Budyko, 1974; Seneviratne et al., 2010). Consequently, regime shifts potentially induce changes in the causality of energy and water availability for ET. This could dampen or amplify land-atmosphere interactions, like evaporative cooling (Seneviratne et al., 2010). Therefore, the critical soil moisture (CSM) associated with this regime shift in the conceptual framework is a crucial parameter.

Traditionally, specific CSM values have been associated with characteristic matric potentials for particular vegetation and soil types (Genuchten, 1987). By doing so, the determination of CSMs is straightforward in areas of homogenous soils and vegetation (Homaee et al., 2002). However, the range of CSMs across soil and vegetation types is substantial: Teuling et al. (2009b) report CSMs within one model ranging from 16.7 Vol-% for sandy soils to 42.4 Vol-% for clayey soils based on pedotransfer functions. Additionally, there is considerable variation between CSMs of different models. Novák and Havrila (2006) determine somewhat different CSMs ranging from 2.7 Vol-% in a sandy soil to 13 Vol-% in a loamy soil, which they refer to as the critical soil water content. These different values illustrate that even at smaller scales, there are discrepancies between CSMs determined with various methods. Further, the uncertainty of the CSM, among other soil hydraulic parameters, is enhanced by different pedotransfer functions and different soil texture data sets (Van Looy et al., 2017). In addition, the dependency of the CSM on local soil and vegetation conditions renders it difficult to derive large-scale estimates from previous analyses and literature.

Besides its conceptual relevance, the CSM is an important parameter and/or emergent property in land models, which are embedded into weather and climate (forecasting) models that serve society. Land models have an inherent assumption of the above-mentioned water- and energy-controlled evaporative regimes and of the transition between them, as marked by the CSM (Arora, 2002; Pitman, 2003; Sellers et al., 1997). As the determination of a large-scale CSM is lacking, considerable difference exists between current model estimations of the CSM (Teuling et al., 2009b), leading to inconsistent simulation results. Additionally, comparison of CSMs between models is not straightforward, as absolute values of soil moisture are model dependent and do not necessarily correspond with observed soil moisture (Koster et al., 2009). Further, as these models operate at relatively large spatial scales, the simulation of the evaporative regimes is hard to validate and a source of considerable uncertainty (Guillod et al., 2013).

Large-scale assessments of evaporative regimes have been performed previously based on various metrics with both observational and modeled data sets; where in some of these studies the determination of the CSM is lacking (Koster et al., 2009; Seneviratne et al., 2006; Teuling et al., 2009a; Zscheischler et al., 2015), other analyses have determined CSMs based on modeled data sets, which reflect implemented relationships between soil moisture (SM) and evaporative fraction (EF) (Schwingshackl et al., 2017). There are only a few recent studies that determine observation-based CSMs at the regional-continental scale. Such large-scale analyses have only recently become feasible thanks to the increasing availability of satellite-derived data sets (e.g., (Liu et al., 2012; Tramontana et al., 2016)). For example, Feldman et al. (2019) estimate the CSM over Africa by assuming a piecewise linear model based on satellite observations of surface soil moisture and diurnal temperature amplitude. Haghighi et al. (2018) determine the CSM in a similar manner but using field observations of SM and EF over semiarid regions outside of the growing season, effectively excluding the effects of plant transpiration from their estimates. Finally, Akbar et al. (2018) determine the CSM over the contiguous United States by assessing the characteristics of dry-downs from satellite surface soil moisture from the National Aeronautics and Space Administration (NASA) Soil Moisture Active Passive (SMAP) mission during three consecutive summers only.

In this study, we focus on determining regional-continental-scale CSMs from observational data in Europe, as regime transitions are known to occur frequently in this region (Seneviratne et al., 2006; Teuling et al., 2009a). Moving beyond the previous studies, we propose a novel correlation-difference metric to characterize the CSM. This metric uses data on energy and water availability, as well as vegetation functioning, and thereby determines the CSM based on comprehensive Earth observations. We estimate the CSM at different spatial scales: (1) a continental-scale estimate will serve as observational constraint for land surface models (large-scale CSM), while (2) small-scale grid cell estimates will reflect the spatial heterogeneity of the CSM (small-scale CSM). Further, we investigate the sensitivity of the CSM to climate, soil, and vegetation characteristics, and its robustness when determined with different data sets.

2.2 Data and Methods

We propose a novel metric to evaluate water- versus energy-limited conditions in each grid cell:

$$\Delta corr = corr(A_E, A_V) - corr(A_W, A_V) \quad (2.1)$$

where A indicates bimonthly (twice per month, concerning the first and second half of the month) anomalies of particular energy (E), vegetation (V), or water (W) variables, and $corr$ denotes a temporal correlation between anomaly time series. The default $\Delta corr$ metric from Eq. 2.1 is calculated using surface soil moisture (from the European Space Agency (ESA) Climate Change

Initiative (CCI) program), surface temperature (from E-OBS), and ET (from FLUXCOM). We note that FLUXCOM ET is not an observational product but derived from multiple data streams using machine learning techniques. This data set is chosen because, unlike process-based models, it does not involve any assumption or implementation of a SM-EF relationship. All time series are linearly detrended, before anomalies are computed by subtracting the mean seasonal cycle. To assure no confounding impacts of nonlinearities, Kendall's rank correlations are computed. $\Delta\text{corr} > 0$ indicates that vegetation anomalies correlate stronger with energy than with water anomalies, such that the grid cell would be referred to as energy limited. Correspondingly, $\Delta\text{corr} < 0$ indicates that a grid cell is water limited. When $\Delta\text{corr} \approx 0$, the magnitudes of energy and water limitations are equal, thus, corresponding to frequent regime shifts and marking the related CSM. Therefore, this metric enables a simple and straightforward determination of the CSM.

All data sets employed in this study are listed in Table 2.A1. All energy, vegetation, and water variables are aggregated to a common $0.5^\circ \times 0.5^\circ$ spatial resolution. Thereafter, bimonthly averages are calculated, to mitigate the effect of synoptic weather variability on our analyses and because at this timescale the response of ET to soil moisture is the strongest (Boese et al., 2019; Teuling et al., 2006). A bimonthly average is only calculated when at least 5 days per 2-week period are available, to account for gaps in the ESA CCI SM data set due to, for example, snowy or extremely dry soil. Given the required concurrent availability of data sets, we consider the time period 2007-2015, which meets the requirements for the minimum of 4-6 years of data recommended for calculating land-atmosphere interactions metrics as in Eq. 2.1 (Findell et al., 2015).

Table 2.1: Data Sets Used in This Study.

Data set	Version	Variable(s)	Spatial res.	Temp. res.	Derived from	Reference
ESA CCI	04.4	Surface soil moisture _w	0.5° x 0.5°	Daily	Satellite observations	(Dorigo et al., 2017) (Gruber et al., 2017) (Liu et al., 2012)
E-OBS	17.0	Surface temperature _E and precipitation	0.25° x 0.25°	Daily	Station observations	(Haylock et al., 2008)
FLUXCOM	2	Terrestrial evaporation ET _V and gross primary production GPP _V	0.25° x 0.25°	8-daily	Multiple datastreams processed with machine learning techniques, using eddy covariance-derived ET observations as target	(Tramontana et al., 2016)
ERA	2	Incoming shortwave radiation _E , net shortwave radiation, net longwave radiation, and vapor pressure deficit _E	0.5° x 0.5°	Daily	Reanalysis model	(Dee et al., 2011)
GIMMS3g	4	normalized difference vegetation index (NDVI) _V	0.025° x 0.025°	Bimonthly	Satellite observations	(Zhu et al., 2013)
GOME-2	GFZ	Sun-induced chlorophyll fluorescence (SIF) _V	0.5° x 0.5°	8-daily	Satellite observations	(Köhler et al., 2015)
Soilgrids	0.5.1	Fraction clay, sand, and silt	0.1° x 0.1°	-	Satellite observations	(Hengl et al., 2017)
MCD12Q1	005	Fraction land cover	500m x 500m	-	Satellite observations	(Friedl et al., 2010)

We focus on the warm season in this study to exclude the impact of ice and snow and to focus on active vegetation functioning. In this context, data will be considered only if the bimonthly temperature exceeds 10°C. This can lead to a different number of bimonths filtered in different grid cells. Correlations (Eq. 2.1) are calculated per grid cell, and per season. Using all available bimonths from a particular season across all years ensures a meaningful amount of data points. No seasonal correlation is computed if less than six data points are available.

2.3 Results and Discussion

Analyzing in a first step the summer (June-August) mean surface soil moisture we find a north-south gradient across Europe (Figure 2.1a). Apart from this general pattern, soil moisture in

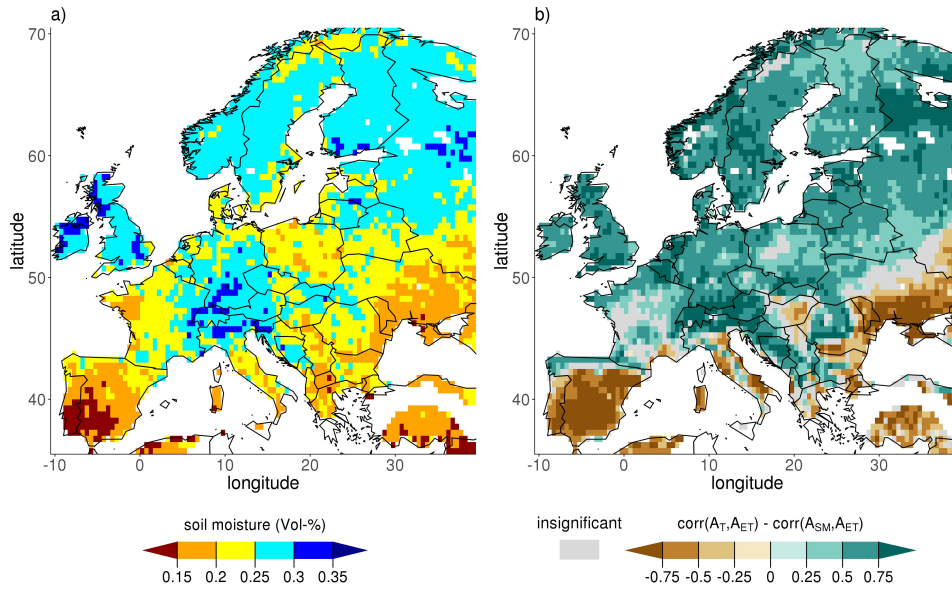


Figure 2.1: Distribution of surface soil moisture and evapotranspiration regimes in Europe. (a) Spatial variability of average surface soil moisture from the ESA CCI data set and (b) Δcorr in the summer (JJA), computed according to Eq. 2.1 with soil moisture from ESA CCI, FLUXCOM ET, and E-OBS surface temperature (see also Table 2.1). The Δcorr is only calculated if it is significant, that is, within the 90% confidence interval.

panel (a) tends to be higher in mountainous regions such as the Alps or the Carpathian Mountains. As expected, negative Δcorr in panel (b), indicating water-limited conditions, generally coincide with lower soil moisture. Correspondingly, energy-limited conditions (positive Δcorr) occur in regions where ample soil moisture is available. Insignificant Δcorr values occur in northern Scandinavia due to a lack of available soil moisture data related to low surface temperatures and in between water- and energy-limited regions across central Europe, marking the transitional regions. Next to these spatial variations, Figure 2.A1 in the supporting information shows seasonal variation of soil moisture in panel (a)-(c) and of Δcorr in panels (d)-(f). Winter is not shown, because there are hardly any significant Δcorr values. Generally, water-limited conditions coincide with dry soils and energy-limited conditions coincide with wet soils. From springtime to summertime, conditions shift from energy limited to transitional in central Europe and parts of the Mediterranean, likely due to a decrease in soil moisture content. In autumn, water-limited conditions persist in the Mediterranean. This possibly reflects that, while surface soil moisture in the Mediterranean is already replenished (panel c), the root zone, where vegetation extracts the majority of its moisture, is still dry. This derived spatial pattern of Δcorr is an important result as it is based solely on (satellite-)observable variables and can hence serve as a benchmark for models, which mostly simulate these variables.

In a next step, we analyze the relation between soil moisture and Δcorr , as depicted in Figure 2.2. Each point in the scatterplot depicts soil moisture and Δcorr at a given grid cell and in a

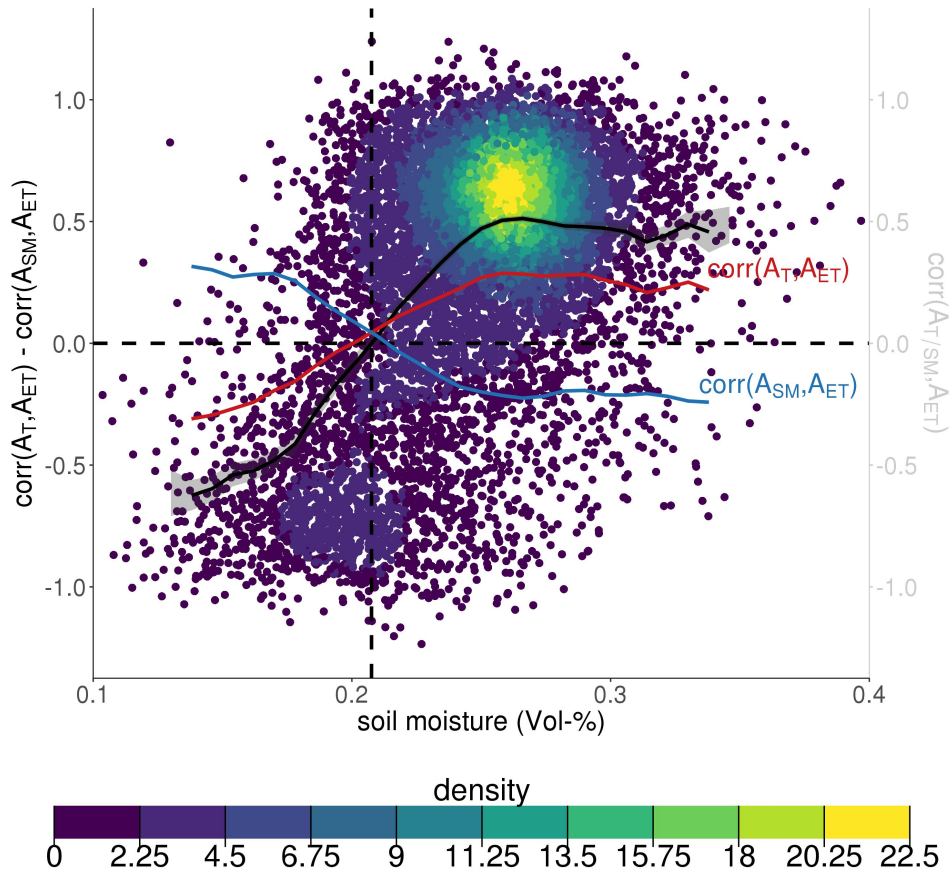


Figure 2.2: Sensitivity of Δcorr to soil moisture across all grid cells in Europe. Each dot represents a particular grid cell and season. The black line is a moving average through the points, while the gray ribbon indicates the 5% and 95% percentiles of moving averages through 1000 bootstrapped samples of the data points. In addition, moving averages are also displayed for individual correlations from Eq. 2.1 where the individual points are not shown. The color imposed on the data points reflect the density of data points.

given season (basically Figure 2.A1 soil moisture in (a)-(c) plotted against the Δcorr in (d)-(f)) and the coloring indicates the density of the data points. The red and blue moving average lines indicate the governing processes in the respective evaporative regimes: When the soil moisture content is low, ET is water limited, resulting in $\text{corr}(A_T, A_{ET}) < 0$ and $\text{corr}(A_{SM}, A_{ET}) > 0$. At wetter soil moisture contents, ET is governed by energy supply, resulting in $\text{corr}(A_T, A_{ET}) > 0$ and $\text{corr}(A_{SM}, A_{ET}) < 0$. The negative $\text{corr}(A_{SM}, A_{ET})$ at higher soil moisture contents might be related to a confounding, negative correlation between surface temperature and soil moisture: A wet soil moisture anomaly might result from a precipitation surplus, which tends to occur jointly with a negative surface temperature anomaly.

The difference between the moving averages of the individual correlations yields the moving average of Δcorr (thick black line), of which negative values indicate water-limited conditions and positive values indicate energy-limited conditions. These fitted lines are likely not representing the behavior at every single grid cell but depict the general relationship. But this illustrates the key advantage of the Δcorr metric over CSM estimation using actual and potential ET (Seneviratne et al., 2010) or the relationship between SM-EF (Haghighi et al., 2018; Schwingshackl et al., 2017): The CSM can be simply inferred from where the moving average switches sign, without applying piecewise linear models with potentially poor fits. In Figure 2.2 we derive a large-scale CSM at approximately 21 Vol-%. This value entails temporal and spatial variability, from different seasons and grid cells, respectively. The ribbon around the moving average line reflects the uncertainty in the moving average and illustrates the 5% and 95% percentiles of moving averages based on 1,000 bootstrapped samples from the data points. This uncertainty is relatively small thanks to the large amount of data used. The ribbon is narrowest between approximately 20 and 30 Vol-%, as the majority of the data points have soil moisture contents in that range, as can be seen by the density of the points. Further, we test the potential role of confounding effects for our analysis using partial correlations in Figure 2.A2. Accounting for the confounding effect of soil moisture on the correlation between temperature and ET, as well as the confounding effects of temperature on the correlation between soil moisture and ET, we find very similar results as in Figure 2.2. This suggests that confounding effects do not significantly influence the individual correlations that form Δcorr .

Note that even though we employ observation-based soil moisture in our analysis, the derived large-scale CSM of 21 Vol-% is somewhat model based. This is because the values of the ESA CCI soil moisture are derived by scaling the satellite-observed temporal dynamics against modeled data (Dorigo et al., 2017). Therefore, only analyses using the same soil moisture product can make use of our absolute derived CSM values, while all other studies should rather use it in a relative sense: 21 Vol-% is drier than 85% of the European grid cell seasonal mean soil moistures. Another study based on satellite-derived surface soil moisture from NASA SMAP mission reports a median of CSMs of 18 Vol-% over the contiguous United States (Akbar et al., 2018). This result, as well as our estimate, is more to the dry side than currently assumed in models, which often become water limited just below or at the field capacity (Teuling et al., 2009b). Therefore, the large-scale CSM is an emergent property of the European land climate system and thus can be used as a continental reference CSM.

It is known that soil, climate, and vegetation characteristics can locally influence the CSM (Feldman et al., 2019; Haghighi et al., 2018; Novák and Havrila, 2006). To investigate this on a large scale, moving average lines based on subselections of data representing particular soil, climate, and vegetation types are shown in Figure 2.3: (a) soil types have been determined using depth-weighted average soil texture fractions of the top meter from the SoilGrids data set (Hengl et al., 2017). Across all grid cells in Europe, the 75% quantile has been calculated for clay, silt, and sand fractions, respectively. Any grid cell exceeding this respective threshold is classified as clay, sand, or silt, leaving a mixed soil class for the remaining grid cells, in

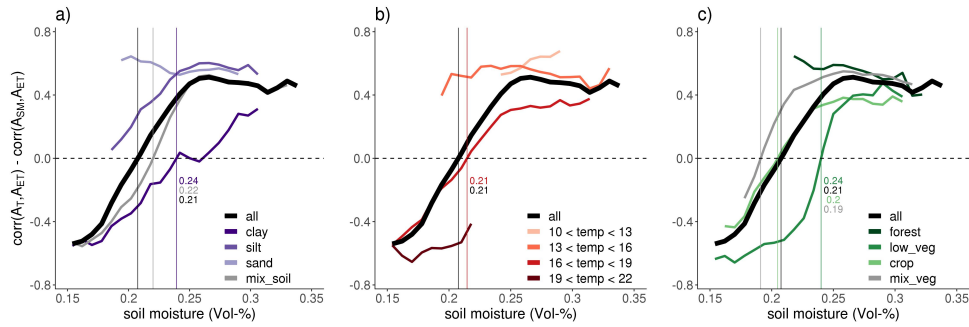


Figure 2.3: Soil, climate, and vegetation effects on the large-scale mean CSM. Moving average lines are calculated with subgroups of the data, based on, from left to right, different soil textures, climate classifications, and vegetation types. The thick black lines are the same as in Figure 2.2.

Figure 2.3; (b) for the climate types, grid cells are classified according to their long-term average surface temperature; and (c) vegetation types have been derived from the Moderate Resolution Imaging Spectroradiometer land cover data set MCD12Q1 (Friedl et al., 2010). The forest class in Figure 2.3 comprises evergreen/deciduous broadleaf/needleleaf and mixed forest categories. Low vegetation includes closed/open shrublands, (woody) savannas, and grasslands. And crop consists of all cropland land cover types. A grid cell is classified as forest, low vegetation, or crop if the respectively considered land cover fractions exceed the European 75% quantile of the respective vegetation type, leaving a mixed vegetation class for the remaining grid cells. Figure 2.3 shows that the large-scale CSM varies by few Vol-% in response to different soil textures, climate conditions, and vegetation classes. These tested characteristics seem to have comparable little influence on the CSM. They might be interdependent with, for example, colder surface temperatures predominantly coinciding with forest. As for the soil types, the CSM for clay is wetter than for all soil textures combined, which is expected because clay has a more negative matric potential than coarser soil textures with dominant sand and silt fractions, and is in line with earlier findings (Akbar et al., 2018; Feldman et al., 2019). The regions within the sand and silt classes appear permanently energy limited. Concerning climate types, interestingly, regime transition, is only observed for the second-warmest class. In contrast, colder climate regions are generally energy-limited and warmer climate regions water limited. Forested regions are not subject to regime transition either, as trees have deep-reaching roots which can access deep(er) water reservoirs to avoid water limitation. Correspondingly, low vegetation and crop with shorter root systems are more water limited, resulting in slightly different CSMs. In summary, in Europe the CSM tends to be slightly wetter for (i) finer soils, (ii) warmer surface temperatures, and (iii) shorter vegetation, which hampers advocacy for a single, representative large-scale CSM.

In the previous analyses, Δcorr was calculated with anomalies from surface soil moisture (water), surface temperature (energy), and ET (vegetation). The largest part of ET is accounted for by plant transpiration (Good et al., 2015; Lawrence et al., 2007; Schlesinger and Jasechko, 2014), associated with photosynthetic activity. Sun-induced chlorophyll fluorescence (SIF), gross primary productivity (GPP), and Normalized Difference Vegetation Index (NDVI) are reflections

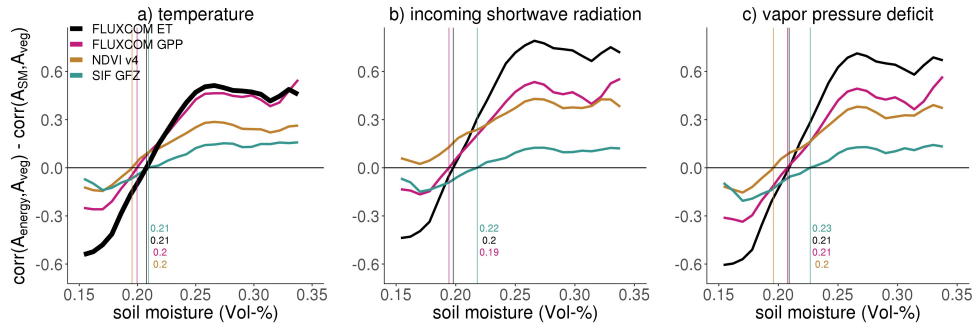


Figure 2.4: Robustness of the large-scale mean CSM across different employed energy and vegetation products. The different panels reflect Δcorr based on anomalies of different energy variables, from left to right: temperature (a), incoming shortwave radiation (b) and VPD (c). The different colored moving averages imply different vegetation data sets. As in Figures 2.2 and 2.3, the thick black line in the left panel (a) shows the reference moving average line, which is computed with bimonthly anomalies of ET and surface temperature.

of photosynthetic activity and can therefore be regarded as reasonable proxies for ET. Next to that, plants adjust their stomatal resistance in response to changes in atmospheric energy availability in the form of leaf temperature, incoming shortwave radiation or vapor pressure deficit. Figure 2.4 shows the corresponding results derived by substituting (a) surface temperature anomalies with (b) incoming shortwave radiation in or (c) vapor pressure deficit anomalies in (c). In addition, ET anomalies are replaced by NDVI, sun-induced chlorophyll fluorescence (SIF), and gross primary production anomalies. Applying alternative data products yields similar CSMs, generally deviating only a few Vol-% from the previously obtained 21 Vol-%. This highlights the robustness of the Δcorr metric across various data products. Further, the choice of data products affects the magnitude of Δcorr denoting the strength of the energy or water limitation, respectively. Regardless of the applied energy variable, the strongest Δcorr signal is derived with the FLUXCOM ET data set. This can be explained as ET represents a flux, which is expected to respond quicker to changing water availability, yielding stronger Δcorr signals than one would expect with state variables. In contrast, NDVI as a state variable responds more slowly, yielding lower Δcorr amplitudes. Moreover, changing water use efficiency under dry conditions can affect ET results in Figure 2.4. The weakest Δcorr signals are obtained with SIF. This is surprising as SIF rather represent a flux as, for example, ET, and not a state. A reason for this could be the relatively early equator overpass time of the GOME-2 satellite, 10:00 local solar time (Köhler et al., 2015), which is when radiation and leaf temperature are usually not at their daily maxima such that the vegetation is not yet most active. Table 2.A1 shows a systematic negative bias and less robust values across energy and vegetation products of large-scale CSMs estimated from $\text{corr}(A_{\text{energy}}, A_{\text{veg}})$ in comparison with CSMs estimated from Δcorr .

In a next step, we further explore small-scale, grid cell CSMs. Whereas the large-scale CSM is mostly inferred from soil moisture variations in space, the small-scale CSMs are estimated from bimonth-of-year soil moisture variations in time. This allows to study the effect of year-to-year

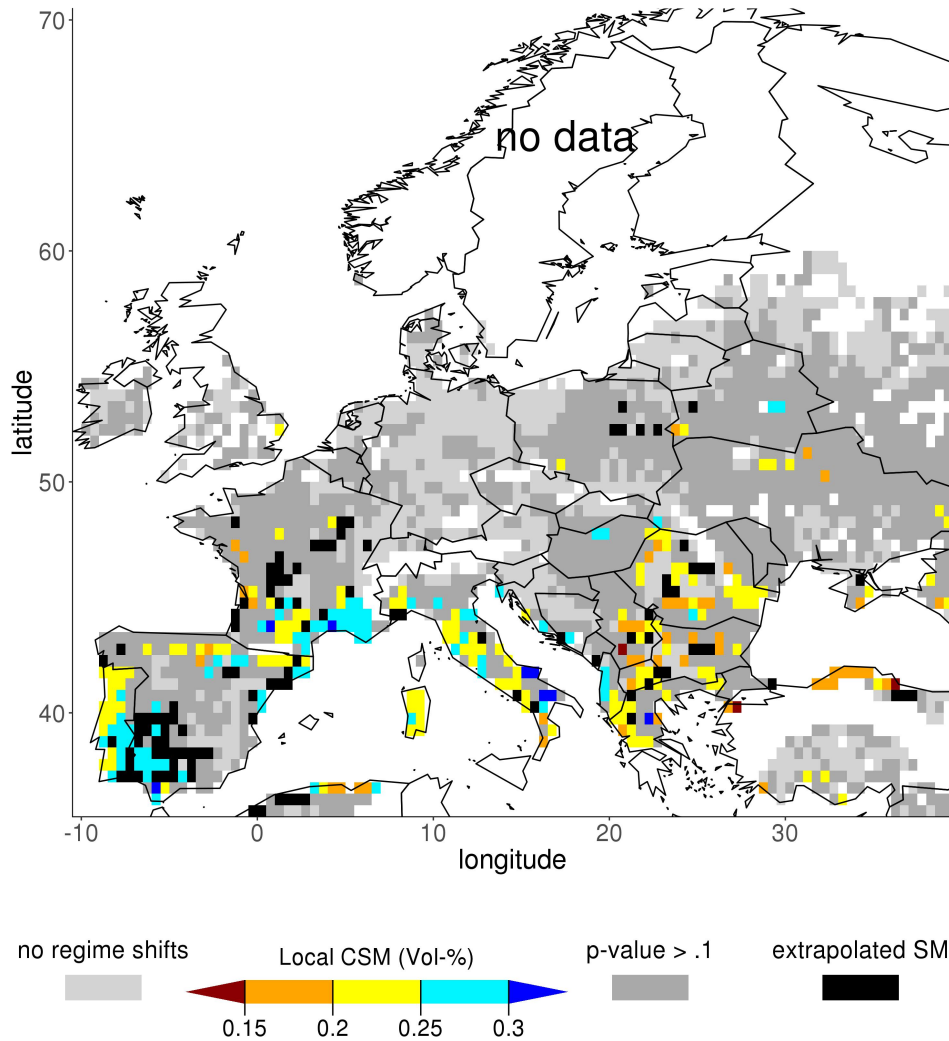


Figure 2.5: Estimation of the small-scale CSM based on linear regression between bimonth-of-year average soil moisture and Δcorr . Light gray grid cells denote regions where no regime shifts occurred. In dark gray regions regime shifts have occurred, but a p-value of the linear model exceeds 0.1. Black grid cells indicate that the value of the CSM falls outside of the local measured range of soil moistures. White regions indicate missing data.

variability of each available bimonth. For this purpose, we focus on grid cells that experience both water- and energy-controlled conditions, that is, where soil moisture crosses the CSM. This is achieved by selecting grid cells where Δcorr is negative and positive for at least one bimonth of year, respectively. In each of the grid cells where regime shifts occur, we fit a linear regression on bimonth-of-year soil moistures and corresponding Δcorr values. The small-scale CSM is then inferred from the regression line at $\Delta\text{corr} = 0$. Several steps ensure a meaningful estimation of the small-scale CSM: (1) There should be at least 10 data points (bimonths of

year) where soil moisture and Δ_{corr} are available. (2) The slope of the linear model should be positive. (3) The p-value of the linear model should not exceed 0.1 to ensure a reasonably strong linear relationship, given that there only 10-24 data points available per grid cell. (4) The CSM needs to be within the range of observed soil moistures to ensure a physically possible CSM. An example of the local estimation of the CSM is shown in Figure 2.A3. Figure 2.5 shows the spatial distribution of the small-scale CSMs. Most of the CSMs are determined in central and southern Europe within the range of 20-25 Vol-%, which is comparable to the previously determined CSMs in Figure 2.3. Next to that, there are ample grid cells where (i) data availability is insufficient (white grid cells), (ii) no regime shifts are occurring (light gray grid cells), (iii) the linear relationship is too weak (dark gray grid cells), or (iv) the estimated CSM falls outside of the range of observed soil moistures (black grid cells). A closer look at the distribution of the range of CSMs is given in Figure 2.A4. We find similar soil, climate, and vegetation controls for the small-scale CSMs (Figure 2.A5), confirming results from Figure 2.3.

2.4 Limitations

The Δ_{corr} metric is computed using ESA CCI surface soil moisture, which is determined from satellite observations. These are based on microwaves that penetrate only into the upper few centimeters of the soil (Ulaby, 1982). The depth of the surface layer in this soil moisture product is not well defined, since this soil moisture product is a composite of multiple microwave sensors with different frequencies and hence slightly different penetration depths (Dorigo et al., 2017). It is not fully representative of the vegetation-accessible soil moisture. However, there is no root zone soil moisture data set with a spatial and temporal coverage comparable to that of the ESA CCI data set. Assessing the potential effect of this shortcoming, we analyze reanalysis and station-based soil moisture from multiple depths and find that surface soil moisture is a reasonable proxy for root zone soil moisture, albeit with seasonal variations in their relationship (Figure 2.A6). Similar results are reported for example by Hirschi et al. (2014) who find similar surface and root zone soil moisture in mean climatological conditions, or Qiu et al. (2016) who find differences only under extremely dry conditions. Some decoupling between surface soil moisture and root-zone also emerges in Figure 2.A1, where similar surface soil moisture values coincide with different Δ_{corr} values. This is also reflected in the seasonal variability of Δ_{corr} results as shown in Figure 2.A7. This pattern can be explained with seasonal discrepancies between surface and root-zone soil moisture: In springtime, root-zone soil moisture is generally still readily available, but the surface soil moisture is generally lower due increased bare soil evaporation. This means that ET could occur at its maximum rate, while lower surface soil moistures are registered by satellites, resulting in a lower springtime CSM. This discrepancy between surface and root-zone soil moisture causes the entire moving average to shift to the dry end, as can be seen in Figure 2.A7. In autumn, the contrary is observed: As precipitation occurs more frequently after summer, first, the surface layer is moistened, but it takes time to replenish the moisture deficit in the root-zone, leading to a higher CSM (shift of the autumn moving

average to the wet end). The seasonal variability in representativeness of surface soil moisture for the root-zone can possibly impact the linear model which is used for the estimation of the local CSM in Figure 2.5, as these linear models are based on maximally 24 data points. Further, surface satellite soil moisture estimates have larger measurement uncertainties on densely vegetated and/or organic soils (Dorigo et al., 2017; Ulaby, 1982).

While similar Δcorr values could in principle be derived with different combinations of the individual correlations, Figure 2.A8 illustrates that Δcorr usually corresponds to unique combinations, making it unambiguous. Further, there is a significant large scatter across data points in Figure 2.2 and illustrated in Figure 2.A8. There are several reasons for this underlying uncertainty, next to the limitations related to using satellite surface soil moisture: (1) Soil moisture is known to have profound memory characteristics (Orth and Seneviratne, 2012), such that legacy effects might play a role but are not considered here for simplicity, (2) confounding impacts of soil moisture on $\text{corr}(A_T, A_{ET})$, and of surface temperature on $\text{corr}(A_{SM}, A_{ET})$, are also not taken into account. The role of these confounding effects is investigated in Figure 2.A2 using partial correlations. We find overall negligible impact of such effects on Δcorr . Finally, (3) human influence on soil moisture and consequently vegetation through, for example, irrigation or land use changes, can introduce non-natural variability into our analysis. Fortunately, none of the limitations listed above affects all grid cells at the same time. Therefore, we are confident that our large-scale analysis with thousands of grid cells employs enough information to derive meaningful results despite the uncertainties introduced by the limitations.

2.5 Conclusions

In this study we build upon the conceptual frameworks of Budyko (1974) and Seneviratne et al. (2010). We introduce a novel metric to infer energy- or water-limited conditions, which does not rely on prior assumptions on the relationship between soil moisture and EF and uses observation-based data sets, which describe water and energy availability and vegetation functioning. This metric is applied to determine the CSM.

We derive a large-scale CSM representative for the European continent, as well as a range of small-scale CSMs representative locally at particular grid cells. Within the large-scale analysis we obtain spatial patterns of water versus energy limitation in Europe and respective dependency on mean surface soil moisture. At this continental scale, the CSM is determined at 21 Vol-%. This is more toward the dry end of the spatiotemporal European soil moisture distribution and therefore in contrast to land models, which often assume water-limited conditions just below or at the field capacity. This finding can help to improve soil moisture stress representations in models. Application of the determined large-scale CSM directly as a land surface parameter in land models, however, should be avoided due to dependency on the employed surface soil moisture data set. Next to the large-scale CSM, we determine a range of small-scale CSMs and find ample variability according to local soil, climate, and vegetation characteristics. With readily

available satellite soil moisture information, the small-scale CSMs allow real-time diagnosis of land-atmosphere interactions and their corresponding role during climate extremes, such as heat waves or droughts.

2.A Appendix

This appendix represents the supplementary materials of the presented publication.

Introduction

In the supporting material 7 figures and 2 tables are presented. Fig. S1 show the seasonal variation of mean surface soil moisture and Δcorr , as an addition to Fig. 1. Fig. S2 shows the effect of excluding the confounding variables surface temperature and surface soil moisture on the Δcorr and its individual components. Fig. S3 until Fig. S5 present auxiliary information to the local CSM as derived in Fig. 5. Fig. S6 illustrates the seasonality of the representativeness of surface soil moisture for root-zone soil moisture. Fig. S7 shows moving averages per season. Fig. S8 shows the relation between Δcorr and its individual components. Table 2.A1 provides information about the bias between spatial CSMs derived with $\text{corr}(A_{\text{energy}}, A_{\text{veg}})$ and Δcorr . Table 2.A2 contains details about the soil moisture stations used in Fig. S3.

Table 2.A1: CSM as estimated through $\text{corr}(A_{\text{energy}}, A_{\text{veg}})$ minus the CSM estimated through Δcorr for different energy and vegetation products. The CSM does not exist when calculated with NDVI v4 and incoming shortwave radiation.

	FLUXCOM ET	FLUXCOM GPP	NDVI v4	SIF GFZ
Temperature	-0.02	-0.04	-0.04	-0.06
Incoming shortwave radiation	-0.03	-0.05	-	-0.05
vapor pressure deficit (VPD)	-0.02	-0.02	-0.02	-0.03

Table 2.A2: Soil moisture stations used in Figure 2.A3 and corresponding details.

Station (country)	Location (lat,lon)	Data period	Soil moisture measurement depths (in cm)
Basel (CH)	47.5°N, 7.60°E	Aug 2009 - Dec 2012	5, 10, 30, 50, 80
Creon 'd Armagnac (FR)	44.0°N, -0.6°E	Jul 2007 - Dec 2015	5, 10, 20, 30
Falkenberg (DE)	52.10°N, 14.07°E	Jan 2003 - Dec 2013	8, 15, 30, 45, 60, 90
Haapaveesi (FIN)	64.10°N, 25.40°E	May 2001 - Oct 2006	10, 30, 50, 70, 90
Kehrigk (DE)	52.11°N, 13.57°E	Jan 2003 - Dec 2013	10, 20, 30, 60, 90, 150
Kuusamo (FIN)	66.30°N, 29.40°	Jun 2004 - May 2012	10, 30, 50, 70, 90
Oensingen (CH)	47.30°N, 7.70°E	Jan 2002 - Dec 2007	5, 10, 30, 50, 80
Payerne (CH)	46.80°N, 6.90°E	Aug 2008 - Dec 2012	5, 10, 30, 50, 80
Peyrusse (FR)	43.38°N, 0.13°E	Jul 2007 - Dec 2015	5, 10, 20, 30
Suomussalmi (FIN)	64.90°N, 28.70°	Jun 2004 - Apr 2011	10, 30, 50, 70, 90
Urgons (FR)	43.64°N, -0.43°E	Jul 2007 - Nov 2015	5, 10, 20, 30

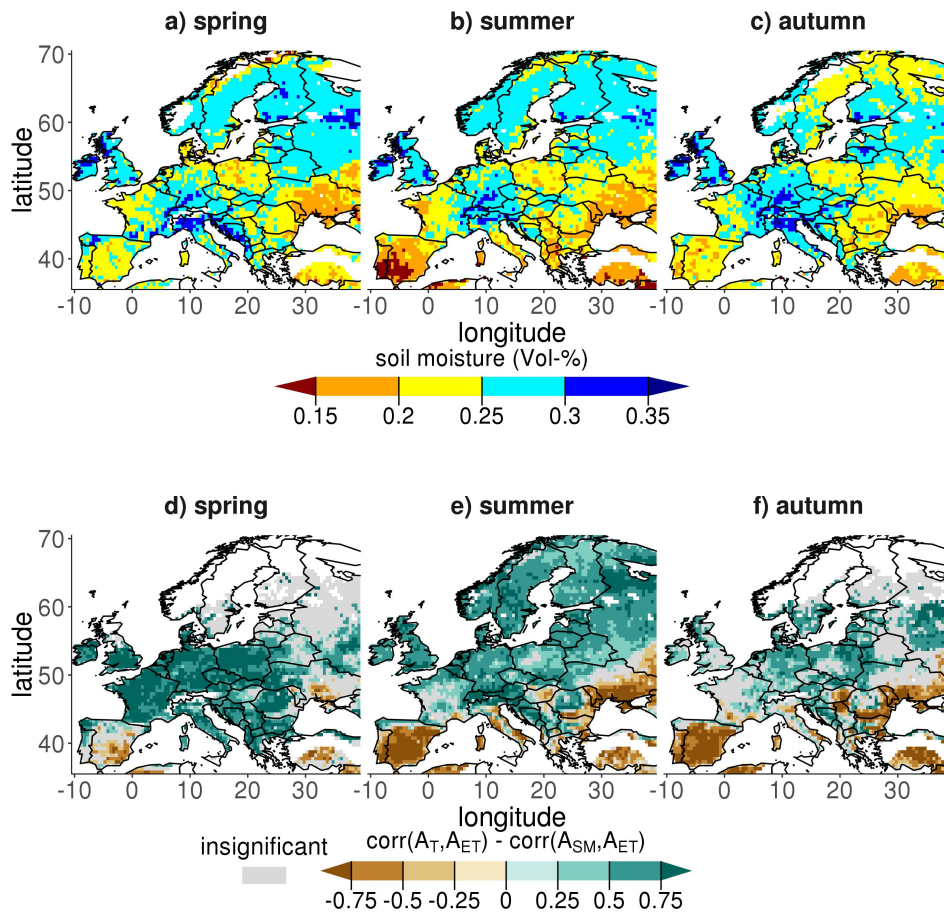


Figure 2.A1: Distribution of surface soil moisture and evapotranspiration regimes in Europe. Spatial variability of surface soil moisture (top) from the ESA CCI dataset and Δcorr (bottom), computed according to Eq. (1) with soil moisture from ESA CCI, FLUXCOM ET and E-OBS surface temperature per season, excluding winter. The Δcorr is only calculated if it is significant, with significance being defined as when the Δcorr falls outside of its 90% confidence interval.

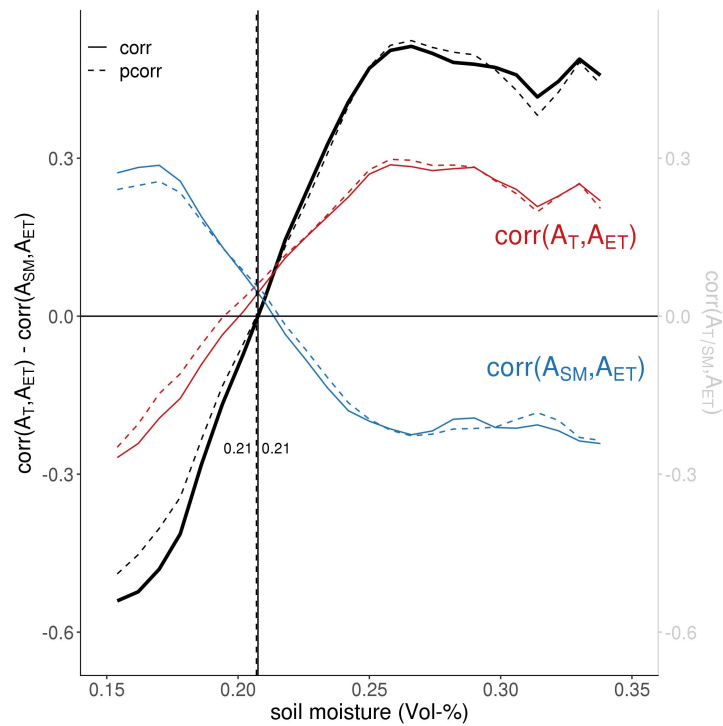


Figure 2.A2: The confounding effects of temperature and soil moisture on the Δcorr . The solid red and blue lines result from taking a moving average through data points with soil moisture on the x-axis and the respective individual correlations on the secondary y-axis. The black solid line is the difference between the solid red and blue lines. The dashed lines denote $\text{corr}(A_T, A_{ET})$ excluding the confounding role of soil moisture (red), $\text{corr}(A_{SM}, A_{ET})$ excluding the confounding role of temperature and the difference between the two (black).

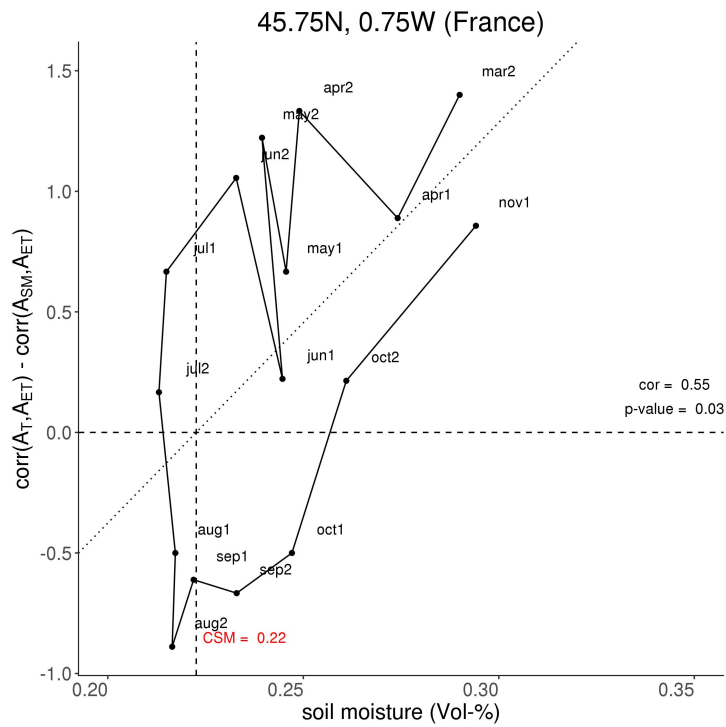


Figure 2.A3: The local estimation of the CSM in a grid cell in France. Bimonth-of-year values of soil moisture and Δcorr values are shown.

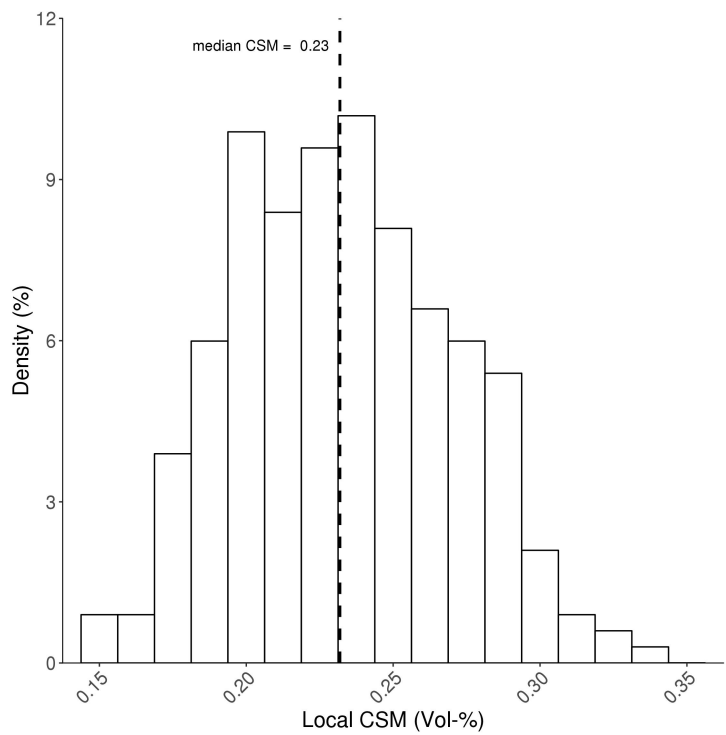


Figure 2.A4: Distribution of the range of local CSMs. The dashed line denotes the median of the full range of CSMs.

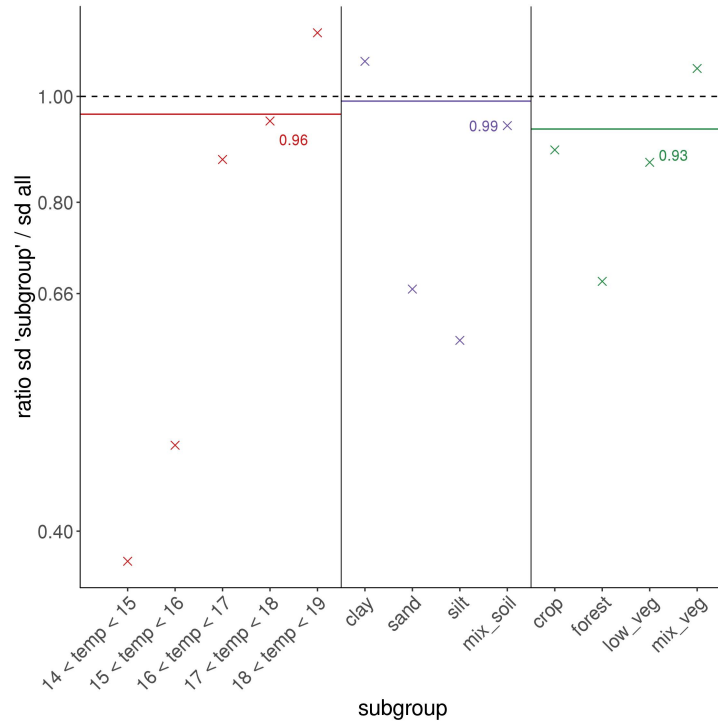


Figure 2.A5: Estimation of the influence of climate, soil and vegetation type on local CSM. The x-axis shows the used subgroups, the y-axis shows the ratio between the standard deviation of the local CSMs per subgroup data and the standard deviation of all local CSMs. The solid colored horizontal lines are average ratios of subgroups combined as climate, soil and vegetation class. Low values indicate a systematic influence of a respective subgroup on the local CSM.

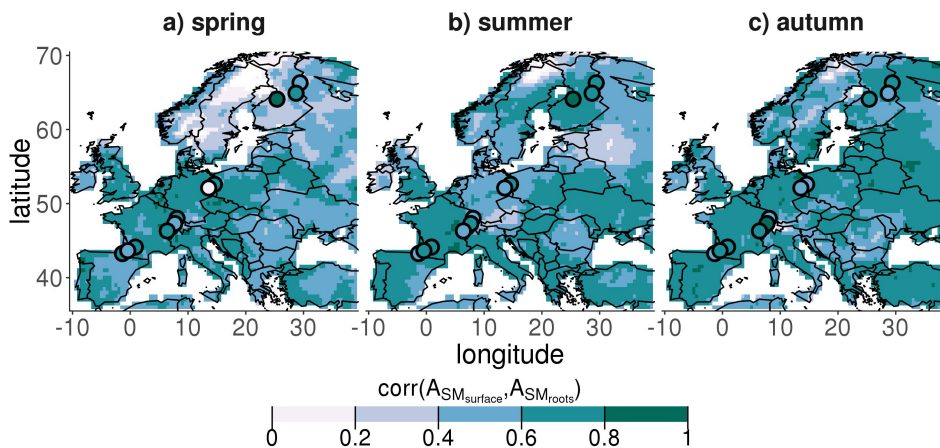


Figure 2.A6: Spatial distribution of representativeness of surface soil moisture for root-zone soil moisture. In colored grids the correlation between bimonthly anomalies of ERA-Interim/Land surface soil moisture and root-zone averaged soil moisture per season over the time period 1979 - 2010. The colored points denote the correlation between surface soil moisture and root-zone averaged soil moisture for soil moisture station in Table 2.A2

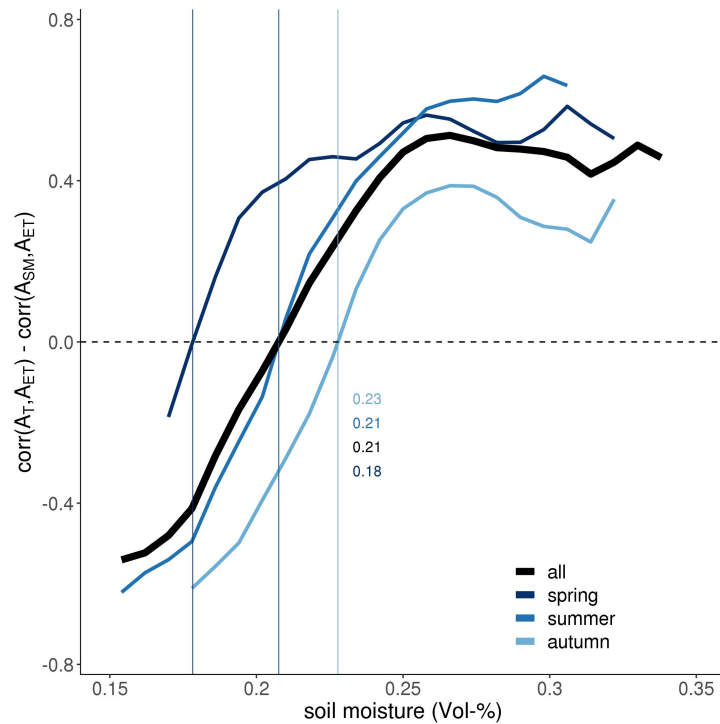


Figure 2.A7: Seasonal effect on the large-scale CSM. The thick black line is the same as in Fig. 2. The colored moving averages are calculated based on different seasons, excluding winter. Data points are only used in the calculation of the colored moving averages, when an average surface soil moisture and Δcorr are available in all seasons, to ensure a fair comparison between seasons.

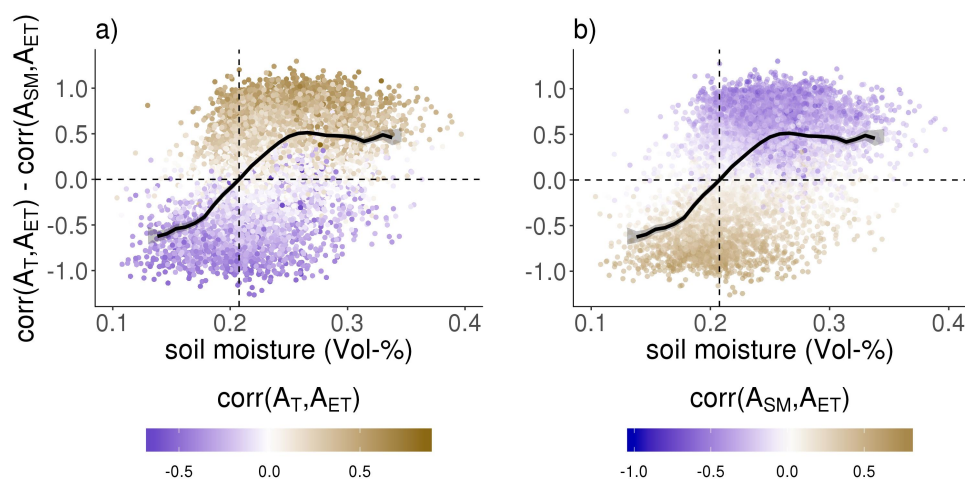


Figure 2.A8: The scatter of data points with regards to soil moisture and Δcorr . The thick black line indicates the moving average line. The color scales indicate the $\text{corr}(A_T, A_{ET})$ (left) and $\text{corr}(A_{SM}, A_{ET})$ (right).

Chapter 3

Terrestrial evaporation regimes from global weather balloon soundings

This chapter is based on:

J. M. C. Denissen, R. Orth, H. Wouters, D. G. Miralles, C. C. van Heerwaarden, J. Vilà-Guerau de Arellano, and A. J. Teuling (2021). “Soil moisture signature in global weather balloon soundings”. *npj Climate and Atmospheric Science* 4.1, 1–8

Abstract

The land surface influences the atmospheric boundary layer (ABL) through its impacts on the partitioning of available energy into evaporation and warming. Previous research on understanding this complex link focused mainly on site-scale flux observations, gridded satellite observations, climate modeling, and machine-learning experiments. Observational evidence of land surface conditions, among which soil moisture, impacting atmospheric boundary layer (ABL) properties at intermediate landscape scales is lacking. Here, we use a combination of global weather balloon soundings, satellite-observed soil moisture, and a coupled land-atmosphere model to infer the soil moisture impact on the ABL. The inferred relationship between soil moisture and surface flux partitioning reflects distinctive energy- and water-limited regimes, even at the landscape scale. We find significantly different behavior between those two regimes, associating dry conditions with on average warmer (≈ 3 K), higher (≈ 400 m) and drier (≈ 1 kPa) afternoon ABLs than wet conditions. This evidence of land-atmosphere coupling from globally distributed atmospheric measurements highlights the need for an accurate representation of land-atmosphere coupling into climate models and their climate change projections.

3.1 Introduction

The diurnal evolution of the atmospheric boundary layer (ABL), the well-mixed layer between the land surface and free troposphere, plays a key role in weather conditions and air quality at the Earth's surface. In particular, it can influence the magnitude of temperature and precipitation extremes (Findell et al., 2011; Guillod et al., 2015; Miralles et al., 2014b; Prein and Heymsfield, 2020; Taylor et al., 2012) and various processes, such as cloud formation (Ek and Holtslag, 2004; Heerwaarden and Arellano, 2008; Lilly, 1968), air pollution (Li et al., 2017), diurnal carbon dioxide (CO_2) dynamics (Arellano et al., 2004), ecosystem carbon exchange (Lasslop et al., 2010), soil respiration (Ekblad et al., 2005), the persistence of urban heat islands (Pal et al., 2012), and even dune formation (Andreotti et al., 2009). ABL dynamics are sensitive to heat and moisture inputs from the land surface, which are directly regulated by soil moisture availability and its impact on the partitioning of surface energy fluxes (Seneviratne et al., 2010), and by incoming solar radiation, which dictates the amount of energy available for partitioning at the land surface. Next to that, the ABL is (in)directly influenced by vegetation, surface albedo, and surface roughness, which are in turn linked to soil moisture (Bou-Zeid et al., 2004; Harman, 2012; Williams and Torn, 2015). By redistributing heat and moisture vertically, ABL dynamics determine how fluxes of water and energy from the land surface combine with free-tropospheric conditions to translate into near-surface temperature and humidity.

Per example, Figure 3.1 depicts the typical diurnal ABL evolution from weather balloon soundings under convective conditions and weak synoptic flows over different land surface conditions at a site in Lincoln, IL, USA. The ABL is influenced by the bottom (land surface) and top (free troposphere) boundaries. At the land surface, available net radiation partitions into sensible heat flux (H) and latent heat flux (LE), transferring heat and moisture into the ABL. Sensible heat warms the air above the land surface, thus creating warm and buoyant, rising air parcels. At the top of the ABL, the temperature inversion serves as a lid, preventing the air to rise higher. However, sensible heat-driven air parcels can overshoot the inversion and entrain warm and dry air from the free troposphere, thereby deepening, warming and drying the ABL during daytime (Vilà-Guerau de Arellano et al., 2015). The ABL is generally less well-mixed in terms of specific humidity than potential temperature, owing to the entrainment of dry air (Mahrt, 1991). Due to vertical convective mixing of air from the land surface to the top of the ABL, the vertical temperature and humidity profiles integrate surface heterogeneity and free tropospheric conditions over distances tens of times the ABL height. We refer to this as the landscape scale throughout this study. In this context, soil moisture leaves its signature in the ABL by regulating the partitioning of energy fluxes at the land surface: Over dry soils, evaporation is water-limited, partitioning more energy into sensible heat than over wet soils, and consequently causing the ABL to grow warmer, deeper and drier (Figure 3.1). Conversely, the distinct signature left by soil moisture in the ABL can be exploited to infer land water availability using weather balloon soundings.

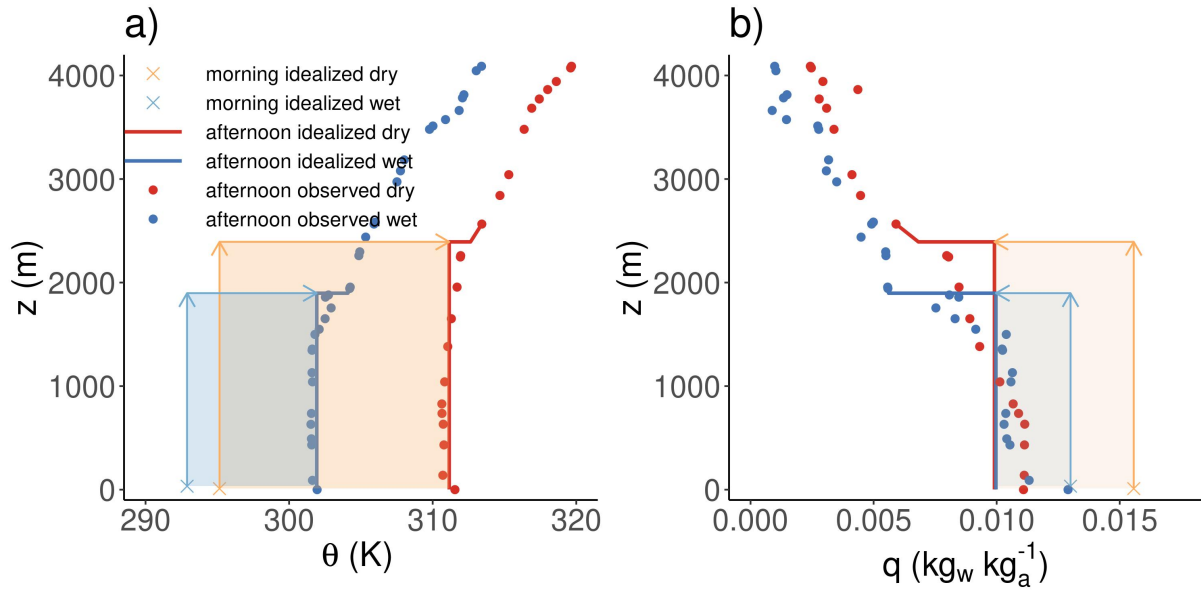


Figure 3.1: Diurnal ABL evolution over wet and dry soils, respectively. θ (a); in K) and q (b); in kg water per kg air) versus height on characteristic dry (07-07-2012) and wet days (25-06-2014; 89.33 W, 40.15 N). The solid lines depict the idealized afternoon profile to which the ABL model validated, inferred from balloon soundings in the data-screening steps (see "Screening of weather balloon sounding measurements" and "Data" in Methods) from afternoon observations (points) while crosses denote the morning ABL that the model is initialized with. Colored boxes and corresponding arrows indicate the growth of the ABL and warming/drying during the day.

In previous research, the complex link between the land surface and the ABL was studied across scales ranging from site scale using tower measurements or models (Findell et al., 2011; Shuttleworth et al., 1989; Williams et al., 2012; Wilson et al., 2002), landscape-scale using satellite observations and/or models, among which convection-resolving Large Eddy Simulations (Brown et al., 2002; Heerwaarden and Arellano, 2008; Rieck et al., 2014; Robinson et al., 2008; Taylor et al., 2011; Taylor et al., 2012), to regional and global scales using climate models, satellite observations, and/or machine-learning techniques (Dirmeyer et al., 2006; Jung et al., 2010; Koster et al., 2006; Prein and Heymsfield, 2020; Sellers et al., 1992). Spatial heterogeneity of soils and vegetation requires parameterizations in these larger-scale studies, inducing uncertainties. This was addressed in recent studies by estimating surface fluxes from near-surface observations of temperature and humidity using mixed-layer theory (Gentine et al., 2016; Salvucci and Gentine, 2013). However, these observations do not allow analyses at the landscape scale, at which land-atmosphere coupling is expected to have more relevant impacts (Robinson et al., 2008; Taylor et al., 2011).

In this study, we infer land-atmosphere coupling from an atmospheric perspective: we translate weather balloon soundings with an ABL model, the Chemistry Land-surface Atmosphere Soil Slab model for Global Studies (CLASS4GL), to make a global estimate of surface flux partitioning at the landscape scale (Wouters et al., 2019). The weather balloon sounding data consist

of ~ 15 million soundings, available from 1905 to near real-time, and from > 2700 stations distributed across the globe (see "Data" in Methods). These comprehensive observations are routinely used to constrain weather forecasts, but so far, their use to study land-atmosphere coupling has been limited. Here, balloon soundings are filtered to select days with convective warm conditions (see "Preprocessing of weather balloon soundings" in Methods), excluding days on which sublimation occurs, avoiding complexities related to frozen surface water and substantial variation in the seasonal cycle of surface flux partitioning during the cold season and focusing on days which are driven by sensible heat and therefore governed by surface flux partitioning. Therefore, the data screening increases, but simultaneously potentially exaggerates, the chance of land states affecting ABL dynamics (Santanello et al., 2018). We identify 4236 suitable sounding days distributed globally over 97 stations, which are used to initialize the ABL model in the morning and to validate it in the afternoon, while the model computes concurrent surface flux estimates. We implement a routine that adjusts the initial morning soil moisture, the main remaining control on energy flux partitioning, in order to minimize the difference between observed and model-estimated vertical temperature and humidity profiles (see "Experimental setup" in Methods). The surface flux partitioning is thus inferred from atmospheric measurements which are interpreted and translated into surface fluxes through a model based on mixed-layer theory, and hence largely independent of potentially uncertain ancillary data of land surface characteristics, in contrast to climate models.

3.2 Results and discussion

3.2.1 Global patterns of energy flux partitioning

In a first step, we compare the flux partitioning inferred from balloon soundings using CLASS4GL with several state-of-the-art gridded data products. Figure 3.2 shows the global distribution of energy flux partitioning, expressed as an evaporative fraction (EF; the ratio between latent heat flux and available energy), for three gridded products (a-c) and for CLASS4GL (d), focusing on warm days (temperature > 278 K). Considerable differences exist between the gridded products, as root-mean-square differences in the evaporative fraction (EF) are as follows: 0.12 (GLEAM-FLUXCOM), 0.1 (GLEAM-ERA5), and 0.15 (ERA5-FLUXCOM), highlighting the ongoing challenges in surface flux estimation. The apparent differences across state-of-the-art gridded products can be due to different model formulations or underlying land surface parameterizations accounting for sub-grid heterogeneity. This problem can be overcome with the balloon sounding-based flux estimations, as these are largely independent of land-surface model assumptions.

There is reasonable agreement with the spatial patterns of the reference products: spatial correlations of CLASS4GL estimated EF, weighted by the number of sounding days per location and only including locations with more than 50 sounding days to avoid sampling biases, with

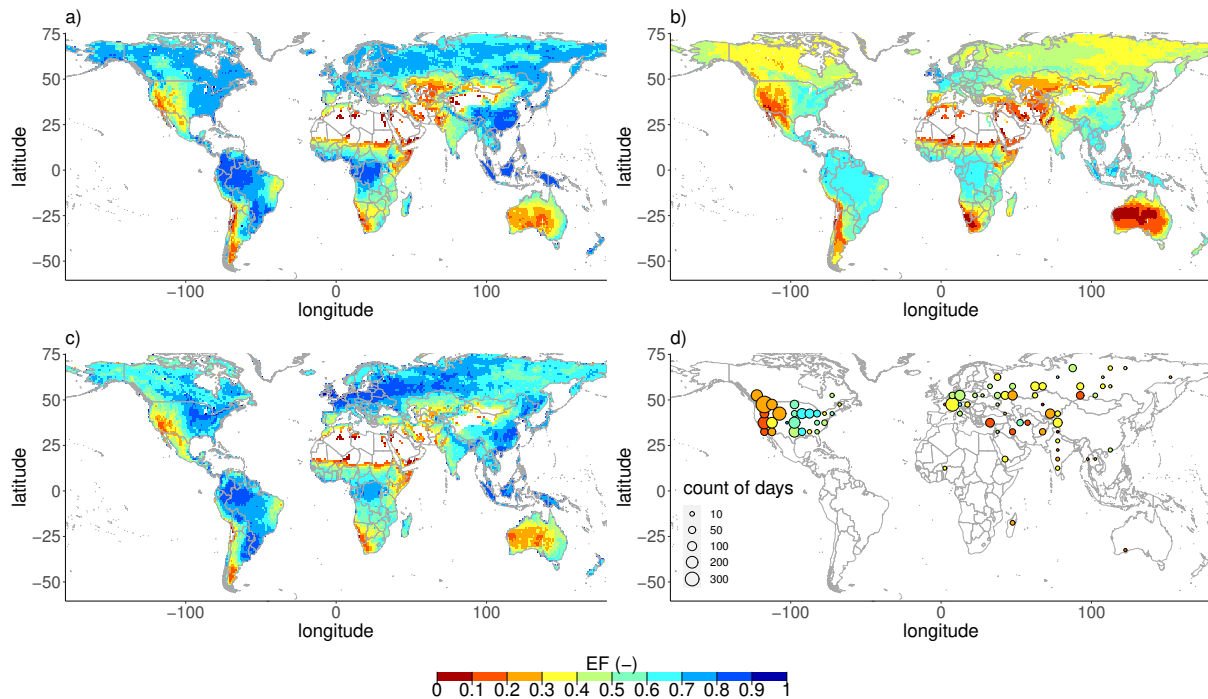


Figure 3.2: Global estimates of mean surface flux partitioning. Colors denote the evaporative fraction averaged over the timespan of the respective data product after filtering for warm days (ERA5 temperature > 278 K) and availability of all gridded data products: (a) GLEAM, 2003–2017, (b) FLUXCOM 2001–2015, and (c) ERA5, 1981–2017 (see "Data" in "Methods"). d) Evaporative fraction inferred from balloon soundings using CLASS4GL in colored circles, averaged over all stations from the morning to the afternoon sounding for all stations within a $5.0^\circ \times 5.0^\circ$ grid cell and all available sounding days. The sizes of the circles correspond to the amount of available sounding days.

GLEAM, FLUXCOM, and ERA5 are 0.67, 0.75, and 0.68, respectively. The fact that these values approach the correlations between gridded products calculated using similar methodology 0.89 (GLEAM-FLUXCOM), 0.88 (GLEAM-ERA5), and 0.93 (ERA5-FLUXCOM) is notable, given different temporal (continuous vs. discontinuous time series and daily vs. sub-daily averages) and spatial ($1^\circ \times 1^\circ$ grid cells vs. landscape-scale footprint from balloon soundings) data characteristics between CLASS4GL (see "Screening of weather balloon soundings" in Methods) and the gridded products. Further, the mean EF from CLASS4GL is slightly below the estimates of the gridded products. This can be explained by the difference in temporal sampling; Whereas the EF for gridded products is averaged over the entire day, the EF from CLASS4GL is averaged between morning and afternoon soundings, with most data available between 08:00 and 14:00 local solar time, shortly after which heating tends to increase EF (Heerwaarden et al., 2009). Finally, we go one step further down the Local Land-Atmosphere Coupling (LoCo) process chain (Santanello et al., 2018), that presumably governs ABL dynamics by validating the main control of EF (soil moisture), instead of directly validating EF. We find that the adjusted initial soil moisture from CLASS4GL correlates well with European Space Agency (ESA) Climate Change Initiative (CCI) soil moisture (0.73; Supplementary Figure

3.A1), which validates both the land surface schemes applied in CLASS4GL and confirms that soil moisture leaves a signature in the vertical profiles, as measured by balloon soundings, by affecting the surface flux partitioning.

3.2.2 Distinguishing evaporative regimes

While it is known that EF and related land-atmosphere coupling changes between energy- and water-limited conditions (Denissen et al., 2020; Feldman et al., 2019; Haghghi et al., 2018; Seneviratne et al., 2010), the potential implications of these modes on the ABL remain unclear. To distinguish these regimes, we use satellite-derived soil moisture observations (Dorigo et al., 2017). Next, we investigate the control of soil moisture on the day-to-day variability of EF by linking the inferred latent and sensible heat fluxes to remotely sensed soil moisture conditions, which are independent of the soil moisture used in the flux estimation. Using remotely sensed soil moisture induces noise in this relationship, as (i) surface soil moisture only represents part of the depth that is relevant for evaporation, and (ii) surface and root-zone are known to decouple in dry conditions (Qiu et al., 2016; Santanello and Carlson, 2001). Nevertheless, this product is the only global observational soil moisture with an adequate time period available and has been used successfully in similar applications before (Denissen et al., 2020; Orth et al., 2020). Figure 3.3a illustrates that the energy flux partitioning is strongly regulated by soil moisture, even at the landscape scale, as the ratio between latent heat flux and surface available energy (the sum of sensible and latent heat flux) changes from dry to wet soils. This apparent sensitivity of energy flux partitioning to soil moisture is quantified by computing a least-squares regression fit for each soil moisture class (Figure 3.3b). The linear slopes in Figure 3.3b are comparable over wet soils, indicating that flux partitioning is insensitive to soil moisture (energy-limited conditions). This changes toward drier soils, where the linear slopes decrease with soil moisture, reflecting an increased sensitivity of flux partitioning to soil moisture (water-limited conditions). The point data underlying the contour lines in Figure 3.3a and the linear models in Figure 3.3b are shown in Supplementary Figure 3.A2. The moving medians in Supplementary Figure 3.A2 indicate that the assumption of linearity for quantifying the relationships in Figure 3.3b is reasonable.

The linear slopes (EF^*) reflect the sensitivity of the change in latent heat flux to changes in available energy (assuming lines without a zero intercept). Therefore, the physical meaning of EF^* and EF is similar, because EF reflects the ratio of the change in latent heat flux to changes in available energy (with a zero intercept). Both the sensitivity of EF^* and EF to soil moisture changes when transitioning between wet and dry soils. We use EF^* here as it fits the data more closely and consequently allows a clearer illustration of the contrast between water- and energy-controlled regimes. We impose a piecewise-linear model to quantify this transition, similarly to existing literature (Feldman et al., 2019; Seneviratne et al., 2010), which is marked by the critical soil moisture (CSM, see "Distinguishing evaporative regimes" in Methods). Separating for environmental conditions is complex because the footprints of balloon soundings are time-varying depending on height, wind speed, and direction; this footprint is also large enough to

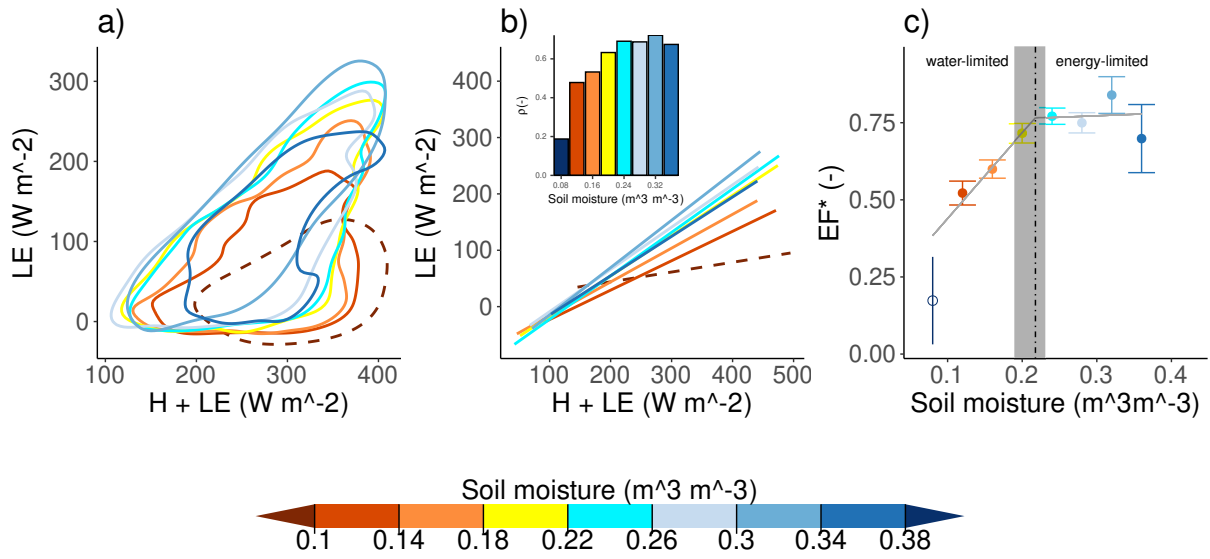


Figure 3.3: Soil moisture control on landscape-scale surface flux partitioning. (a) Surface energy flux estimates from CLASS4GL. Point clouds illustrated through 80th percentile contour lines and colored according to independent, satellite-derived soil moisture (SM) observations (Dorigo et al., 2017). (b) Least-squares regression fits (full lines indicate statistical significance, $p < 0.05$), with corresponding correlations (ρ) in the inset. (c) Relation between the slope of the linear models (EF^* , see text) with SM (full dots indicate statistical significance, $p < 0.05$). Error bars show the standard deviation of EF^* . Dark-grey solid lines result from a piecewise linear regression between SM and EF^* with according to breakpoint (dot-dashed) and interquartile range from bootstrapping (light-grey ribbon).

integrate surface heterogeneity in terms of soil, vegetation, and climate characteristics. Different environmental conditions across sites and decoupling between the surface and root-zone soil moisture could, however, cause slightly different EF^* for the same surface soil moisture values. The dark-grey ribbon in Figure 3.3c reflects the sensitivity of the critical soil moisture (CSM) to this uncertainty. As this ribbon is relatively narrow, it justifies the use of the breakpoint as a sharp threshold to quantify the transition. We emphasize that it is not our intention to determine the sensitivity of this transition to environmental conditions, but merely to find a threshold to distinguish energy- and water-limited conditions that is valid for our data selection, and can be used as a first-order distinction between water and energy-controlled conditions in our subsequent analyses. Next to that, this first-order estimate is robust with respect to (i) different soil moisture bin setups (Supplementary Figure 3.A3), and (ii) different surface soil moisture products (Supplementary Figure 3.A4).

3.2.3 Land surface effect on the atmospheric boundary layer

When classified based on CSM, ABL properties show distinct differences between water- and energy-limited conditions (Figure 3.4). Figure 3.4b shows that EF, as produced by CLASS4GL, is generally higher in energy-limited conditions than in water-limited conditions. Figure 3.4d-i shows that, according to the CLASS4GL simulations, in water-limited conditions, the ABL warms (2.72 K), dries (0.86 kPa) and, most notable, deepens (409 m) more during daytime than in energy-limited conditions. Strong differences in height are found due to higher heat capacities of deeper water-limited ABLs (Heerwaarden et al., 2009; Orth et al., 2020). Despite higher moisture input through evaporation in energy-limited conditions, we find that diurnal VPD increases driven by the temperature increase during the course of the day. In addition, the daily ABL evolution is influenced by upper air processes driven by synoptic systems, which are different between evaporative regimes, as can be seen from the tropospheric temperature lapse rate (Figure 3.4c). Warm and dry days leading up to water-limited conditions are associated with lower tropospheric lapse rates, favoring a rapid deepening of the ABL (Findell et al., 2011; Panwar et al., 2019; Santanello et al., 2005). Further, the ABL's relative humidity decreases more strongly during daytime in water-limited conditions than in energy-limited conditions, favored by the stronger entrainment of dry tropospheric air, which is mainly driven by surface sensible heat in convective ABLs (Santanello et al., 2009). Next to that, entrainment of dry air triggers contrasting upper air feedbacks in both evaporative regimes. In energy-limited conditions, entrainment of dry air increases the moisture gradient between the land surface and the ABL, thereby enhancing evaporation and leading to less sensible heat and shallower ABLs; in water-limited conditions, this entrained dry air may further constrain evaporation due to the influence of VPD on stomatal conductance under dry soils, and thus sensible heat is increased and the ABL grows deeper.

In Figure 3.4, we effectively separate wet and dry regions using soil moisture data. We assess the more direct effect of surface flux partitioning on the ABL by computing regimes based on EF (Supplementary Figure 3.A5). As expected, the diurnal deepening of the ABL is even stronger given the more direct influence of energy flux partitioning compared with that of soil moisture. At the same time, warming and drying are less pronounced which is possibly due to the enhanced heat capacity of the ABL. Interestingly, where the difference in morning ABL growth is greater when the data is separated based on EF than on soil moisture (Figure 3.4), differences in θ and VPD are less pronounced. This could be explained by the nature of the variables that are used to separate the data: EF could theoretically vary from 0 to 1 during daytime hours, whereas daytime variability in soil moisture is much lower. Therefore, the stronger the water-limited conditions, the higher the probability that the days leading to these dry conditions have been water-limited too, accompanied by higher morning θ and VPD differences in Figure 3.4d, f. As EF responds on shorter timescales than soil moisture, days leading to low EF days need not be water-limited and therefore morning θ and VPD differences in Supplementary Figure 3.A5d, f is less pronounced. However, by separating on EF we ensure high sensible heat on low EF days,

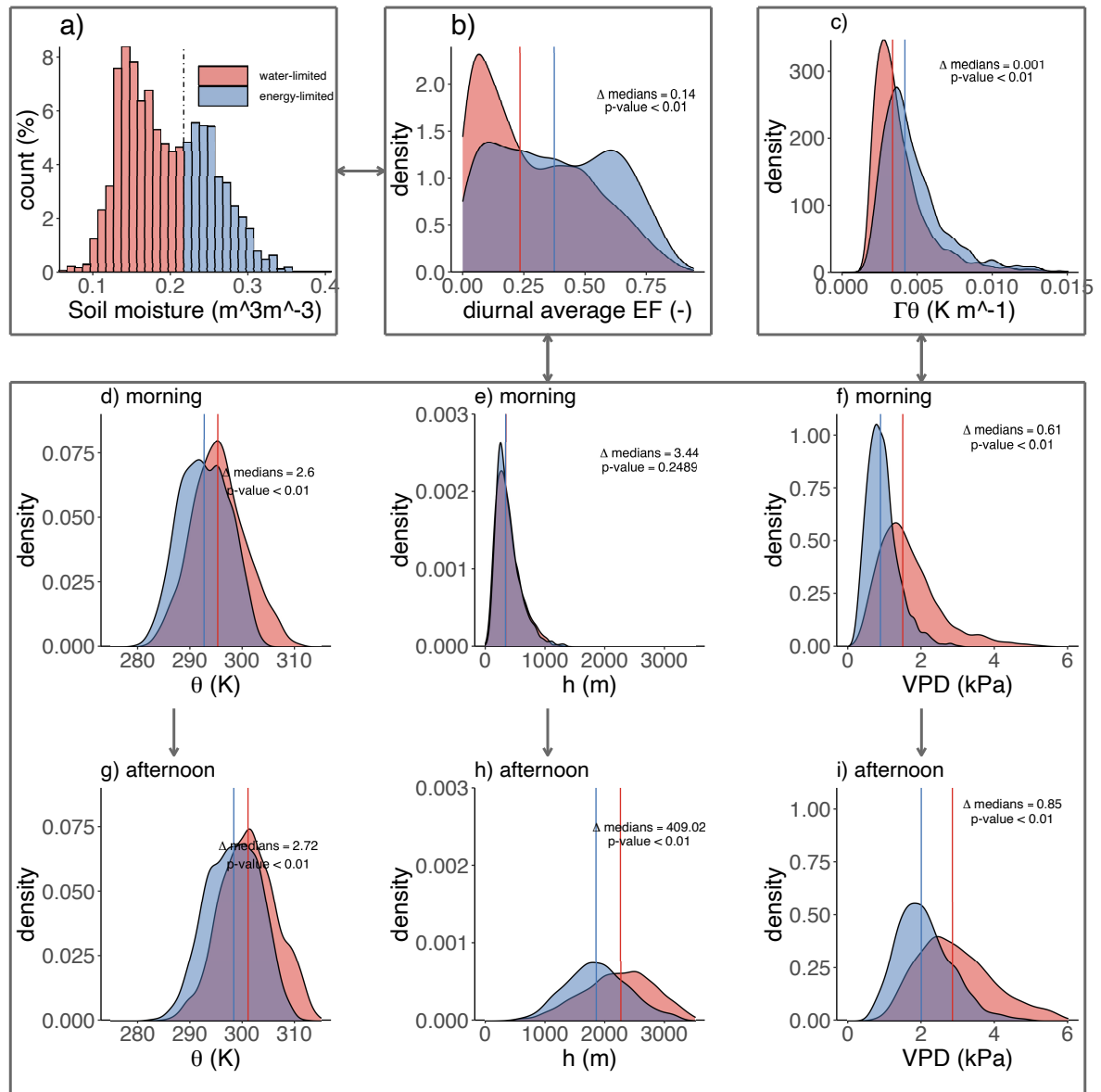


Figure 3.4: Global soil moisture influence on diurnal ABL evolution. (a) Surface soil moisture for available sounding days. When soil moisture is below critical soil moisture (dot-dashed vertical line in Figure 3.3c and here), we distinguish water-limited conditions (red), and energy-limited conditions otherwise (blue). Evaporative fraction (b) and potential temperature lapse rate (c) from CLASS4GL averaged between 08:00 and 14:00 local solar time. Potential temperature (d, g), ABL height (e, h), and the vapor pressure deficit (f, i) from CLASS4GL at 08:00 and 14:00. Vertical blue and red lines denote the medians from the respective distributions. Annotations show the difference between the medians and the p values of the Kolmogorov-Smirnov test. Dark grey arrows indicate assumed causal relations between variables.

growing the ABL from sunrise to 08:00. Some, but not all, stations transition between water- and energy-limited conditions, due to the seasonal cycle in soil moisture. To isolate the role of

seasonality in the results shown in Figure 3.4, we recompute the figure for regimes of available energy, replacing the soil-moisture-derived regimes and instead of depicting seasonal variation in the meteorological forcing (Supplementary Figure 3.A6). We consistently find smaller diurnal changes in ABL characteristics in terms of warming, growth, and drying, confirming that our results in Figure 3.4 are not an artifact of seasonal and latitudinal forcing variations, thereby justifying the separation between evaporative regimes based on CSM.

In conclusion, we illustrate that soil moisture conditions are reflected in the ABL, enabling the inference of energy flux partitioning from ABL-based measurements such as balloon soundings. Benefitting from a comprehensive archive of balloon soundings covering locations across the globe and spanning over decades, our approach can provide robust and largely independent EF estimates at the impact-relevant landscape scale. More generally, the relevance of the ABL for land-atmosphere coupling is increasingly recognized and has for example triggered efforts to add continuous ABL measurements to existing flux towers (Helbig et al., 2020). Such an extension would enable the application of our approach at these sites, and the reconciliation with local energy fluxes. In summary, we present an observation-based assessment of the ABL response to soil moisture variations worldwide and quantify the changes in ABL characteristics induced by soil moisture.

3.3 Methods

3.3.1 CLASS4GL

We use the CLASS4GL framework (Wouters et al., 2019) (<https://class4gl.eu/>). CLASS4GL initializes and runs a mixed-layer model (CLASS (Vilà-Guerau de Arellano et al., 2015); <http://classmodel.github.io/>) with ancillary reanalysis, satellite, survey, and weather balloon sounding data worldwide. CLASS uses the mixed-layer equations originally proposed by Tennekes (1973) and later adapted by Tennekes and Driedonks (1981) to compute the daytime evolution of the mixed-layer. The advantage of using mixed-layer equations is that the mixed-layer, which is the well-mixed part of the ABL where potential temperature (θ), specific humidity (q), and wind components (u, v) are assumed to be constant with height due to turbulent mixing, can be summarized with one value for θ and one for q . Therefore, CLASS is computationally cheap, but at the same time, the mixed-layer theory on which it relies is well-established through, amongst other basic physical laws, the conservation of mass and energy. This way, CLASS represents the daily atmospheric boundary layer evolution and meteorological processes at the landscape scale, and can efficiently be used to analyze thousands of sounding days measured across the globe. In CLASS, available energy at the land surface is partitioned into sensible and latent heat flux, which is influencing mixed-layer θ , q , and height (h) from the bottom of the mixed-layer. The top of the mixed-layer is characterized by a θ and q inversion, which separates the well-mixed layer from the warmer and drier free troposphere. In the free

troposphere, the θ and q lapse rates describe how θ and q change with height. At the top of the mixed-layer, the heat and moisture that is entrained from free-tropospheric air is controlled by the inversions of θ , q , and wind components. Recent developments in CLASS4GL include dynamic free-tropospheric θ and q lapse rates according to the different (observed) vertical air layers during the mixed-layer growth, which also change due to large-scale dynamic forcing of advection and subsidence and entrainment by shear (Vilà-Guerau de Arellano et al., 2015; Wouters et al., 2019). A mixed-layer representation of the ABL as assumed in CLASS approximates the idealized θ and q profiles in Figure 3.1. In selecting the appropriate observed vertical profiles for our analysis, CLASS4GL is equipped with necessary filters and criteria to ensure that the vertical profiles selected closely follow the convective (mixing) assumptions (see Figures 3.3 and 3.4 in Wouters et al. (2019) and Figure 3.4 in Heerwaarden et al. (2010)), represented by the idealized profiles in Figure 3.1. Within these assumptions, the effect of entrainment on vertical profiles is of second-order importance, as the entrainment flux is a generally agreed-upon fixed fraction (0.2) of the surface kinematic heat flux. This constant holds for shear-free conditions, supported by atmospheric observations (see Conzemius and Fedorovich (2006) for a comprehensive discussion). However, even while the mixed-layer theory is deemed well-established and with appropriate data screening, deviations from well-mixed assumptions exist, slightly more so in the case of q than θ . The main reason for this is that the q difference between the mixed layer and the free troposphere can be of the same order of magnitude as the well-mixed q value (Figure 3.1b), whereas the θ difference is much smaller (Figure 3.1a). Therefore, the observed q -profile could slightly deviate from the well-mixed profile at the top of the ABL due to entrainment of dry and warm free-tropospheric air, which in turn can be partially compensated by evaporation from the land surface. Moisture skewness could also exist at the land surface under high EF conditions. Where in reality the moisture gradient is reduced due to this skewness, thereby reducing evaporation, this does not occur in CLASS4GL, because this skewness is mixed throughout the ABL. Therefore, the moisture gradient is maintained accompanied by slightly higher evaporation. However, we do not expect this to be the case often in our selection of convective days, as in such conditions moisture is effectively mixed throughout the ABL. More information on the original formulation of CLASS within the CLASS4GL framework and its data sources, which are the main input parameters, their default values and the latest updates can be found in the previous studies (Heerwaarden and Teuling, 2014; Heerwaarden et al., 2010; Vilà-Guerau de Arellano et al., 2015; Wouters et al., 2019). We highlight one of several updates within the CLASS4GL framework: bulk transfer coefficients of momentum and heat have been calculated non-iteratively according to Wouters et al. (2019), which holds for stable and unstable surface conditions, further reducing the computational cost of CLASS4GL.

3.3.2 Screening of weather balloon sounding measurements

Approximately, 15 million weather balloon sounding measurements from > 2700 stations across the globe are available from the Integrated Global Radiosonde Archive (IGRA) data set

(Durre et al., 2006), from as early as 1905 to near real-time. The radiosondes provide vertical measurements of, amongst others, temperature, pressure, relative humidity, wind direction, and speed.

Before data screening can take place, all the necessary mixed-layer properties to describe an idealized vertical profile have to be calculated from the measurements: h is determined as the height at which the Richardson number exceeds a certain threshold: 0.24 for strongly stable conditions, 0.31 for weakly stable conditions and 0.39 for unstable conditions (Zhang et al., 2014). The uncertainty range, used at a later step, can be derived from computing h across this range of Richardson numbers. The mixed-layer average θ and q are the mean of the observations between the land surface and h . The upper air conditions are linearly extrapolated between the two measurement heights above h : First, the tropospheric lapse rate is calculated as the change of θ and q with height. Second, the inversion is the difference between the mixed-layer θ and q and the extrapolated θ and q from the tropospheric lapse rate.

Once the mixed-layer properties are calculated, they go through a series of data-screening steps, which are largely the same as described Wouters et al. (2019). The screening of weather balloon sounding measurements is necessary to ensure the selection of convective warm days, on which the described mixed-layer theory assumptions are met. By doing so, we consider only convective days that are driven by sensible heat flux, which is sensitive to land states (water- versus energy-limited conditions), governing the surface flux partitioning and the entrainment flux of heat. Therefore, the data screening yields days where the chances of land states being drivers for surface flux partitioning and ABL dynamics are higher. However, vertical profiles from excluded days also carry soil moisture signatures, albeit less pronounced due to larger influences of other meteorological processes. The criteria are the following: (i) A morning profile needs to be available before 12:00 local solar time. (ii) There should be at least 7 measurements below 3000 m. (iii) The uncertainty range of the determined h , as described above, should be smaller than 150 m. (iv) The mixed-layer should be well-mixed in terms of θ , ensured by omitting sounding days where the root mean square deviation of observed θ within the mixed-layer exceeds 1.5 K. (v) $\theta > 278$ K, to exclude the possibility of having freezing temperatures on sounding days. (vi) An afternoon sounding, confirming to the same requirements as the morning sounding, should be available between local noon and 1 h before local sunset. (vii) The growth of h should be between 20 and 400 m h^{-1} and the mixed-layer should warm during daytime, to ensure a reasonable daytime mixed-layer evolution. (viii) ESA CCI soil moisture should be available in the $1^\circ \times 1^\circ$ degree grid cell resolution at the same time and location as the sounding (Dorigo et al., 2017). After the data screening procedure, the weather balloon sounding measurements are eligible to use for estimating energy flux partitioning with CLASS.

3.3.3 Experimental setup

We extend the existing framework of CLASS4GL with an additional routine that forces CLASS to reproduce the afternoon mixed-layer average θ and q from observations within an acceptable range of uncertainty. This routine iteratively scales modeled soil moisture, assuming identical values for the surface and root-zone, and consequently, the energy flux partitioning to match the estimated θ and q to afternoon mixed-layer averages from observations. This iterative converging method has been used in earlier work, where Miralles et al. (2014b) matched Bowen ratios from the Global Land Evaporation Amsterdam Model (GLEAM) ((Martens et al., 2017)) and Wouters et al. (2019) matched EF from GLEAM to CLASS4GL produced values by iteratively adjusting initial soil moisture. By iteratively scaling the initial soil moisture, we assume that a mismatch in afternoon temperature or humidity results exclusively from the modeled soil moisture, and that any mismatch due to entrainment of the warm and dry free troposphere, is indirectly driven by soil moisture at multi-day timescales (Vilà-Guerau de Arellano et al., 2015). Two separate procedures and at least two model runs are necessary to ensure the matching of both afternoon mixed-layer average θ and q . We do this by first computing

$$f_X = \frac{X_{CLASS} - X_{OBS}}{\sigma_{X_{OBS}}} \quad (3.1)$$

where X is either θ or q , $\sigma_{X_{OBS}}$ is the standard deviation of the respective variable with height across the observations within the mixed-layer, X_{CLASS} the mixed-layer average estimated from running CLASS4GL from the morning to the afternoon sounding based on a converged modeled soil moisture, X_{OBS} the mixed-layer average based on balloon sounding observations and f_X the difference in standard deviations. CLASS4GL estimated θ or q matches the observations adequately if $f_X < 0.5$, otherwise the soil moisture is iteratively converged toward a value that satisfies $f_X < 0.5$, by combining two zero-finding algorithms: the bisection method (Burden et al., 2016) and the secant method. If $f_X < 0.5$ cannot be met within 10 iterations, the sounding day will be discarded. The two resulting soil moistures from matching on θ and q should be within a range of 0.05 from each other, to ensure that the resulting flux estimates from observations of θ and q are consistent. If so, the average from the two soil moistures will be used to initialize CLASS4GL in the morning and to compute the results used in this study. Otherwise, the sounding day will be discarded. Energy fluxes are successfully estimated on 4236 sounding days distributed globally over 97 stations after the filtering procedure and matching on afternoon mixed-layer average θ and q . Because we require ESA CCI soil moisture to be available on a sounding day, the sounding days are available from 1981 to 2015, with the highest data availability in the later years. CLASS4GL has been run with default settings and thereby does not account for large-scale air circulation from subsidence and advection, and entrainment by shear. Ample uncertainties are expected with this large-scale circulation, as these estimates are based on 6-hourly values and validation is impossible. However, for our data selection, there are hardly any differences in the evolution of the ABL during daytime for experiments with and

without large-scale circulation from subsidence and advection, and entrainment by shear (not shown). Moreover, our experimental setup secures that only sounding days are retained where a satisfactory match between modeled and observed afternoon temperature and humidity is found. When meteorological processes not accounted for in the model experiments could influence observed vertical temperature and humidity profiles, this is compensated for by adjusting initial soil moisture and consequently surface flux partitioning, thereby matching modeled vs. observed afternoon temperature and humidity. As Supplementary Figure 3.A1 shows, the adjusted soil moisture closely resembles the satellite-observed soil moisture with a correlation coefficient of 0.73, underlining the small importance of meteorological processes not accounted for in our model experiments for soil moisture and consequently surface flux partitioning.

3.3.4 Data

Table 1 displays the data sets that are used for analysis outside of application in CLASS4GL. All these gridded data sets are regridded to a $1^\circ \times 1^\circ$ spatial grid cell resolution to more closely resemble footprints from weather balloon soundings.

Table 3.1: All soil moisture data sets are used to infer the relation between soil moisture and energy flux partitioning in Figure 3.3 and Supplementary Figure 3.A1-3.A4. Energy fluxes from gridded data sets are used to validate the CLASS4GL estimated energy fluxes in Figure 3.2.

Data set	Version	Variable(s)	Original spatial res.	Temp. res.	Source	Reference
ESA CCI	04.4	Surface soil moisture	$0.5^\circ \times 0.5^\circ$	Daily	Satellite observations	(Dorigo et al., 2017) (Gruber et al., 2017) (Liu et al., 2012)
GLEAM	3.4	Surface soil moisture, sensible- and latent heat flux	$0.5^\circ \times 0.5^\circ$	Daily	Land model constrained by satellite observations	(Martens et al., 2017)
ERA5	-	Soil moisture (layers 1-3), sensible- and latent heat flux, 2-m temperature	$0.1^\circ \times 0.1^\circ$	Daily	Reanalysis model	(Hersbach et al., 2020)
FLUXCOM (RS)	2	Sensible- and latent heat flux	$0.1^\circ \times 0.1^\circ$	8-daily	Multiple data streams processed with machine learning, using eddy covariance-derived fluxes as target	(Jung et al., 2019)

3.3.5 Distinguishing evaporative regimes

In Figure 3.3b, we use CLASS4GL estimated surface energy fluxes in combination with satellite observations of surface soil moisture from ESA CCI to distinguish the evaporative regimes and the related transition between them. To this end, we compute linear least-squares regressions per soil moisture class. A linear model is only computed if there is sufficient data available (more than 30 sounding days) within the respective soil moisture class.

In Figure 3.3c, we apply a piecewise linear regression to expose the two distinctive evaporative regimes and the associated transitions between them, marked by the CSM. This piecewise linear regression is weighted by the number of sounding days per soil moisture class, to account for the

uneven distribution of soil moisture values, which ranges from 43 (soil moisture $< 0.1 \text{ m}^3 \text{ m}^{-3}$) to 1039 ($0.14 < \text{soil moisture} < 0.18 \text{ m}^3 \text{ m}^{-3}$). Finally, the slopes of the linear model's EF^* and therefore the breakpoint in the piecewise linear regression are subject to uncertainty, potentially related to differences between stations in terms of soil and vegetation conditions, decoupling between surface- and root-zone soil moisture, and balloon sounding footprints varying with height, wind speed and -direction. To account for these uncertainties that are reflected in the standard deviation around EF^* , we resample the EF^* by drawing from a normal distribution with the mean of the actual EF^* and its standard deviation per soil moisture class. Subsequently, these 1000 resampled EF^* were used to compute 1000 piecewise linear regressions and breakpoints (CSM). Note that the CSM depends on soil and vegetation characteristics and is hence reflecting the selection of sites used in this study (Denissen et al., 2020; Feldman et al., 2019; Haghighi et al., 2018). We use it to distinguish water and energy-limited regimes across the sites, and subsequently to study ABL characteristics, while different CSM values might be derived for different (selections of) locations. The estimation of the CSM should be regarded as a first-order estimate as (i) the varying soil and vegetation characteristics of grid cells contributing to each soil moisture class considered in Figure 3.3 induce uncertainty to our CSM estimation, and (ii) while root-zone soil moisture is regulating evaporation and surface flux partitioning, only surface soil moisture is readily observed across the globe, which is known to decouple from root-zone soil moisture, especially in extremely dry conditions (Qiu et al., 2016; Santanello and Carlson, 2001).

3.A Appendix

This appendix represents the supplementary materials of the presented publication.

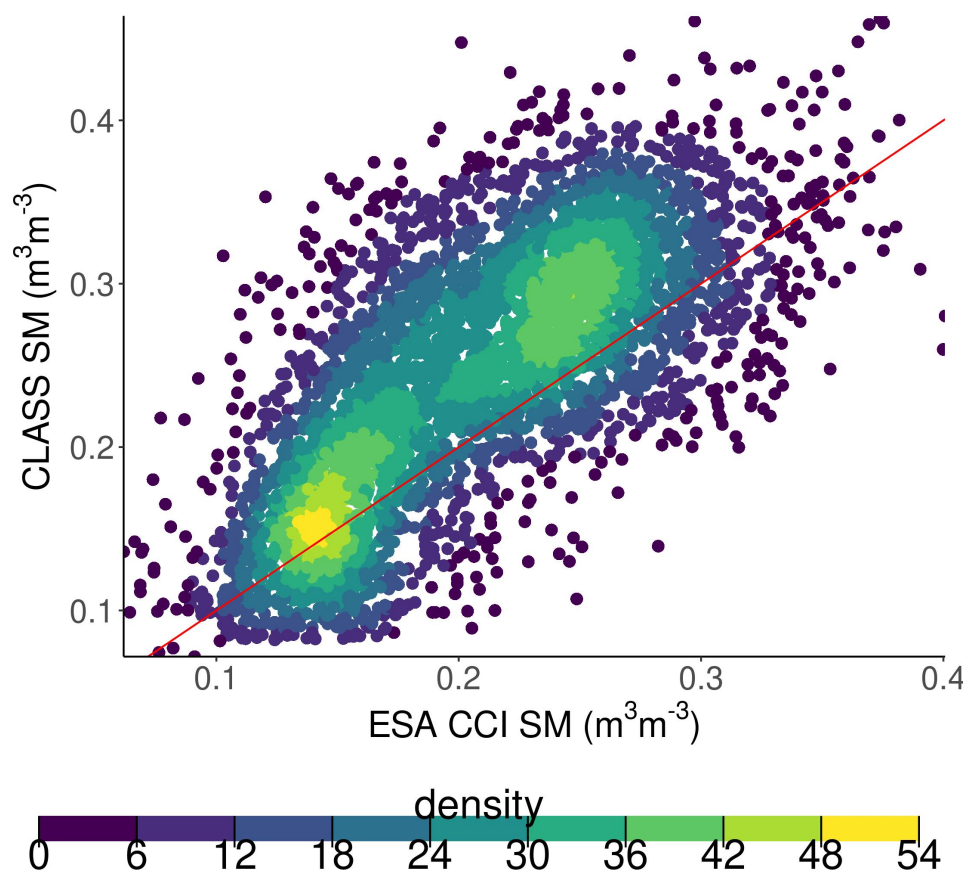


Figure 3.A1: Validation of soil moisture fitted with balloon sounding data. The x-axis displays remotely sensed soil moisture from ESA CCI in the 1.0° x 1.0° grid cell where sounding data is available. The y-axis displays the soil moisture that was fitted with balloon sounding data and CLASS. The colors denote the density of the scatter points and the red line is the 1:1 line.

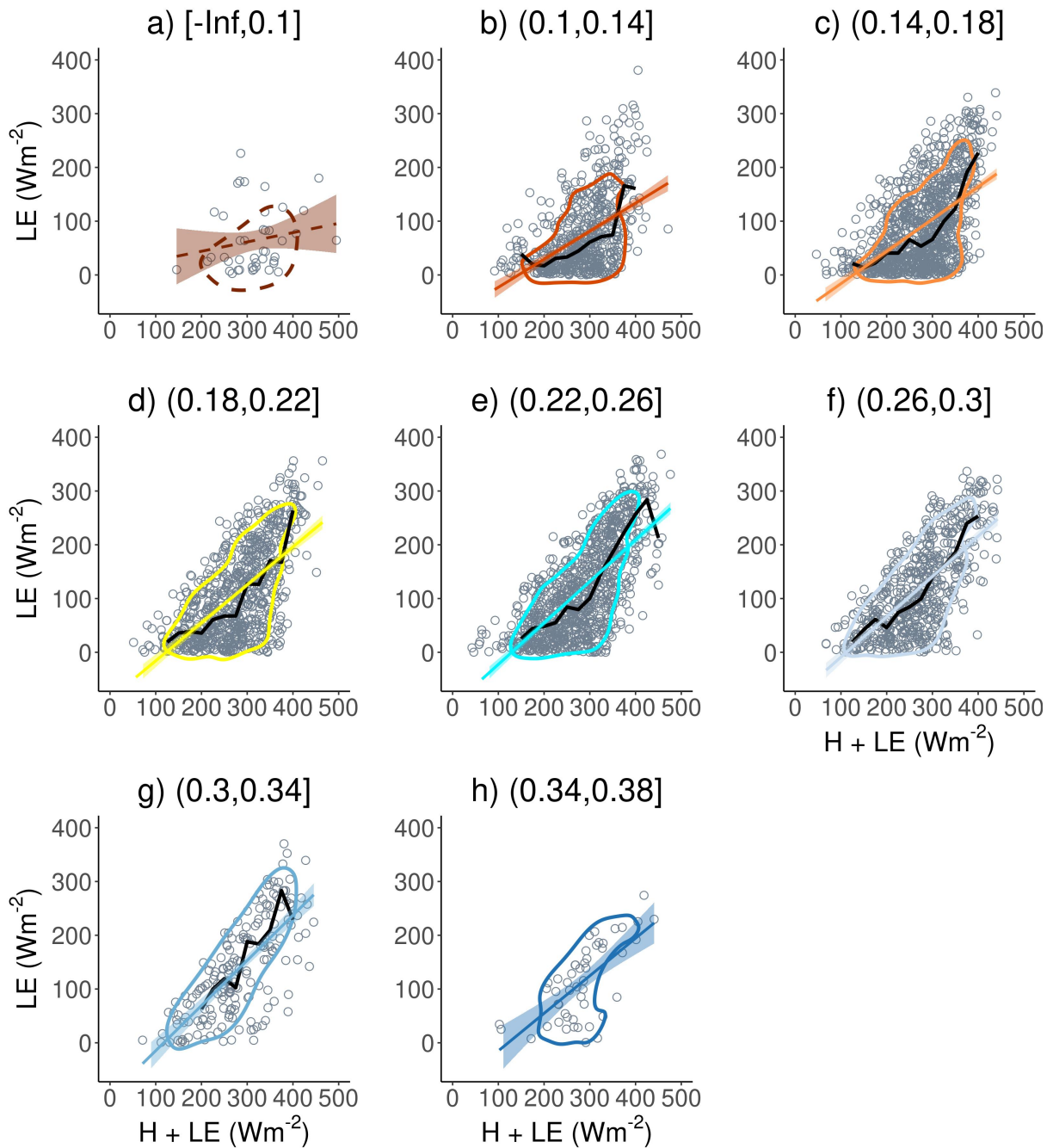


Figure 3.A2: Energy flux partitioning per soil moisture class. Available energy ($H + LE$) and LE estimates from all available balloon soundings across stations (points). Point clouds are summarized by 80th percentile contour lines and colored according to respective soil moisture. Least-squares regression fits with corresponding 95% confidence intervals are shown in colored lines. The black lines denote the moving median through the point cloud.

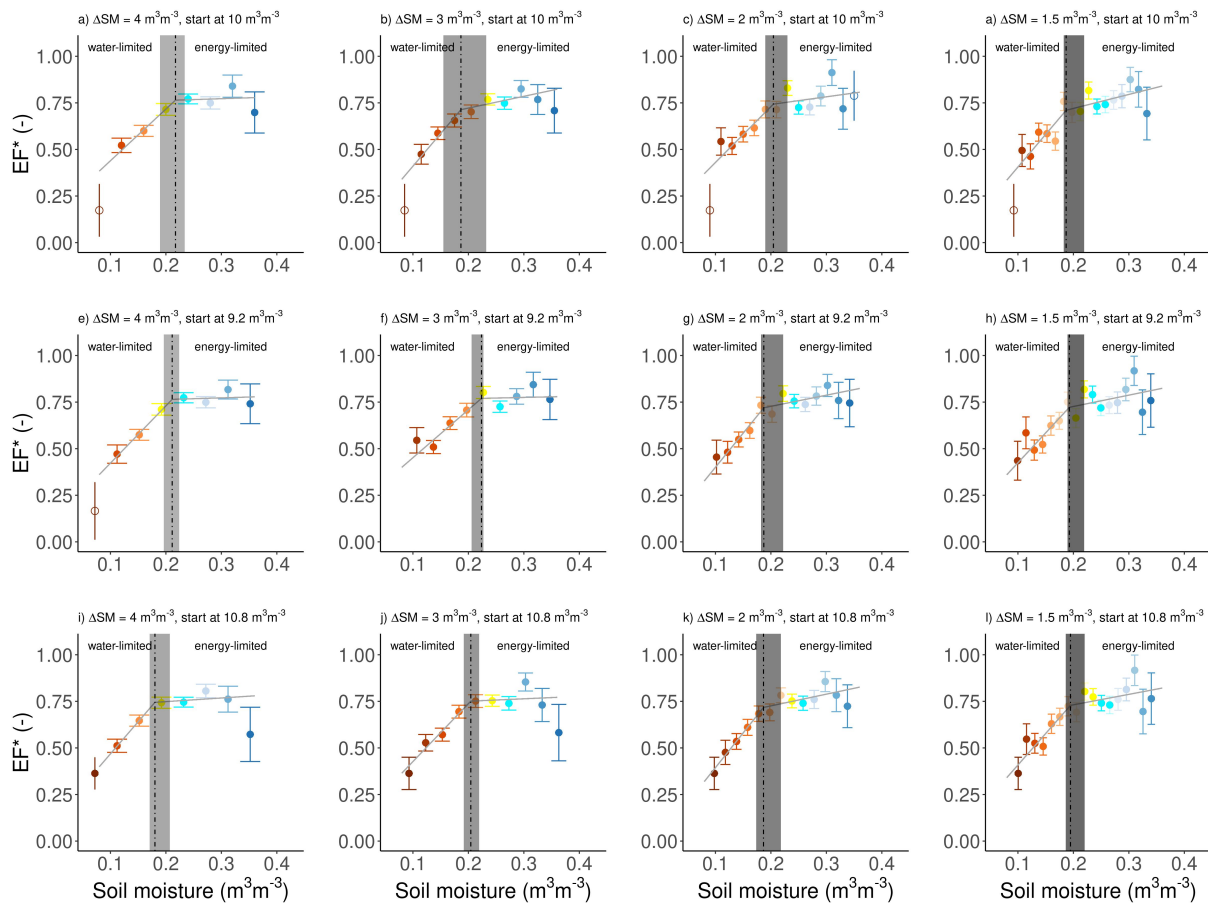


Figure 3.A3: Robustness of EF^* and piecewise linear regressions with respect to soil moisture class bin width and soil moisture lower boundaries. Relation between the slope of the linear models (EF^*) with SM (full dots indicate statistical significance, $p < 0.05$). 4 different bin widths have been used for SM classes: $0.04 \text{ m}^3 \text{ m}^{-3}$ (a,e,i), $0.03 \text{ m}^3 \text{ m}^{-3}$ (b,f,j), $0.02 \text{ m}^3 \text{ m}^{-3}$ (c,g,k) and $0.015 \text{ m}^3 \text{ m}^{-3}$ (d,h,l). Different lower boundaries of the SM classes have been used: $.1 \text{ m}^3 \text{ m}^{-3}$ (top), $0.092 \text{ m}^3 \text{ m}^{-3}$ (middle) and $0.108 \text{ m}^3 \text{ m}^{-3}$ (bottom). Error bars show the standard deviation of EF^* . Dark-grey solid lines result from a piecewise linear regression between SM and EF^* with the black dot-dashed line indicating the breakpoint and the light-grey ribbon the respective interquartile range derived with bootstrapping.

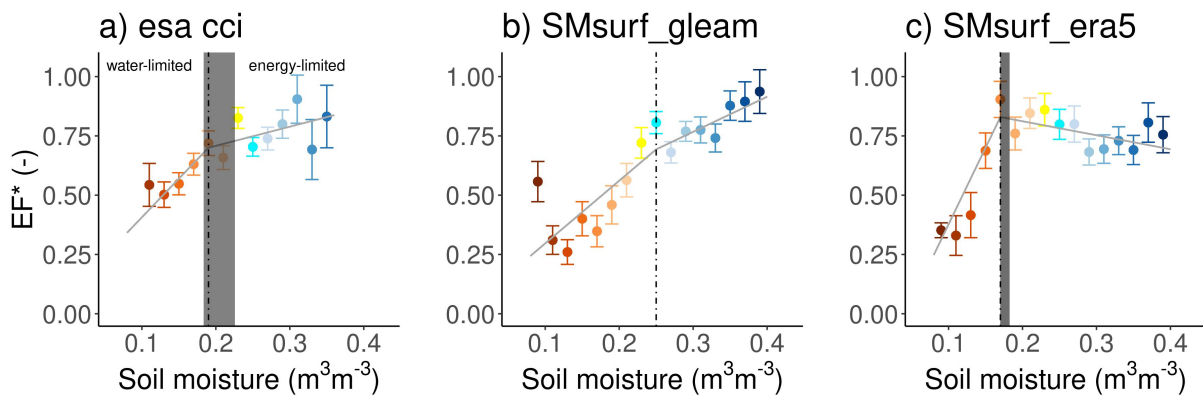


Figure 3.A4: Robustness of EF^* and piecewise linear regressions according to different soil moisture datasets. Relation between the slope of the linear models (EF^*) with soil moisture from ESA CCI (a), GLEAM (b) and ERA5 (c). Solid points depict EF^* when $p < 0.05$. Error bars show the standard deviation of the linear models. Error bars show the standard deviation of EF^* . Dark-grey solid lines result from a piecewise linear regression between SM and EF^* with the black dot-dashed line indicating the breakpoint and the light-grey ribbon the respective interquartile range derived with bootstrapping.

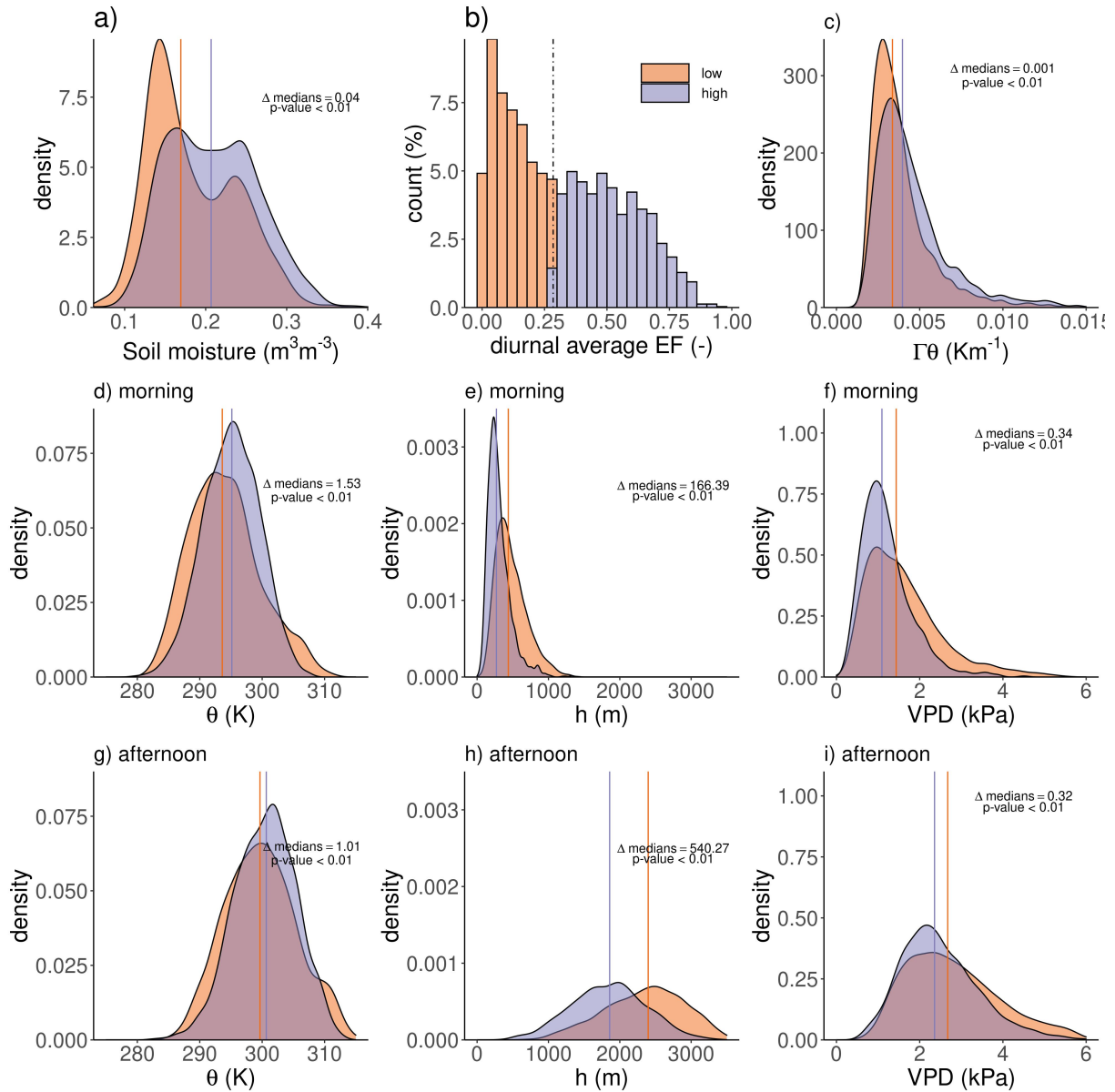


Figure 3.A5: Evaporative fraction control on diurnal ABL evolution. Data has been divided into sounding days with a lower (orange) or higher (blue) evaporative fraction (EF) than the median. a) Surface soil moisture for available sounding days from the ESA CCI data set (Dorigo et al., 2017). EF b) and potential temperature lapse rate c) averaged between 08:00 and 14:00 local solar time. Potential temperature (d, g), ABL height (e, h) and the vapor pressure deficit (f, i) at 08:00 and 14:00. Vertical orange and blue lines denote the medians from the respective distributions. Annotations show the difference between the medians and the p-values of the Kolmogorov-Smirnov test.

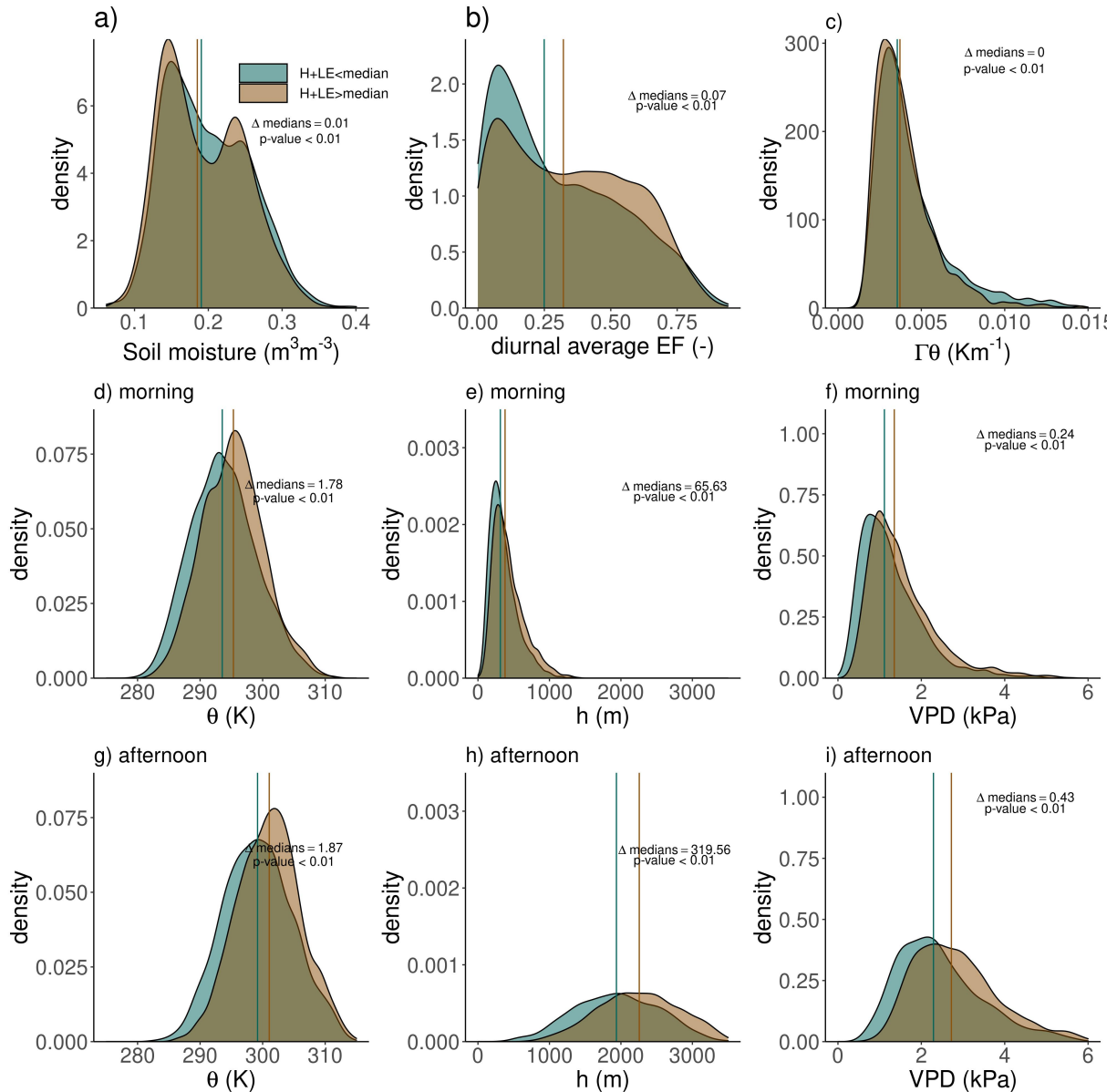


Figure 3.A6: The effect of seasonality on diurnal ABL evolution. Data has been divided in sounding days with more (brown) or less (green) available energy (H+LE) than the local median, thereby accounting for latitudinal differences in H + LE. a) Surface soil moisture for available sounding days from the ESA CCI data set (Dorigo et al., 2017). Evaporative fraction b) and potential temperature lapse rate c) averaged between 08:00 and 14:00 local solar time. Potential temperature (d, g), ABL height (e, h) and the vapor pressure deficit (f, i) at 08:00 and 14:00. Vertical brown and teal lines denote the medians from the respective distributions. Annotations show the difference between the medians and the p-values of the Kolmogorov-Smirnov test.

Chapter 4

Ecosystem water limitation under climate change

This chapter is based on:

J. M. C. Denissen, A. J. Teuling, A. J. Pitman, S. Koirala, M. Migliavacca, W. Li, M. Reichstein, A. J. Winkler, C. Zhan, and R. Orth (2022b). “Widespread shift from ecosystem energy to water limitation with climate change”. *Nature Climate Change*, *accepted*

4.1 Abstract

Terrestrial ecosystems are essential for food and water security, and carbon dioxide (CO₂) uptake. Ecosystem function is dependent on the availability of soil moisture, yet it is unclear how climate change will alter soil moisture limitation on vegetation. Here we use an ecosystem index that distinguishes energy and water limitation in Earth System Model simulations to show a widespread regime shift from energy to water limitation between 1980-2100. This shift is found both in space and time. While this is mainly related to a reduction in energy-limited regions associated with increasing surface net radiation, the largest shift towards water limitation is found in regions where net radiation increases are accompanied by soil moisture decreases. We therefore demonstrate a widespread regime shift in ecosystem function that is stronger than implied by individual trends in net radiation, soil moisture and terrestrial evaporation, with important implications for future ecosystem services.

4.2 Main Text

The provision of food and water, the uptake of carbon dioxide (CO₂), and evaporative cooling depend on a sufficient moisture supply to the land surface (Mekonnen and Hoekstra, 2016; Piao et al., 2010). Climate change affects moisture supply, and in combination with rising atmospheric CO₂, affects ecosystem function (Ciais et al., 2005; Gampe et al., 2021; Green et al., 2019; Jiao et al., 2021; Reichstein et al., 2013; Rockström et al., 2009). The water and carbon cycles are coupled via vegetation, which assimilates CO₂ during photosynthesis, while simultaneously transpiring through the stomata. From an energy balance perspective, transpiration (T) cools the surface air at the expense of energy which would otherwise contribute to surface heating (Budyko, 1974; Denissen et al., 2021; Seneviratne et al., 2010). Through this water-vegetation-climate feedback, changes in soil moisture influence evaporative cooling and consequently surface warming (Seneviratne et al., 2010). However, regional changes in water availability do not affect ecosystem function uniformly. Ecosystem responses depend on whether the region is energy- or water-limited (Ciais et al., 2005; Denissen et al., 2020; Flach et al., 2018; Kroll* et al., 2022). In addition, rising atmospheric CO₂ is expected to influence physiological processes that create more favorable conditions for photosynthesis and consequently plant growth (Donohue et al., 2013; Ukkola et al., 2016; Zhu et al., 2016) with contrasting impacts on plant transpiration and therefore energy and water cycles (Donohue et al., 2013; Ukkola et al., 2016).

Fundamental to the future of the terrestrial carbon sink is the extent to which terrestrial ecosystems are becoming more water limited (Berg and McColl, 2021; Berg and Sheffield, 2019a; Feng and Fu, 2013; Green et al., 2019; Greve et al., 2014; Huang et al., 2016; Jiao et al., 2021; Jung et al., 2010; Zhou et al., 2021). Agreement in trends of individual water-related variables such as soil moisture and terrestrial evaporation (usually referred to as evapotranspiration (Miralles et al., 2020)) is lacking. This extends to traditional drought or aridity indices, irrespective whether observations (Albergel et al., 2013a; Dorigo et al., 2012; Huang et al., 2016; Mueller et al., 2013), reanalyses (Mueller et al., 2013), climate model simulations (Mueller et al., 2013; Zhang et al., 2016), or future climate projections (Berg and Sheffield, 2018; Böhnisch et al., 2021; Feng and Zhang, 2015; Huang et al., 2016; Lian et al., 2021; Sherwood and Fu, 2014) are used. The analysis of the ecosystem response to a changing climate is complicated by various processes involved at different temporal scales and operating in different directions. For instance, while the observed widespread vegetation greening in recent decades does not support the notion of increased water limitation (Berg and Sheffield, 2019a; Donohue et al., 2013; Ukkola et al., 2016; Zhu et al., 2016), it is mostly driven by CO₂ fertilization which can at least temporarily overshadow ongoing changes in water availability. Further, by controlling water availability in water-limited regions, large-scale modes of variability (e.g., the El Niño Southern Oscillation) exert strong controls over interannual variability in ecosystem water limitation (Miralles et al., 2014a). Reconciling the degree to which ecosystem water limitation can affect vegetation through drought stress (Brodribb et al., 2020), tree mortality (McDowell and Allen, 2015) and lead to changes in surface properties including albedo (Lobell and Asner, 2002; Tollerud

et al., 2020) and roughness (Anderegg et al., 2013) is crucial. Existing uncertainty is partly related to differing approaches (Berg and Sheffield, 2018). Some studies analyzed water supply through soil moisture (Berg and McColl, 2021; Green et al., 2019; Jiao et al., 2021; Jung et al., 2010; Zhou et al., 2021), others focused on water demand by considering precipitation alongside (potential) evaporation (Berg and Sheffield, 2019a; Feng and Fu, 2013; Huang et al., 2016). These differing approaches can lead to different outcomes (Greve et al., 2019).

In contrast to the debate on water availability, increasing trends in energy availability are clear, consistent and coincide with increasing temperatures (IPCC, 2021). This affects ecosystems in multiple ways; The RuBisCO enzyme activity is crucial for photosynthesis and is sensitive to increasing temperatures (Busch and Sage, 2017; Perdomo et al., 2017). Further, temperature influences vapour pressure deficit (Novick et al., 2016; Sherwood and Fu, 2014; Yuan et al., 2019); higher temperatures increase atmospheric evaporative demand, increasing ecosystem water limitation, and potentially cause plants to close their stomata to prevent excessive water loss (Cowan, 1977; Humphrey et al., 2021; Oren et al., 1999). This highlights the necessity of considering energy and water variables together in a comprehensive characterization of ecosystem water limitation (Green et al., 2019; Novick et al., 2016).

Here, we study ecosystem energy and water limitation together, to reconcile whether the surface is drying or wetting from an ecosystem function perspective. We employ the Ecosystem Limitation Index (ELI) (Denissen et al., 2020), Methods) that reflects the fundamental concepts of water- and energy limitation. These typically focus on the sensitivity of ecosystem function (represented through terrestrial evaporation anomalies) to water (soil moisture anomalies) and energy availability (surface net radiation anomalies) in energy-limited conditions. Here, these sensitivities are assessed statistically with correlations between anomalies of terrestrial evaporation with soil moisture ($\text{cor}(\text{SM}', \text{ET}')$, typically positive in water-limited conditions) and net surface radiation ($\text{cor}(\text{surface net radiation } (R_n)', \text{ET}')$, typically positive in energy-limited conditions (Denissen et al., 2020; Teuling et al., 2009a)), respectively. The ELI is then computed as $\text{cor}(\text{SM}', \text{ET}') - \text{cor}(R_n', \text{ET}')$, where the prime denotes monthly anomalies of soil moisture (SM), terrestrial evaporation (ET) and surface net radiation (R_n), respectively. Positive ELI values denote water-limited conditions and negative values indicate energy-limited conditions. This way, the ELI moves beyond traditional drought indices based on meteorological information by evaluating the functional ecosystem response to hydro-meteorological conditions. Further, the ELI permits studying deviations from the seasonal cycle by using monthly anomalies. Within the ELI, the terrestrial evaporation reflects the total ecosystem response, as it comprises bare soil evaporation, canopy interception and plant transpiration. Soil moisture is used as it reflects water available for terrestrial evaporation. Net surface radiation functions as the main proxy for energy availability, as it drives the surface energy balance, therefore directly controlling ET. As such, it has empirically been found as the main control of ET (Maes et al., 2019). In addition to surface net radiation, we use air temperature as a simple and widely-available proxy for energy availability. The ELI is calculated using historical and 'business as usual' SSP5-8.5 simulations

from the Coupled Model Intercomparison Project (CMIP6 (Eyring et al., 2016)) from 11 models (Methods) for the period 1980-2100.

4.2.1 Continuation of present ecosystem limitation trends

We find a steady increase in ELI throughout 1980 - 2100, mainly reflecting a weakening correlation between terrestrial evaporation anomalies and surface net radiation anomalies, but also a strengthening correlation with soil moisture anomalies (Figure 4.1a). A comparable ELI trend can be found when computed with anomalies of air temperature as an alternative energy variable (Supplementary Figure 4.A1), due to high correlation of surface net radiation and air temperature at the monthly time scale. A similar agreement between ELI trends from different can be found when exchanging time on the x-axis for air temperature warming since 1980 (Supplementary Figure 4.A2), pointing to similar climate sensitivities between these models. This comparison also indicates that beyond a global warming of 1.5°C, all considered models agree on the increasing sign of the ELI change. The relatively small change in water limitation corroborates the projections of hardly any dryland expansion as previously reported (Berg and McColl, 2021). However, despite a larger contribution of energy limitation, the strong ELI trend is a result of contributions of both components.

We find that the role of net surface radiation versus soil moisture is more pronounced when comparing their respective global trends (Figure 4.1b,c). Widespread increasing net radiation is associated with declining energy limitation, thereby increasing the ELI. Simultaneously, this involves increasing atmospheric water demand associated with higher temperatures (Supplementary Figure 4.A3c), as reflected in variables such as relative humidity or vapour pressure deficit (Supplementary Figure 4.A3a,b (Lian et al., 2021; Novick et al., 2016; Yuan et al., 2019)). This further increases ecosystem water limitation and consequently temperature through the water-vegetation-climate feedback. In contrast to multi-model net radiation trends, global changes in soil moisture are not significant (Figure 4.1c), with substantial uncertainty across models. This uncertainty is related to inconclusive trends in precipitation ((Orth et al., 2016) and Supplementary Figure 4.A3d) and land surface dryness, which varies between regions and soil depths (Berg et al., 2016), and differences between root-zone depths amongst the models.

Until approximately 2030 the CMIP6 models agree on a global terrestrial evaporation increase (Figure 4.1d). From 2030 onwards, multi-model uncertainty increases substantially, as some models show continued increases in terrestrial evaporation, while others suggest decreases. The increase in uncertainty of terrestrial evaporation trends over time is also apparent for precipitation (Supplementary Figure 4.A3d), which leads to a net zero change in water storage in the root-zone with increasing uncertainties (Figure 4.1c). The sign and magnitude of global multi-model terrestrial evaporation trends compare well with a sample of state-of-the-art datasets, suggesting that CMIP6 models represent terrestrial evaporation reasonably and that terrestrial evaporation from these models can be used to evaluate changes in land-atmosphere interactions.

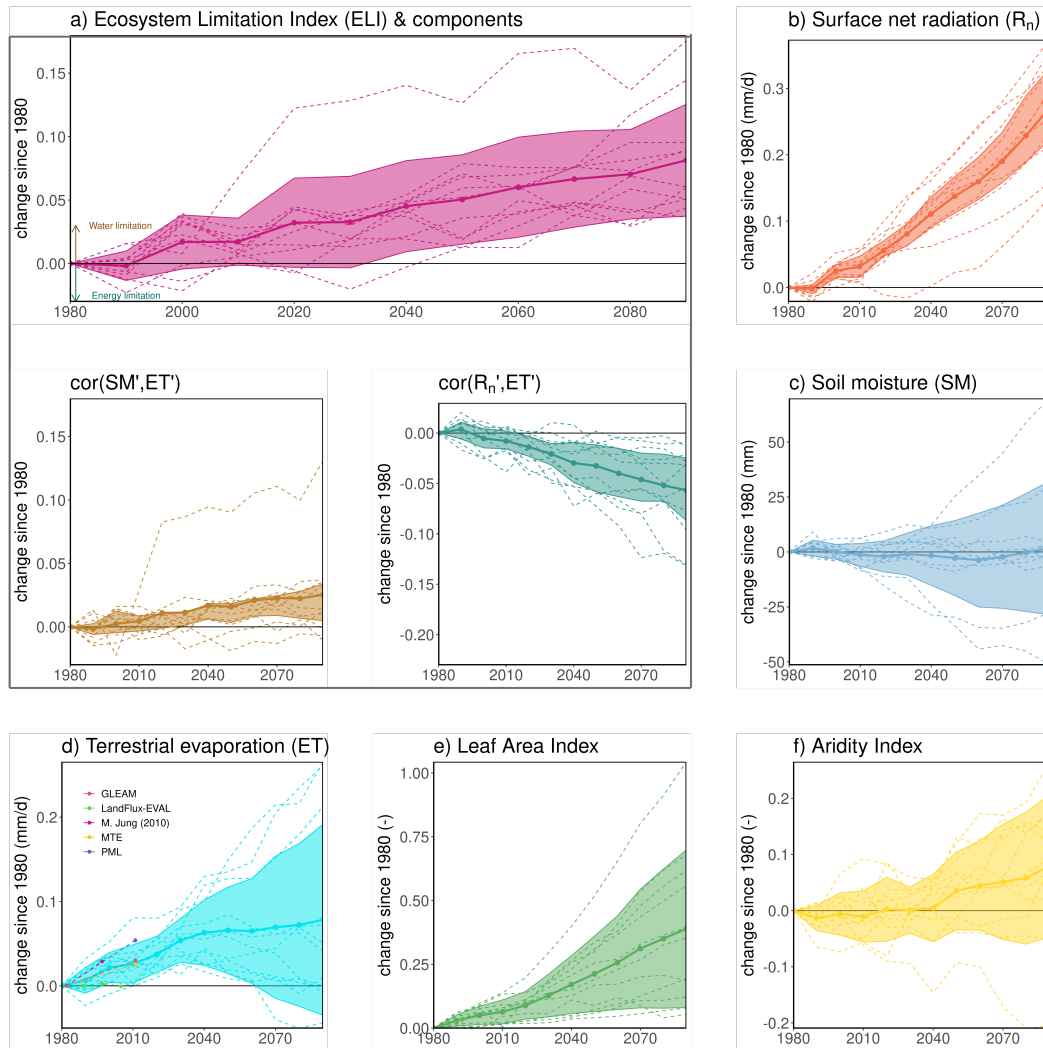


Figure 4.1: Past and projected global trends in climate and ecosystem variables. Global evolution of a) Ecosystem Limitation Index (ELI) and its individual components $\text{cor}(\text{SM}', \text{ET}')$ and $\text{cor}(\text{R}_n', \text{ET}')$ and related variables b) Surface net radiation (divided by the latent heat of vaporization and assuming a density of 1000 kg/m^3), c) Soil moisture, d) Terrestrial evaporation, e) Leaf Area Index and f) Aridity Index. Dashed colored lines depict the globally and decadal averaged time series of all respective variables per individual model. Solid lines with dots depict multi-model mean time series inferred from the model-specific time series (the median is used in panel f), as aridity index can approach infinity in regions with low precipitation), where the shaded regions cover ± 1 multi-model standard deviation. The y-axis denotes the change since. Global averages are calculated over land grid cells that have complete time series for all models and variables and are weighted according to the surface area per grid cell. Dot-dashed lines in panel d) denote reference terrestrial evaporation data sets (Jung et al., 2010; Martens et al., 2017; Mueller et al., 2013; Zhang et al., 2016). This figure is created with the ggplot2 package (Wickham et al., 2022).

The consistent increase of leaf area index (LAI) during the study period, with increasing multi-model spread, reflects the impact of CO₂ fertilization (Donohue et al., 2013; Ukkola et al., 2016; Zhu et al., 2016), (Winkler et al., 2021). Enhanced LAI in turn contributes to increased plant transpiration (Supplementary Figure 4.A4c (Wei et al., 2017)). Combined with the levelling off of increases in the multi-model mean of the sum of bare soil evaporation and canopy interception around 2030 (Supplementary Figure 4.A4b), the fraction of transpiration with regards to terrestrial evaporation increases in the future too (T/ET; Supplementary Figure 4.A4a,c,d). This suggests an increasing influence of vegetation for the land water and energy balances. Additionally, when only considering plant transpiration anomalies for ELI (ELI_T) instead of terrestrial evaporation anomalies (default ELI), we find a similar but slightly weaker signal (Supplementary Figure 4.A5). While energy limitation in ELI and ELI_T are very similar, water limitation is stronger in ELI, which corroborates earlier findings (Berg and Sheffield, 2019b). This is not solely due to plant transpiration relying mostly on root-zone soil moisture with large uncertainties (Figure 4.1c), but also to plant transpiration being parametrized differently by models and it being likely more uncertain than terrestrial evaporation due to a lack of observations (Wei et al., 2017). The higher values for $\text{cor}(\text{SM}', \text{ET}')$ can be related to, and confounded by, canopy interception, as precipitation evaporates from leaves instead of infiltrating into the root zone (Berg and Sheffield, 2019b). In this context, we use partial correlations $\text{cor}(\text{SM}', \text{ET}' | R_n')$ and $\text{cor}(R_n', \text{ET}' | \text{SM}')$ for computing an alternative ELI to exclude confounding effects of energy on water limitation and vice versa, and show that the ELI trend remains similar, but slightly weaker (Supplementary Figure 4.A6). This is similar to earlier observation-based findings in Europe (Denissen et al., 2020). Pure water limitation is more sensitive to confounding energy effects than vice versa, due to the globally consistent net radiation trend (Figure 4.1b) as opposed to the more uncertain global soil moisture trend (Figure 4.1c).

Finally, the long-term land surface dryness as expressed by the multi-model mean Aridity Index (unit-normalized net radiation divided by precipitation) tends to increase (Figure 4.1f), but less consistently than the ELI. This i) suggests that the ELI trend cannot be explained without considering those ecosystem feedbacks that amplify water limitation and ii) shows the importance of comprehensively analyzing regime shifts from an ecosystem perspective. Further, we compare the trends across all considered variables that are normalized by the interannual standard deviation of the respective detrended time series (Supplementary Figure 4.A7). Here, the normalized ELI trend is most notable, even more than its individual components. This underlines the importance of the combined effect of changes in energy and water availability alongside respective ecosystem feedbacks. We note that the uncertainties shown for the trends of net radiation, terrestrial evaporation and particularly soil moisture do not directly affect the estimation of the ELI. The ELI is computed from detrended and de-seasonalized data (see Methods) where this pre-processing is done separately for each model and grid cell such that different trends and seasonal cycles are removed. The remaining uncertainty between the (interplay) of the anomalies induces the observed inter-model spread in the estimation of the ELI

as shown in Figure 4.1a; however, this only concerns the magnitude of the increasing ELI trend, not the trend itself which is apparent from all individual models.

4.2.2 Expansion of ecosystem water limitation

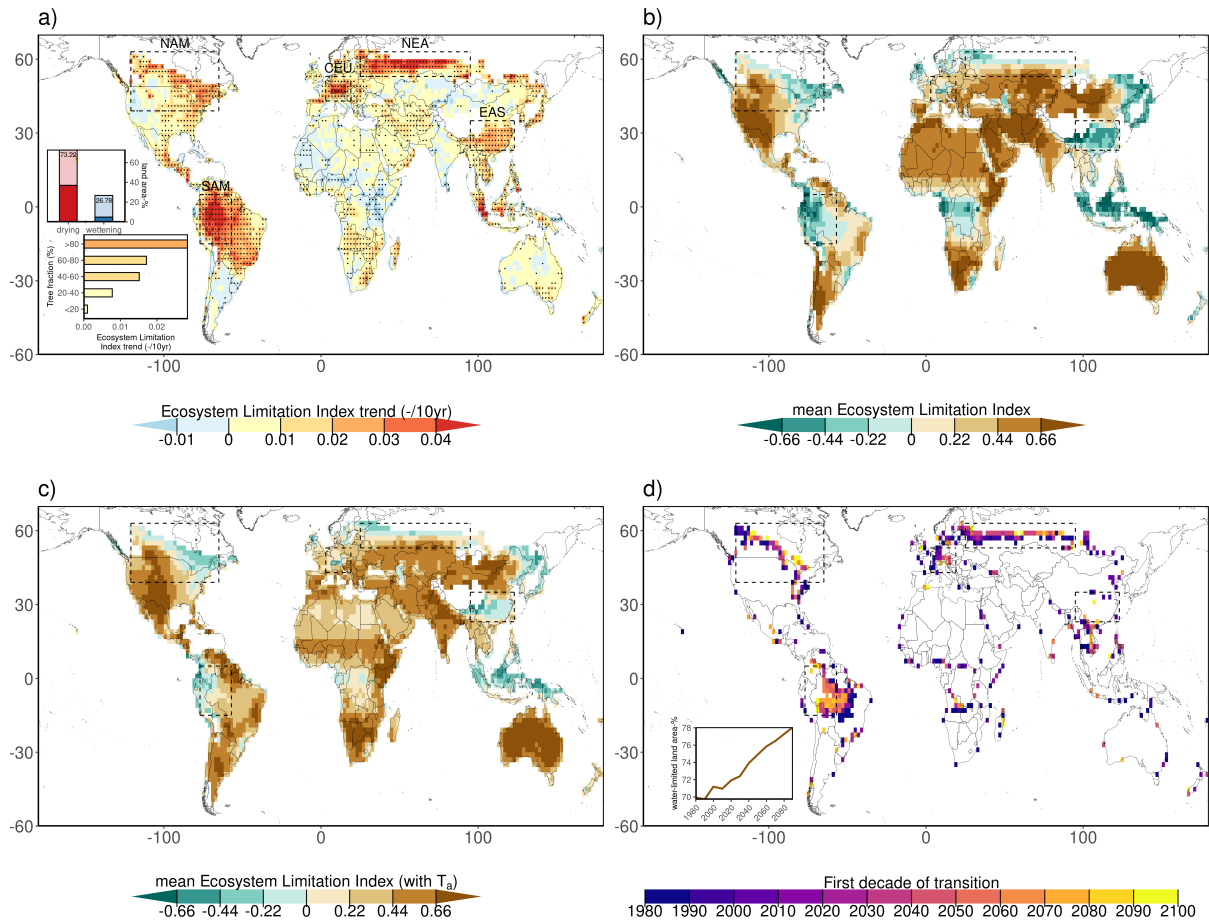


Figure 4.2: Global distribution and trends of ecosystem water limitation. a) Trend in the multi-model mean of ELI (dots indicate significance: $p < 0.05$ based on Kendall's tau statistic). The dashed boxes indicate regions of interest to aid easier cross-comparisons with other maps. The top inset displays the fraction of the warm land area that is drying or wetting according to ELI trends ($p < 0.05$ is hued darker). The bottom inset displays area-weighted average ELI trends for regions with different tree fractions based on six CMIP6 models (Methods). b) Multi-model mean ELI between 1980-2100. c) Same as b), but derived with T_a instead of surface net radiation anomalies. d) Timing of regime shift from energy to water limitation as indicated by ELI values becoming positive. The inset shows the global time series of the water-limited fraction of the warm land area (Methods). This figure is created with the ggplot2 package and the country borders using the maptools package (Bivand et al., 2022; Wickham et al., 2022).

As shown in Figure 4.2a, we find increasing ELI trends across approximately 73% of the warm land area (all grid cells with a sufficient number of months with $T_a > 10^\circ\text{C}$ in at least 4 models, see Methods). Positive ELI trends are more widespread than negative trends: $p < 0.05$ in 38% of the warm land area for positive trends in contrast to 4% for negative trends. We defined regions of interest (dashed boxes) around those areas with the strongest ELI trends: North America (NAM), South America (SAM), Central Europe (CEU), Northern Eurasia (NEU) and East Asia (EAS). As shown in the inset, ELI increases tend to be strongest over regions with large tree coverage. The increasing drought stress, particularly in these regions in northern latitudes, has substantial implications for the magnitude, and potentially sign, of CO_2 exchange (Gampe et al., 2021; Keenan et al., 2014). The ELI trends of the individual CMIP6 models show similar spatial patterns (Supplementary Figure 4.A8) and agree well with the sign of the multi-model mean ELI trend (Supplementary Figure 4.A9a), particularly in the regions of interest. This agreement between individual CMIP6 models emerges despite the relatively high standard deviation between trends of individual CMIP6 models in the regions of interest (Supplementary Figure 4.A9b), illustrating that CMIP6 models generally agree on the sign of the ELI trend, but less on the magnitude. Elaborating further on the individual contributions of water and energy limitation on regional ecosystem regime shifts (Figure 4.1), we show that particularly in the regions of interest, the ELI trend is driven by both an increasing water limitation and a decreasing energy limitation (Supplementary Figure 4.A10).

Figure 4.2b shows that in the regions of interest, current conditions are either slightly energy limited or transitional, hinting at an expansion of water-limited area from 1980 to 2100. We also observe further shifts towards ecosystem water limitation in current water-limited regions, such as parts of South America, North Africa, Australia and the west of North America. Interestingly, not all tropical regions are consistently subjected to increasing ELI. For example, there is a contrast between South America and tropical Africa because soil moisture is decreasing across large parts of South America (Supplementary Figure 4.A10b), while for Central Africa the CMIP5 ensemble estimates increasing soil moistures related to projected precipitation increases (Collins et al., 2013). Spatial patterns of ELI (trends) computed with air temperature anomalies are comparable (Figure 4.2c), with SAM and Central Africa being slightly less energy limited. This indicates a higher sensitivity of tropical ecosystems to incoming radiation due to typically dense cloud cover making radiation a limiting factor for terrestrial evaporation (Nemani et al., 2003).

Next, we assess the timing of shifts of energy-limited to water-limited regions over the study period (Figure 4.2c). We detect the time of regime shifts as the first decade after which the ELI is of positive sign. We find that transitional regions are migrating in space throughout 1980 - 2100, most notably in the Northern Hemisphere (NAM and NEA). This causes the water-limited fraction of the warm land area to expand from 82% to 88% (inset), representing approximately an additional 6 million km^2 in 2100 as compared to 1980. ELI increases occur continuously over time and in similar ways across different regions of interest (Supplementary Figure 4.A12). This foreshadows a further expansion of areas in water deficit, continuing an observed trend over

1982 - 2015 (Jiao et al., 2021). Further, this indicates that global ELI trends (Figures 1a, 2a) are not simply strengthening (weakening) pre-existing water-limited (energy-limited) conditions, but lead to actual regime shifts. We find similar ELI trends when applying air temperature anomalies as a proxy for energy availability (Supplementary Figure 4.A13a), but since especially the tropics show a lower sensitivity to temperature anomalies, spatial shifts in the transitional regions are particularly different in SAM (Supplementary Figure 4.A13b).

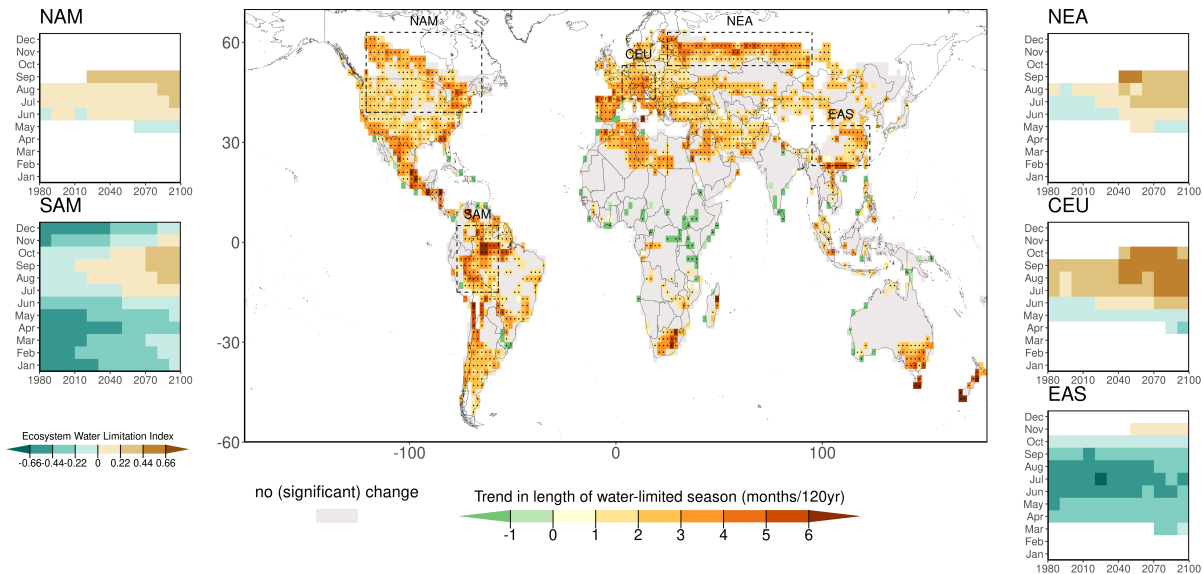


Figure 4.3: Lengthening of water-limited periods across the globe from 1980 to 2100. The central panel displays trends of the number of water-limited months-of-year expressed as Theil-Sen slope across decades (dots indicate significance: $p < 0.05$ based on Kendall's tau statistic, Methods). Grey denotes regions where no significant changes in the length of the water-limited season were detected. Side panels show the multi-model mean month-of-year ELI evolution in the regions of interest (Methods). White color denotes cold months ($T_a < 10^\circ\text{C}$). This figure is created with the ggplot2 package and the country borders using the maptools package (Bivand et al., 2022; Wickham et al., 2022).

In addition to assessing ELI trends in space, we show trends in water-limited months-of-year to investigate ELI changes in time across seasons (Figure 4.3). In 45% of the warm land area and particularly in our regions of interest, we detect an increase in the duration of the water-limited season by up to 6 months, as opposed to a decrease in water-limited months in 4% of the warm land area. This corresponds with observational analyses that found the period during the year associated with water surplus is diminishing (Jiao et al., 2021). The side panels in Figure 4.3 show the changes over time in the duration of the water-limited season. For NAM, NEA, CEU and EAS the warm season length (months-of-year with temperature $> 10^\circ\text{C}$) increases while in SAM it already covers all months. In all regions, the water-limited season expands to earlier and/or later months which were previously energy-limited or cold. Further, the maximum water-limitation intensifies.

4.2.3 Attribution of trends towards ecosystem water limitation

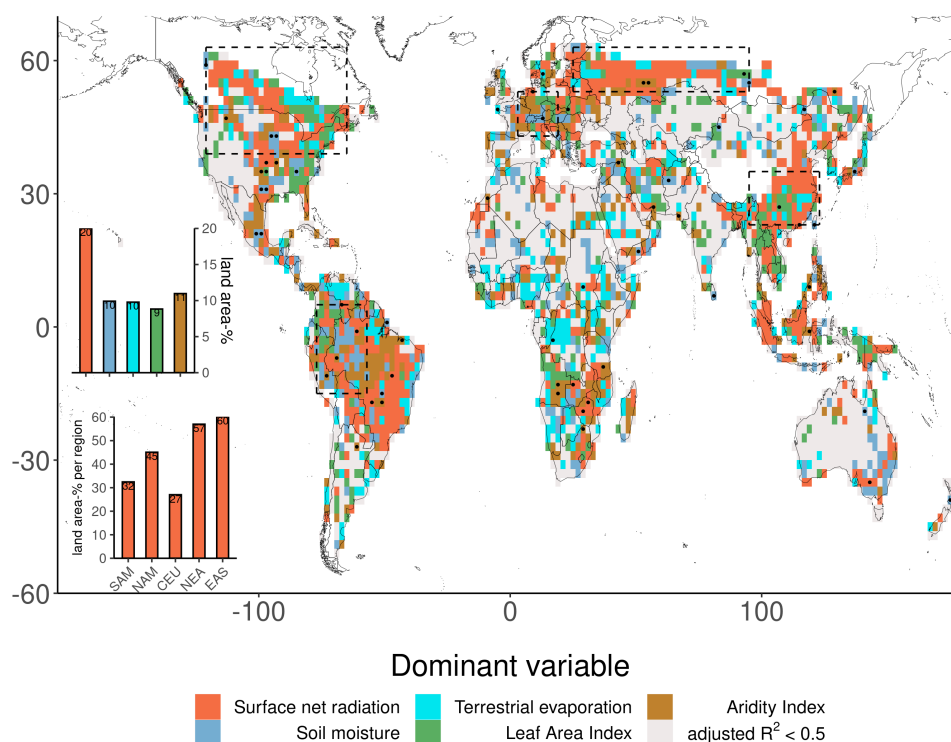


Figure 4.4: Attribution of ELI trends to land-atmosphere variables. Colors indicate the variables that best predict the decadal ELI dynamics calculated using multivariate linear regression with a set of equally well-performing models, across which the most meaningful predictor is selected (Methods). Stippling indicates grid cells where only one linear model performs well ($\text{adjusted } R^2 > 0.5$) and contains only a single explanatory variable. Grey color denotes grid cells without any model with reliable performance ($\text{adjusted } R^2 < 0.5$). Insets show the total fraction of warm land area controlled by respective variables (top) and the fraction of ELI trends controlled by net radiation per region of interest (bottom). This figure is created with the ggplot2 package and the country borders using the maptools package (Bivand et al., 2022; Wickham et al., 2022).

Attributing ELI trends to land-atmosphere variables, in Figure 4.4 we identify relevant variables in approximately 59% of the warm land area, where sufficient variance of the ELI time series (12 decadal values) can be explained by the optimal combination of hydrological, meteorological and ecological predictors. Figure 4.4 does not necessarily rely on one multiple linear model only; all possible combinations of predictors are attempted and we consider all similarly performing multiple linear models ($\text{adjusted } R^2 > 0.5$, see Methods). By doing so, we effectively exclude predictors that carry similar information, which means that if multiple predictors are included in the best model, they must carry different information about ELI variability. Net radiation is the most important ELI predictor and is dominant in 20% of the warm land area. The other predictors are less dominant (9-11% of the warm land). Clearly, net radiation is relatively most important in terms of the area where it can predict ELI trends, but the full set of variables is required to

explain the trends globally as evidenced by the few grid cells that only have one predictor, which confirms earlier attribution analyses based on observations and model simulations (Humphrey et al., 2021; Jiao et al., 2021). Similar results are obtained with different thresholds for model performance (adjusted $R^2 > 0.3$ or adjusted $R^2 > 0.7$, Supplementary Figure 4.A14).

The scattered pattern in Figure 4.4 underlines the relevance of local climate, vegetation and/or soil characteristics and by extension land use changes in inducing shifts in ELI. We therefore extend the analysis in Figure 4.4, by expanding the number of considered predictors in the multivariate linear regression by including the time series of crop and tree fraction as proxies for land use change (Supplementary Figure 4.A15). The importances of changes in crop and tree fraction does not exceed the other variables. Moreover, the global average adjusted R^2 across the considered well-performing multivariate linear models in all grid cells is similar (0.42 versus 0.43 in the default analysis) indicating that the additional predictors are not important at the large spatial scales investigated here. Finally, the robustness of the multi-model mean attribution analysis is further confirmed by net radiation emerging as the most important predictor for most of the individual Earth system models (Supplementary Figure 4.A16).

Across the regions of interest, net radiation is the most relevant predictor in 27-60% of the respective regional areas where well-performing linear models could be fitted. Net radiation is the most important predictor across almost regions of interest, apart from CEU (Supplementary Figure 4.A17). This is corroborating the widespread alleviating energy limitation pushing ecosystems towards water limitation (Figure 4.1a, Supplementary Figure 4.A10b). The trends in the individual variables confirm that within the regions of interest, both increasing net radiation and decreasing soil moisture contribute to increasing ecosystem water limitation (Supplementary Figure 4.A11). In addition, increasing CO_2 and favorable energy- and water availability cause plants to increase their LAI and consequently terrestrial evaporation rates. LAI is increasing in regions close to transitioning between water- and energy-limited conditions and particularly at the northern latitudes: Plants may compete for light when water is abundant (and light is limiting) by allocating part of the increased carbon uptake to growing more leaves (Heijden et al., 2013).

While our study presents clear evidence of globally increasing ELI and physical mechanisms behind the changes, the accuracy of the analyses is intrinsically limited due to inherent uncertainties in the models. For example, different representations of some processes that are relevant for ecosystem function cause uncertainty in CMIP6 model simulations including the expected effects of CO_2 fertilization on LAI (Winkler et al., 2021; Zhu et al., 2016), water use efficiency (Donohue et al., 2013; Ukkola et al., 2016) and the implementation of dynamic vegetation (Methods). Some models have also been shown to be over-sensitive to CO_2 fertilization (Kolby Smith et al., 2016). Other processes, such as the development of deeper roots in response to increased water (or nutrient) demands (Fan et al., 2017; Smith-Martin et al., 2020), are typically not represented. Further, models have difficulty capturing evaporative regime changes (Best et al., 2015; Dirmeyer et al., 2018; O et al., 2020a) which can arise from different representations within the complex

coupled land-atmosphere system. This affects the multi-model spread, both with respect to the ELI trends and means, that are largest in the regions of interest (Supplementary Figure 4.A7). Finally, next to energy and water limitation, nutrient limitation on plant transpiration potentially plays an increasingly important role in the future (Peñuelas et al., 2017). We do not consider nutrient limitation; it is difficult to validate models given the sparsely available observational data and uncertainties associated with human involvement in the phosphorus and nitrogen cycles (Peñuelas et al., 2013). Despite these shortcomings, the multi-model mean terrestrial evaporation closely resembles state-of-the-art data sets. We suggest that these uncertainties may influence the magnitude but not the sign of ELI trends (Supplementary Figure 4.A9). Finally, we have established the ability of the ELI to reflect spatiotemporal variability in water-limited conditions by using a conceptual soil moisture model, within which the concept of water limitation is implemented through a soil moisture stress function. Using model output, we successfully validate the ELI against the number of days that soil moisture is drier than the critical soil moisture, effectively reflecting water-limited conditions, in a number of grid cells spanning from energy- to water-limited conditions (Supplementary Material and Supplementary Figure 4.A20).

Our study reveals a widespread regime shift from ecosystem energy to water limitation which can be attributed to a large extent to global warming. The strongest regional ELI trends are attributed to a combination of reduced energy limitation and exacerbated water limitation. Moreover, we find that net radiation is the most important predictor for the trend towards ecosystem water limitation, but not exclusively so, as global patterns can only be explained using a wider range of variables, including soil moisture, terrestrial evaporation, LAI and Aridity Index.

The ongoing debate on the importance of energy versus water limitation for terrestrial evaporation and ecosystem productivity (Green et al., 2019; Humphrey et al., 2021; Humphrey et al., 2018; Jung et al., 2010; Jung et al., 2017) can therefore be resolved by simultaneously considering energy and water limitation trends for ecosystem function. While globally soil moisture is important for making ecosystems water or energy-limited (Budyko, 1974; Denissen et al., 2020; Seneviratne et al., 2010), net radiation trends prove more consistent and dominate trends in ecosystem function.

Our analysis demonstrates a globally increasing ecosystem water limitation over 73% of the warm land area. This has implications for food and water scarcity, land degradation, disruption of CO₂ sequestration by terrestrial ecosystems, reduction in biodiversity and the duration, intensity and frequency of extreme events. By simultaneously considering both energy and water limitation, a fuller explanation of regional changes in ecosystem function, and a clearer view of future changes in these systems, can be obtained.

4.3 Methods

4.3.1 Ecosystem Limitation Index

The Ecosystem Limitation Index (ELI) is based on the correlation-difference index introduced by Denissen et al. (2020):

$$ELI = cor(SM', ET') - cor(R_n', ET') \quad (4.1)$$

For which Kendall's rank correlation is used to avoid assuming linear relationships between variables and where ' denotes monthly anomalies of soil moisture (SM), terrestrial evaporation (ET) and surface net radiation (R_n), respectively, which are derived by removing long-term trends and mean seasonal cycles (see "Data pre-processing"). We use monthly time resolution to mitigate the influence of synoptic weather variability. The ELI combines information on water ($cor(SM', ET')$) and energy availability $cor(R_n', ET')$ for a considerate estimate of ecosystem function. The choices of the variables representing energy (surface net radiation) and water availability (soil moisture) and ecosystem function (terrestrial evaporation) are motivated in the introduction.

The purpose of ELI is to distinguish water and energy-limited regimes (Supplementary table 1). With the soil moisture content below the wilting point (wilting point (SM_{wilt})), no water can be extracted from the soil for evaporation, neither for plant transpiration nor bare soil evaporation. The associated extremely low variability in terrestrial evaporation leads to near-zero $cor(SM', ET')$, $cor(R_n', ET')$ and ELI.

In water-limited regions, typically $ELI > 0$, $cor(SM', ET') > 0$ and $cor(R_n', ET')$ is either close to zero or negative. In these regions, the soil moisture is typically between the wilting point and the critical soil moisture content (critical soil moisture (SM_{crit})), which is defined as the soil moisture content above which plants can sustain their maximum evaporative fraction⁹⁻¹¹. So when $SM_{wilt} < SM < SM_{crit}$, positive soil moisture anomalies tend to increase the terrestrial evaporation, while negative soil moisture anomalies achieve the contrary ($cor(SM', ET') > 0$). Further, a positive soil moisture anomaly arises from precipitation; Alongside, the related cloudiness prevents radiation from reaching the land surface, which leads to a negative net radiation anomaly ($cor(R_n', ET') < 0$).

In energy-limited conditions, typically $ELI < 0$, $cor(R_n', ET') > 0$ and $cor(SM', ET')$ is either close to zero or negative. When the soil moisture content exceeds the critical soil moisture, the maximum evaporative fraction can be sustained and any soil moisture anomaly will not affect terrestrial evaporation directly ($cor(SM', ET') \approx 0$). Next to water, ample energy should be available in the form of adequate surface net radiation. Therefore, any positive (negative) radiation anomalies will increase (decrease) terrestrial evaporation $cor(R_n', ET') > 0$.

Table 1 explains that, according to average soil moisture conditions, soil moisture anomalies play an obvious role for terrestrial evaporation. But in energy limitation, surface net radiation anomalies dictate terrestrial evaporation. Therefore it is important to consider energy availability $\text{cor}(R_n', ET')$ alongside water availability $\text{cor}(SM', ET')$ when assessing ecosystem function. Note that the ELI is a correlative index, which cannot prove causality.

Table 4.1: Conceptual typical behavior of ELI ($\text{cor}(SM', ET') - \text{cor}(R_n', ET')$) and its individual components $\text{cor}(SM', ET')$ and $\text{cor}(R_n', ET')$ across soil moisture regimes.

	$SM < SM_{\text{wilt}}$	$SM_{\text{wilt}} < SM < SM_{\text{crit}}$	$SM > SM_{\text{crit}}$
Regime	dry	water limitation	energy limitation
$\text{cor}(SM', ET')$	≈ 0	> 0	< 0 or ≈ 0
$\text{cor}(R_n', ET')$	≈ 0	< 0 or ≈ 0	> 0
ELI	≈ 0	> 0	< 0

The different combinations of individual correlations in Supplementary table 2 reveal characteristic local temporal dynamics that could lead to either general energy limitation ($ELI < 0$) or water limitation ($ELI > 0$). For example, water limitation is concluded when $ELI > 0$, which follows when $\text{cor}(SM', ET') > \text{cor}(R_n', ET')$ is satisfied. The opposite is true for energy-limited conditions: when $ELI < 0$, $\text{cor}(SM', ET') < \text{cor}(R_n', ET')$. Supplementary table 2, which summarizes the most common combinations of the individual correlations to conclude water-limited ($ELI > 0$), or energy-limited conditions ($ELI < 0$), shows that the most common combination across all models and decades (see "Data pre-processing") is when both individual correlations are of opposing sign (84% of the water-limited warm land area and 58% for energy limitation), indicating that almost if not all months in that respective decade are consistently water or energy limited. Positive correlations of the same sign indicate that that decade is characterized by both intermittent energy and water limitation. Slightly negative individual correlations might co-occur, but are usually insignificant and therefore excluded.

Table 4.2: Overview of signs of individual correlations of the ELI typically associated with water and energy-limited conditions, respectively. All values denote the median area fraction of water-limited or energy-limited warm land area that satisfies the combinations; within brackets the interquartile range.

water limitation ($ELI > 0$)	energy limitation ($ELI < 0$)
$\text{cor}(SM', ET') > 0$ & $\text{cor}(R_n', ET') < 0$: 84% (7)	$\text{cor}(SM', ET') < 0$ & $\text{cor}(R_n', ET') > 0$: 58% (10)
$\text{cor}(SM', ET') > 0$ & $\text{cor}(R_n', ET') > 0$: 15% (5)	$\text{cor}(SM', ET') > 0$ & $\text{cor}(R_n', ET') > 0$: 40% (10)

4.3.2 Coupled Model Intercomparison Project Phase 6 (CMIP6) Data

We use publicly available simulations from 11 models included in the Coupled Model Intercomparison Project (CMIP6; (Eyring et al., 2016)), of which the most important aspects are

summarized in Table 3. For the historical period, we use the model simulations from 1980 to 2015. From the future scenario (2015 - 2100), we use simulations from the 'business as usual' SSP5-8.5 scenario from ScenarioMIP (O'Neill et al., 2016), which combines the 2100 forcing level of 8.5 Wm^{-2} of the CMIP5 Representative Concentration Pathways simulations (RCP8.5) with newly defined Shared Socioeconomic Pathways simulations for fossil-fueled development (SSP5). We do so assuming that this worst-case scenario will give insight into the potential implications on ecosystem function. All data is downloaded at the monthly time scale and aggregated to a common 2×2 degree grid cell spatial resolution.

Table 4.3: An overview of the CMIP6 models used in this study. For all models, variables temperature (tas), root-zone soil moisture (mrso), terrestrial evaporation (hfls), Leaf Area Index (lai), precipitation (pr) and in- and outgoing short- and longwave radiation (rlds,rsds,rflus,rsus) have been downloaded; here, all variables are abbreviated according to CMIP6 standardized names. *models that additionally provide variables evaporation from the canopy (evspsblveg) and near-surface relative humidity (hurs). **models that additionally provide variables crop fraction (cropFrac) and tree fraction (treeFrac). ***CAMS-CSM1-0 does not contain output for the year 2100, which is copied from 2099, and TaiESM1 does not contain data from December 2100, which is copied from November 2099. Dynamic vegetation reflects whether or not plant functional traits (PFT) can vary in time, responding to competition for resources. However, the resources considered in this context vary between models.

Institution	Model	Member	Version	Dynamic	Citation
National oceanic and Atmospheric Administration (NOAA) Geophysical Fluid Dynamics Laboratory (GFDL)*	GFDL-CM4	r1i1p1f1	v20180701	yes	(Guo et al., 2018a; Guo et al., 2018b; Held et al., 2019)
Centre National de Recherches Meteorologiques (CNRM)*/**	CNRM-ESM2-1	r1i1p1f2	v20191021	no	(Seferian, 2018; Séférian et al., 2019; Volodire, 2019)
Beijing Climate Center (BCC)	BCC-CSM2-MR	r1i1p1f1	v20190314	no	(Wu et al., 2018; Wu et al., 2019; Xin et al., 2019)
EC-Earth-Consortium */**	EC-Earth3-Veg	R ² i1p1f1	v20200226	yes	(Consortium (EC-Earth), 2019; Consortium (EC-Earth), 2020; Döscher et al., 2021)
Met Office Hadley Centre (MOHD)*	UKESM1-0-LL	R ² i1p1f2	v20190507	yes	(Good et al., 2019; Sellar et al., 2019; Tang et al., 2019)
Institute for Numerical Mathematics (INM)	INM-CM4-8	r1i1p1f1	v20190603	no	(Volodin et al., 2018; Volodin et al., 2019a; Volodin et al., 2019b)
Chinese Academy of Meteorological Sciences (CAMS)***	CAMS-CSM1-0	R ² i1p1f1	v20190924	yes	(Rong, 2019a; Rong, 2019b; Rong et al., 2019)
National Center for Atmospheric Research (NCAR)	CESM2	r4i1p1f1	v20200528	yes	(Danabasoglu et al., 2020; Danabasoglu, 2019a; Danabasoglu, 2019b)
Commonwealth Scientific and Industrial Research Organisation (CSIRO)**	ACCESS-ESM1-5	r1i1p1f1	v20191115	yes	(Ziehn et al., 2020; Ziehn et al., 2019a; Ziehn et al., 2019b)
Fondazione Centro Euro-Mediterraneo sui Cambiamenti (CMCC)*/**	CMCC-CM2-SR5	r1i1p1f1	v20200622	yes	(Cherchi et al., 2019; Lovato and Peano, 2020a; Lovato and Peano, 2020b)
Research Center for Environmental Changes (AS-RCEC)***	TaiESM1	r1i1p1f1	v20200901	no	(Lee and Liang, 2019; Lee and Liang, 2020; Lee et al., 2020)

4.3.3 Data pre-processing

After acquiring the data, a series of steps is taken to compute the ELI from the raw time series of the respective variables, which we have illustrated for two typically water- and energy-limited grid cells, respectively (Supplementary Figure 4.A18 and 4.A19). Per individual CMIP6 model, the entire 120-year period is divided into 12 decades (top row). Detrending is done per decade by removing linear regression fits (left panel middle row), to minimize biases in the anomaly

estimation that relate to assuming trend linearity over the entire 120-year period. Alongside, the seasonal cycle is calculated per decade as the month-of-year average of the respective variable (middle panel middle row). The anomalies result from subtracting the seasonal cycle from the detrended time series (right panel middle row). From the resulting time series we exclude all months colder than 10°C to remove periods with presumably inactive or sparse vegetation and frozen soils (dashed lines right panel middle row), at the same time ensuring that there is sufficient variability in terrestrial evaporation for computing the correlations that constitute the ELI. Thereafter, we compute the ELI for each decade and model. Thereby, we ignore grid cells with less than 30 data points. Whereas we use model data in this analysis to study potential long-term shifts in ecosystem water limitation, we highlight that this methodology can also be used in near-real time to monitor climate change in observational data with a trailing period of a decade. In addition, trends could be obtained by applying a moving window of a decade.

The warm land area as referred to in the manuscript then constitutes all grid cells that have full ELI time series from 1980 - 2100 for at least 4 models. The decadal month-of-year ELI time series (Figure 4.3) are only calculated when in the respective decade and month-of-year all 10 data points are available (temperature is warmer than 10°C).

The saturated vapour pressure was calculated with temperature and relative humidity as:

$$VP_{SAT} = \frac{610.7 * 10(7.5T_a)/(237.3 + T_a)}{1000} \quad (4.2)$$

where T_a is air temperature in °C. Then, the vapor pressure deficit (VPD) is:

$$VPD = VP_{sat} \left(1 - \frac{RH}{100}\right) \quad (4.3)$$

where RH is the relative humidity.

The sum of bare soil evaporation and canopy interception was calculated by subtracting plant transpiration from terrestrial evaporation (ET - T).

4.3.4 Computing Theil-Sen slopes and slope significance

The trends shown in Figures 4.2 and 4.3 and Supplementary Figures 4.A8, 4.A10, 4.A11 and 4.A13 are based on Theil-Sen slopes (Sen, 1968; Theil, 1992). This approach is insensitive to statistical outliers, as the median slope from a range of possible slopes is selected as the best fit. The significance of these slopes is determined based on Kendall's tau statistic from Mann-Kendall tests.

4.3.5 Multi-model inference using the Akaike Information Criteria

We assess the skill of a range of predictors (Table 4) to predict decadal ELI time series by using multivariate linear regression in combination with the dredge function in the MuMin package in R (Barton, 2018; Burnham and Anderson, 2004), thereby adopting a similar methodology to Fernández-Martínez et al. (2020). This function tries all possible combinations of predictors and ranks them based on the Akaike Information Criterion (AIC), allowing the selection of a range of similarly well-performing multivariate linear models with respect to model performance (likelihood) and complexity (number of parameters). From this, we select all models whose difference in AIC with the best ranked model is smaller than 4, which results in 1 to a maximum of 15 similarly performing multivariate linear models per grid cell. Only multivariate linear models with sufficient predictive power ($\text{adjusted } R^2 > 0.5$) are considered in the attribution analysis. In the case that there is only 1 model with one explanatory variable, this is assumed the most important predictor in that respective grid cell. Given just one multivariate linear model with multiple predictors, the most important variable is determined according to the variance explained per variable according to the 'lmg' metric in the 'relaimpo' R package (Groemping, 2007). When there are multiple multivariate linear models with multiple predictors, the most important predictor is picked according to the average variance explained across all multiple linear models, weighted by the Akaike weights assigned to all models.

Table 4.4: Indicates which predictors have been applied for which figures. From which models the predictors are available can be found in Table 3. *A denotes a Supplementary figure.

Predictors	Used for Figure*
Surface net radiation, soil moisture, terrestrial evaporation, Leaf Area Index, Aridity Index	4.4, 4.A14–4.A16
Crop & tree fraction	4.A15

4.A Appendix

4.A.1 Figures

This appendix represents the supplementary materials of the presented publication. All figures are created with the ggplot2 package and, if applicable, the country borders using the maptools package (Bivand et al., 2022; Wickham et al., 2022).

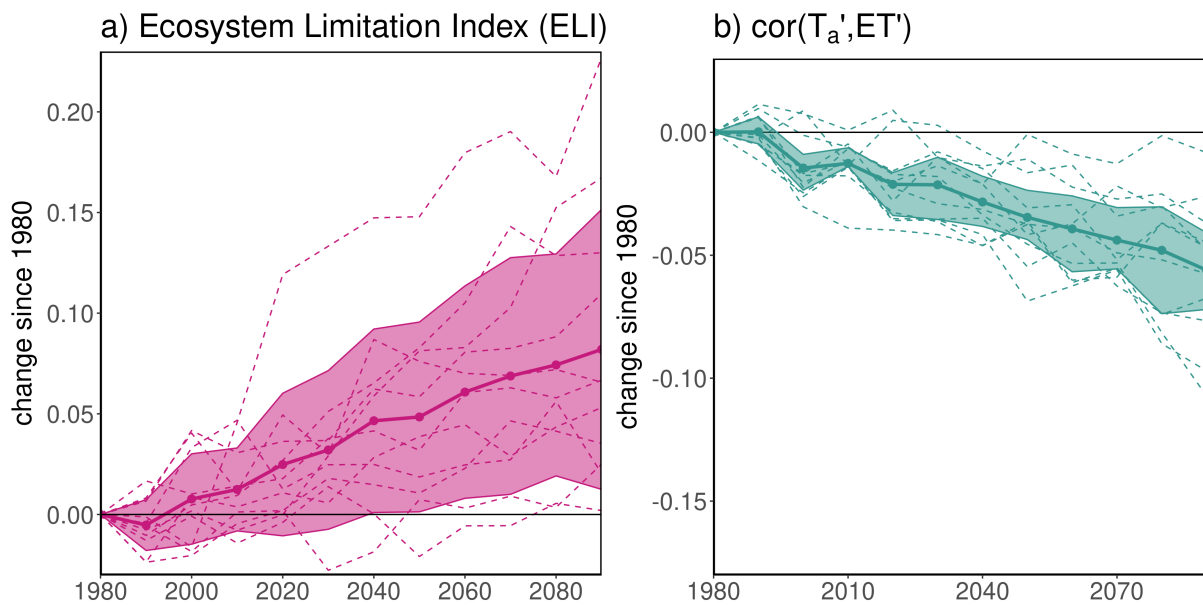


Figure 4.A1: a) Past and projected global trends in ELI based on air temperature anomalies and b) $\text{cor}(T_a', ET')$. Dashed colored lines depict the globally and decadal average time series of all respective variables per individual model. Solid lines with dots depict multi-model mean time series inferred from the model-specific time series, where the shaded regions cover ± 1 multi-model standard deviation. The y-axis denotes the change since 1980 in respective units. Global averages are calculated over land grid cells that have complete time series for all models and variables and are weighted according to the surface area per grid cell.

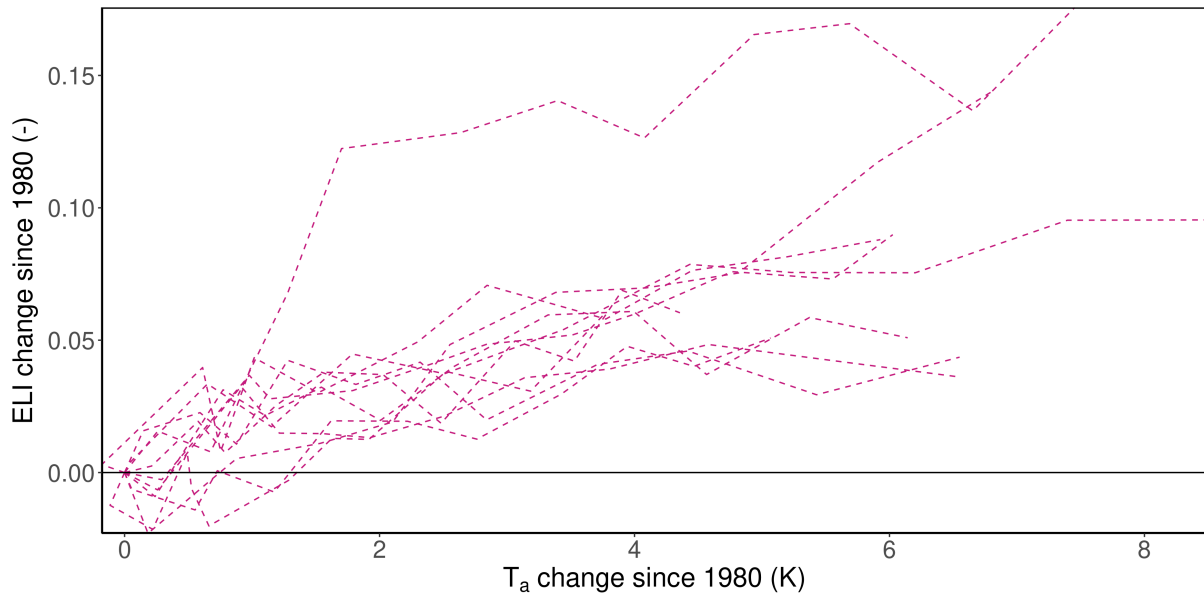


Figure 4.A2: : Past and projected global trends in ELLI for model-specific air temperature warming levels. Dashed colored lines depict the globally and decadal average time series of ELLI per individual model.

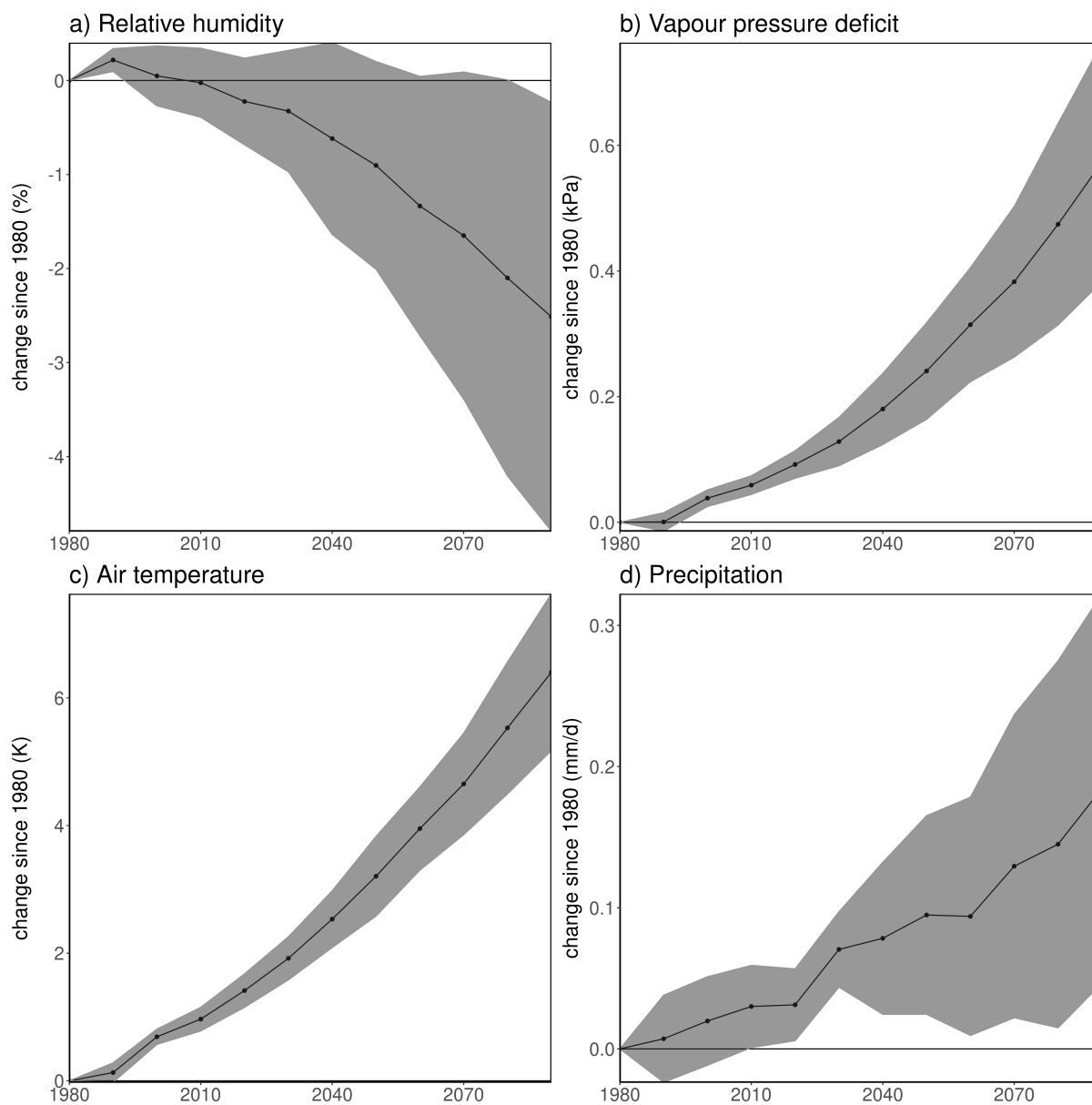


Figure 4.A3: Past and projected global climate trends. Global trends of a) relative humidity, b) vapour pressure deficit, c) air temperature and d) precipitation from 1980 - 2100 for 7 models only (Methods). Solid lines with dots depict the multi-model mean time series of the respective variables inferred from model-specific globally and decadal averaged time series, where the shaded regions cover ± 1 multi-model standard deviation. The y-axis denotes the change since 1980 in respective units. Global averages are calculated over land grid cells that have complete time series for all models and variables and are weighted according to the surface area per grid cell.

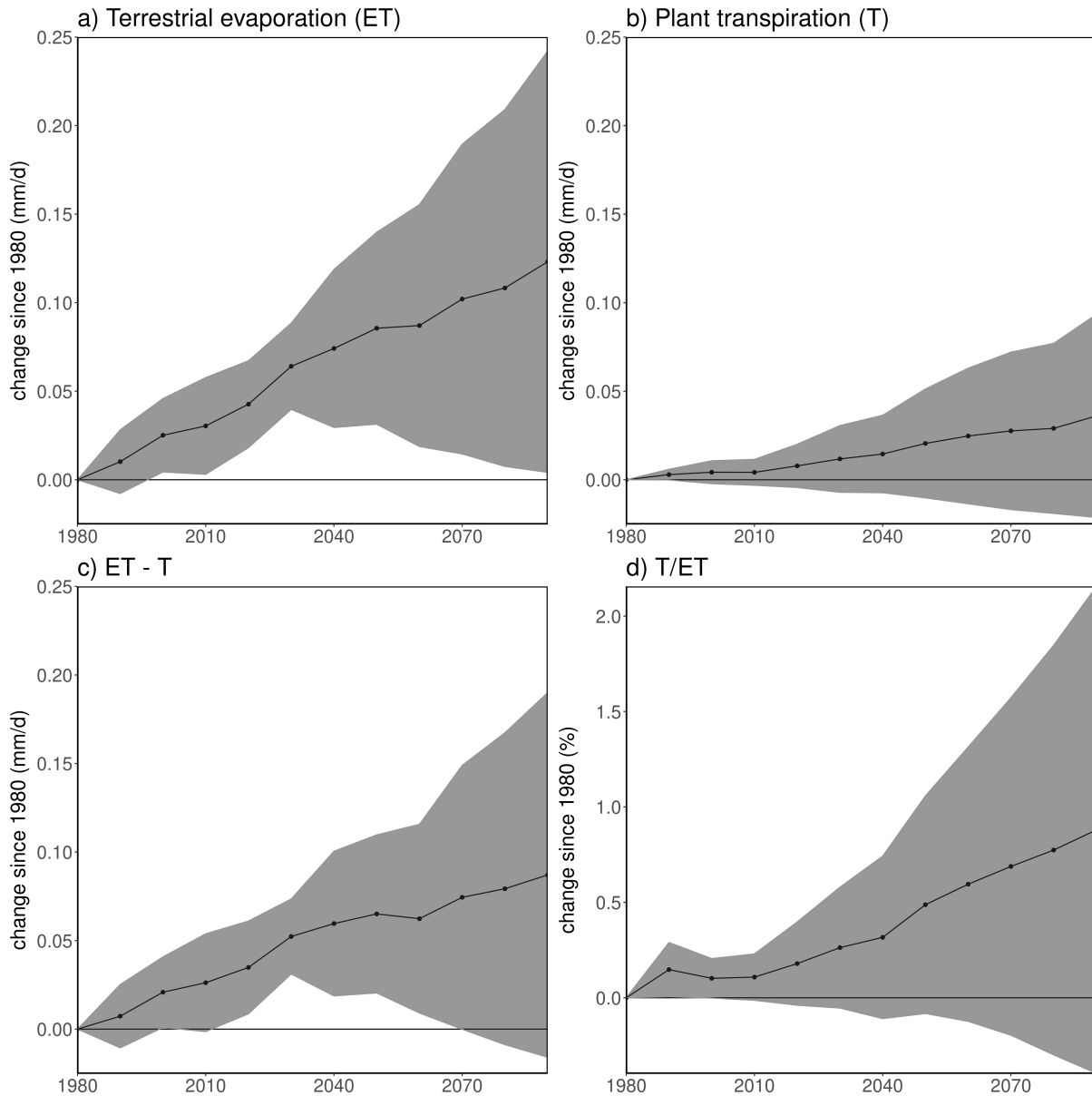


Figure 4.A4: Past and projected global trends of evaporative components. Global trends of a) terrestrial evaporation, b) plant transpiration (Methods), c) $ET - T$, effectively the sum of bare soil evaporation and canopy interception, d) fraction plant transpired water (plant transpiration over terrestrial evaporation) from 1980 - 2100 for 7 models only (Methods). Solid lines with dots depict the multi-model mean time series of the respective variables inferred from model-specific globally and decadal averaged time series, where the shaded regions cover ± 1 multi-model standard deviation. The y-axis denotes the change since 1980 in respective units. Global averages are calculated over land grid cells that have complete time series for all models and variables and are weighted according to the surface area per grid cell.

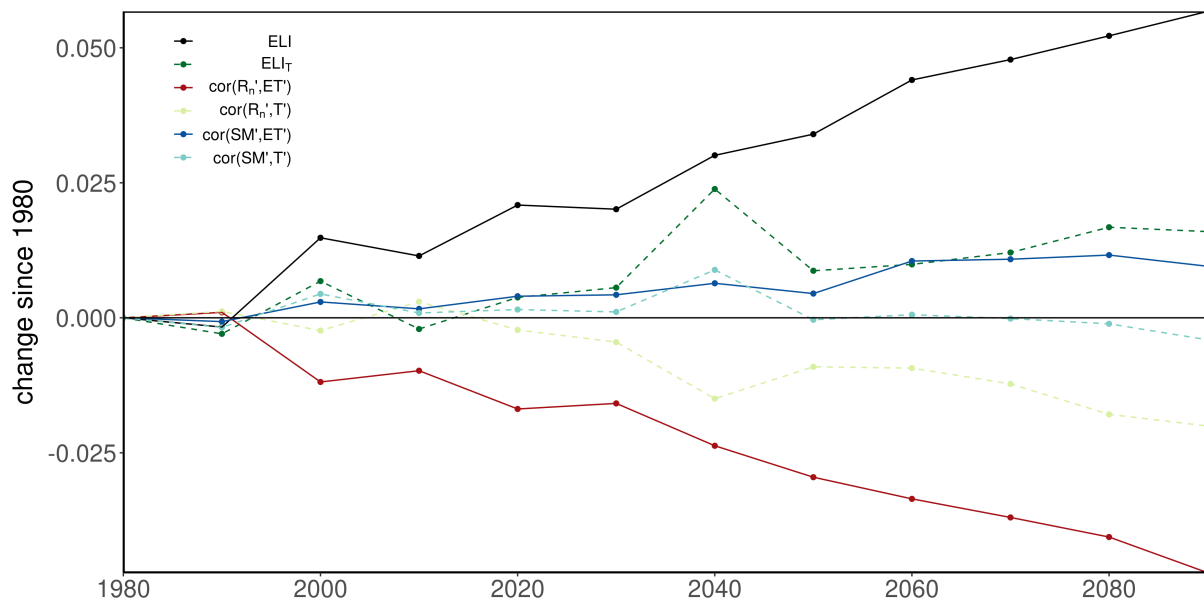


Figure 4.A5: Global trends of Ecosystem Water Limitation Index and its individual components with terrestrial evaporation and transpiration for 7 models only (Methods). Individual components consist of the correlation between anomalies of either surface net radiation (R_n) or soil moisture (SM) with either terrestrial evaporation (solid lines) or transpiration (dashed lines). Global averages are calculated over land grid cells that have complete time series for all models and variables and are weighted according to the surface area per grid cell. Solid and dashed lines with dots depict the multi-model mean time series of the variables displayed in the legend inferred from model-specific globally and decadal averaged time series, where the shaded regions cover ± 1 multi-model standard deviation. All y-axes denote changes since 1980.

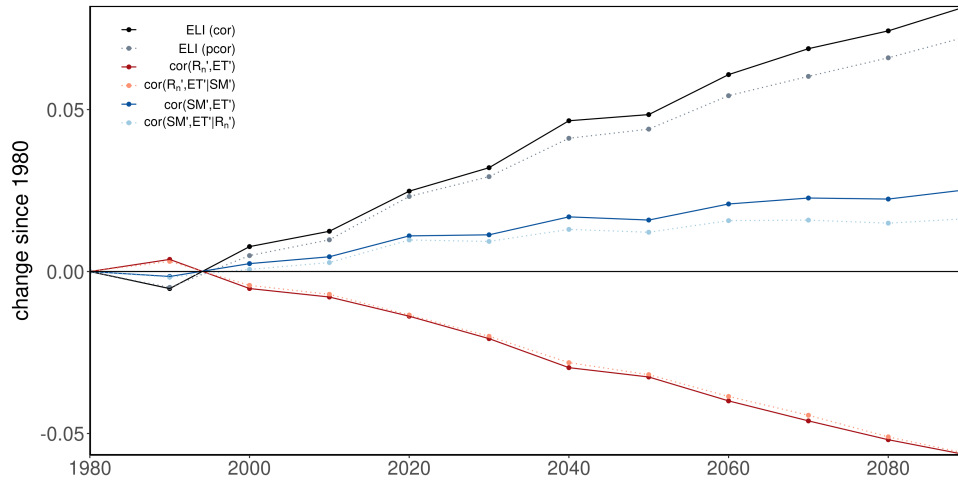


Figure 4.A6: Confounding effects of energy on water control and vice versa on the Ecosystem Water Limitation Index and its individual components. Solid and dotted lines with dots depict the multi-model mean time series of the variables displayed in the legend inferred from model-specific globally and decadal averaged time series, where the shaded regions cover ± 1 multi-model standard deviation. Global averages are calculated over land grid cells that have complete time series for all models and variables and are weighted according to the surface area per grid cell. Solid lines with dots are the ELI from Figure 4.1a) (black) and components (red, blue), where the dotted lines with dots are the ELI based on partial correlations. All y-axes denote changes since 1980.

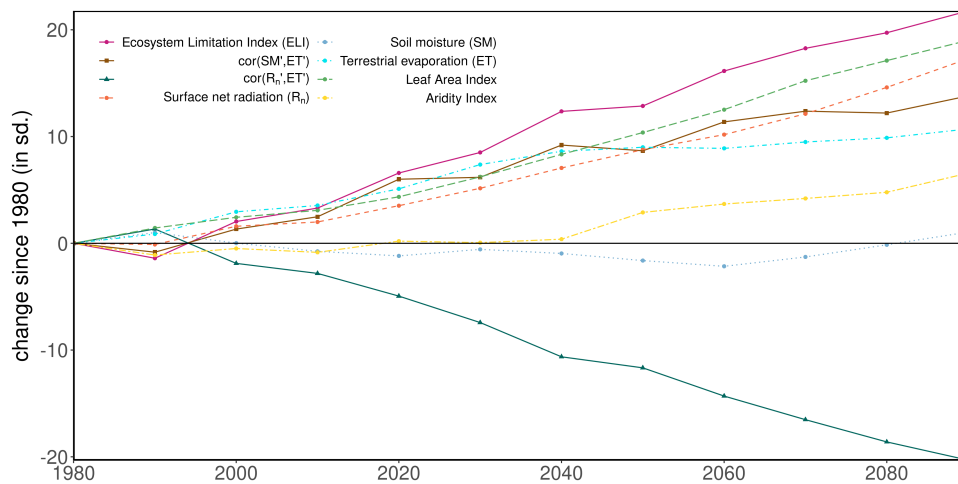


Figure 4.A7: Past and projected global climate and vegetation trends normalized by natural variability (standard deviation of respective detrended decadal time series per variable; solid dotted lines). Solid lines with dots denote ELI and its individual components, the other line types denote other variables displayed in the legend. All lines with dots depict the multi-model mean time series of the variables displayed in the legend inferred from model-specific globally and decadal averaged time series. The y-axis denotes the change since 1980 in standard deviations (sd). Global averages are calculated over land grid cells that have complete time series for all models and variables and are weighted according to the surface area per grid cell.

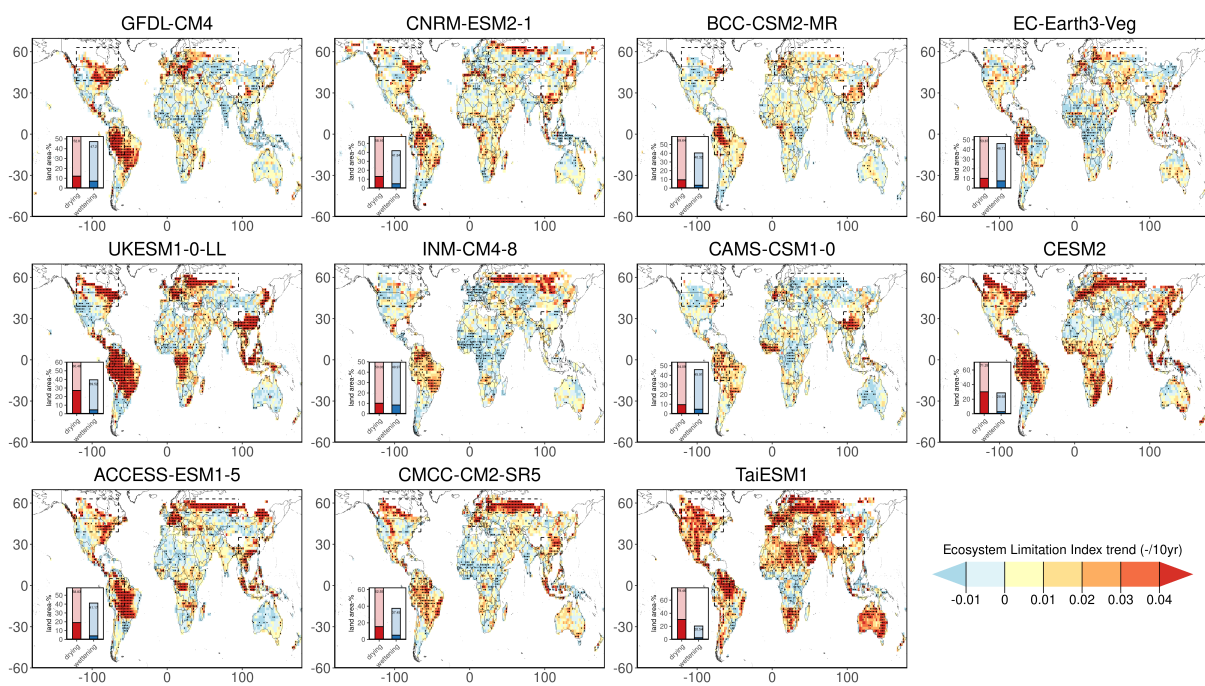


Figure 4.A8: Ecosystem Water Limitation Index trends calculated per individual model. The trend in the multi-model mean time series of ELI (dots indicate significance: $p < 0.05$) is based on Kendall's tau statistic. The dashed boxes indicate regions of interest. The inset displays the fraction of the warm land area that is drying or wetting according to ELI trends.

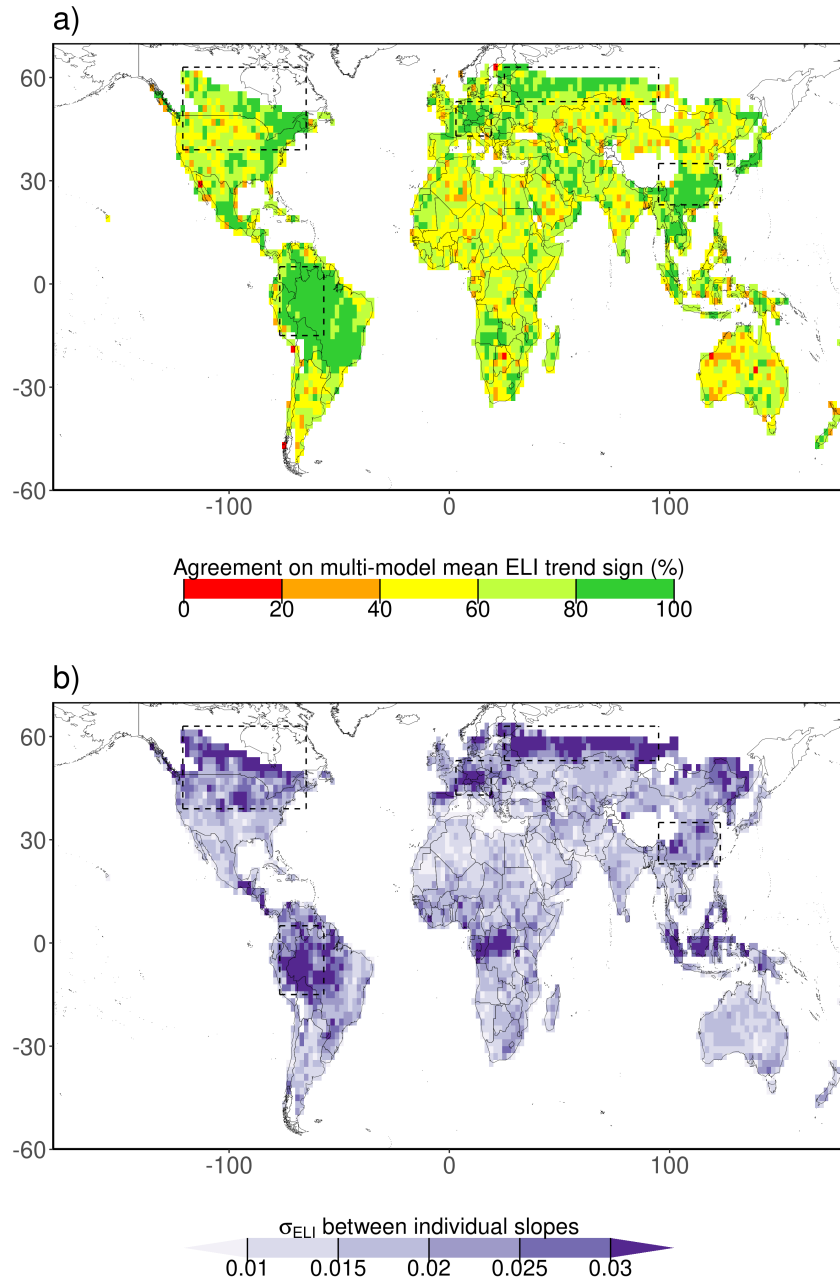


Figure 4.A9: Comparison between trends of individual CMIP6 models from 1980 - 2100 (Supplementary Figure 4.A5) a) The percentage of models (from models that actually have a value in the respective grid cell) for which their respective ELI trends agree with the sign of the multi-model mean (Figure 4.2a). b) The standard deviation (σ_{ELI}) between individual slopes of CMIP6 models (Supplementary Figure 4.A4).

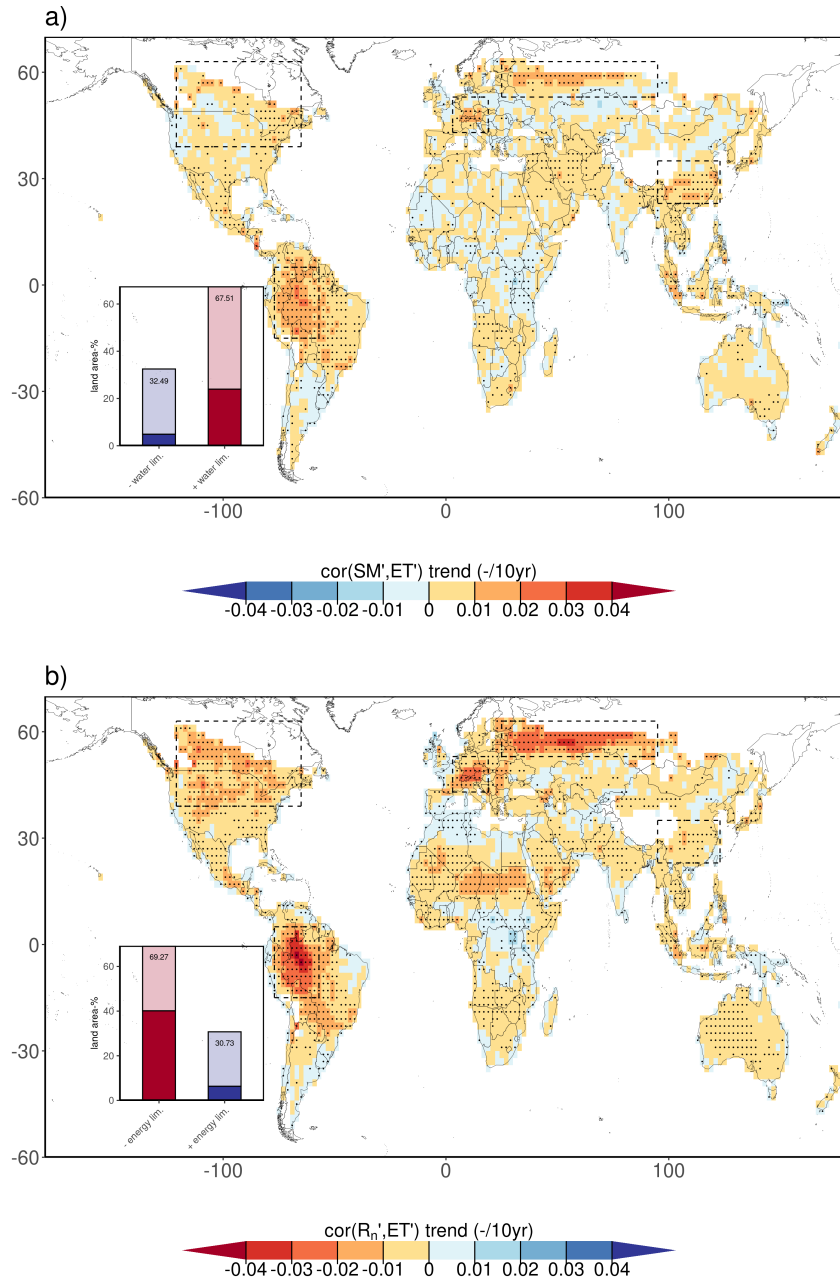


Figure 4.A10: Mapping of the trends of individual components of ELI, $\text{cor}(\text{SM}', \text{ET}')$ (a) and $\text{cor}(\text{R}_n', \text{ET}')$ (b) from 1980 to 2100. The trends are based on Kendall's tau statistic (dots indicate significance: $p < 0.05$). The dashed boxes indicate regions of interest. Inset plots display the fraction of warm land area with a decrease or increase in energy or water control ($p < 0.05$ is hued darker).

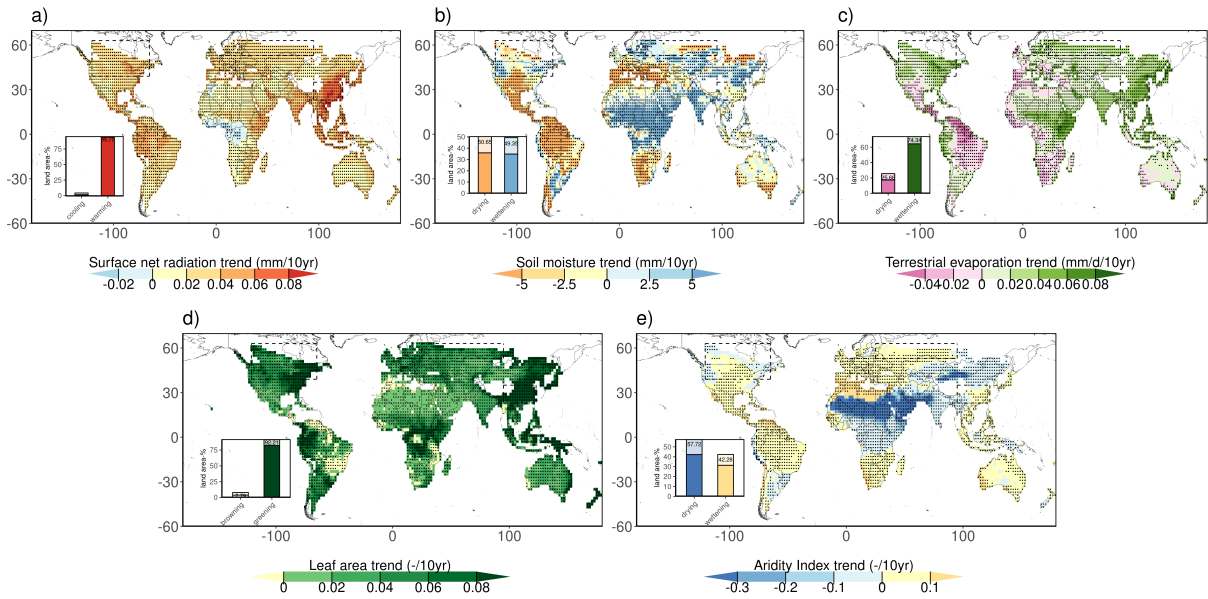


Figure 4.A11: Trends based on multi-model mean time series of land-atmosphere variables from 1980 to 2100. The trends are based on Kendall’s tau statistic (dots indicate significance: $p < 0.05$). The dashed boxes indicate regions of interest. Inset plots display the fraction of warm land area with negative or positive trends of all respective variables ($p < 0.05$ is hued darker).

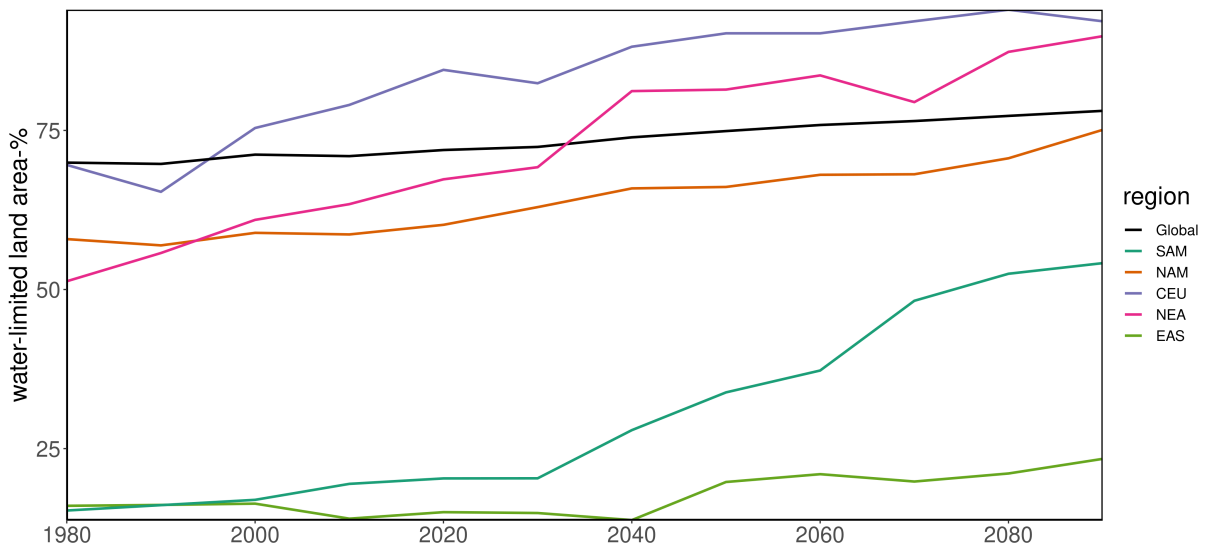


Figure 4.A12: Trends in water-limited area fraction across the globe and regions of interest. Colored lines depict the globally and decadal average time series of water-limited fraction of the warm land area, averaged over all individual models.

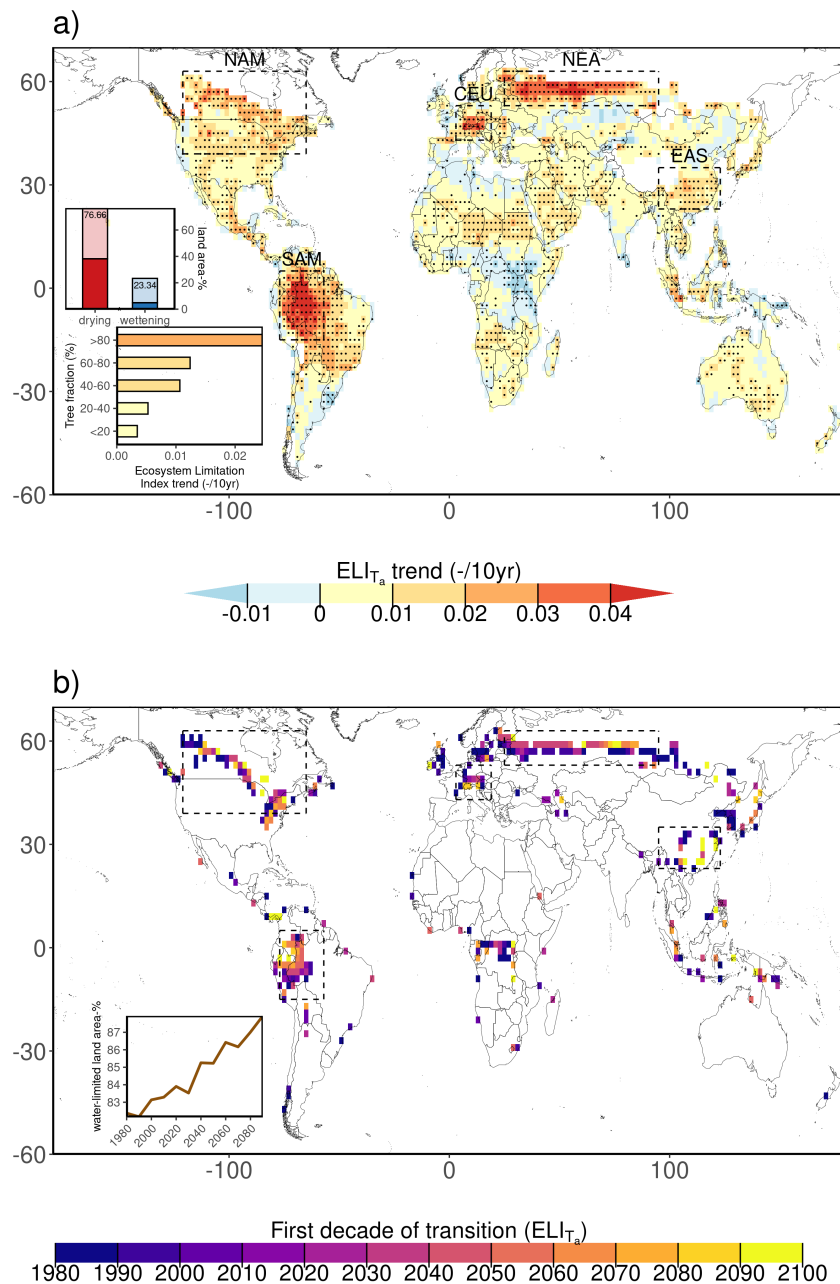


Figure 4.A13: Global distribution and trends of ecosystem water limitation derived with air temperature (T_a) instead of surface net radiation (R_n) anomalies. a) Trend in the multi-model mean of ELI (dots indicate significance: $p < 0.05$ based on Kendall's tau statistic). The dashed boxes indicate regions of interest, which allow easier cross-comparisons with other maps. The top inset displays the fraction of the warm land area that is drying or wetting according to ELI trends ($p < 0.05$ is hued darker). The bottom inset displays area-weighted average ELI trends for regions with different tree fractions based on 6 CMIP6 models (Methods). b) Timing of regime shift from energy to water limitation as indicated by ELI values becoming positive. The inset shows the global time series of the water-limited fraction of the warm land area (Methods).

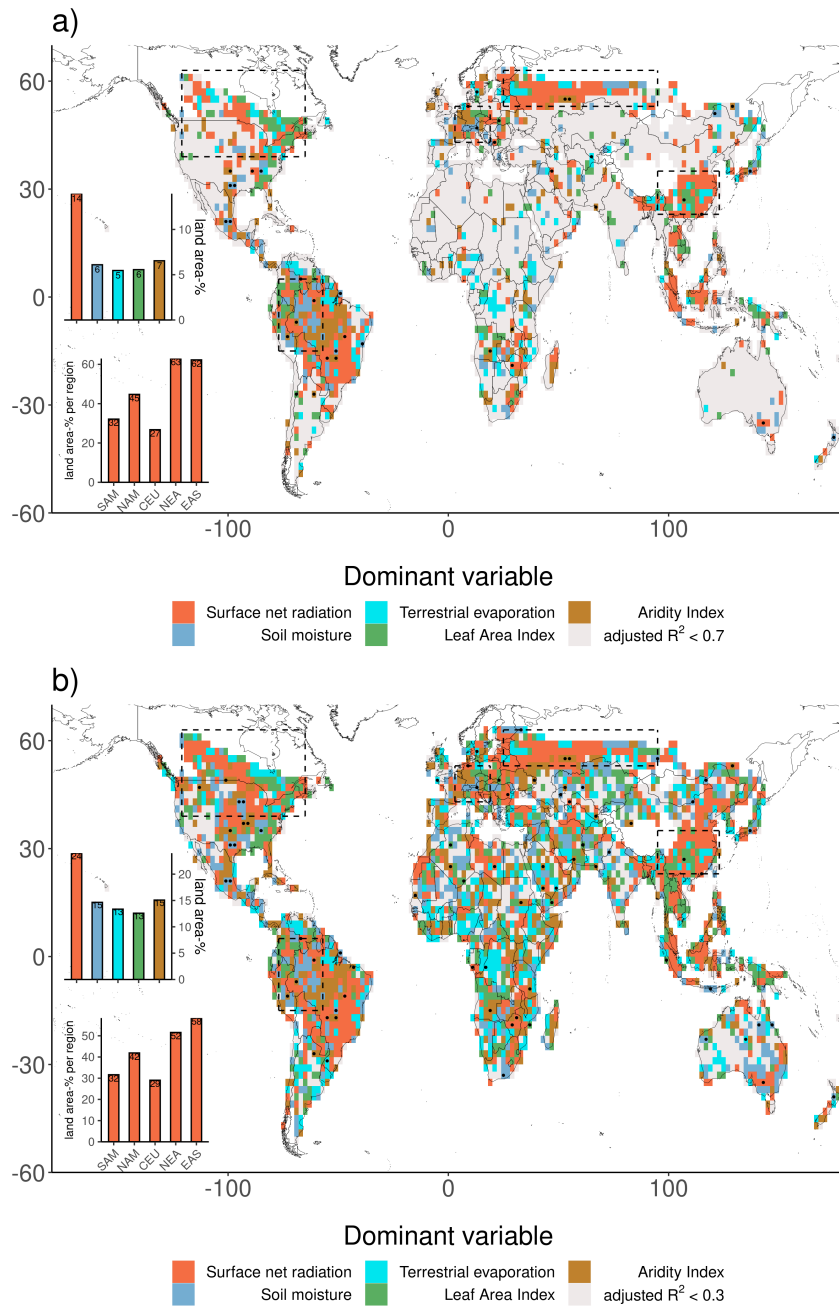


Figure 4.A14: Attribution of ELI trends to land-atmosphere variables with different thresholds for explanatory power of the multiple linear models. Adjusted $R^2 > 0.7$ a) and adjusted $R^2 > 0.3$ b). Colors indicate the variables that best predict the decadal ELI dynamics calculated using multivariate linear regression with a set of equally well-performing models, across which the most meaningful predictor is selected (Methods). Stippling indicates grid cells where only one linear model performs well (exceeding the respective adjusted R^2 threshold) and contains only a single explanatory variable. Grey color denotes grid cells without any model with reliable performance (not exceeding the respective adjusted R^2 threshold). Inset plots indicate the total fraction of warm land area controlled by respective variables (top) and the fraction of ELI trends controlled by temperature per region of interest.

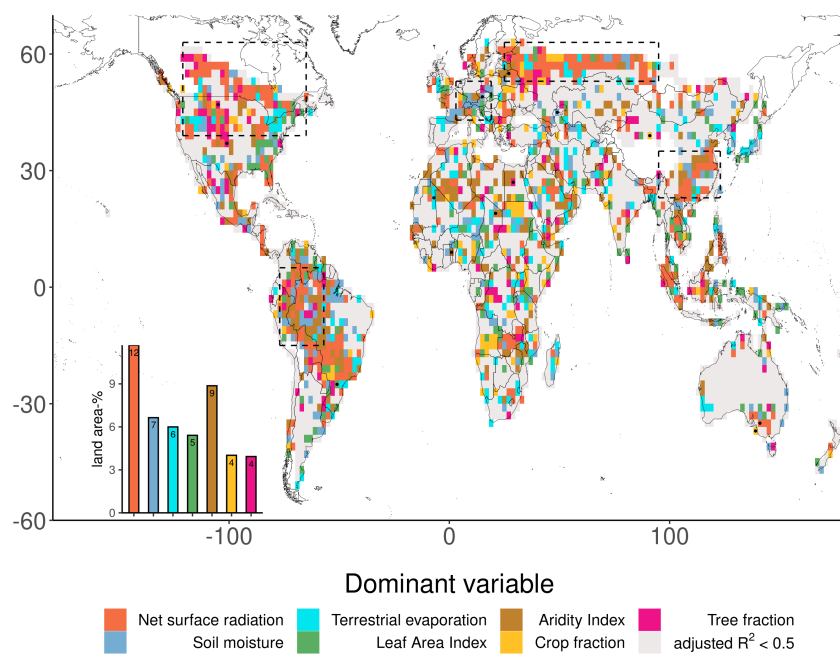


Figure 4.A15: Attribution of ELI trends to land-atmosphere variables including proxies for land use change, crop and tree fraction (for 6 CMIP6 models only; Methods). Dots indicate that there is only one linear model that is significant ($\text{adjusted } R^2 > 0.5$) and contains only one single explanatory variable, and grey warm land area lacking any significant multivariate linear model ($\text{adjusted } R^2 < 0.5$). Inset plots indicate the total fraction of warm land area governed by respective variables.

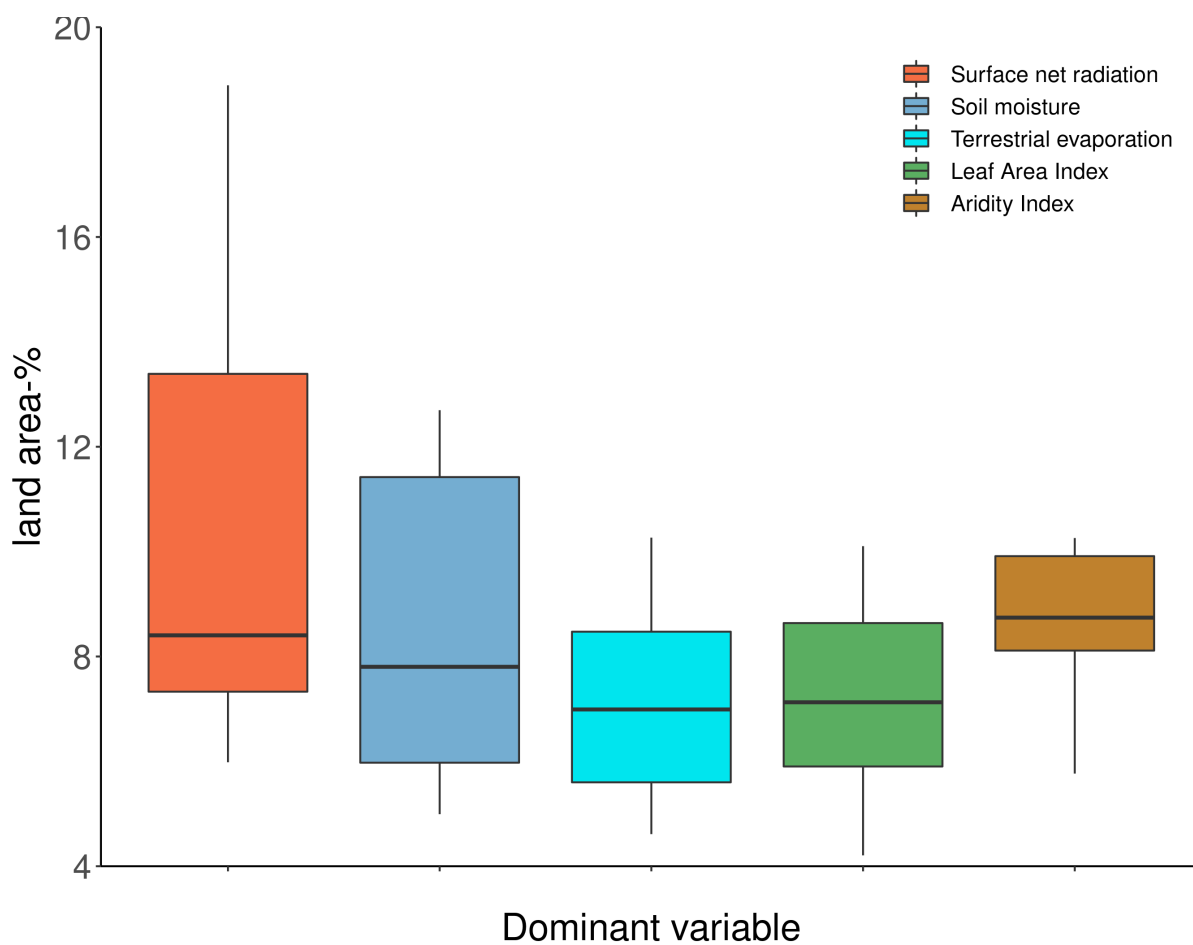


Figure 4.A16: The importance of land-atmosphere variables per CMIP6 model. Area fraction of grid cells with adjusted $R^2 > 0.5$ that is governed by a respective variable. Box-and-whisker plots display the median (horizontal bar), 25th and 75th percentiles (hinges) and largest and smallest values that do not exceed 1.5 * of the inter-quartile range.

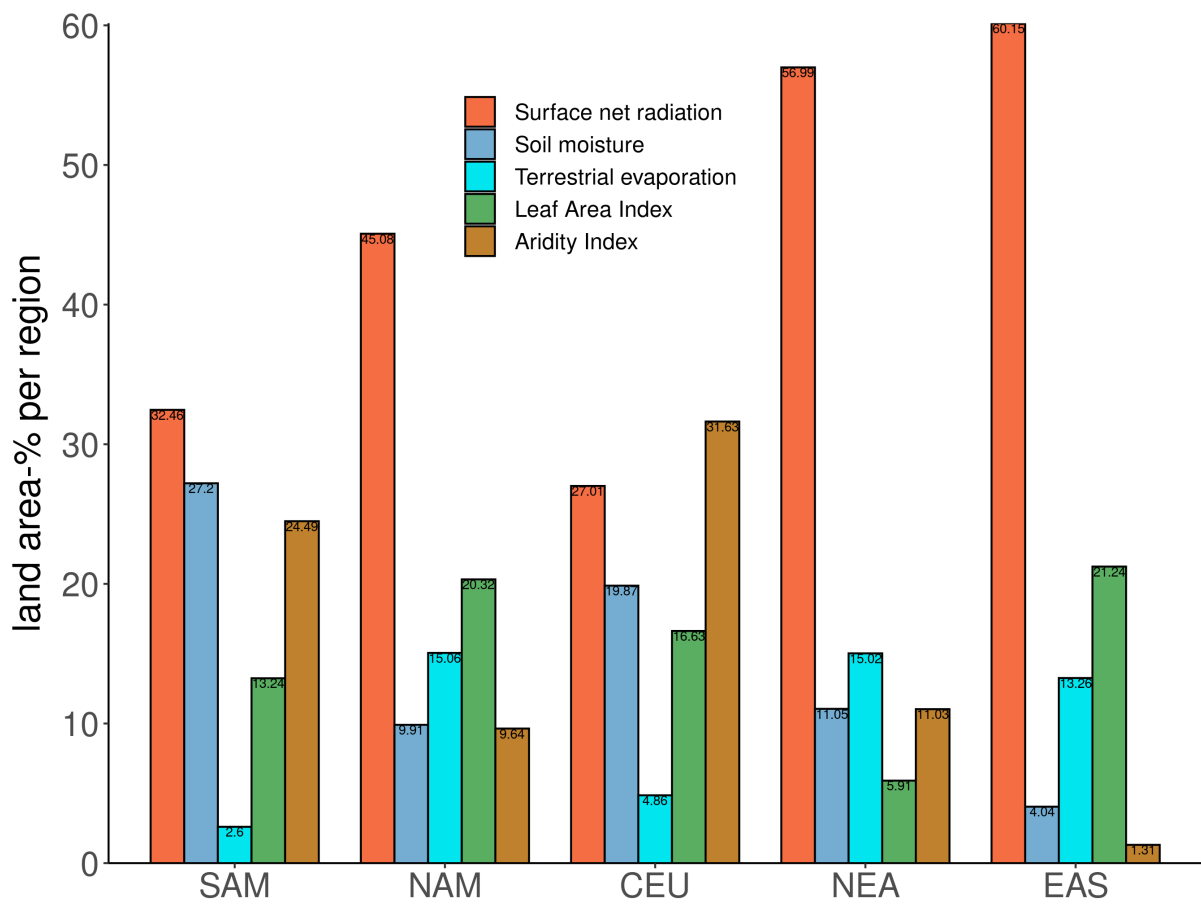


Figure 4.A17: The importance of land-atmosphere variables per region of interest. Area fraction of grid cells within regions of interest with adjusted $R^2 > 0.5$ that is governed by a respective variable.

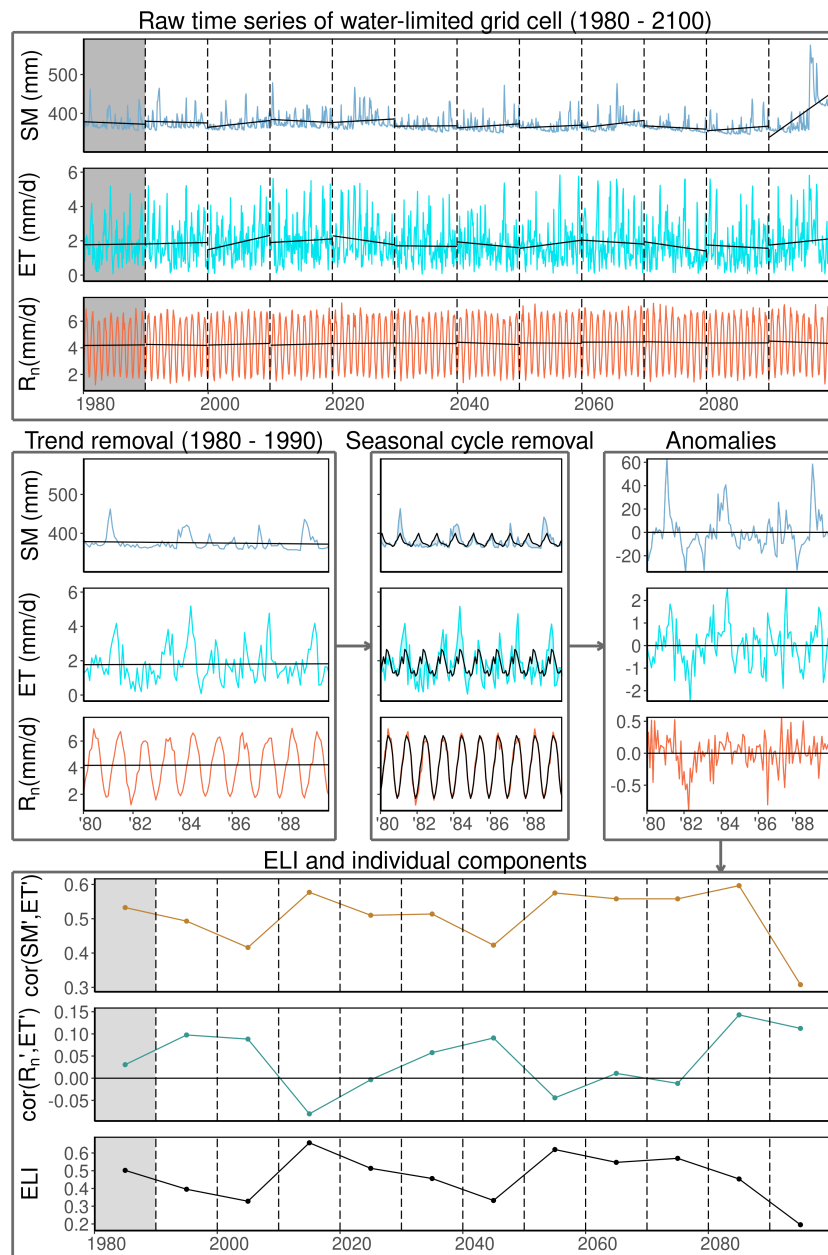


Figure 4.A18: Illustration of procedure of computing the ELI in a water-limited example grid cell (29°N and 101°W). The colored lines in the top panel show, from top to bottom, the raw time series for the 120-year study period for soil moisture (SM), terrestrial evaporation (ET) and surface net radiation. Vertical dashed lines separate the time series into decades, within which we determined the linear trends (black solid lines) we use for detrending. The grey shading indicates the decade that we use to illustrate the computation of the monthly anomalies. The left panel in the middle row shows the same as the top panel, but just for 1980-1990. The middle panel in the middle row shows the detrended time series (colored lines) imposed on the seasonal cycle (black), revealing the monthly anomalies (shaded region between colored and black lines). The colored lines in the right panel in the middle row show the anomalies, where dashed lines indicate monthly temperatures colder than 10 °C. Only the data in months with temperature exceeding 10°C (solid lines) are used to compute the correlations that constitute the ELI. The bottom panel shows, from top to bottom, $\text{cor}(SM', ET')$, $\text{cor}(R_n', ET')$ and the ELI. The arrows in the figure indicate step-wise computation of the ELI. All results are from the INM-CM4-8 model (Supplementary table 3).

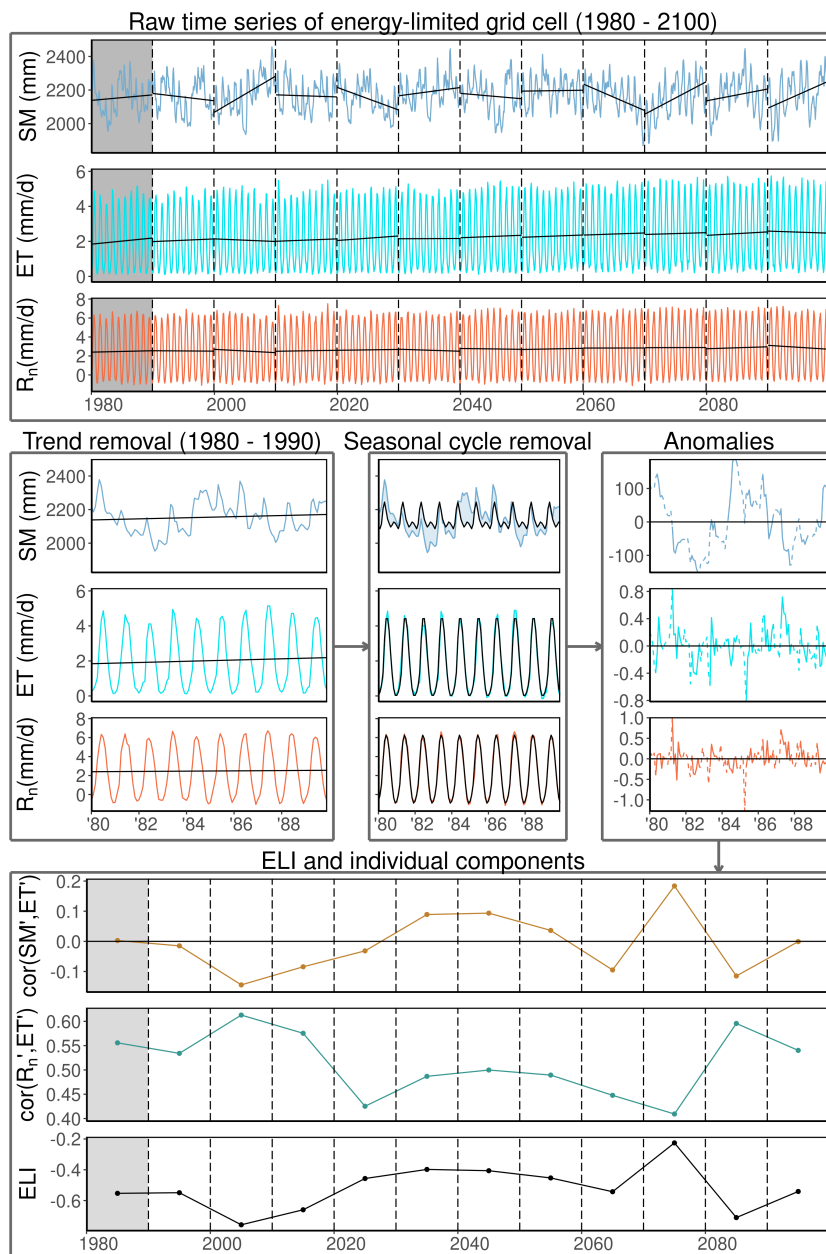


Figure 4.A19: Similar to Supplementary Figure 4.A17 but for an energy-limited example grid cell (49°N and 75°W).

4.A.2 Validation of ELI with conceptual model

Our motivation for the application of ELI to indicate water- versus energy-limited conditions was explained in the introduction. Here, we establish the ability of ELI to reflect water-limited conditions by using a conceptual soil moisture model, which is forced by the potential ET (ET_p) and precipitation, and computes actual ET, leakage from the root-zone ($Q_{leakage}$) and soil moisture (SM). The actual ET is computed as a function of ET_p and SM, as follows:

$$ET = ET_p * \beta_{SM} \quad (4.4)$$

where the soil moisture stress function (β_{SM}) can be defined with three linear relationships:

$$\beta_{SM} = \begin{cases} 0 & \text{if } SM < SM_{wilt} \\ \frac{SM - SM_{wilt}}{SM_{crit} - SM_{wilt}} & \text{if } SM_{wilt} < SM < SM_{crit} \\ 1 & \text{if } SM_{crit} < SM < SM_{sat} \end{cases} \quad (4.5)$$

where SM_{wilt} is the wilting point, SM_{crit} the critical soil moisture and soil moisture content at saturation (SM_{sat}) the soil moisture content at saturation. Soil parameters were adopted from the HTESSEL model ($SM_{wilt} = 0.171$, $SM_{crit} = 0.323$ and $SM_{sat} = 0.472$). ET_p is computed using a simplification of the Priestley-Taylor method (as previously done by Lofgren et al. Lofgren et al. (2011), Milly and Dunne Milly and Dunne (2016) and Maes et al. Maes et al. (2019)):

$$ET_p = \alpha_{MD} * R_n \quad (4.6)$$

Here, ET_p is assumed to be a fraction ($\alpha_{MD} = 0.8$) of the surface net radiation. The $Q_{leakage}$ is based on Clapp and Hornberger Clapp and Hornberger (1978) and Buitink et al. Buitink et al. (2021):

$$Q_{leakage} = LSM_T - LSM_{sat} \left[\frac{SM_t^{-2b-2}}{SM_{sat}} + \frac{(2b+2)k_s \Delta t}{SM_{sat} L} \right]^{-\frac{1}{2b+2}} \quad (4.7)$$

where L denotes the rooting depth (1000mm), SM_t the soil moisture content at time t, k_s is the hydraulic conductivity (50mm/d), Δt is the length of time step and b an empirical constant (taken as 5.39). Using Equations 1-4, the root-zone soil moisture is prognosed by solving the water balance, as follows:

$$SM_{t+1} = SM_t + \frac{1}{L}(P - ET - Q_{leakage}) \quad (4.8)$$

where P is total precipitation. The concept of water limitation is straightforward through the implementation of the soil moisture stress function in Eq. (2) in the model, which renders this

model suitable to validate the ability of ELI to reflect water limited conditions. In climate models, water limitation is more complex as it is related to several interacting processes and resulting complex soil moisture stress functions are not readily available as model output, warranting the application of a more descriptive index, such as the ELI. Here, we define an index that computes the fraction of days where water-limited conditions prevail (when $SM < SM_{crit}$, although it should be noted that this is just one definition of water limitation used here for illustration only).

We solve this set of equations using surface net radiation and total precipitation from ERA5 at the daily time scale at a 0.5×0.5 degree grid cell resolution from 1981-2016 (Hersbach et al., 2019; Hersbach et al., 2020). The fraction of days where $SM < SM_{crit}$ is computed for every 5-year time interval. In concert, the ELI is computed as described in the Methods section. We modify this methodology by computing the ELI i) with the net radiation from ERA5 that is used as model input and the soil moisture and terrestrial evaporation directly computed by the conceptual model (Equations 4.4 and 4.8) and ii) for every 5-year time interval to obtain a reasonable time sample, excluding data where there are fewer than 15 data points with temperatures above 10°C .

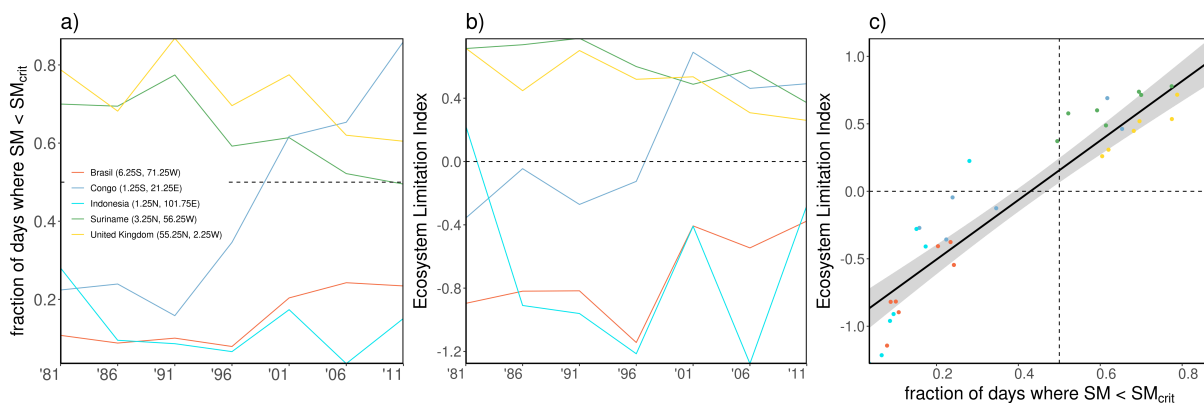


Figure 4.A20: Validation of the ability of ELI to reflect water-limited conditions. Time series of a) fraction of days where $SM < SM_{crit}$ and b) ELI and c) fraction of days where $SM < SM_{crit}$ versus ELI with data from the conceptual model (points). The solid black line in c) denotes a linear regression with a 95% confidence interval. Colors denote different grid cells, selected across the globe and different climate regimes. Conditions above and right of the dashed lines are assumed water-limited.

Time series of the fraction of days where $SM < SM_{crit}$ and the ELI are shown in Supplementary Figure 4.A20a and b for a number of grid cells distributed across the globe. Note that grid cells have been selected to reflect a wide range of average climate conditions; from energy- to water-limited conditions. The order of the time series in both panels are similar, suggesting comparable spatial variability between the two indices. Further, all grid cells show ample temporal variability; Whereas the magnitude of the temporal variability is not as straightforward to compare between a) and b), the sign of the changes in time of both indices match well. Also, the high correlation between ELI and the conceptual water balance estimates of water limitation shown in Supplementary Figure 4.A20c confirms the similarity between these two indices and

validates, at least for this selection of grid cells, that the ELI is able to reflect water-limited conditions.

Chapter 5

Hydrometeorological drivers of vegetation productivity extremes

This chapter is based on:

J. Kroll*, J. M. C. Denissen*, M. Migliavacca, W. Li, A. Hildebrandt, and R. Orth (2022). “Spatially varying relevance of hydrometeorological hazards for vegetation productivity extremes”. *Biogeosciences* 19.2, 477–489, [*These authors contributed equally to this work]

Abstract

Vegetation plays a vital role in the Earth system by sequestering carbon, producing food and oxygen, and providing evaporative cooling. Vegetation productivity extremes have multi-faceted implications, for example on crop yields or the atmospheric carbon dioxide (CO₂) concentration. Here, we focus on productivity extremes as possible impacts of coinciding, potentially extreme hydrometeorological anomalies. Using monthly global satellite-based sun-induced chlorophyll fluorescence (SIF) data as a proxy for vegetation productivity from 2007-2015, we show that vegetation productivity extremes are related to hydrometeorological hazards as characterized through ERA5-Land reanalysis data in approximately 50% of our global study area. For the latter, we are considering sufficiently vegetated and cloud-free regions, and we refer to hydrometeorological hazards as water- or energy-related extremes inducing productivity extremes. The relevance of the different hazard types varies in space; temperature-related hazards dominate at higher latitudes with cold spells contributing to productivity minima and heat waves supporting productivity maxima, while water-related hazards are relevant in the (sub-)tropics with droughts being associated with productivity minima and wet spells with the maxima. Alongside single hazards compound events such as joint droughts and heat waves or joint wet and cold spells also play a role, particularly in dry and hot regions. Further, we detect regions where energy control transitions to water control between maxima and minima of vegetation productivity. Therefore, these areas represent hotspots of land-atmosphere coupling where vegetation efficiently translates soil moisture dynamics into surface fluxes such that the land affects near-surface weather. Overall, our results contribute to pinpointing how potential future changes in temperature and precipitation could propagate to shifting vegetation productivity extremes and related ecosystem services.

5.1 Introduction

Vegetation is a crucial component of the Earth system because it provides ecosystem services like food and oxygen production, carbon dioxide (CO₂) sequestration and evaporative cooling. Therefore, the effects of changes in vegetation productivity are diverse; it influences crop yields (Orth et al., 2020), cloud formation (Freedman et al., 2001; Hong et al., 1995), precipitation (Pielke et al., 2007), atmospheric pollution (Otu-Larbi et al., 2020) and heat wave intensity (Li et al., 2021a).

Photosynthesis requires a sufficient water (soil moisture) and energy (incoming short-wave radiation) supply. In regions that are water-limited (energy-limited), plants usually benefit from water (energy) surpluses and suffer from respective deficits. Many studies confirm that, depending on the evaporative regime, vegetation productivity follows the temporal evolution of influential variables such as soil moisture or temperature which summarize the water or energy dynamics (Beer et al., 2010; Denissen et al., 2020; Li et al., 2021b; Madani et al., 2017; Orth, 2021; Piao et al., 2020; Seddon et al., 2016).

Correspondingly, hydrometeorological hazards, such as temperature and precipitation extremes, have implications on vegetation productivity. Many studies investigated the influence of such hazards on vegetation productivity, highlighting their impact on the biosphere (Ciais et al., 2005; Flach et al., 2018; Qiu et al., 2020; Wang et al., 2019; Zhang et al., 2019; Zhao and Running, 2010; Zscheischler et al., 2014a; Zscheischler et al., 2014b; Zscheischler et al., 2013). However, usually these studies focus on particular types of hydrometeorological hazards such as droughts or heat waves, or they use vegetation productivity data from models or other proxies rather than the recent satellite-derived sun-induced chlorophyll fluorescence (SIF) data (Frankenberg et al., 2011; Joiner et al., 2013).

In this study, we re-visit the relationship between vegetation productivity and hydrometeorological hazards by analysing the implications of both single and compound hazards on vegetation productivity extremes, as has been highlighted before (Sun et al., 2015; Zhou et al., 2019). However, to our knowledge for the first time, we do so comprehensively by approximating variable importance during vegetation productivity extremes inferred from SIF data on a global scale. This analysis is done from an impact perspective; we first detect impacts (productivity extremes) before relating them to coinciding, potentially extreme hydrometeorological anomalies (Smith, 2011). Finally, we investigate where the full vegetation productivity range between minima and maxima involves transitions from energy to water controls. In regions where this occurs, the feedback of the land surface on the climate can be stronger, as the water-controlled vegetation translates soil moisture dynamics through its energy and water fluxes to affect the boundary layer and consequently also near-surface weather. Hence, our vegetation-based analysis can indicate hotspots of land-atmosphere coupling (Guo and Dirmeyer, 2013; Koster et al., 2004).

In Sect. 5.3.1 we investigate the co-occurrence of vegetation productivity extremes and hydrometeorological hazards. Further, we show the timing of such vegetation productivity extremes in Sect. 5.3.2. Additionally, we determine the main drivers of vegetation productivity extremes and assess the influence of underlying evaporative regimes in Sect. 5.3.3. We summarize our results across climate regimes in Sect. 5.3.4 and investigate regions with vegetation productivity controls switching between water and energy variables in Sect. 5.3.5.

5.2 Data and methods

In order to characterize vegetation behaviour, we use SIF and enhanced vegetation index (EVI) data in this study. SIF is used as a proxy for vegetation productivity. We employ satellite-observed SIF data retrieved from the Global Ozone Monitoring Experiment (GOME-2; (Köhler et al., 2015)). In the derivation of this SIF product, multiple corrections for varying solar zenith angles, differences in overpass times and cloud fraction have been applied to yield reliable SIF estimates. In addition to vegetation productivity, we also study changes related to vegetation greenness by using satellite-observed EVI data from the Moderate Resolution Imaging Spectroradiometer (MODIS; (Didan, 2015)).

As for the hydrometeorological variables, representing energy and water availability, we consider 2m temperature, short-wave incoming radiation, vapour pressure deficit, soil moisture from four layers (1: 0–7 cm, 2: 7–28 cm, 3: 28–100 cm and 4: 100–289 cm) and total precipitation, all from the ERA5-Land reanalysis data (Muñoz Sabater, 2019). In addition to this and to validate the robustness of our results, we use an alternative soil moisture product, SoMo.ml, which provides data for three layers (1: 0–10 cm, 2: 10–30 cm and 3: 30–50 cm) and which is derived through a machine learning approach that is trained with in situ soil moisture measurements from across the globe (O and Orth, 2021). All datasets used in this study are summarized in Table 1.

Table 5.1: Data Sets Used in This Study. GLEAM: Global Land Evaporation Amsterdam Model. GFZ: German Research Centre for Geosciences. VCF: vegetation continuous fields.

Variables	Dataset	Version	Application	Reference
Sun-induced chlorophyll fluorescence	GOME-2	GFZ	Vegetation productivity proxy	(Köhler et al., 2015)
Enhanced vegetation index	MOD13C2	V006	Vegetation greenness proxy	(Didan, 2015)
Soil moisture layer 1–4, short-wave incoming radiation, temperature, vapour pressure, deficit	ERA5-Land		Hydrometeorological variables indicating energy and water availability	(Muñoz Sabater, 2019)
Precipitation, net solar radiation, net thermal radiation	ERA5		Computation of aridity to evaluate resulting patterns	(Hersbach et al., 2020)
Soil moisture layer 1–3	SoMo.ml	1	Alternative soil moisture dataset	(O and Orth, 2021)
Fraction of vegetation cover	VCF5KYR	1	Evaluation of resulting patterns with respect to vegetation characteristics	(Hansen and Song, 2018)
Evapotranspiration	GLEAM	3.3b	Vegetation productivity proxy	(Martens et al., 2017)

The workflow applied to these datasets is illustrated in Figure 5.1. At first, all data are pre-processed for comparability by (i) aggregating it to the monthly temporal and the $0.5^\circ \times 0.5^\circ$ spatial resolution and by (ii) focusing on the time period 2007–2015. Next, we compute anomalies by removing linear trends and the mean seasonal cycle from the data for both the vegetation and hydrometeorological variables. In each grid cell, we disregard months with an absolute SIF value below $0.5 \text{ mW m}^{-2} \text{ sr}^{-1} \text{ nm}^{-1}$ to focus on times with sufficiently active vegetation (as in Li et al. (2021b)). Additionally, grid cells with a fractional vegetation cover $< 5\%$ are excluded from the analysis. Finally, we assure the necessary data availability by considering only grid cells with > 15 monthly anomalies across the study period remaining after the filtering. Out of the identified suitable months in each grid cell, we determine the five strongest negative and five strongest positive monthly SIF anomalies. The sum of all grid cells for which five SIF maxima and minima can be detected is referred to as the total study area.

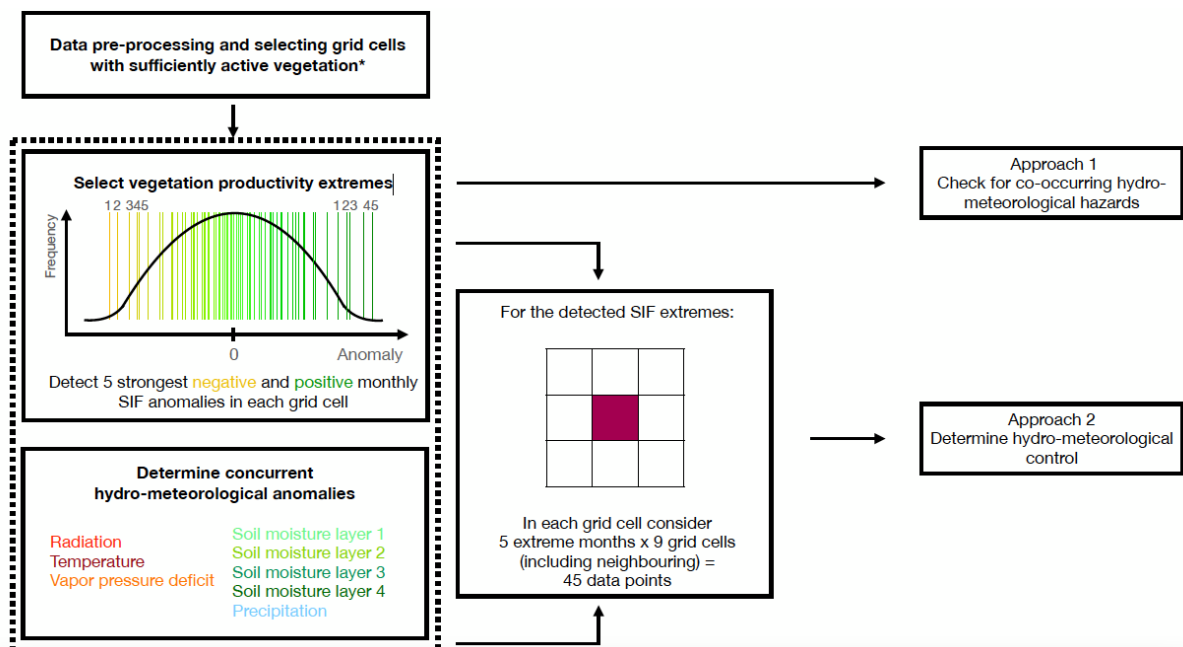


Figure 5.1: Schematic representation of our methodological approach. *Filtering for sufficiently active vegetation is explained in Sect. 5.2.

After this filtering, we follow two approaches in our analysis. In the first approach, we check for hydrometeorological hazards coinciding with the determined extreme vegetation productivity events. Thereby, we consider air temperature and soil moisture layer 2, as these variables were previously found to be globally most relevant for vegetation productivity (Li et al., 2021b). At first, we average the monthly temperature and soil moisture anomalies across the 5 months of maximum and minimum SIF anomalies. Then, a series of steps is taken to test if the coinciding hydrometeorological anomalies during SIF extremes are actually hazardous. (i) We randomly sample 5 months with sufficiently active vegetation and average the soil moisture and temperature anomalies, respectively, across them. (ii) We repeat this 100 times to obtain a distribution from which we determine the 10th and 90th percentile. (iii) A hydrometeorological hazard is detected if

the actual, averaged temperature and/or soil moisture anomalies associated with the SIF extremes are below the 10th (cold spell or drought) or above the 90th percentile (heat wave or wet spell) of the distribution of randomly sampled averaged anomalies. Note that with this approach we can detect both single and compound hydrometeorological hazards.

Complementing this analysis, in the second approach we analyse the temporal co-variation between SIF extremes and hydrometeorological anomalies. For this purpose, we correlate the five SIF extreme anomalies with anomalies of all considered hydrometeorological variables in each grid cell. We include respective SIF and hydrometeorological data from the surrounding grid cells to yield a larger data sample consisting of $5 \times (8 + 1) = 45$ data pairs. We disregard negative and insignificant (p value > 0.05) correlations, as we assume these do not indicate actual physical controls but rather represent the influence of noise or confounding effects such as low precipitation during times of high radiation. This also serves to deal with uncertainty in the SIF dataset. When systematic patterns emerge from either of the approaches with adequate significance, they are unlikely confounded by underlying SIF patterns: as we focus solely on either SIF maxima or minima, statistically significant relations only emerge when concurrent hydrometeorological anomalies of an appropriate magnitude exist. Finally, the hydrometeorological variable that yields the highest correlation coefficient with the extreme SIF anomalies is regarded as the main SIF-controlling variable during vegetation productivity maxima or minima.

5.3 Results and discussion

5.3.1 Hydrometeorological hazards and vegetation productivity extremes

Figure 5.2 shows which hydrometeorological hazards are associated with SIF extremes as inferred with approach 1 described in Sect. 5.2 and in Figure 5.1. In approximately 50% of the global study area, we find that vegetation productivity extremes are associated with hydrometeorological hazards. This is in line with previous research (Zscheischler et al., 2014a). For both maximum and minimum vegetation productivity, we find spatially coherent patterns of associated hydrometeorological hazards. In the Northern Hemisphere, SIF maxima (minima) at high latitudes relate to heat waves (cold spells), where in mid latitudes they occur jointly with wet spells (droughts). This suggests that hydrometeorological hazards associated with SIF extremes vary systematically according to energy and water control of the local vegetation. Thereby, the boundary between both regimes and the respectively determined relevant hydrometeorological hazards is surprisingly sharp, for example in North America and in eastern Europe and Russia (Flach et al., 2018).

Further, single hydrometeorological hazards (either an extreme temperature or soil moisture anomaly) are relevant in more areas than compound hazards (combination of extreme temperature and extreme soil moisture anomaly). Compound hazards seem to be particularly important in

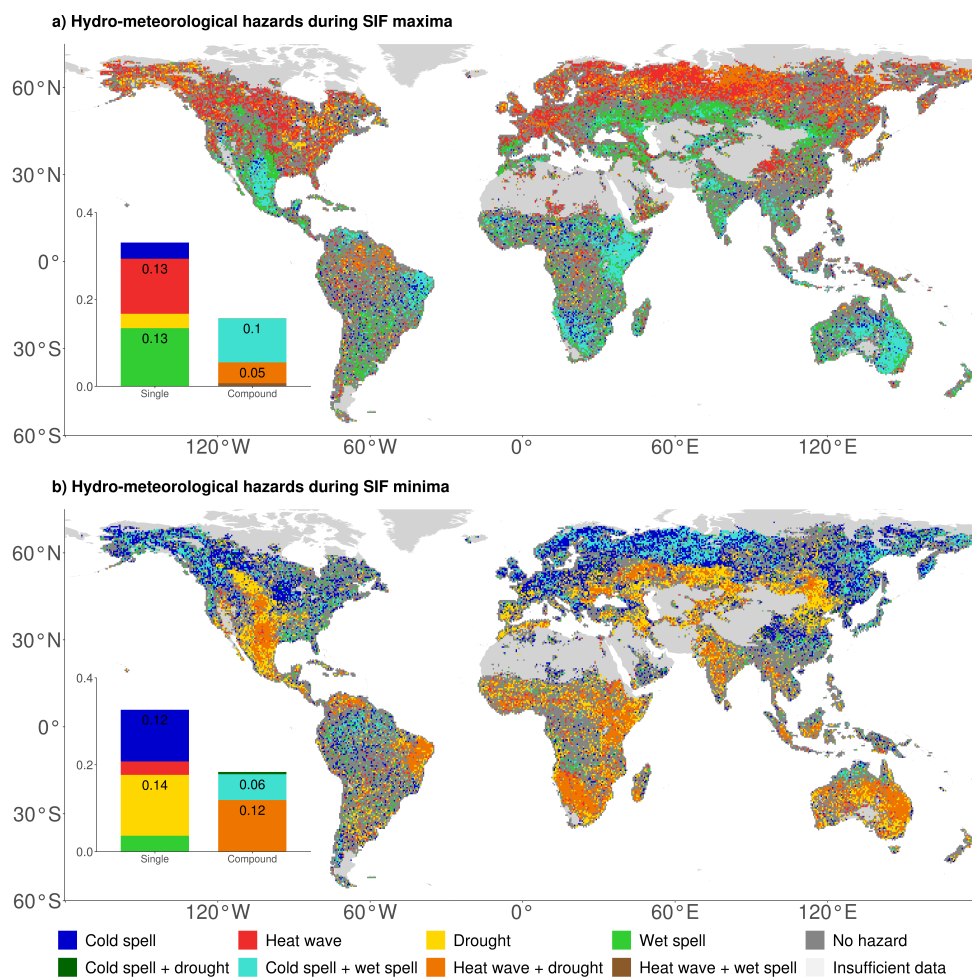


Figure 5.2: Hydrometeorological hazards co-occurring with (a) SIF maxima and (b) SIF minima. Colours denote the type of hydrometeorological hazard. Bar plots indicate the area affected by each hazard type relative to the total study area.

the sub-tropics on both hemispheres. Differences also exist between maximum and minimum vegetation productivity extremes, the latter being slightly more associated with compound hazards.

Overall, the most frequent hazards during vegetation productivity minima are droughts and cold spells. Previous studies have reported the relevance of drought in this context (Zscheischler et al., 2014a; Zscheischler et al., 2014b; Zscheischler et al., 2013) even though for different vegetation productivity proxies. On the contrary, the importance of cold spells is not analysed, probably because vegetation productivity in boreal regions is comparably smaller than in e.g. tropical regions (Li and Xiao, 2020).

The results in Figure 5.2 are based on averages of the 5 months with strongest SIF anomalies in each grid cell. Supplementary Figure 5.A1 in the Supplement shows co-occurring hydrometeorological hazards separately for each of the five SIF maxima and minima. The patterns are similar

to those in Figure 5.2; we consistently find temperature-related hazards to be relevant in energy-controlled regions and water-related hazards in water-controlled regions across all five individual SIF extremes. Weaker SIF extremes tend to be less associated with hydrometeorological hazards. This could be because the signal-to-noise ratio is decreased for weaker extremes, or other factors such as disturbances (fire or insect outbreaks) play a more prominent role for these productivity extremes. As mentioned, soil moisture layer 2 is used here to detect droughts and wet spells, but similar results are obtained with soil moisture layers 1 and 3, respectively (not shown).

5.3.2 Timing of strongest SIF extremes

To further understand the spatially varying relevance of hydrometeorological hazards, we show the months of the year associated with the strongest SIF extreme in each grid cell in Figure 5.3. The spatial pattern is quite different from that in Figure 5.2; for example the sharp transitions between regions with energy- and water-related hydrometeorological hazards are not present in Figure 5.3. Hence, this transition is apparently not related to SIF extremes occurring in different seasons and might be rather related to different evaporative regimes which will be further investigated in Sect. 5.3.3. The spatial variability in Figure 5.3 is lower at high latitudes compared with (sub-)tropical regions. At high latitudes the growing season is short and constrained by energy availability. In the tropics, we find an increased smaller-scale variability, presumably due to the weak seasonal cycle of hydrometeorological variables. Most SIF extremes in North America and Eurasia occur in the early growing season, presumably when either vegetation starts to grow or growing is limited due to energy or water control. While here we show the months of the year associated with the strongest SIF extreme, in Supplementary Figure 5.A2 we show similar patterns in the timing of the second to fifth strongest SIF extremes, indicating that each of the remaining SIF extremes occurs in similar months of the year.

5.3.3 Hydrometeorological drivers of vegetation productivity extremes

After showing the co-occurrence of hydrometeorological hazards with SIF extremes, we apply a correlation analysis (approach 2 in Sect. 5.2) to characterize the co-variability between extreme SIF anomalies and concurrent hydrometeorological anomalies. Figure 5.4 shows the hydrometeorological variable that correlates strongest with SIF during months of extreme vegetation productivity, indicating respective controls. At high latitudes and in the tropics SIF extremes are generally energy-controlled, while in the mid latitudes and sub-tropics they are water-controlled. Overall, we find similar spatial patterns as in Figure 5.2, demonstrating consistent results across the co-occurrence and co-variability of SIF extremes and hydrometeorological hazards. This coherence suggests that hydrometeorological hazards play a key role in inducing SIF extremes.

The bar plot insets in Figure 5.3 indicate that SIF maxima are equally controlled by energy and water variables, while SIF minima are overall more water-controlled. Even though weaker, this

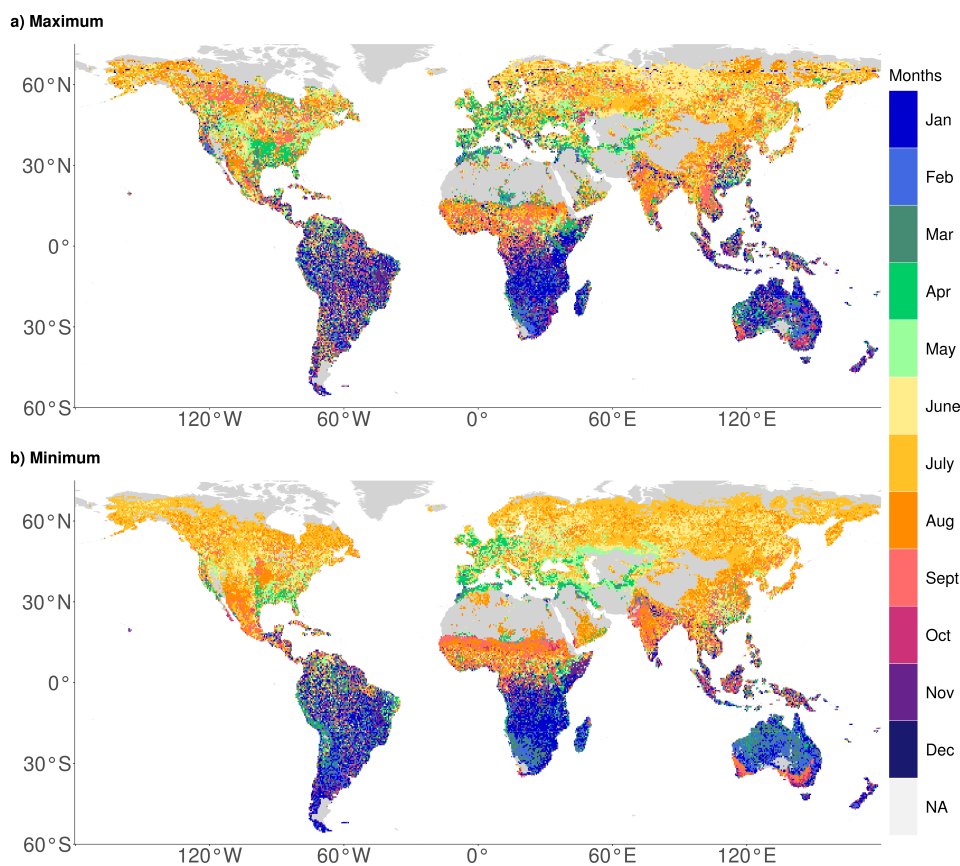


Figure 5.3: Global distribution of the month of the year in which the strongest SIF (a) maximum and (b) minimum anomaly occur. Data gaps (grey) are caused by filtering for active vegetation and excluding insignificant and negative correlations.

shift is also present in Figure 5.2. This difference can be explained with transitional regions, which have energy-controlled SIF maxima but water-controlled SIF minima. This is illustrated for example by the northward shift of the transition between energy and water control in Russia when comparing the results for maximum and minimum SIF. These transitional regions will be further investigated in Sect. 5.3.5.

We repeated this analysis with SoMo.ml soil moisture and found similar spatial patterns of energy- and water-controlled regions (Supplementary Figure 5.A3), underlining that our results are robust with respect to the choice of the soil moisture product. Furthermore, we repeat our co-variability analysis for EVI instead of SIF in Supplementary Figure 5.A4, which allows us to contrast to some extent the behaviour of vegetation physiology (SIF) and vegetation structure (EVI). Similar to the spatial patterns of energy- and water-controlled vegetation in Figure 5.4, EVI shows predominant energy control at high latitudes, while the mid latitudes are largely water-controlled. Further, as in Figure 5.4 for SIF, EVI minima are more associated with water variables than EVI maxima.

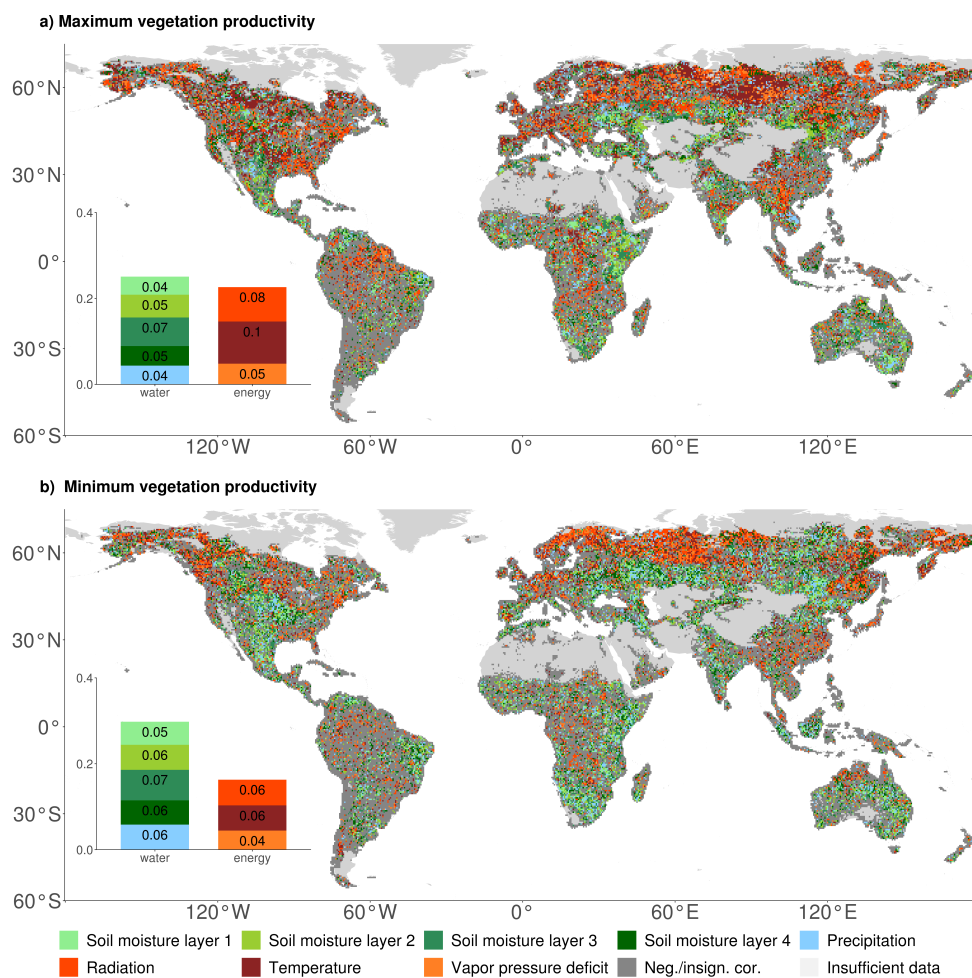


Figure 5.4: Global distribution of hydrometeorological controls of sun-induced chlorophyll fluorescence (SIF) (a) maxima and (b) minima in respective colours, as assessed from the strongest correlations. The inset bar plot indicates the area controlled by each variable relative to the total study area. Dark-grey colour denotes the study area in which correlations are negative/insignificant.

However, the overall extent of water-controlled areas is clearly larger in the case of EVI compared with the SIF results. This could (i) be partly related to the fact that EVI, being less dynamic than SIF because it is more related to vegetation greenness and structure, tends to vary at timescales more in line with that of soil moisture (Turner et al., 2020), which can support stronger correlations, or (ii) be due to confounding effects of the changing soil/vegetation colour between dry and wet states on the EVI signal.

5.3.4 Hydrometeorological controls across climate regimes

In addition to analysing the spatial variation of the main drivers of vegetation productivity extremes, we attempt to further understand the large-scale patterns along temperature and aridity gradients. To this end, we bin grid cells by their climate characteristics as denoted by long-term

mean temperature and aridity (the ratio between unit-adjusted net radiation and precipitation). The results in Figure 5.5 illustrate which hydrometeorological variable most often has the highest correlation with SIF anomalies in each climate regime.

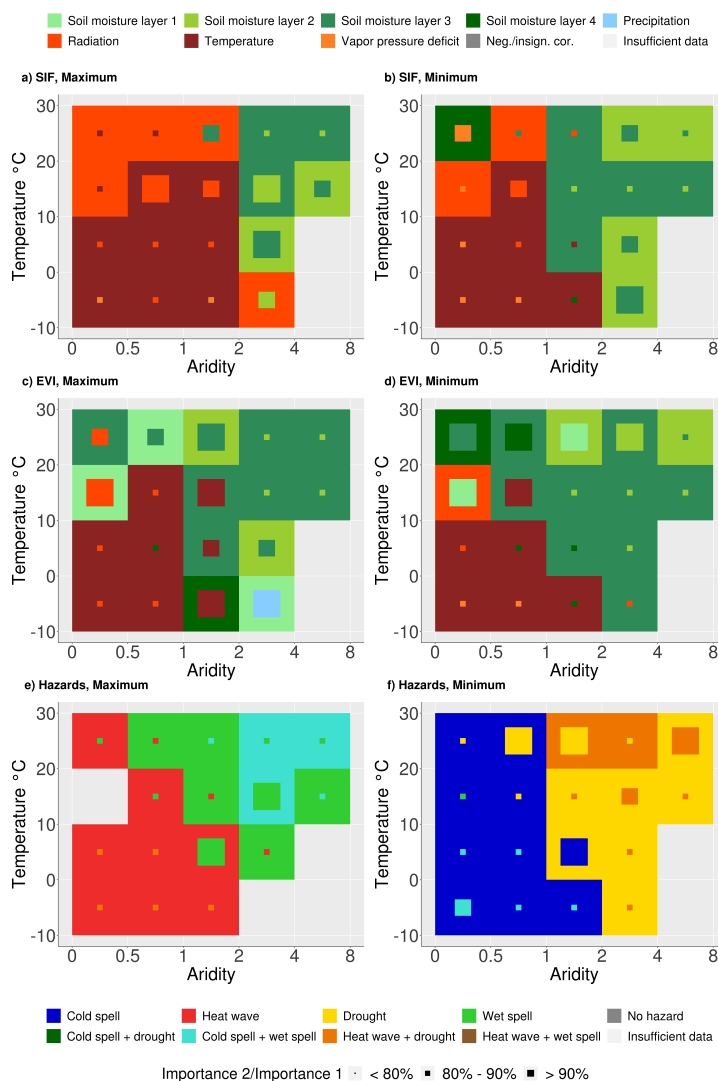


Figure 5.5: Hydrometeorological controls of vegetation productivity extremes summarized across climate regimes: (a, b) sun-induced chlorophyll fluorescence (SIF) extremes and (c, d) enhanced vegetation index (EVI) extremes. (e, f) Hydrometeorological hazards co-occurring with the sun-induced chlorophyll fluorescence (SIF) extremes. Box colour denotes the main controlling hydrometeorological variable; the second most important variable is indicated in the smaller squares' colour, while its size represents the ratio between the highest and second highest number of grid cells.

Figure 5.5a and b show that vegetation productivity extremes in humid regions (aridity < 1; (Budyko, 1974)) are mostly energy-controlled, with temperature controlling in cold regions (long-term average temperature < 10 °C) and radiation controlling in warm regions (long-term temperature > 10 °C). In contrast, productivity extremes in arid regions (aridity > 2; (Budyko, 1974)) are mainly water-controlled, with soil moisture layers 2 and 3 as the most

important water controls. The main difference between maximum and minimum sun-induced chlorophyll fluorescence (SIF) results is detectable in semi-arid regions ($1 < \text{aridity} < 2$). While for maximum sun-induced chlorophyll fluorescence (SIF) those climate regimes show mostly energy control, sun-induced chlorophyll fluorescence (SIF) minima in these regimes are largely water-controlled. From this, we deduce that semi-arid regions represent the transitional regime, as the main drivers change from energy to water variables from sun-induced chlorophyll fluorescence (SIF) maximum to sun-induced chlorophyll fluorescence (SIF) minimum.

Supplementary Figure 5.A5 indicates that hydrometeorological anomalies do elicit not only immediate but also lagged vegetation responses. A clear difference between water- and energy-controlled conditions is already visible when correlating hydrometeorological anomalies of the preceding month with the respective sun-induced chlorophyll fluorescence (SIF) extreme. Energy and water surpluses and deficits establish over time, which is most clearly EVIDenced in arid regions, where precipitation and shallow soil moisture of the preceding month is found to be the most important variable. With time, deeper soil moisture becomes more important (Figure 5.5a,b), as in the case of sun-induced chlorophyll fluorescence (SIF) maxima, where precipitation needs time to infiltrate the soil, and in the case of sun-induced chlorophyll fluorescence (SIF) minima, where the soil dries most rapidly from the top down.

The results for EVI show similar patterns despite an increased overall water control as seen earlier in the global maps (Supplementary Figure 5.A4). For example, where in humid regions sun-induced chlorophyll fluorescence (SIF) extremes are mainly energy-controlled, EVI extremes are more often water-controlled, which is also reflected in the global maps in Supplementary Figure 5.A4.

Supplementary Figure 5.A6 illustrates similar controlling hydrometeorological variables for sun-induced chlorophyll fluorescence (SIF) and terrestrial evaporation (ET) extremes. This suggests that carbon and water cycles are sensitive to similar hazards, which in turn enhances their impact on the land climate system via both carbon and water pathways. This further demonstrates the usefulness of sun-induced chlorophyll fluorescence (SIF) observations for reflecting plant transpiration (Jonard et al., 2020). Further, Supplementary Figure 5.A6 shows that GLEAM ET extremes relate much more strongly to surface soil moisture than GOME-2 sun-induced chlorophyll fluorescence (SIF) extremes. This could be due to the part of ET that partitions into an unproductive part, bare-soil evaporation, which evaporates water from the surface layer directly, and a productive part, which is connected to carbon uptake and therefore sun-induced chlorophyll fluorescence (SIF). Surface soil moisture affects the unproductive part while overall enhancing the role of surface soil moisture for ET.

Figure 5.5e and f show the results of Figure 5.2 binned according to their long-term climate characteristics. In humid regions, both sun-induced chlorophyll fluorescence (SIF) extremes are co-occurring with temperature hazards. In contrast, in arid regions water-related hazards co-occur with maximum and minimum sun-induced chlorophyll fluorescence (SIF). Thereby,

Figure 5.5 underlines once more the similarity of the results obtained with approaches 1 (Figure 5.2) and 2 (Figure 5.4).

To additionally explore the influence of different vegetation types and their respective plant physiological differences on the main controls of vegetation productivity, we bin the grid cell results by the respective fraction of tree cover of the entire vegetation cover and by aridity in Supplementary Figure 5.A7. We find that the radiation control of sun-induced chlorophyll fluorescence (SIF) extremes in humid regions is mostly associated with forests and that the water control in semi-arid regions largely occurs for shorter vegetation, with presumably more shallow root systems, while productivity extremes in more forested semi-arid regions tend to be energy-controlled. In very strong droughts, tall trees with deep rooting systems are particularly prone to suffer hydraulic failure (Brum et al., 2019). However, in our analysis we consider five events in a 15-year time period such that we likely do not exclusively capture very strong droughts that might result in tree mortality. Generally, hardly any changes in the most important variables can be seen with variations in tree cover, suggesting that on a global scale plant physiological differences only have a limited effect on determining the most important control for sun-induced chlorophyll fluorescence (SIF) extremes. As in Figure 5.5, similar patterns are found for EVI extremes with an overall increased relevance of water variables particularly in short vegetation-dominated regions.

5.3.5 Switching hydrometeorological controls between sun-induced chlorophyll fluorescence (SIF) maxima and minima

In a final step, we focus on shifts between energy and water control when moving from sun-induced chlorophyll fluorescence (SIF) maxima to sun-induced chlorophyll fluorescence (SIF) minima. The respective transitional regions represent hotspots of land-atmosphere coupling such that (i) in these regions the land surface (soil moisture) affects near-surface weather at least during productivity minima (therefore also influencing transpiration) and (ii) this effect can be significant, as transpiration (variability) is relatively high compared with drier regions where vegetation productivity would be water-limited across its entire range from minimum to maximum. The results are depicted in Figure 5.6, which illustrates these emerging transitions from water to energy control (yellow) and vice versa (blue, denoting land-atmosphere hotspots). Grid cells that stay within water or energy control, even with a change between the water or energy variables, respectively, are shown in black, indicating no transition. Figure 5.6a reveals many regions with no transition. Transitions are found mostly in northern Eurasia and North America. Globally, a change from energy control during maximum sun-induced chlorophyll fluorescence (SIF) to water control during minimum sun-induced chlorophyll fluorescence (SIF) occurs more often (7% of the study area) than the opposite transition (4%).

Figure 5.6b and c display the percentage of grid cells in each climate regime changing from water to energy control and vice versa with grid cells binned with respect to long-term climate

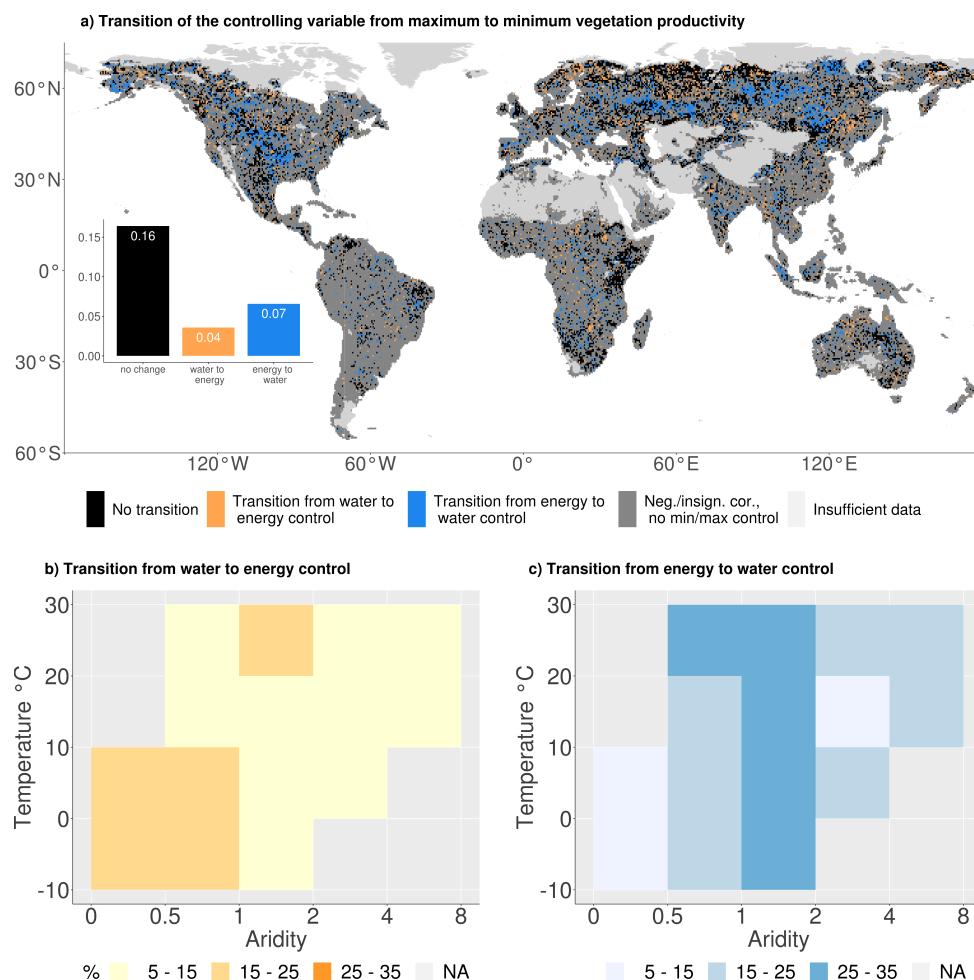


Figure 5.6: Changing hydrometeorological controls between vegetation productivity maxima and minima. (a) Global distribution of changing controls: in panels (b) and (c) grid cells are binned by their long-term climate characteristics. Panel (b) indicates the percentage of grid cells in each climate regime switching from water to energy control; panel (c) denotes the percentage of grid cells changing from an energy-controlled maxima to a water-controlled minima.

conditions, similar to Figure 5.5. The highest fraction of grid cells in each climate regime would show no change, but as we focus on transitioning grid cells, only they are displayed. Transitions from water to energy control between sun-induced chlorophyll fluorescence (SIF) maxima and sun-induced chlorophyll fluorescence (SIF) minima happen most often in cold, humid regions. This deviates from the prevailing energy control in these climate regimes and is probably related to local-scale features and/or micro-meteorological conditions. Figure 5.6c indicates that changes from energy control during maximum sun-induced chlorophyll fluorescence (SIF) to water control during minimum sun-induced chlorophyll fluorescence (SIF) most frequently occur in the semi-arid transitional regions. These are land-atmosphere coupling hotspots as described above. The transition from energy to water limitation could be caused by energy-controlled maxima in spring, when presumably soil water resources are available after being

replenished during autumn and winter. With sufficient water supply, energy surpluses could induce vegetation productivity maxima. During summer, soil moisture could be depleted for example by the high vegetation demand and therefore take over the sun-induced chlorophyll fluorescence (SIF) control of photosynthesis that is reflected into the sun-induced chlorophyll fluorescence (SIF) dynamics.

5.3.6 Limitations

Our results are obtained at and valid for relatively large spatial (0.5°) and temporal (monthly) scales. Previous studies have shown differences in the vegetation-climate coupling across scales (Linscheid et al., 2020), suggesting it would be worthwhile to repeat our analysis for different spatiotemporal scales in the future, possibly with new satellite data products. In this context it should be noted, however, that while the relationship between sun-induced chlorophyll fluorescence (SIF) and gross primary productivity (GPP) as actual vegetation productivity is strong for large spatiotemporal scales (Frankenberg et al., 2011; Guanter et al., 2012; Joiner et al., 2013), it can deteriorate towards smaller scales (He et al., 2020; Magney et al., 2020; Maguire et al., 2020; Marrs et al., 2020; Wohlfahrt et al., 2018). The spatiotemporal range within which there is an acceptable sun-induced chlorophyll fluorescence (SIF)-GPP relationship is not entirely clear yet.

As a second source of uncertainty, sun-induced chlorophyll fluorescence (SIF) data with their relatively large spatial footprint are more vulnerable to cloud contamination compared to finer-scale satellite products (Joiner et al., 2013). Also, especially across South America the sun-induced chlorophyll fluorescence (SIF) data quality is decreased to additional noise (Joiner et al., 2013; Köhler et al., 2015). In our study, many grid cells in these regions and other tropical, cloud-dominated regions exhibit insignificant or negative correlations between sun-induced chlorophyll fluorescence (SIF) and hydrometeorological anomalies, which is why no hydrometeorological controls can be determined there (Figure 5.4). Confirming the validity of our results for the tropical grid cells where results can be obtained, we find mostly consistent and physically meaningful results, e.g. radiation being a main driver of vegetation productivity, as the cloud cover limits radiation (reported similarly for non-extreme conditions by Green et al. (2020), and Li et al. (2021b)).

Next to the sun-induced chlorophyll fluorescence (SIF) data, there is also noteworthy uncertainty in the soil moisture data from ERA5. While data quality of surface soil moisture benefits from (satellite) data assimilation, the soil moisture dynamics in deeper layers are more model-based, which somewhat contradicts the observational character of our study. Therefore, we use soil moisture data from SoMo.ml as an independent dataset, which is not based on physical modelling and the related assumptions and parameterizations, as it is derived with machine learning applied to in situ measurements from different depths. Overall, the similar results obtained with ERA5-

Land and SoMo.ml soil moisture confirm the robustness of our results despite uncertainties in the soil moisture data.

Finally, the use of correlation methods for inferring causal relations is potentially insufficient and under debate (Krich et al., 2020). We want to emphasize that in our study when referring to "drivers" or "controls" of vegetation productivity, we simply base this on correlation and do not imply causality. Nevertheless, we try to filter out confounding effects by disregarding negative and insignificant correlations. Additionally, testing our methodology (approach 2) for non-anomalous vegetation productivity (Supplementary Figure 5.A8), which allows for comparing results with those of Li et al. (2021b), reveals similar results, while they use a different methodology based on random forests and Shapley Additive Explanations (SHAP) values, which are more robust against confounding effects. Next to this, in our study we apply two different methodologies in approaches 1 and 2 and find similar results, further underlining the robustness of our conclusions.

5.4 Conclusion

In this observation-based study, we quantify that vegetation productivity extremes are related to hydrometeorological hazards in about 50% of the global land area that is sufficiently vegetated and cloud-free. The most relevant hazards for vegetation productivity extremes vary along climate gradients. For vegetation productivity maxima the most relevant hydrometeorological extremes are heat waves in northern latitudes above 50° N and wet spells in latitudes below 50° N. For productivity minima, drought and cold spells are globally most detrimental to large-scale photosynthesis and carbon uptake. The results of our impact-centric analysis are similar to and complement more traditional climate-centric studies (Ciais et al., 2005; Flach et al., 2018; Qiu et al., 2020). Compound extremes also play a role in 15%-20% of our study area; they are somewhat more relevant for productivity minima than for the maxima, with joint drought-heat extremes being most important. Semi-arid, grass-dominated ecosystems tend to transition between water and energy control within the range of their productivity variability. This results in a sensitivity to both water- and energy-related hazards. Thereby, we illustrate how global land-atmosphere coupling hotspots (Koster et al., 2004), where the land surface affects near-surface weather, can be verified using novel vegetation productivity data.

Overall, this study highlights the profound role of (compound) hydrometeorological hazards for global vegetation productivity extremes. Understanding these complex, climate-dependent relationships with present-day observational data is a starting point to more reliably foresee respective changes in a changing future climate with e.g. fewer cold spells but probably more droughts.

5.A Appendix

This appendix represents the supplementary materials of the presented publication.

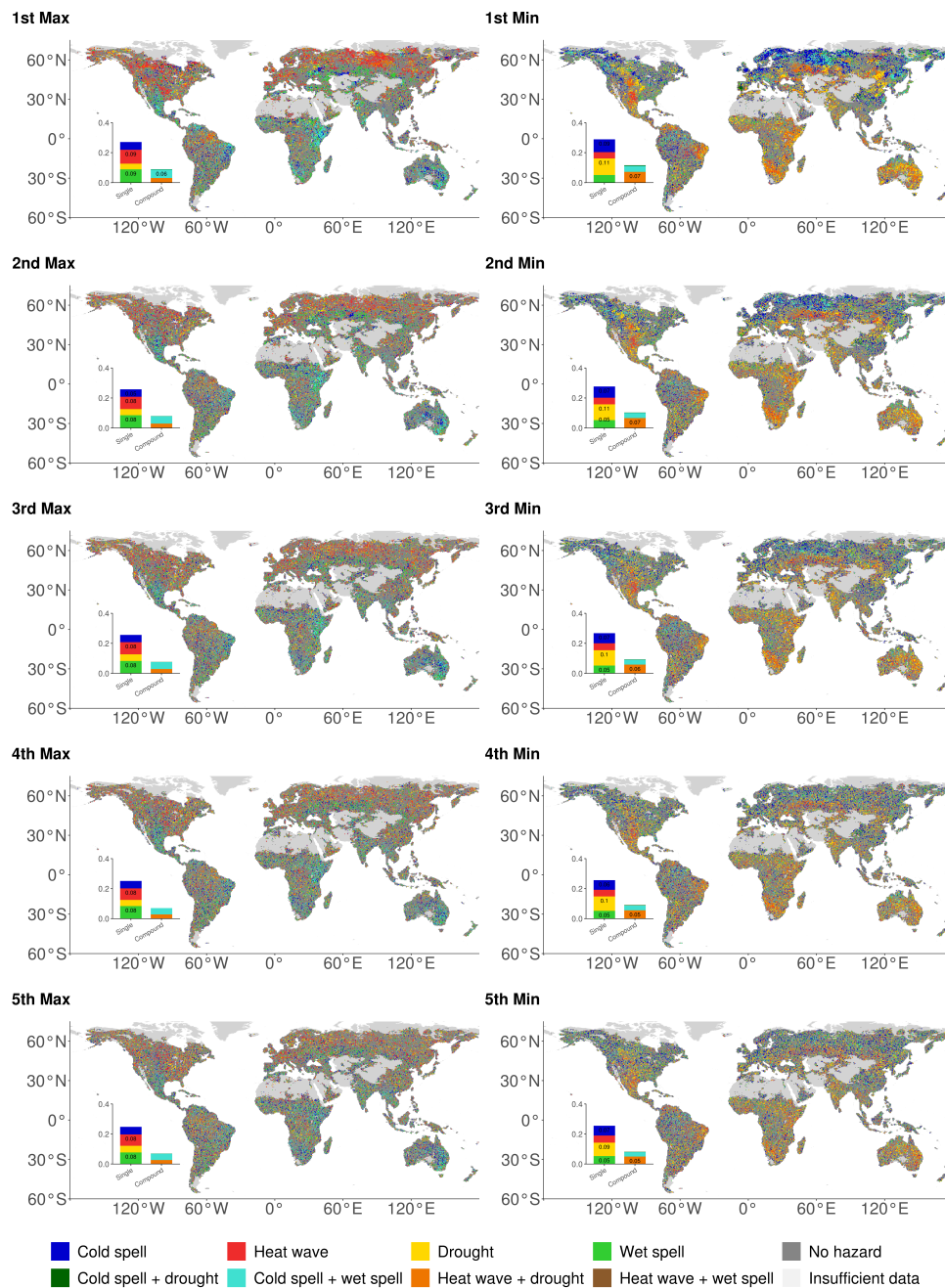


Figure 5.A1: Hydrometeorological hazards co-occurring with each of the five sun-induced chlorophyll fluorescence (SIF) maxima and minima (1st is the strongest extreme, 5th the weakest one). Temperature and soil moisture anomalies are considered as extreme if they are below/above the 10/90th percentile of 100 randomly sampled temperature and soil moisture anomalies.

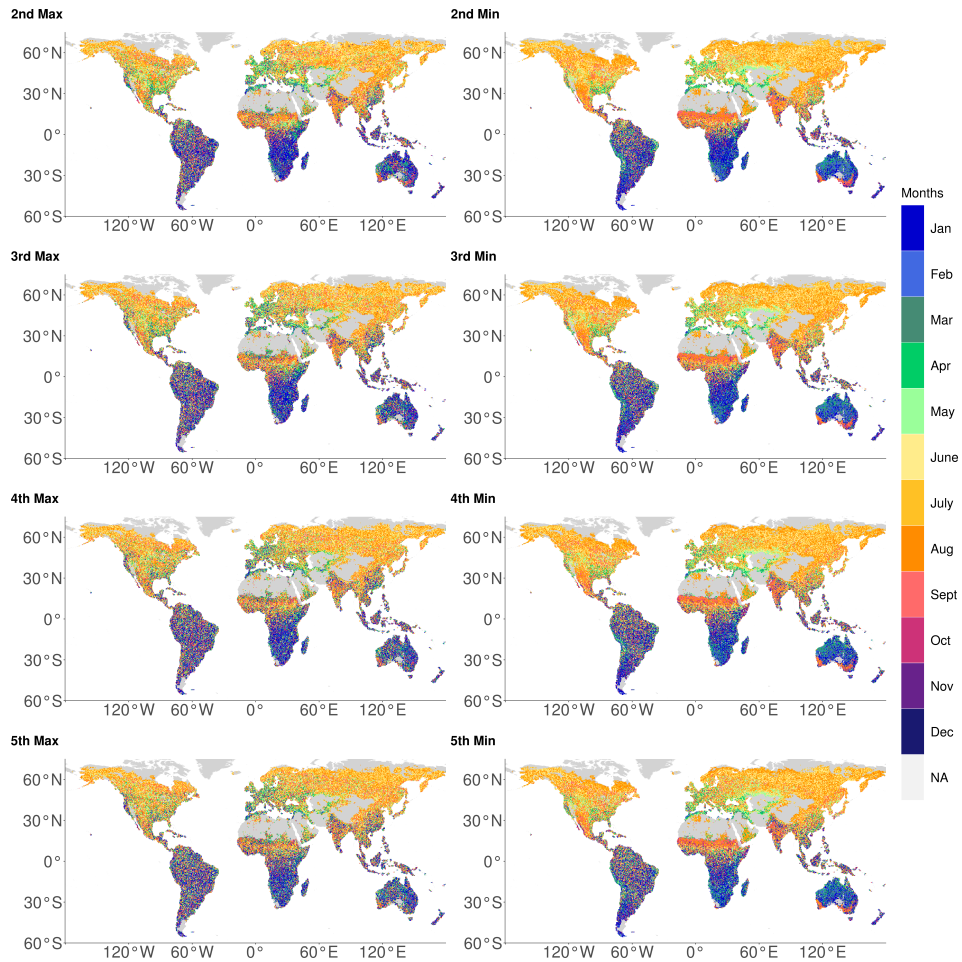


Figure 5.A2: Global distribution of the month-of-year in which each of the four remaining sun-induced chlorophyll fluorescence (SIF) maxima and minima occurred (2nd is the second strongest extreme, 5th the weakest one).

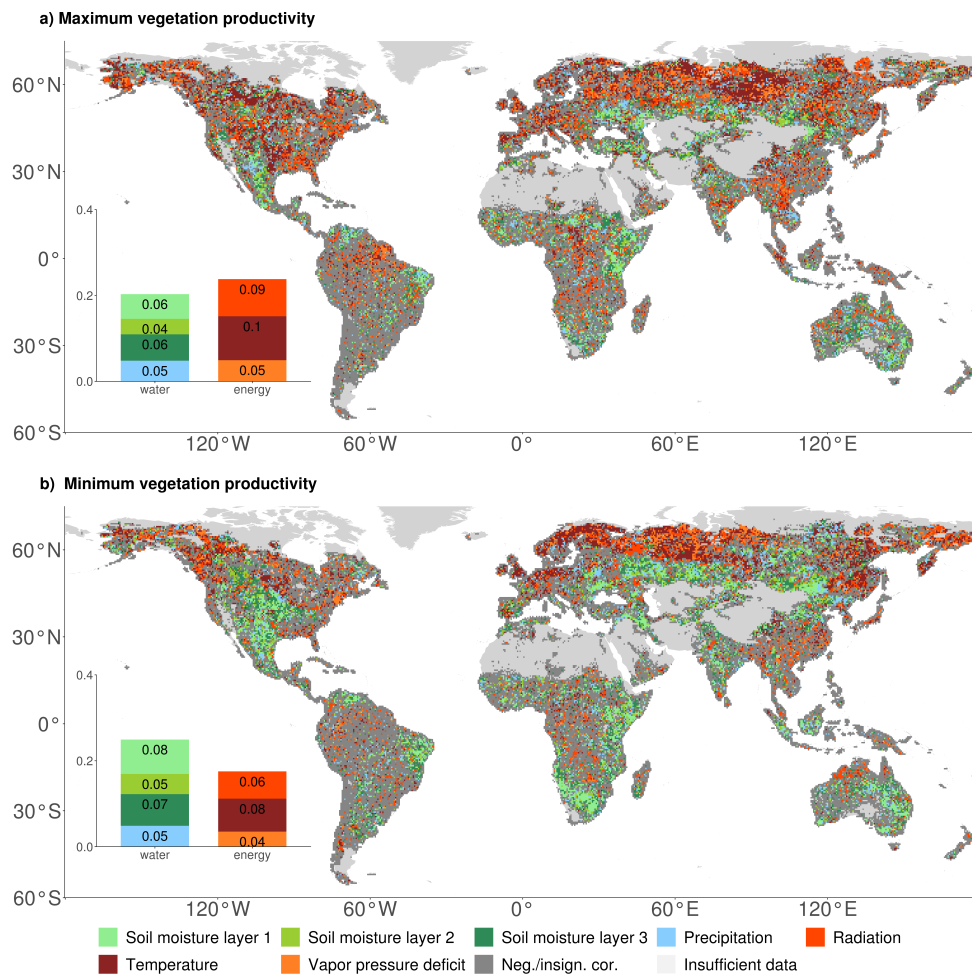


Figure 5.A3: Global distribution of hydrometeorological controls (with soil moisture from SoMo.ml) of sun-induced chlorophyll fluorescence (SIF) (a) maxima and (b) minima. The displayed variable correlates strongest with sun-induced chlorophyll fluorescence (SIF) in the extreme months, considering only significant and positive correlations. The bar plot indicates the area controlled by each variable relative to the total land area.

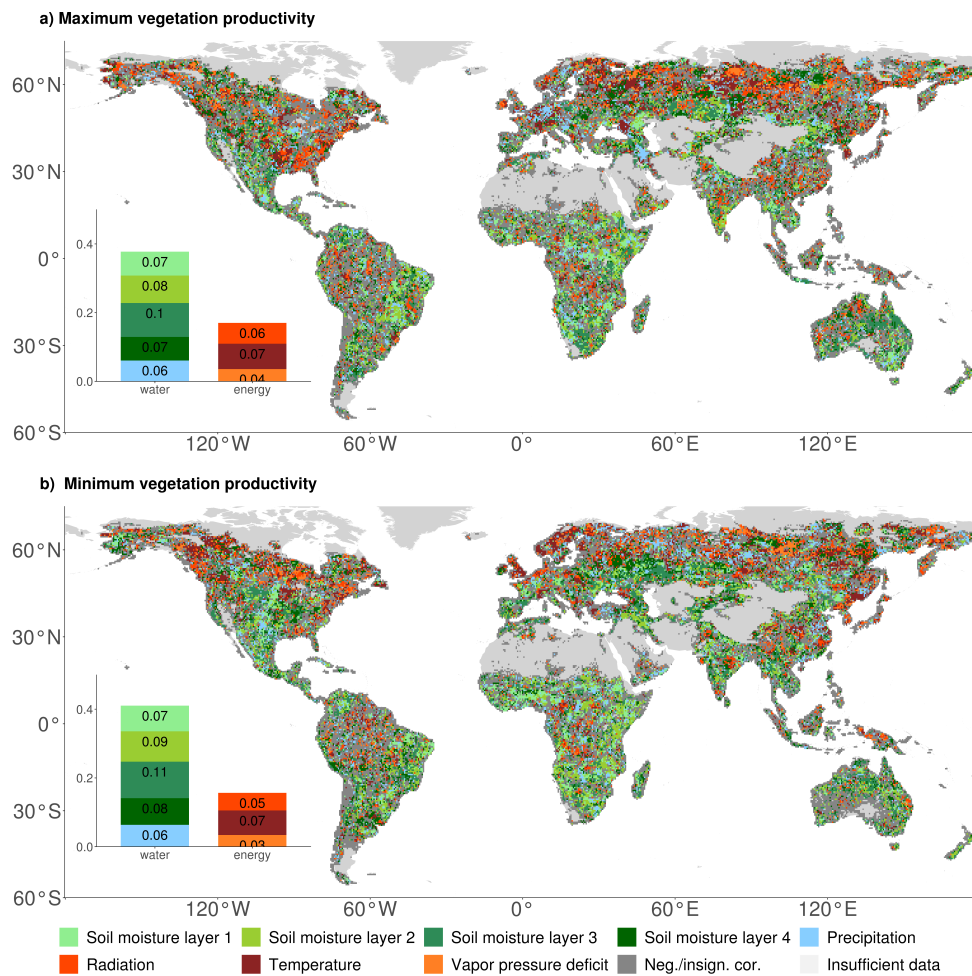


Figure 5.A4: Global distribution of hydrometeorological controls (ERA5 land) of EVI (a) maxima and (b) minima. The displayed variable correlates strongest with EVI in the extreme months, considering only significant and positive correlations. The bar plot indicates the area controlled by each variable relative to the total study area.

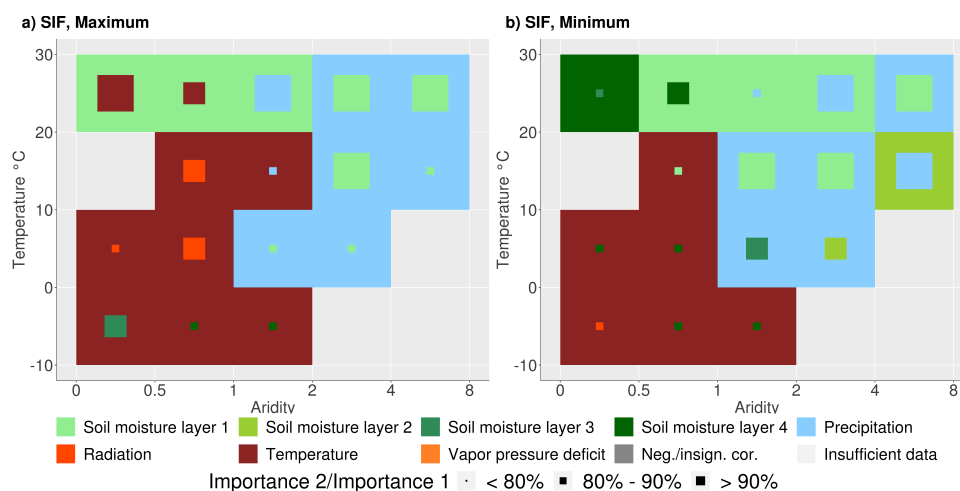


Figure 5.A5: Hydrometeorological controls (ERA5 land) of different climate regimes with a lag time of 1 month. Grid cells are grouped by their long-term temperature and aridity (unit-adjusted net radiation/precipitation). The hydrometeorological variables of the month preceding the sun-induced chlorophyll fluorescence (SIF) extreme have been used in the computation of most important variable. The variable which is important for most of the grid cells for vegetation productivity maxima (a) and minima b), inferred using sun-induced chlorophyll fluorescence (SIF), in one climate regime is used to color the box. The second most important variable colors the smaller squares. Their ratio is denoted in the size of the squares.

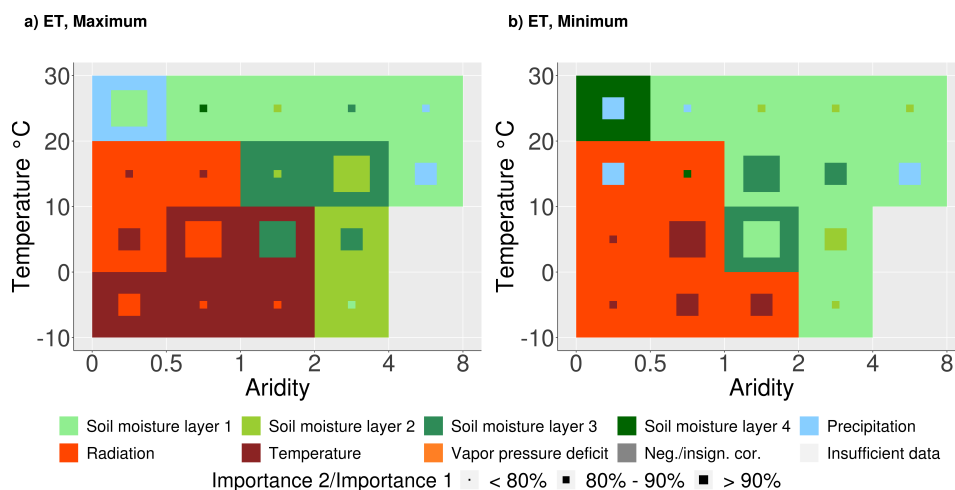


Figure 5.A6: Hydrometeorological controls (ERA5 land) of different climate regimes on ET from GLEAM. Grid cells are grouped by their long-term temperature and aridity (unit-adjusted net radiation/precipitation). The variable which is important for most of the grid cells for vegetation productivity maxima (a) and minima b), inferred using ET, in one climate regime is used to color the box. The second most important variable colors the smaller squares. Their ratio is denoted in the size of the squares.

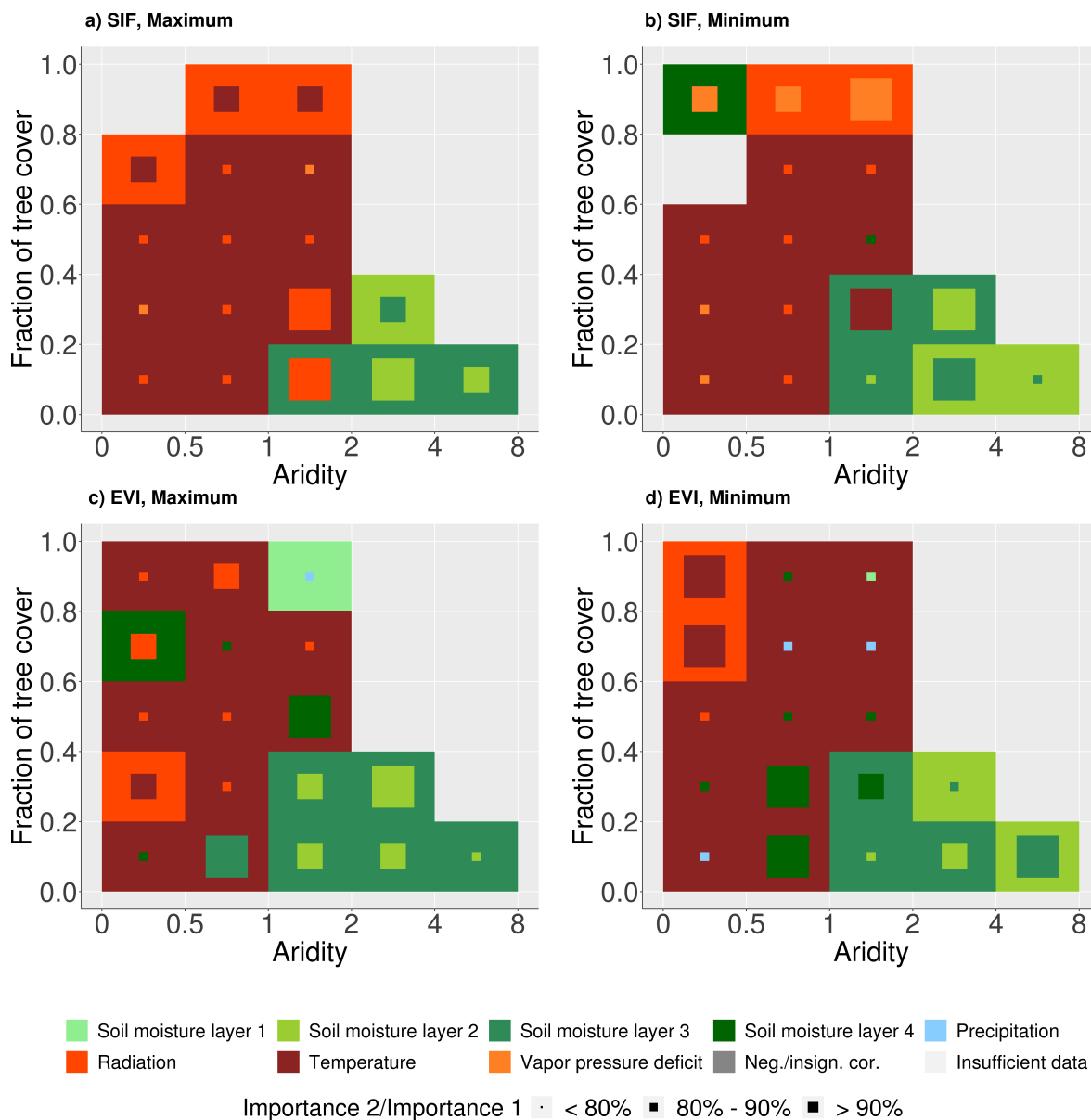


Figure 5.A7: Hydrometeorological controls (ERA5 land) of different vegetation regimes. Grid cells are grouped by their fraction of tree cover and aridity (unit-adjusted net radiation/precipitation). The variable which is important for most of the grid cells for vegetation productivity extremes (a) and (b) sun-induced chlorophyll fluorescence (SIF); (c) and (d) EVI) in one vegetation regime is used to color the box. The second most important variable colors the smaller squares. Their ratio is denoted in the size of the squares.

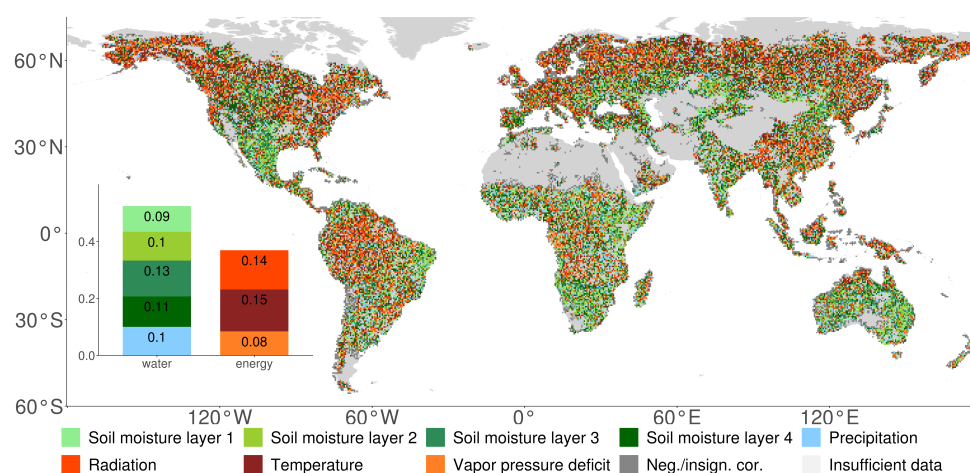


Figure 5.A8: Global distribution of hydrometeorological controls of non-anomalous sun-induced chlorophyll fluorescence (SIF). The displayed variable correlates strongest with sun-induced chlorophyll fluorescence (SIF) in 5 randomly chosen months (from 25-75% range of the sun-induced chlorophyll fluorescence (SIF) anomaly distribution), which have a similar variation as the 5 maximum sun-induced chlorophyll fluorescence (SIF) months. Only significant and positive correlations are considered. The bar plot indicates the area controlled by each variable relative to the total study area (which is slightly different here compared with Figure 5.4 as non-extreme sun-induced chlorophyll fluorescence (SIF) anomalies with similar variability might not be found in every grid cell).

Chapter 6

Future ecosystem water limitation and heat extremes

This chapter is based on:

J. M. C. Denissen, A. J. Teuling, G. Balsamo, X. Yu, M. M. Vogel, S. I. Seneviratne, and R. Orth (2022a). “Increasing ecosystem water limitation fuels future heat extremes”. *Global Change Biology, in review*

6.1 Abstract

Heat extremes have severe implications for human health, ecosystems and the initiation of wildfires. Whereas they are mostly introduced by atmospheric circulation patterns, the intensity of heat extremes is modulated by vegetation functioning associated with soil moisture availability. Thereby, vegetation provides evaporative cooling through transpiration, which can be reduced under water stress. While it has been shown that ecosystem water limitation is projected to increase in the future (Denissen et al., 2022b), the respective repercussions on heat extremes are unclear.

In this study we use projections from Earth system models to show that future changes in heat extremes are amplified by increasing ecosystem water limitation in regions across the globe. We represent ecosystem water limitation with the Ecosystem Limitation Index (ELI, (Denissen et al., 2020)), and quantify temperature extremes through the differences between warm-season mean and maximum temperatures. We identify hotspot regions in tropical South America and across Canada and Central Europe where relatively strong trends towards increased ecosystem water limitation translate into amplified heat extremes. This is governed by the magnitude of the ELI trends and the present-day ELI which denotes the land-atmosphere coupling strength determining the temperature sensitivity to evaporative cooling. Many regions where vegetation functioning is predominantly energy-limited in present climate exhibit strong trends towards increasingly occurring water limitation, inducing the strongest increases in heat extremes in these areas. Therefore, considering the ecosystem's water limitation is key for assessing the intensity of future heat extremes and their corresponding impacts.

6.2 Main Text

6.2.1 Introduction

Heat extremes affect ecosystems and society through their implications on human health, crop yields and tree mortality, and the initiation of wildfires (Anderegg et al., 2013; Goulart et al., 2021; McDowell and Allen, 2015; O et al., 2020b; Orth et al., 2022; Ruffault et al., 2020). In the recent past, temperature extremes increased in intensity, duration and frequency; these changes are related to climate change (Seneviratne et al., 2021) and they even accelerated in recent years in some regions (Seneviratne et al., 2014). In the future, heat extremes are projected to intensify further, alongside the ongoing global warming (Seneviratne et al., 2021).

Hot temperatures can be fueled by dynamic and thermodynamic processes (Harrington et al., 2019; Trenberth et al., 2015). The relevance of atmospheric dynamics for recent heat waves has been highlighted for the case of large-scale blocking patterns which support heat accumulation across consecutive dry days (Cassou et al., 2005; Jézéquel et al., 2018) as well as the entrainment of warm air aloft (Miralles et al., 2014b). Also, large-scale circulation patterns advecting warm air, or air from regions with dry soils, have been suggested to contribute to heat waves (Schumacher et al., 2019). Additionally, thermodynamic processes can amplify heat extremes; the land surface determines the partitioning of incoming radiative energy into sensible heating and latent heat (Seneviratne et al., 2010). Changes in this flux partitioning can be induced through soil moisture drying as water-stressed vegetation tends to reduce transpiration; this way, a larger fraction of the incoming energy is available for sensible heating which leads to higher temperatures (Budyko, 1974; Denissen et al., 2021; Vogel et al., 2017). As a consequence, circulation-induced rainfall deficits are translated by ecosystem water limitation to reduced evaporative cooling and amplified local temperatures (Miralles et al., 2012; Quesada et al., 2012; Teuling et al., 2010; Ukkola et al., 2018).

It has been shown that climate change may involve long-term trends in soil moisture and land-atmosphere coupling in some regions (Berg and Sheffield, 2018; Berg et al., 2017; Denissen et al., 2022b; Seneviratne et al., 2021; Sippel et al., 2017) and that these can contribute to amplified heat extremes (Lorenz et al., 2016; Seneviratne et al., 2006; Vogel et al., 2017) especially in the case of depletion of soil moisture preceding the warm season (Rasmijn et al., 2018; Stegehuis et al., 2021). However, the representation of land-atmosphere coupling and ecosystem water limitation in Earth system models is uncertain (Greve et al., 2019; Vogel et al., 2018). This is because the vegetation's response to soil moisture drying is difficult to capture due to heterogeneous soil and vegetation characteristics and limited observational constraints for rooting depths and soil moisture dynamics in respective soil layers. For these reasons, we revisit the response of heat extremes to long-term changes in land-atmosphere coupling using the latest generation of Earth System models from the Coupled Model Intercomparison Project Phase 6 (CMIP6, (Eyring et al., 2016)).

In this study, we jointly assess trends in ecosystem water limitation and heat extremes in fully coupled CMIP6 simulations from five state-of-the-art Earth system models at the monthly time scale and $2^\circ \times 2^\circ$ spatial resolution from 1980 - 2100 (Eyring et al., 2016). For this purpose, we use novel indices to describe ecosystem water limitation and the magnitude of heat waves, respectively. For analyzing heat extremes, we focus on the difference between warm-season average and maximum temperatures, hereafter referred to as maximum daily temperature ($\overline{T_{\max}}$) divergence. While the maximum temperature is known to be affected by land-atmosphere coupling (Dirmeyer et al., 2021; Donat et al., 2017; Lorenz et al., 2016; Schwingshackl et al., 2018; Seneviratne et al., 2006; Sippel et al., 2017; Ukkola et al., 2018; Vogel et al., 2017), the average temperatures are largely driven by large-scale circulation (Cassou et al., 2005; Miralles et al., 2014b; Schumacher et al., 2019). This way, by focusing on the divergence between mean and maximum temperatures, we can isolate the thermodynamic component from the dynamic component in heat wave development. $\overline{T_{\max}}$ divergence is computed for each grid cell and decade as the difference between the means of (i) the 10 warm-season average temperatures from the individual years and (ii) the 10 temperature maxima in the individual years (see Methods). Next to this, we assess ecosystem water limitation with the Ecosystem Limitation Index (ELI, (Denissen et al., 2020)) which is computed as the difference of the correlations of terrestrial evaporation (ET) with (i) water supply (represented through soil moisture, SM) and (ii) energy availability (air temperature (T_a) and surface net radiation (R_n)) (Methods). Positive ELI is indicative of water-limited conditions, whereas negative ELI denotes energy limitation. Therefore, the ELI captures the interplay of water and energy controls on evaporative cooling.

6.3 Materials and Methods

6.3.1 Ecosystem Limitation Index

The Ecosystem Limitation Index (ELI), referred to as the correlation-difference metric (Denissen et al., 2020), is formulated as follows:

$$ELI = cor(SM', ET') - cor(T_a', ET') \quad (6.1)$$

The prime denotes monthly anomalies of soil moisture (SM), terrestrial evaporation (ET) and air temperature (T_a). In Figure 6.4 and 6.A10, we considered net surface radiation (R_n) as a different proxy for energy availability alongside air temperature anomalies. Between energy- and water-limited conditions, the ELI expresses different typical sensitivities to energy and water supply: High and positive $cor(T_a'/R_n', ET')$ is indicative of energy-limited conditions, whereas high and positive $cor(SM', ET')$ concerns water-limited conditions. The ELI combines both the relevance of energy and water supply for evaporative cooling by taking the difference between

those two correlations, so that positive values denote water-limited conditions and negative values indicate energy-limited conditions. Thereby, the ELI can be used to pin-point transitional areas, where ELI is approximately zero. Further, in contrast to other traditional indices such as the Aridity Index that rely on climatological means, the ELI can be used to study (parts of) the seasonal cycle. For a more extensive assessment of air temperature or net surface radiation and soil moisture as the choices for energy and water proxies as well as a detailed elaboration on the interpretation of ELI, we refer to Denissen et al. (2022b).

6.3.2 Coupled Model Intercomparison Project Phase 6 (CMIP6) data

We use historical (1980 - 2015) and 'business-as-usual' SSP5-8.5 (2015 - 2100, (O'Neill et al., 2016)) simulations from five different fully coupled models that provide the necessary variables at $2^\circ \times 2^\circ$ spatial and monthly temporal resolution from the Coupled Model Intercomparison Project (CMIP6, (Eyring et al., 2016)). The most important information on the used data is summarized in Table 1. By taking the SSP5-8.5 scenario we intend to focus on the climate scenario most influenced by human activity and related emissions of greenhouse gasses, with presumably the hottest temperature extremes with the biggest impacts.

Table 6.1: Important details related to the model output used in this study. The following variables have been downloaded from all the models: temperature (tas), root-zone soil moisture (mrso), terrestrial evaporation (hfls), maximum daily temperature (tasmax) and in- and outgoing short- and longwave radiation (rlds,rsds,rhus,rsus). *: the first number denotes the version of the historical simulation, whereas the second number concerns the SSP5-8.5 simulation.

Institution	Model	Member	Version*	Citation
National oceanic and Atmospheric Administration (NOAA) Geophysical Fluid Dynamics Laboratory (GFDL)	GFDL-CM4	r1i1p1f1	v20180701 & v20180701	(Held et al., 2019)
Centre National de Recherches Meteorologiques (CNRM)	CNRM-ESM2-1	r1i1p1f2	v20181206 & v20191021	(Séférian et al., 2019)
Beijing Climate Center (BCC)	BCC-CSM2-MR	r1i1p1f1	v20181126 & v20190314	(Wu et al., 2019)
Met Office Hadley Centre (MOHD)	UKESM1-0-LL	r2i1p1f2	v20190627 & v20190726	(Sellar et al., 2019)
Institute for Numerical Mathematics (INM)	INM-CM4-8	r1i1p1f1	v20190530 & v20190603	(Volodin et al., 2018)

6.3.3 Pre-processing data

After data acquisition, several steps are taken to assure a meaningful selection of data for the analysis: i) To assure vegetated conditions during the warm season, which would allow the

vegetation to respond to anomalies in energy and water supply and consequently affect the surface flux partitioning, all months with $T_a < 10^\circ\text{C}$ and $\text{LAI} < 0.5$ are excluded from the analysis. ii) To pin-point the hottest heat extremes, we additionally focus on the three hottest months a year (warm season), defined as the 3 months-of-year with the highest maximum daily temperature averaged decadally. This selection of data results in what we refer to in this manuscript as the "warm vegetated land area", which includes the spatiotemporal mask where data is available after filtering. This data is then used to compute decadal time series of the desired diagnostics, which are ELI, EF and $\overline{T_{\max}}$ divergence. The advantage of considering only the warm season lies in the comparison of concomitant trends of ELI, EF and $\overline{T_{\max}}$ divergence, as these might be subject to seasonal variability. EF is computed as the fraction of the net surface radiation (the sum of all radiative components) that is used to evaporate water. In order to compute $\overline{T_{\max}}$, we consider first all the yearly temperature maxima, which we average decadally. $\overline{T_{\max}}$ divergence results from excluding background mean climate warming (subtracting mean temperature from $\overline{T_{\max}}$).

6.3.4 Computing Theil-Sen slopes and slope significance

The trends shown in Figure 6.1 and 6.4 and Supplementary figures 6.A1, 6.A2, 6.A6, 6.A9, 6.A10 are based on Theil-Sen slopes (Sen, 1968; Theil, 1992). This approach is insensitive to statistical outliers, as the median slope from a range of possible slopes is selected as the best fit. The significance of these slopes is determined based on Kendall's tau statistic from Mann-Kendall tests.

6.3.5 Regional bootstrapping

For the regional correlation estimates (Supplementary Figure 6.A9a, c), the grid-specific time series of $\overline{T_{\max}}$ divergence and ELI are bootstrapped; They are based on a hundred different selections of grid-specific time series of $\overline{T_{\max}}$ divergence and ELI.

6.3.6 Results

We identify increased $\overline{T_{\max}}$ divergence trends across over 77% of the warm vegetated land area (Figure 6.1a, Methods). Model confidence is higher for increasing than for decreasing $\overline{T_{\max}}$ divergence (inset plot Figure 6.1a), as in more than half of the area with increasing $\overline{T_{\max}}$ divergence at least four out of five CMIP6 models agree, while this is less than a third for decreasing $\overline{T_{\max}}$ divergence (see also Supplementary Figure 6.A1). This reveals high confidence in an accelerated increase of heat extremes compared with warm-season average temperatures. We define four regions of interest where $\overline{T_{\max}}$ divergence increases are particularly rapid and spatially coherent, as denoted in Figure 6.1a: North and South America (NAM and SAM), Central Europe (CEU) and Northern Asia (NAS).

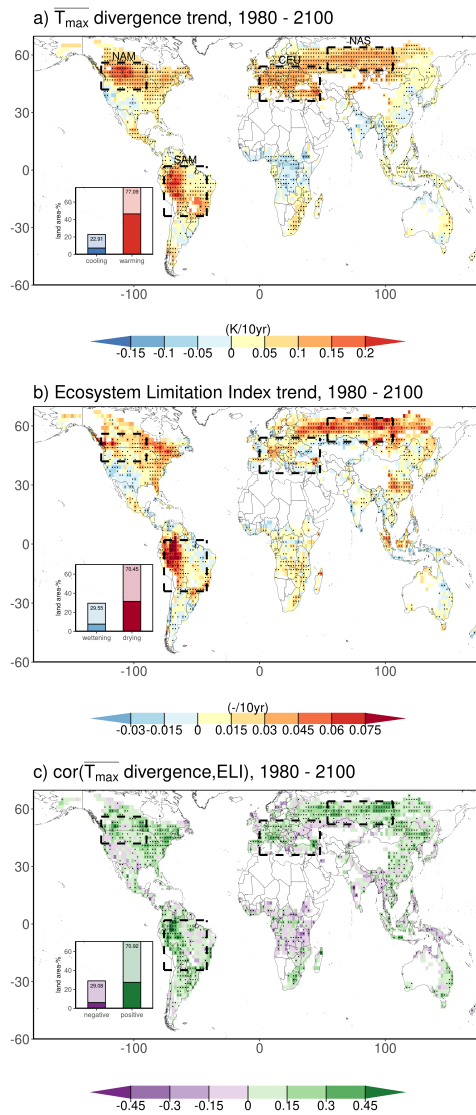


Figure 6.1: Similarity of global patterns of change in maximum temperature divergence and ecosystem water limitation. Multi-model means of trends based on decadal time series per respective CMIP6 model of a) normalized temperature extremes $\overline{T_{\max}}$ divergence; Methods) and b) Ecosystem Limitation Index (ELI, Methods). c) Multi-model means of Kendall's rank correlation coefficient between model-specific time series of ELI and $\overline{T_{\max}}$ divergence. The insets display the fraction of the warm land area that with positive or negative trends or correlations, respectively (at least 4 out of 5 models agreeing on the sign of the trend or correlation are hues darker). Stippling indicates that at least 4 out of 5 CMIP6 models agree on the sign of the trend or correlation. All trends and correlations are calculated over the warm season (see Methods). The dashed boxes indicate regions of interest.

Similar to the $\overline{T_{\max}}$ divergence trends, there is an increase of ELI in more than 70% of the warm vegetated land area, signaling widespread shift towards water limitation (Figure 6.1b). This widespread increase is confirming results from a recent study focusing on the growing season (Denissen et al., 2022b). Interestingly the ELI increases found here are stronger, suggesting a

particularly rapid shift towards ecosystem water limitation in the warmest months. Especially in the regions of interest, except for CEU, ELI increases are robust across models (Supplementary Figure 6.A2).

Spatial patterns of trends in $\overline{T_{\max}}$ divergence and ELI are very similar. Areas with highest $\overline{T_{\max}}$ divergence trends (>0.1 K/10yr) are predominantly characterized by ELI increases (found in 90% of these areas). More importantly, also the temporal evolution of decadal time series of $\overline{T_{\max}}$ divergence and ELI is similar in many regions. This is evidenced by significant correlations in many areas (Figure 6.1c, Supplementary Figure 6.A3), suggesting that increasing ELI contributes to hotter temperature extremes. We also find regions with insignificant correlations such as tropical Africa, India and western North America. There, ELI is apparently not affecting $\overline{T_{\max}}$ divergence which might instead be affected by alternative processes such as (changes in) advection of warm air masses through large-scale circulation patterns.

While the use of temperature as energy variable in the computation of the ELI is established (Denissen et al., 2020), we note that this prevents ELI from being fully independent from $\overline{T_{\max}}$ divergence. Therefore, we repeat the analysis in Figure 6.1c using net radiation as an energy variable in the ELI computation (Supplementary Figure 6.A4a). The resulting spatial patterns are very similar, underlining the usefulness of ELI in its original temperature-based formulation in our context. Further, we investigate the role of net radiation as a potential confounding effect influencing both ELI and $\overline{T_{\max}}$ divergence to create a spurious correlation between them. This is done by computing a partial correlation (Supplementary Figure 6.A4b) which again yields similar spatial patterns supporting the notion of ELI physically affecting $\overline{T_{\max}}$ divergence.

Furthermore, in order to illustrate the physical link between ELI and $\overline{T_{\max}}$ divergence, which presumably is through evaporative cooling, we analyze terrestrial evaporation normalized by net surface radiation. The resulting evaporative fraction (EF) links the surface energy and water balances. The EF is generally decreasing in all regions of interest with high agreement between individual models (Figure 6.A5a). Moreover, EF is generally significantly correlated with both $\overline{T_{\max}}$ divergence and ELI, respectively, establishing the physical link between these quantities. This way, in more than 80% of the warm vegetated land area, trends in EF fraction are negatively correlated with $\overline{T_{\max}}$ divergence, meaning that a decreasing (increasing) trend in EF, renders more (less) energy available for sensible heating, which elevates (reduces) heat extremes (Supplementary Figure 6.A5b). In about two thirds of the warm vegetated land area, the correlation between EF and ELI is negative (Supplementary Figure 6.A5c), verifying that a shift towards ecosystem water limitation jointly occurs with the expected decreases in evaporative cooling. Some regions exhibit insignificant or even negative correlations pointing to other processes such as irrigation or land use changes.

Next, we compare the temporal evolution of $\overline{T_{\max}}$ divergence and ELI averaged across the regions of interest and the entire warm vegetated land area between historical and future time periods. Figure 6.2a shows a steady global increase of $\overline{T_{\max}}$ divergence, with heat extremes experiencing an additional 0.5K warming with respect to the average warm-season warming over 1980 -

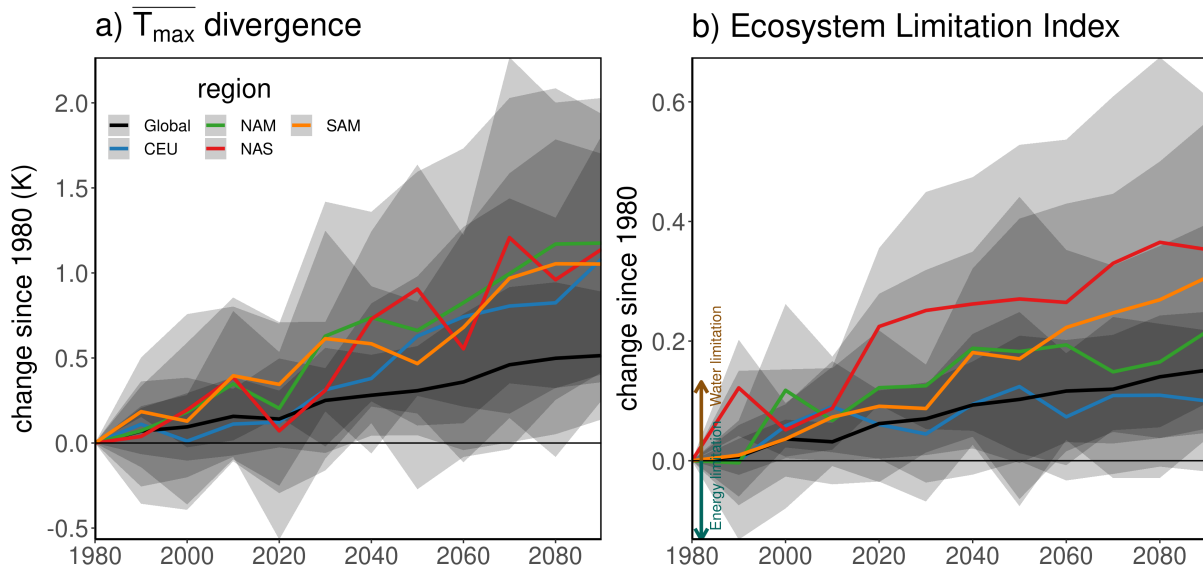


Figure 6.2: Changes in global and regional maximum temperature divergence in line with increasing ecosystem water limitation. Temporal evolution of a) $\overline{T_{\max}}$ divergence and of b) Ecosystem Limitation Index (ELI) globally and for the regions of interest. Solid lines depict multi-model mean time series, where shaded regions cover ± 1 multi-model standard deviation. Global averages are calculated over land grid cells that have complete time series for all models and variables and are weighted according to the surface area per grid cell.

2100. In the regions of interest, $\overline{T_{\max}}$ divergence is increasing twice as fast. Even though the shaded regions denote an increasing uncertainty in the $\overline{T_{\max}}$ divergence, the models agree that both globally and regionally $\overline{T_{\max}}$ will increase faster than the mean warm-season temperature (Supplementary Figure 6.A6a).

ELI trends differ more strongly in magnitude across the regions of interest as the $\overline{T_{\max}}$ divergence trends (Figure 6.2b), even though they are also robustly positive across individual models (Supplementary Figure 6.A6b). This indicates different contributions of the ELI to the observed $\overline{T_{\max}}$ divergence trends; while the ELI contribution is particularly strong in NAS and SAM, as can also be seen from the correlations in Figure 6.1c, it is weaker but still considerable in CEU and NAM where probably other processes play a role such as changes in large-scale circulation patterns or boundary layer dynamics.

Further, the effect of ELI trends on $\overline{T_{\max}}$ divergence is even more clear when only regions are included where at least 80% of CMIP6 models agree on the sign of the $\overline{T_{\max}}$ divergence trends. This is evidenced by a stronger increase of ELI in regions with robust trends $\overline{T_{\max}}$ divergence trends (Supplementary Figure 6.A7). ELI trends are even larger for regions with robust and positive $\overline{T_{\max}}$ divergence trends. At the same time no clear trends in ELI are found for regions with robust and negative $\overline{T_{\max}}$ divergence trends. This suggests that factors other than evaporative

cooling, such as changes in circulation, render the $\overline{T_{\max}}$ divergence trends negative in these regions.

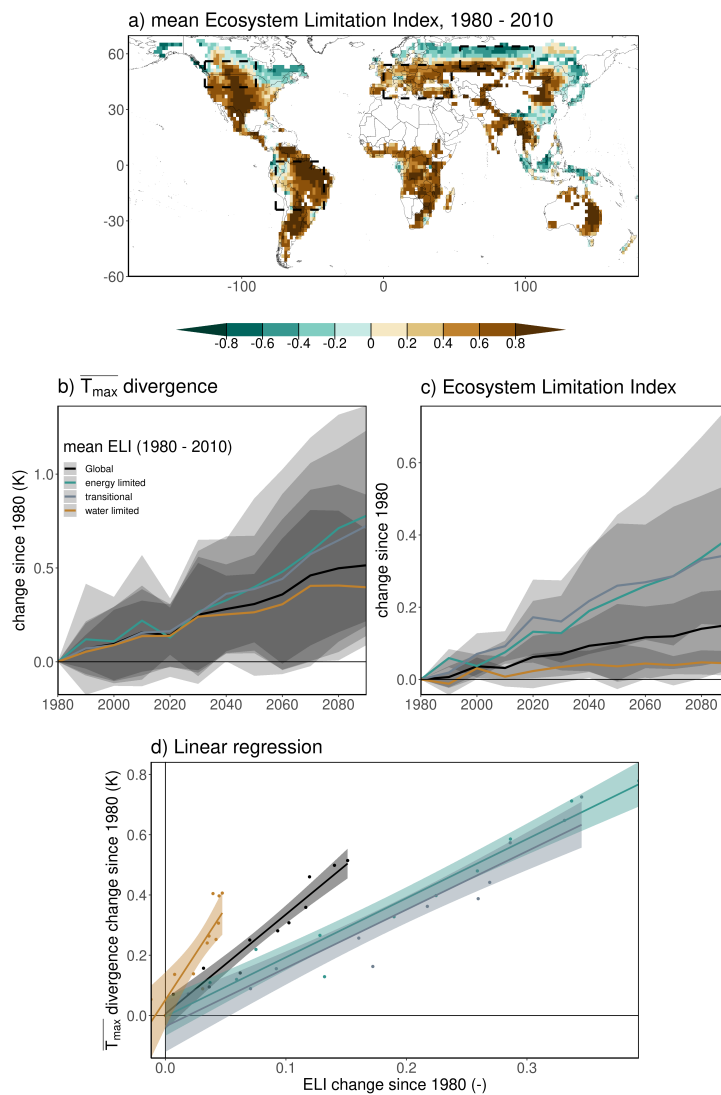


Figure 6.3: Relation between maximum temperature divergence and ecosystem water limitation.

a) Multi-model means Ecosystem Limitation Index (1980 - 2010). Solid lines depict the time series of multi-model means inferred from globally (black) and regionally (colored) decadal averaged model simulations for a) $\overline{T_{\max}}$ divergence and b) Ecosystem Limitation Index, where shaded regions cover ± 1 multi-model standard deviation. The classification is defined based on the model-specific mean ELI over 1980 - 2010 (Supplementary Figure 6.A8): Energy limited ($ELI < -0.2$), transitional ($-0.2 < ELI < 0.2$) and water limited ($ELI > 0.2$). d) Points denote the global (black) and regional (colored) decadal multi-model means of ELI (x-axis) and $\overline{T_{\max}}$ divergence (y-axis), expressed as change since 1980. The lines denote linear regressions, with a shaded colored 95% confidence interval. Only land grid cells that have complete time series for all models and variables are considered. Global and regional averages are weighted according to the surface area per grid cell.

To test this hypothesis, we classify all grid cells based on their respective mean ELI over 1980 - 2010 (Figure 6.3a) to define energy-limited ($ELI < -0.2$), transitional ($-0.2 < ELI < 0.2$) and water-limited ($ELI > 0.2$) conditions. We analyze $\overline{T_{max}}$ divergence trends across these three regimes and find that over initially water-limited areas they are below the global average, while trends over initially transitional or energy-limited areas are above the global average (Figure 6.3b). This is against our initial expectation but can be explained by the corresponding ELI trends which are much more pronounced in energy-limited regions (Figure 6.3c), leading to more often occurring water-limited conditions in these areas. Moving beyond trends we also analyze the sensitivity of decadal $\overline{T_{max}}$ divergence with respect to ELI and find the strongest relationship in the case of water-limited regions (Figure 6.3d). This confirms that the relatively weak impact of ELI trends on $\overline{T_{max}}$ divergence trends in these regions are related to the small ELI trends rather than a lack of physical coupling.

To quantify the strength of the relationships displayed in Figure 6.3d we compute correlations for the relationships shown for the three regimes, respectively (Supplementary Figure 6.A9a). This highlights again the stronger link between ELI and $\overline{T_{max}}$ divergence in initially energy-limited areas resulting from the strong ELI trends moving these areas towards water-limitation. In order to study the relevance of spatial variability across the grid cells that are initially energy- or water-limited or transitional for the correlation estimates, the grid-specific time series of $\overline{T_{max}}$ divergence and ELI are bootstrapped (Methods) and displayed as boxplots in Supplementary Figure 6.A9a, with overall similar results. Substantial variability exists across model-specific correlations (Supplementary Figure 6.A9b,c). Although they generally agree on the sign of the correlations, the magnitude of ELI contribution to $\overline{T_{max}}$ divergence differs strongly, possibly relating to different representations of land-atmosphere coupling and resulting differences in initial ELI states and trends (Figure 6.2 and 6.A8).

In order to further analyze the role of the magnitude of ELI trends for the coinciding $\overline{T_{max}}$ divergence trends, we group the global grid cells with respect to their ELI trends and show the multi-model mean and model-specific $\overline{T_{max}}$ divergence trends (Figure 6.4). Higher $\overline{T_{max}}$ divergence trends correspond with stronger increasing ELI trends. Such strong increases in ELI indicate more often occurring water-limited conditions, potentially also during heat wave events, such that $\overline{T_{max}}$ divergence gets more sensitive to ELI. Analyzing results from individual models shows that stronger ELI trends are associated with stronger trends in $\overline{T_{max}}$ divergence in almost all models, albeit with substantial variability between individual models, owing to different representations and strength of land-atmosphere coupling. Again, we re-compute ELI using surface net radiation instead of air temperature in this context (Figure 6.A10) and find very similar results, underlining the existence of an actual rather than spurious relationship between trends in $\overline{T_{max}}$ divergence and ELI.

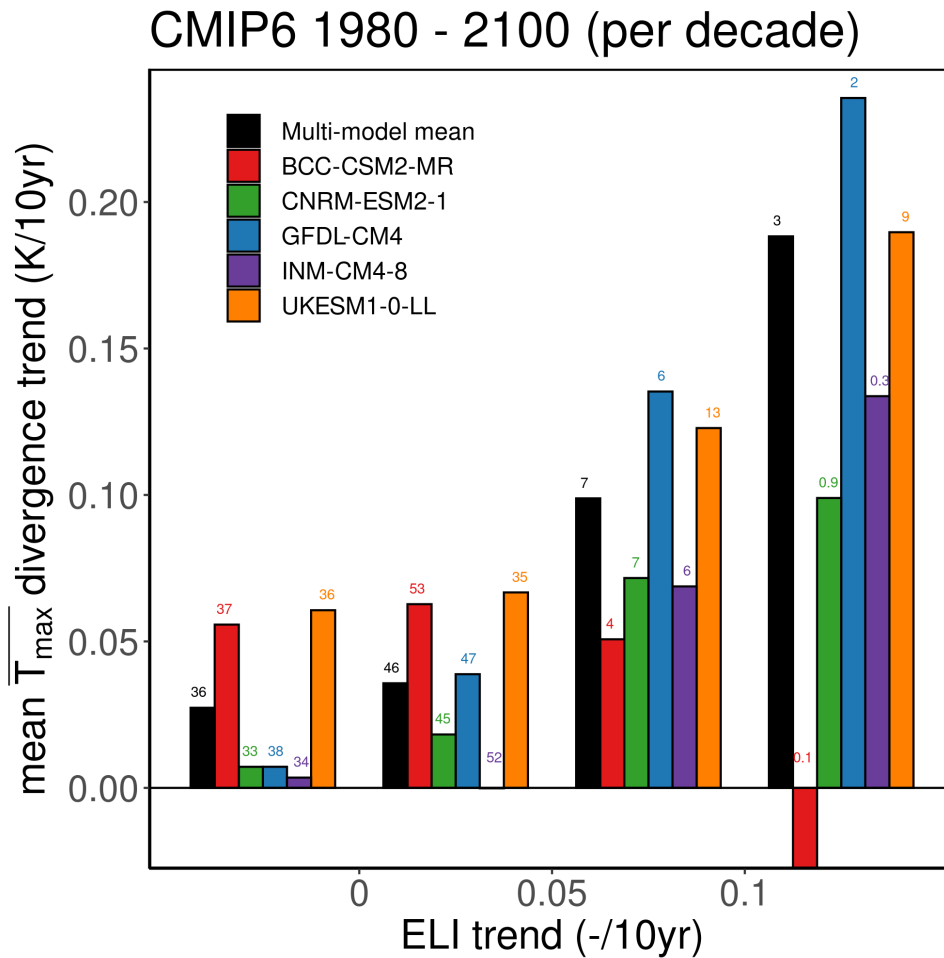


Figure 6.4: Maximum temperature divergence trends increase with stronger trends in ecosystem water limitation. The bars denote the multi-model mean and model-specific $\overline{T_{\max}}$ divergence trends (y-axis) binned according to their respective ELI trends (x-axis) for the multi-model mean trends (black) and all individual models (colors). The numbers display the fraction of warm vegetated land area in which respective $\overline{T_{\max}}$ divergence and ELI trends occur and do not add up to 100%, because there might be ELI trends outside of the defined classes.

6.3.7 Discussion

While the link between ELI and heat wave temperatures is robust across models, we find substantial differences between individual models in terms of the strength of this link (e.g. Figure 6.4 and Supplementary Figures 3, 6, 9, 10). This is related to a different representation of land-atmosphere interactions in general, which is related to e.g. different vegetation water stress functions, soil moisture layers and depths, as well as different underlying soil and vegetation types and related traits. Another reason is that measurements of soil moisture and terrestrial evaporation are scarce, such that large-scale observational constraints for these key quantities have been lacking and are only recently available following the advent of machine-learning techniques to

efficiently interpolate global gridded datasets from the available in-situ measurements (Jung et al., 2019; O and Orth, 2021). On the other hand, surface air temperature extremes from CMIP5 and CMIP6 compare well with observation-based data sets, albeit with model-specific performance that varies in space and time (Thorarinsdottir et al., 2020).

However, despite the apparent difficulty that Earth System Models experience with representing soil moisture trends and related trends in land-atmosphere processes (Albergel et al., 2013b; Berg and Sheffield, 2018; Berg et al., 2017; Greve et al., 2019), widespread shifts towards water limitation are robustly projected (Figure 6.1; (Denissen et al., 2022b)). Further highlighting the complex nature of land-atmosphere interactions, we note that ecosystem water limitation is not only affected by climate, but also by changes in vegetation physiology (e.g. stomatal regulation) and structure (e.g. LAI) in response to increasing carbon dioxide (CO_2) (CO_2 fertilization; (Donohue et al., 2013; Ukkola et al., 2016; Zhu et al., 2016)), which has also been shown to modulate heat extremes (Lemordant and Gentine, 2019). This way, changes of both CO_2 and climate jointly affect ELI which in turn influences heat wave magnitudes. Given this situation, future research should focus on the link between ELI and heat wave intensities using observation-based datasets, particularly as longer-term interpolations or reconstructions of key variables become available. This can help to corroborate our model-based findings, and to constrain the variable relevance of ELI across models.

Finally, we focus on the intensity of the heat extremes by considering temperature only rather than more impact-relevant indices. Heat stress for humans is dependent not only on temperature, but also on wind speed and humidity (Buzan and Huber, 2020; Matthews, 2018). Through reduced evaporative cooling and increased entrainment of dry air above the atmospheric boundary layer, the lethality of heat extremes above dry soils can be reduced (Wouters et al., 2022). In this study, we find an increasing $\overline{T_{\max}}$ divergence alongside increasing EF in 20% of the warm vegetated land area (Supplementary Figure 6.A6b), which suggests potentially higher heat stress than reflected by temperature alone as terrestrial evaporation can increase humidity and related lethality. On the other hand, combined hot and dry conditions can lead to increased wildfires (O et al., 2020b) and can be associated with severe impacts on agriculture and infrastructure. In that perspective, our results on the correspondence between increased ecosystem water limitation and amplified heat waves confirm findings from Teuling (2018) indicating that droughts in Europe will become hotter under future warming. This is in line with future projections, suggesting that concurrent hot and dry extremes will continue to increase in future (Seneviratne et al., 2021; Vogel et al., 2020).

In conclusion, we show an increased relevance of the land surface to modulate the intensity of future heat waves. In this context we focus on novel indices by focusing on ecosystem water limitation and the temperature divergence between warm-season mean and maximum temperatures. This way, we find a widespread increase in $\overline{T_{\max}}$ divergence in $\sim 77\%$ of our study area. We identify several regions of interest where $\overline{T_{\max}}$ divergence is increasing more rapidly than the global mean. These increases are partly related to trends towards ecosystem

water limitation which lead to reduced evaporative cooling. Thereby, the relevance of trends in ecosystem water limitation for trends in $\overline{T_{\max}}$ divergence depends on (i) the magnitude of the ELI trends, which is largest in initially energy-limited and transitional areas, and (ii) the initial ELI regime as (maximum) temperatures are more sensitive to evaporative cooling in a water-limited regime. These findings corroborate earlier research which demonstrated the relevance of soil moisture to (future) heat extremes via its control on surface flux partitioning based on idealized Earth system model experiments in which long-term soil moisture trends are artificially compensated (Fischer et al., 2007; Schwingshackl et al., 2018; Seneviratne et al., 2006; Vogel et al., 2017; Vogel et al., 2018). While our analysis cannot disentangle the direction of causality between land surface dynamics and heat extremes to the same extent, it benefits from fully coupled simulations with unperturbed water balances, such that it effectively complements the existing body of research. Finally, identifying regions where ELI trends and related evaporative cooling are important for future heat extremes can inform long-term adaptation strategies. Human activities play a key role here, as we can implement agricultural practices and/or tillage, irrigation and land cover management, afforestation and city greening to mitigate the impact of heat extremes (Schwaab et al., 2021; Sillmann et al., 2017).

6.A Appendix

This appendix represents the supplementary materials of the presented publication.

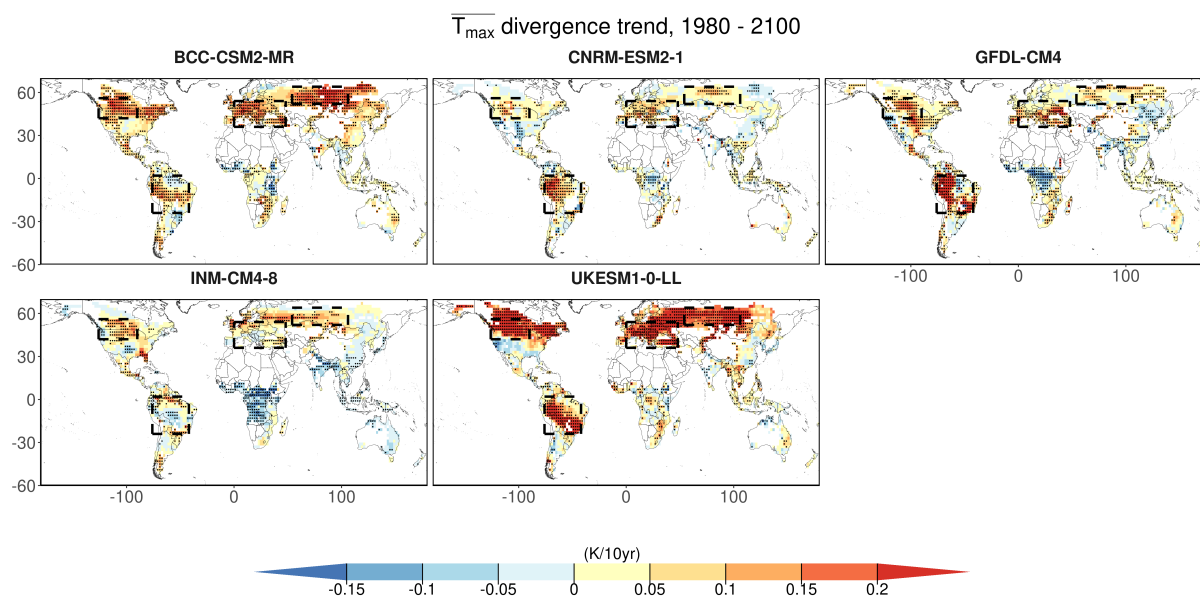


Figure 6.A1: Trends of maximum temperature divergence for individual CMIP6 models. The model-specific trends across decadal $\overline{T_{\max}}$ divergence time series (dots indicate significance: $p < 0.05$ based on Kendall's tau statistic).

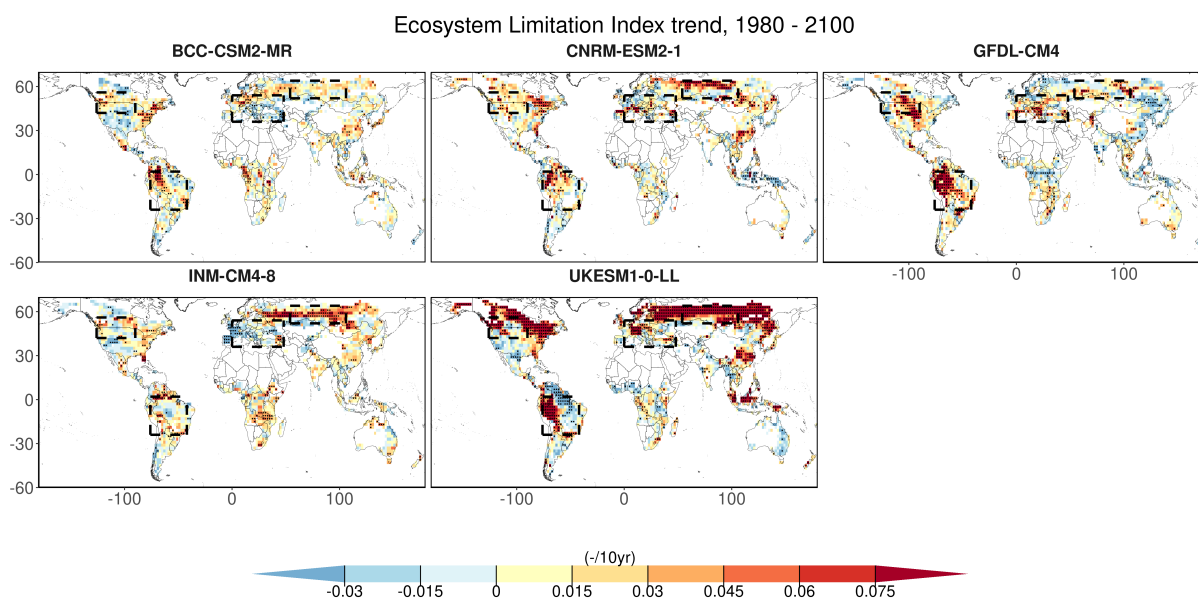


Figure 6.A2: Trends in ecosystem water limitation for individual CMIP6 models. The models-specific trends across decadal ELI time series (dots indicate significance: $p < 0.05$ based on Kendall's tau statistic).

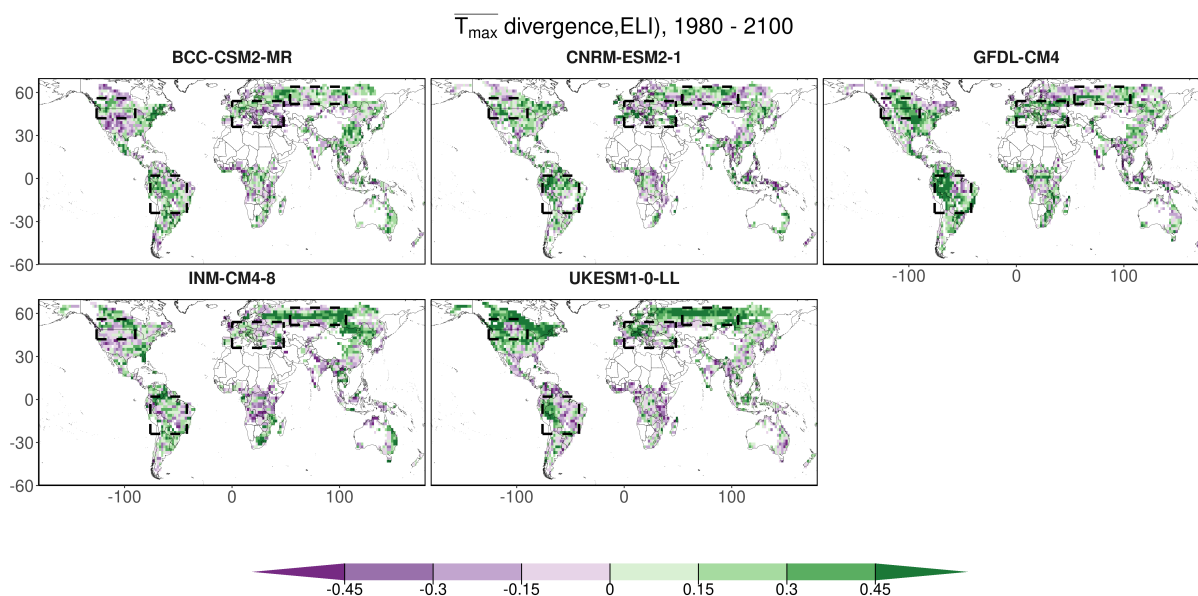


Figure 6.A3: Kendall's rank correlation coefficient between ecosystem water limitation and maximum temperature divergence per individual CMIP6 model.

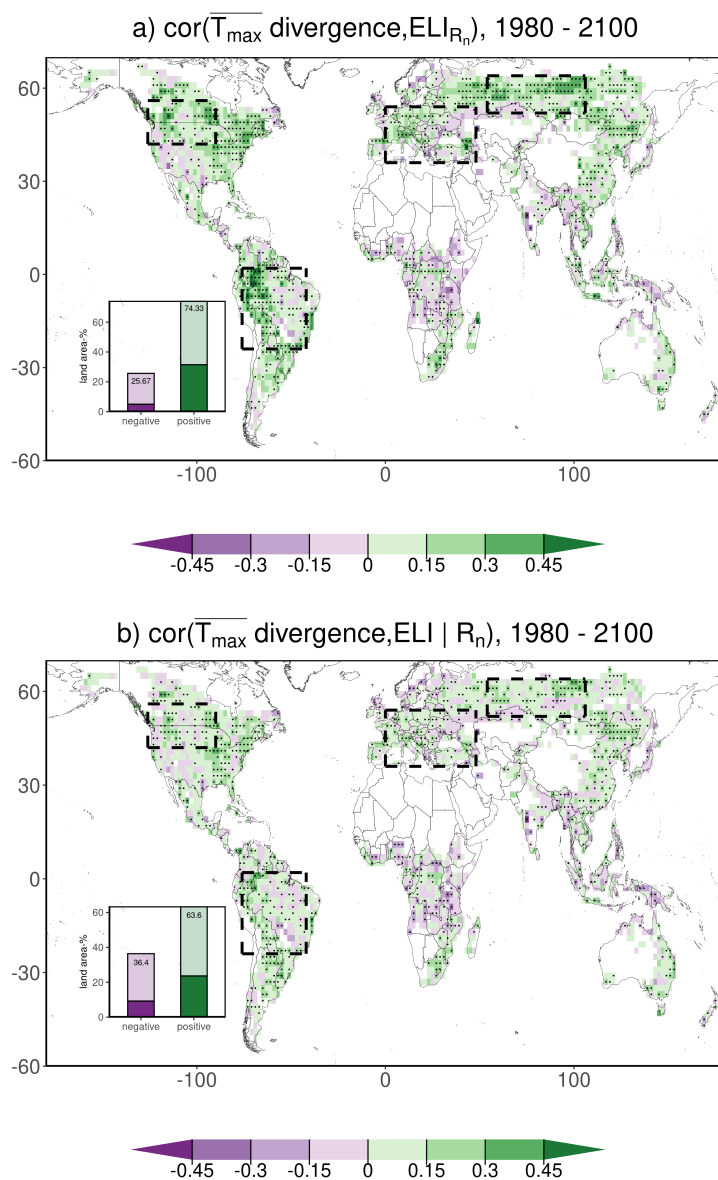


Figure 6.A4: Kendall's rank correlation coefficient between multi-model mean decadal time series of ecosystem water limitation and maximum temperature divergence. a) The ELI has been calculated with anomalies of surface net radiation instead of air temperature. b) The confounding effect of surface net radiation has been excluded from the correlation between $\overline{T_{\max} \text{ divergence}}$ and ELI.

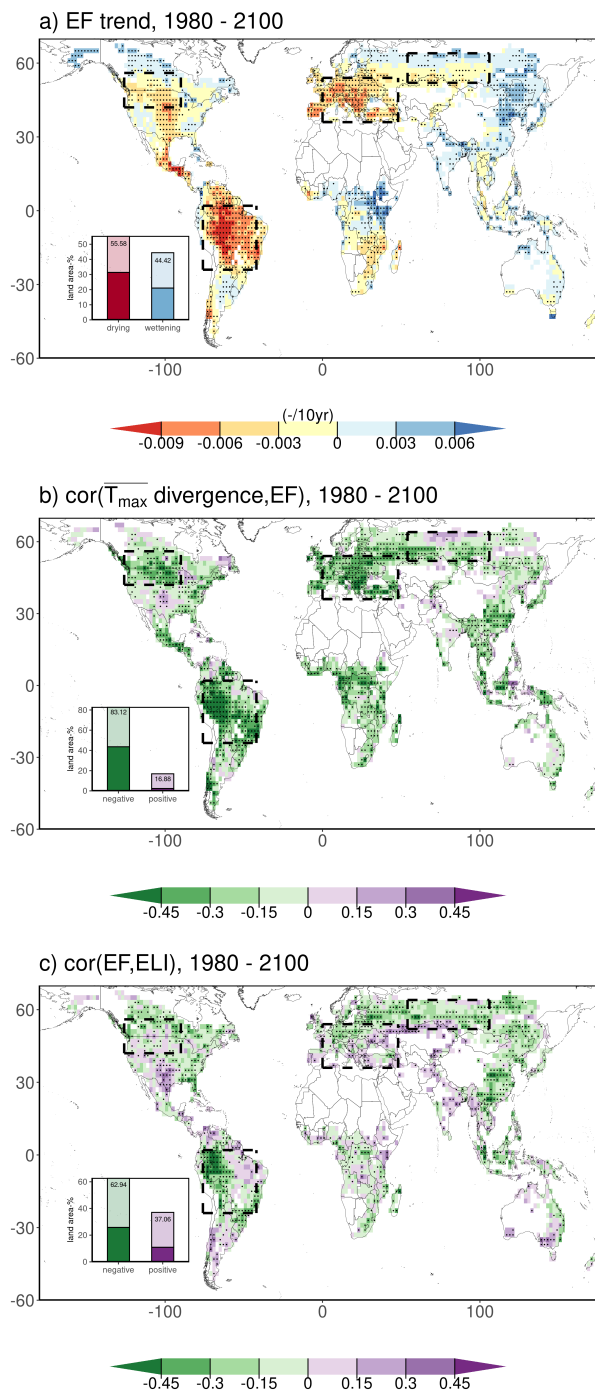


Figure 6.A5: Global multi-model mean distribution and trends of Evaporative Fraction (EF). Multi-model mean of trends based on decadal time series per respective CMIP6 model of a) EF and b) Ecosystem Limitation Index (ELI). c) Multi-model mean of Kendall's rank correlation coefficient between model-specific time series of ELI and $\overline{T_{\max} \text{ divergence}}$. The insets display the fraction of the warm land area that with positive or negative trends or correlations, respectively (at least 4 out of 5 models agreeing on the sign of the trend or correlation are hues darker). Stippling indicates that at least 4 out of 5 CMIP6 models agree on the sign of the trend or correlation. All trends and correlations are calculated over the three hottest months-of-year, defined as the 3 months-of-year which have the highest average temperature over 1980 - 2100. The dashed boxes indicate regions of interest.

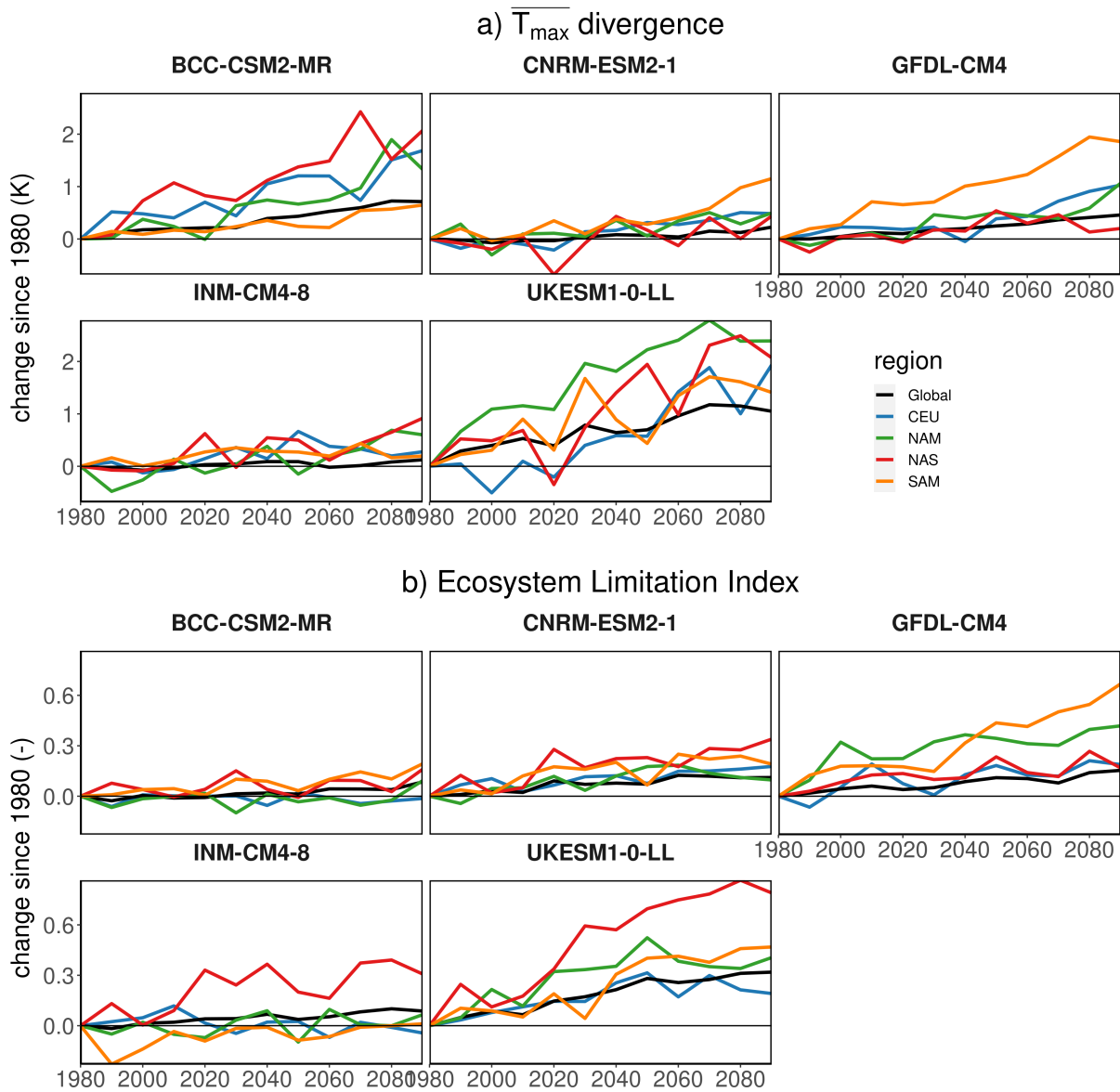


Figure 6.A6: Model-specific changes in global and regional maximum temperature divergence in line with increasing ecosystem water limitation. Temporal evolution of a) $\overline{T_{\max}}$ divergence and of b) Ecosystem Limitation Index (ELI) globally and for the regions of interest. Solid lines depict global and regional time series, where shaded regions cover ± 1 multi-model standard deviation. Global averages are calculated over land grid cells that have complete time series for all models and variables and are weighted according to the surface area per grid cell.

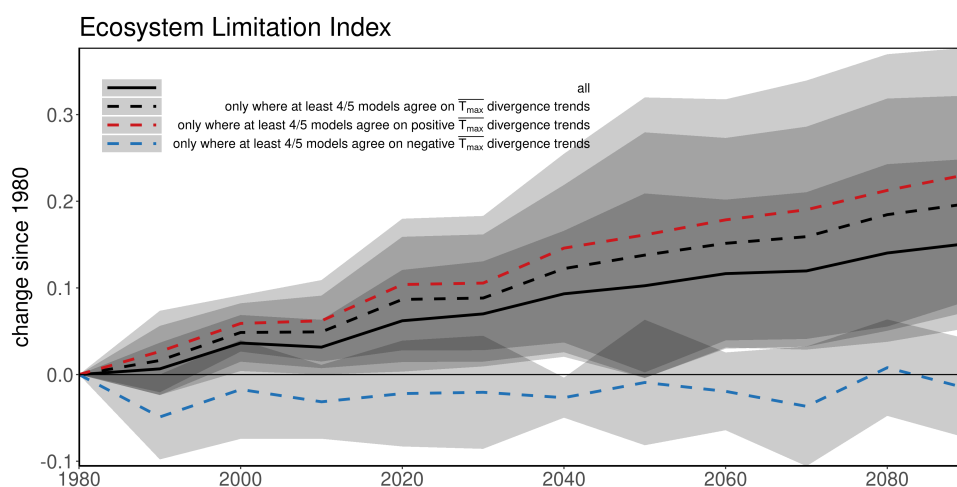


Figure 6.A7: Contrasting trends of ecosystem water limitation from areas with different robustness of maximum temperature divergence. All lines depict multi-model mean time series inferred from the model-specific time series, where shaded regions cover ± 1 multi-model standard deviation. The solid black line is the same as in Figure 6.2b. The colored dashed lines only consider grid cells where at least 4 out of 5 CMIP6 models agree on $\overline{T_{\max}}$ divergence trends of either sign (black), positive (red) or negative (blue).

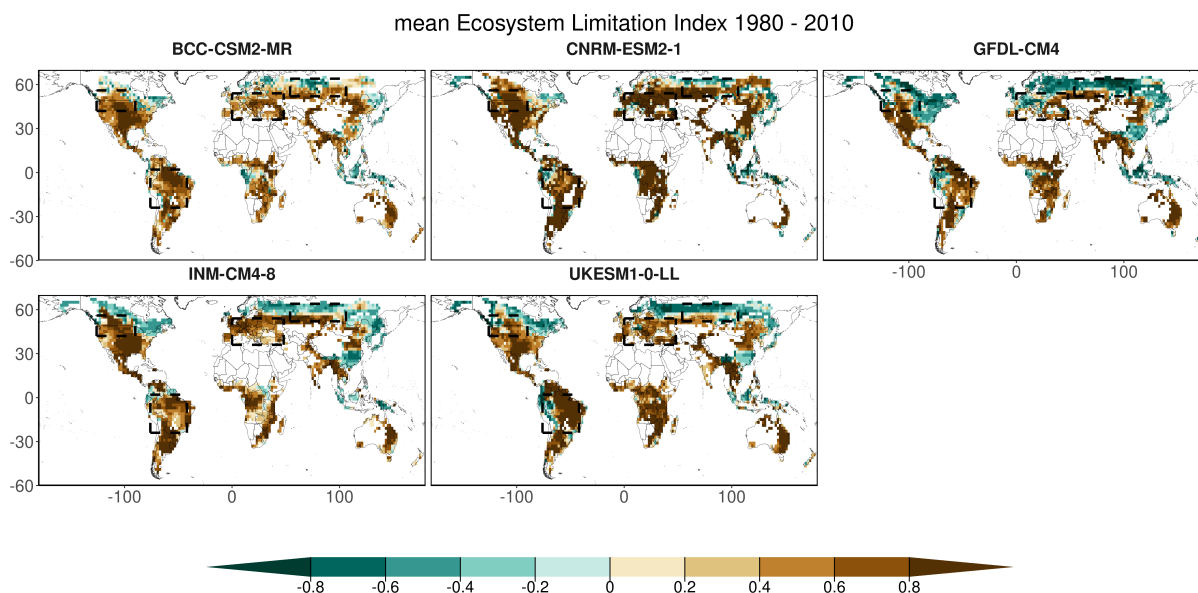


Figure 6.A8: Model-specific initial ecosystem water limitation. Model-specific initial ELI averaged across 1980 - 2010.

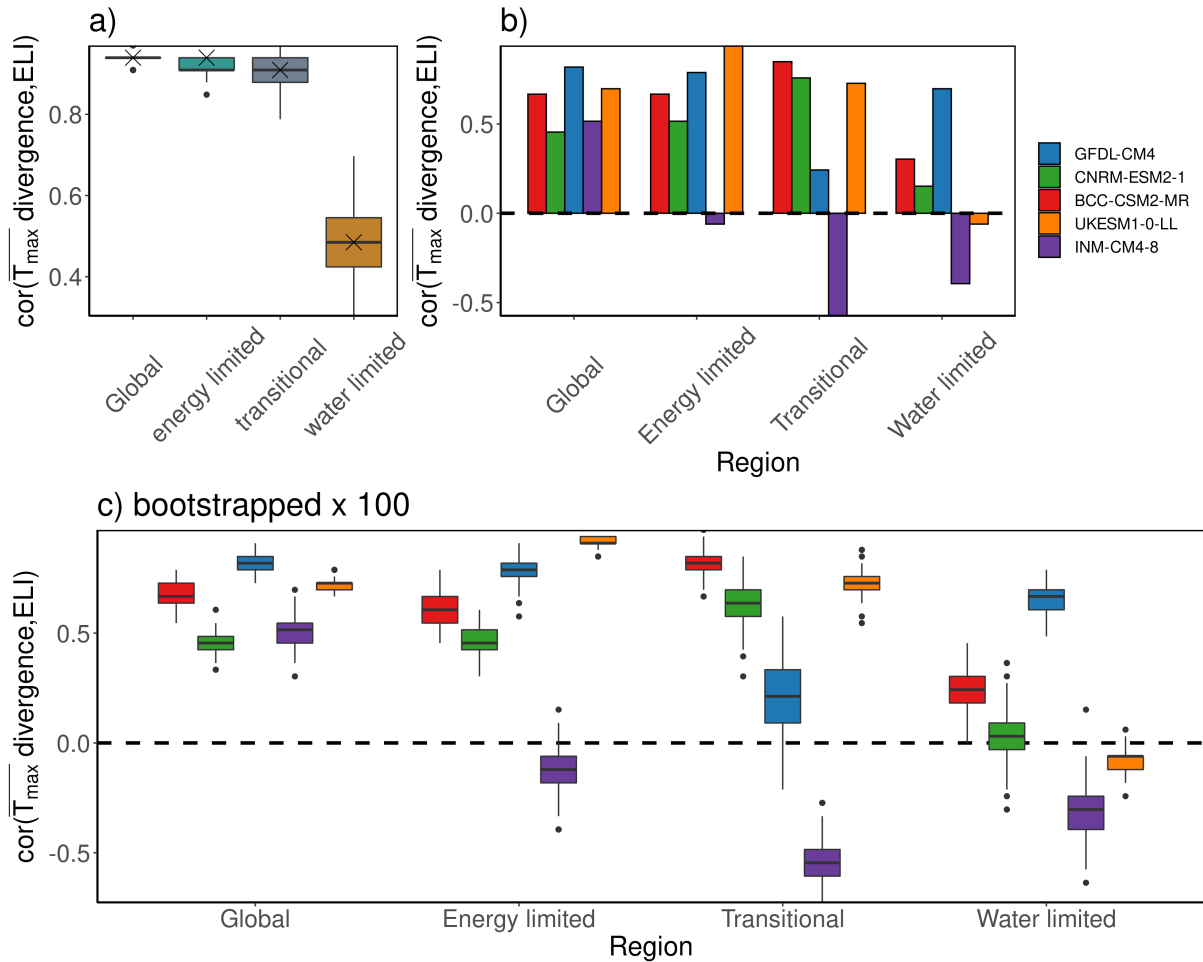


Figure 6.A9: Model-specific global and regional correlations between maximum temperature divergence and ecosystem water limitation. a) Correlations between decadal multi-model and regionally averaged time series of $\overline{T_{\max}}$ divergence and ELI, where crosses denote the correlation based on the original data and the box plots denote the uncertainty as obtained from bootstrapping (Methods). b) Barplots of correlations between decadal regionally averaged time series of $\overline{T_{\max}}$ divergence and ELI. c) The same as panel b), but with a hundred estimates obtained from bootstrapping. The regions are defined based on the mean ELI (1980 - 2010; Supplementary Figure 6.A8): Energy limited ($\text{ELI} < -0.2$), transitional ($-0.2 < \text{ELI} < 0.2$) and water limited ($\text{ELI} > 0.2$).

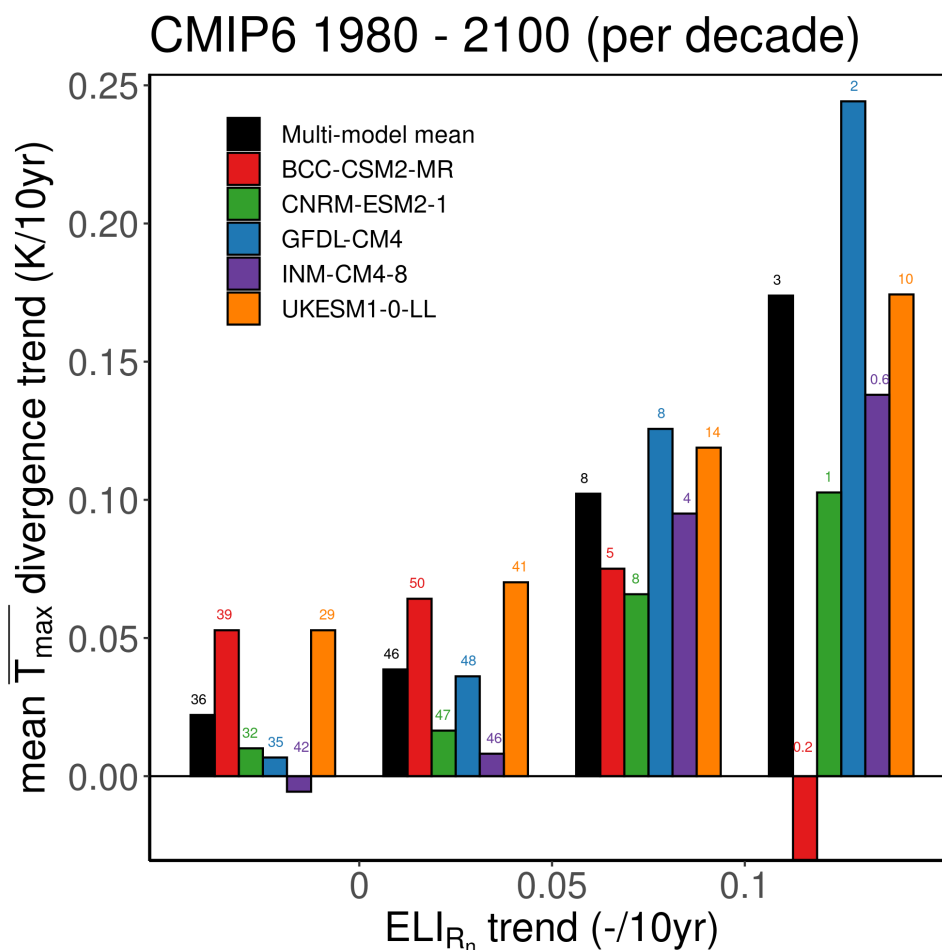


Figure 6.A10: Maximum temperature divergence trends increase with stronger trends in ecosystem water limitation. Note that the ELIRn has been calculated with surface net radiation anomalies instead of air temperature. The bars denote the multi-model mean and model-specific $\overline{T_{\max}}$ divergence trends (y-axis) binned according to their respective ELI trends (x-axis) for the multi-model mean trends (black) and all individual models (colors). The numbers display the fraction of warm vegetated land area in which respective $\overline{T_{\max}}$ divergence and ELI trends occur.

Chapter 7

Synthesis

7.1 Introduction

Vegetation plays a vital role in the global carbon, energy and water cycles through stomatal regulation of plant transpiration (Berg and Sheffield, 2019b; Gentine et al., 2019; Good et al., 2015; Humphrey et al., 2021; Lawrence et al., 2007; Schlesinger and Jasechko, 2014). As such, the interplay between vegetation activity and its dominant drivers, the availability of energy and water, is a key component to understand the land-atmosphere interactions that affect our weather and climate (Guilod et al., 2015; Hirschi et al., 2011; Koster et al., 2016; Koster et al., 2004; Taylor et al., 2012; Zhou et al., 2021) and related extremes (Hauser et al., 2016; Hirschi et al., 2011; Miralles et al., 2014b). Classical drought indices, such as the widely-used Aridity Index, do not accurately capture the role of water availability for vegetation activity (Greve et al., 2019; Greve et al., 2017; Scheff et al., 2021; Scheff et al., 2017) and fail to represent at all the role of energy availability, which closely relates to atmospheric water demand (Novick et al., 2016; Yuan et al., 2019). As the debate on the importance of energy versus water limitation for vegetation activity has not yet been settled (Green et al., 2019; Humphrey et al., 2021; Humphrey et al., 2018; Jung et al., 2010; Jung et al., 2017), it expresses the need for a new perspective on the interactions between energy, water and vegetation and their underlying terrestrial evaporation regimes (Berg and Sheffield, 2018).

In this thesis, I build upon a classical conceptual framework first introduced by Budyko (1974) and later adapted by Koster et al. (2009) and Seneviratne et al. (2010) and move beyond recently introduced inventive indices by Zscheischler et al. (2015) and Berg and McColl (2021) by presenting a novel index, the Ecosystem Limitation Index (ELI), that considers respective relevances of energy and water supply for vegetation activity. This index can be used at the bi-weekly to monthly time and at any spatial scale to distinguish terrestrial evaporation regimes in space and time, both seasonally and in the long-term, spanning decades. Within this context, I highlight the role of soil moisture, as below a certain soil moisture threshold, the critical soil moisture (CSM), the ELI denotes water-limited conditions, both at a continental and the landscape scale. Using various data streams at varying spatial scales underlines the robustness of the ELI with respect to spatial heterogeneity. Soil moisture modulates the surface flux partitioning between these terrestrial evaporation regimes and feeds back into the atmospheric boundary layer (ABL). This can be measured by weather balloons all across the globe, effectively demonstrating characteristic differences between diurnal evolution of the near-surface weather in response to water versus energy limited land surfaces, for the first time, at the landscape scale. At the same time, this emphasizes the need to consider land surface conditions for extreme events, as the prevailing evaporative regime modulates impacts of hydrometeorological hazards on vegetation activity. Finally, I note the importance of land-atmosphere coupling for the magnitude of future heat extremes. In the following sections, I discuss first the specific contributions of the chapters presented in the thesis by answering the research question posed in **Chapter 1** and put these findings in context by comparing with other literature. Thereafter, I discuss which

difficulties are overcome in this thesis and which challenges remain. Further, I suggest several exciting opportunities for future research that emerge from this thesis.

7.2 Specific contributions of this thesis

The specific contributions of this thesis will be explained at the hand of the research questions introduced in **Chapter 1** based on the analyses in **Chapter 2–6**.

7.2.1 What is the role of soil moisture for terrestrial evaporation regimes?

In **Chapter 2**, I explore the role of soil moisture for terrestrial evaporation regimes by introducing a novel index, the ELI, that distinguishes water versus energy-limited regimes and transitions between them. This index arises from the fundamental concepts of water and energy limitation; Under strong water limitation, there is by definition a high sensitivity of terrestrial evaporation (ET) to water availability and a low sensitivity to energy availability. The ELI reflects this by taking correlation as a measure of sensitivity, and moves beyond traditional drought indices through the inclusion of functionally relevant variables (bi-weekly anomalies of soil moisture, air temperature and terrestrial evaporation). I evaluate the ELI at the seasonal time scale using observation-based data over Europe. Both at the landscape and the continental scale, a soil moisture threshold, the CSM, emerges, below which the seasonally averaged ELI denotes water-limited conditions. The CSM is modulated by apparent climate, soil and vegetation characteristics. In itself, estimating the CSM is not novel (Akbar et al., 2018; Feldman et al., 2019; Haghghi et al., 2018; Schwingshackl et al., 2017; Schwingshackl et al., 2018; Seneviratne et al., 2010), but it has not been done before based solely on observation-based data by considering simultaneously the relevance of soil moisture and air temperature for ET. Equipped with this threshold and readily available satellite soil moisture measurements, real-time first-order monitoring of terrestrial evaporation regimes, and consequently the land surface driving the atmosphere or vice-versa, is easily achieved.

The implications of soil moisture and corresponding terrestrial evaporation regimes reach into the ABL, as I show in **Chapter 3**. In this chapter, I use vertical temperature and humidity profiles to initialize a mixed-layer ABL model, Chemistry Land-surface Atmosphere Soil Slab model for Global Studies (CLASS4GL) (Wouters et al., 2019), in the morning and validate it in the afternoon, thereby computing concurrent surface fluxes that reflect heat and moisture input into the ABL and therefore directly affect vertical profiles. I do so by adjusting the morning soil moisture, effectively modulating the partitioning of surface heat fluxes, to match the modeled to the observed vertical profiles of temperature and humidity in the afternoon. I find that (i) the retrieved surface fluxes show similar spatial patterns as other state-of-the-art data sets and (ii) that the scaled soil moistures compare well against satellite-observed surface soil moisture, which validates the land surface schemes applied in CLASS4GL and its findings. As such I provide

an additional method to estimate surface fluxes at the landscape scale, thereby underlining the potential of atmospheric measurements to reflect land surface conditions, which has recently been noted by the eddy covariance (EC) community (Helbig et al., 2020).

7.2.2 How do terrestrial evaporation regimes vary regionally, across seasons and with climate change?

In **Chapter 2**, I apply the ELI together with observation-based data and find a gradient from energy limitation in Northern Europe to water limitation in the Mediterranean, separated by a transitional zone across Central Europe. Especially, the transitional regime is of importance, as it denotes conditions where the evaporative fraction (EF) responds to soil moisture, establishing strong land-atmosphere coupling and related hot spots that can modulate the impact of climate extremes (Koster et al., 2004; Koster et al., 2006; Santanello et al., 2018; Schwingshackl et al., 2018; Seneviratne et al., 2010; Seneviratne et al., 2006). Seasonally, transitional conditions shift from the Mediterranean in the spring to Central Europe in the summer and autumn, as typically soils dry out and energy is abundant due to increasingly long summer days and corresponding gains of incoming radiation.

Widening the focus of variability of terrestrial evaporation regimes to the global and long-term (1980 - 2100) scale, I compute trends of ELI in **Chapter 4** with historical simulations and future projections from a suite of state-of-the-art Earth system models from the Coupled Model Intercomparison Project Phase 6 (CMIP6) (Eyring et al., 2016; O'Neill et al., 2016). Whereas it is fairly certain that these future conditions entail consistently increasing energy availability, in line with global warming (IPCC, 2021), future water availability remains uncertain (Berg and Sheffield, 2018; Berg et al., 2017; Greve et al., 2019; Scheff et al., 2021). Using these CMIP6 data, I find a widespread shift of ecosystem energy to water limitation with climate change, thereby continuing increasing water constraints on vegetation from observations over recent decades (Gampe et al., 2021; Jiao et al., 2021). I identify hot spots with particularly strong trends over forested regions in Northern Eurasia, Canada, the Amazon and Central Europe. In the Northern Hemisphere and in the Amazon, this actually converts energy- into water-limited areas, thereby shrinking even further the energy-limited area across the globe. Further, this uncovers migrations of transitional areas, involving in many areas a shift from energy to water limitation, rendering surface flux partitioning in those areas dependent on soil moisture rather than air temperature or surface net radiation. In addition to this, shifts towards ecosystem water limitation are also induced seasonally, increasing the length of the water-limited season. An attribution analysis suggests a dominant role for air temperature as predictor, but only a full range of variables can explain regional reductions in energy limitation alongside exacerbations of water limitation. This underlines that vegetation functioning and associated terrestrial evaporation regimes are not exclusively influenced by soil moisture. As such, it is critical to reflect respective roles of both energy and water availability. This adds to existing research on determining (future changes in) spatiotemporal variability of terrestrial evaporation regimes (Berg and McColl, 2021;

Koster et al., 2004; Koster et al., 2006; Santanello et al., 2018; Schwingshackl et al., 2018; Seneviratne et al., 2010; Seneviratne et al., 2006), by simultaneously considering energy and water availability for vegetation functioning based on observations, thereby offering a holistic explanation of regional changes in ecosystem function. Generally there is a widespread increase in ecosystem water limitation, but particularly so for several hot spots regions. Identifying these regions is key for developing adaptation strategies, as increasing ecosystem water limitation has far-reaching implications for carbon dioxide (CO₂) sequestration by terrestrial ecosystems, biodiversity losses, shrinking water and food provisions, land degradation and intensity, frequency and duration of extreme events.

7.2.3 How do terrestrial evaporation regimes affect climate extremes?

In **Chapter 3**, I established that diurnal evolution of the ABL develops differently over energy and water limited land surfaces by constraining an ABL model with global weather balloon soundings. More specifically, the afternoon ABL over a water-limited area is on average approximately 3K warmer, 400m higher and 1 kPa drier than over an energy-limited area. As such, local land-atmosphere interactions have implications for the magnitude of temperature and precipitation extremes (Findell et al., 2011; Guillod et al., 2015; Miralles et al., 2014b; Prein and Heymsfield, 2020; Taylor et al., 2012; Vogel et al., 2018).

As plant transpiration is globally the most dominant evaporative process (Berg and Sheffield, 2019b; Good et al., 2015; Lawrence et al., 2007; Schlesinger and Jasechko, 2014), I analyze the role of hydrometeorological hazards for vegetation productivity in **Chapter 5**, where hydrometeorological hazards are defined as water- and/or energy-related extremes inducing vegetation productivity extremes. Whereas other studies tend to focus particularly on singular extreme events, such as heat waves or droughts, and corresponding vegetation productivity reductions and/or use data from models (Ciais et al., 2005; Qiu et al., 2020; Wang et al., 2019; Zhang et al., 2019; Zhao and Running, 2010; Zscheischler et al., 2014a; Zscheischler et al., 2014b; Zscheischler et al., 2013), I use a satellite-observed proxy for vegetation productivity (sun-induced chlorophyll fluorescence (SIF); (Frankenberg et al., 2011; Joiner et al., 2013)) to comprehensively approach these extreme climate-vegetation interactions from an impact perspective: I focus on both minimum and maximum vegetation productivity extremes and check for co-occurring single and compound hydrometeorological hazards, as compound events impose greater risk for terrestrial ecosystems (Sun et al., 2015; Zhou et al., 2019). I find that in about half of the land area with active vegetation, vegetation productivity extremes and hydrometeorological hazards occur simultaneously. More specifically, vegetation productivity extremes in the higher latitudes are temperature-dominated, as minima relate to cold spells and maxima to heat waves. In the (sub-)tropics, vegetation productivity extremes are similarly driven by water-related hazards. Further, I detect areas where vegetation productivity maxima are water-related, but minima are energy-related, which is indicative of frequent transitioning between underlying terrestrial evaporation regimes and corresponding hot spots of strong land-atmosphere coupling (Koster

et al., 2004; Koster et al., 2006; Santanello et al., 2018; Schwingshackl et al., 2018; Seneviratne et al., 2010; Seneviratne et al., 2006). As such, vegetation productivity could have a contrasting response to hydrometeorological hazards, depending on the timing of such an event and the underlying evaporative regime. I provide an observation-based reference of climate-vegetation interactions during extremes, which could serve as a starting point for studies analyzing how such interactions are affected by climate change.

I show such an analysis in **Chapter 6**, where I investigate the role of increasing ecosystem water limitation and corresponding reductions of evaporative cooling for future heat extremes (1980 - 2100) with historical and projected data from the CMIP6 ensemble of Earth system models. In general, heat extremes are influenced by (thermo)dynamical processes (Harrington et al., 2019; Trenberth et al., 2015). Mesoscale weather systems introduce heat extremes through large-scale blocking patterns involving heat accumulating over consecutive dry days (Cassou et al., 2005; Jézéquel et al., 2018). These heat extremes can be further exacerbated by warm and dry air advected from adjacent areas with dry land surfaces and/or entrained from the free-tropospheric above the ABL (Miralles et al., 2014b; Schumacher et al., 2019). In addition, local land-atmosphere interactions exert a crucial influence on the magnitude of heat extremes (Miralles et al., 2012; Quesada et al., 2012; Seneviratne et al., 2010; Teuling et al., 2010; Ukkola et al., 2018; Vogel et al., 2017; Vogel et al., 2018). As such, changes in mean versus maximum daily temperature ($\overline{T_{\max}}$) are driven by different processes; whereas mean temperatures are generally driven by large-scale circulation (Dirmeyer et al., 2021; Donat et al., 2017; Lorenz et al., 2016; Schwingshackl et al., 2018; Seneviratne et al., 2006; Sippel et al., 2017; Ukkola et al., 2018; Vogel et al., 2017), maximum temperatures could be capped by evaporative cooling (Cassou et al., 2005; Miralles et al., 2014b; Schumacher et al., 2019). In this study, I disentangle these processes by normalizing maximum with mean temperatures: $\overline{T_{\max}}$ divergence. I juxtapose the long-term trends of $\overline{T_{\max}}$ divergence to ELI and identify hot spots with accelerated heating of maximum versus mean temperatures, alongside increasing ecosystem water limitation and corresponding reductions in evaporative cooling across Canada, in the Amazon and in Central Europe. The correlation between $\overline{T_{\max}}$ divergence and ELI is most robust in initially energy-limited and transitional areas, where ELI trends are most consistent. Conversely, the largest sensitivity of $\overline{T_{\max}}$ divergence to ELI is found in initially water-limited regions, as there evaporative cooling is most strongly affected by a shift towards ecosystem water limitation, reflected by the ELI.

To summarize, terrestrial evaporation regimes can affect climate and related extremes in different ways: In energy-limited conditions, a heat wave could be dampened by evaporative cooling as a result of this surplus of energy. Consequently, these beneficial conditions can lead to vegetation productivity increases. This is not the case in water-limited conditions, where this surplus of energy does not lead to enhanced evaporative cooling and might further reduce vegetation productivity. In the long-term, I report widespread shifts towards ecosystem water limitation and associated reductions in evaporative cooling, which lead to intensification of heat extremes across several hot spot regions. In these hot spot regions, human interventions, such as agricultural practices and/or tillage, irrigation, land cover management, afforestation and city greening could

help to artificially sustain elevated evaporative cooling to mitigate the worst of the heat extremes to come (Davin et al., 2014; Schwaab et al., 2021; Sillmann et al., 2017).

7.3 Discussion

The following sections put the findings of this thesis into context, reflect on some of the limitations found in the thesis and summarize the efforts made to reconcile these limitations.

7.3.1 Shortcomings of applied data streams

In this thesis, I use a wealth of data from various data streams, including satellite observations (**Chapter 2, 3 and 5**), in-situ observations, such as station soil moisture (**Chapter 2**) and weather balloons (**Chapter 3**), gridded datasets upscaled with machine learning from in-situ observations (**Chapters 2, 3 and 5**), historical simulations from heavily constrained Earth system models (**Chapters 2, 3 and 5**) and future projection from Earth system models (**Chapter 4 and 6**). Although using this plethora of different data products prevents from drawing conclusions based on a limited set of (model) assumptions, these data sets involve several limitations. I discuss here how I overcame several limitations and which remain.

Satellite observations

In **Chapter 1** I stress several implications of using satellite observations. There, I emphasize that some shortcomings related to satellite observations are data product and variable-specific. In the case of satellite-observed surface soil moisture, for example, this introduces uncertainty in the estimation of the CSM in **Chapter 2**, which is affected directly, because it is based on surface soil moisture and indirectly, as surface soil moisture is used as a proxy for water availability in the estimation of ELI. In that study, I show that surface soil moisture is a reasonable proxy for root-zone soil moisture using data from soil moisture stations (Dorigo et al., 2021) and reanalysis models (Dee et al., 2011), which is in line with other findings (Ford et al., 2014; Qiu et al., 2014), albeit with substantial seasonal variability, particularly so during dry conditions (Hirschi et al., 2014; Qiu et al., 2016). Even though I note that variability in the regional average of CSM could exist because of seasonality in climate and vegetation characteristics, it could be amplified by using surface soil moisture: During spring, root-zone soil moisture in Europe is generally abundant after a dark and wet winter, while the surface layer starts drying out due to increased energy availability. As I use surface soil moisture, the CSM is underestimated due to spring drying of the surface layer. The opposite is true in the autumn, when the root-zone is depleted of soil moisture, while precipitation starts occurring more frequently and days become shorter, leading to an overestimation of the CSM based on surface soil moisture. I advise to

use these CSM estimates only on similar spatial scales exclusively based on European Space Agency (ESA) Climate Change Initiative (CCI) surface satellite soil moisture observations.

In **Chapter 5**, I determine vegetation productivity extremes and respective drivers based on satellite-observed SIF. Cloud contamination induces enough noise to prevent any spatially coherent drivers to emerge over the Amazon. In the few grid cells that a statistically relevant driver can be obtained, I find that SIF extremes are radiation-driven, which is in line with other findings for non-extreme vegetation productivity (Green et al., 2020; Li et al., 2021b; Nemani et al., 2003). Further, I apply different vegetation productivity indices such as Global Inventory Monitoring and Modeling System (GIMMS) enhanced vegetation index (EVI) to circumvent this problem, finding a similar pattern of hydrometeorological drivers across climate regimes. The satellite data products applied in these studies are currently the best trade-off between data quality of an observational character and sufficiently long data records. More recent satellite initiatives, such as soil moisture from the Soil Moisture Active Passive (SMAP) mission and SIF from the TROPospheric Monitoring Instrument (TROPOMI) are promising in that they provide high-resolution observations and, as their records grow longer, will soon be the state-of-the-art (Entekhabi et al., 2010; Köhler et al., 2018).

In-situ observations and gridded upscaled data products from machine learning

The analysis in **Chapter 3** could only be carried out with sites where balloon sounding measurements were actually available. The amount of sounding days available per station varies between 1 and 268 out of a total of 4236. The determination of the breakpoint in the piecewise-linear regression, the CSM, is biased in the first place towards the stations with available balloon soundings and in the second place to the stations and their respective climate, soil and vegetation characteristics that deliver more sounding days. Other uncertainties include variability in balloon sounding footprints, due to varying wind speeds- and directions between stations and sounding days. To prevent the CSM estimation to be biased by the soil and vegetation characteristics at the few stations with the majority of the soundings, the entire collection of sounding days is randomly resampled a 1000 times, leading to 50% of the CSM estimates falling within the range of $.19-.23 \text{ m}^3 \text{ m}^{-3}$.

In **Chapter 2**, I use FLUXCOM ET to distinguish terrestrial evaporation regimes and the CSM in Europe, focusing on the warm season (air temperature $> 10^\circ\text{C}$). As such, erroneous data related to cold extremes and regions with less densely EC distributed towers are excluded from the analysis (Pastorello et al., 2020). Extremely dry and hot conditions are still retained in the analysis, but are outweighed by mean-climate conditions. Even so, there might be other limitations specifically relevant for FLUXCOM ET, which are reconciled by applying other proxies for ET, such as satellite-observed Normalized Difference Vegetation Index (NDVI) and SIF, yielding similar CSMs. I address a similar issue in **Chapter 5**, where I use reanalysis

alongside and machine-learning based estimates of surface and root-zone soil moisture, finding similar results (Muñoz-Sabater et al., 2021; O and Orth, 2021).

Earth system models

In **Chapter 4 and 6**, I use historical simulations and future projections from several Earth system models (1980 - 2100) and find spatial patterns of shifts towards ecosystem water limitation, identified by increasing trends of ELI, and related amplification of heat extremes across large areas. The purpose of using an ensemble of Earth system models is to prevent a unique set of model assumptions to bias our findings. Still, validation of our findings based on model simulations is necessary. Whereas there is no way to validate the future projections, this is possible for the spatial patterns from historical simulations. I only partly resolve this by deriving spatial ELI patterns using a similar methodology based on satellite observations over Europe (**Chapter 2**), albeit at the $0.5^\circ \times 0.5^\circ$ spatial scale and using bi-weekly anomalies from 2007 - 2015, which roughly confirm model-based spatial patterns of terrestrial evaporation regimes in Europe. Performance varies between models and depends on respective implementation of dynamic vegetation, CO₂ fertilization effects (Kolby Smith et al., 2016; Winkler et al., 2021; Zhu et al., 2016), water use efficiency (Donohue et al., 2013; Ukkola et al., 2016), development of deeper root systems (Fan et al., 2017; Smith-Martin et al., 2020) and nutrient availability (Peñuelas et al., 2017; Peñuelas et al., 2013). Because of these and other factors, Earth system models struggle to accurately represent transitions between terrestrial evaporation regimes (Best et al., 2015; Dirmeyer et al., 2018; O et al., 2020a), which calls for more comprehensive research. In addition to validation of model-based spatial ELI patterns, direct validation of heat extreme amplification is lacking in this thesis, although (i) temperature variables from Earth system models are typically better constrained, such that surface air temperature extremes from CMIP5 and CMIP6 models compare well against observations (Thorarinsdottir et al., 2020) and (ii) observations of recent decades also indicate accelerated heating of hot temperature extremes (Quesada et al., 2012; Seneviratne et al., 2014). Moreover, other studies use different methodologies and/or model experiments to find amplified heat extremes to continue in the future (Seneviratne et al., 2021; Vogel et al., 2020; Wiel and Bintanja, 2021) and link these increases to changes in terrestrial evaporation regimes and related reductions in evaporative cooling (Fischer et al., 2007; Schwingshackl et al., 2018; Seneviratne et al., 2006; Vogel et al., 2017; Vogel et al., 2018; Wiel et al., 2021).

Further, the model output from the Earth system models that are heavily constrained by observations has (partly) been shaped by model assumptions, albeit with higher uncertainties for variables that have scarce or poor quality observations, such as root-zone soil moisture and surface heat fluxes (Beck et al., 2021; Muñoz-Sabater et al., 2021). Because of this, other data sets have been applied as well in **Chapters 2, 3 and 5**, which might be subject to a different set of measurement errors and/or modelling assumptions. The same strategy cannot be applied when using projections of future climate conditions from the CMIP6 ensemble (Eyring

et al., 2016; O'Neill et al., 2016), which makes this issue difficult to address. However, as a first-order validation, I find that global averages of ET closely resemble other state-of-the-art observation-based estimates of ET in 4 over historical time periods. Further, I rely on initiatives from the scientific community (i) to comprehensively collect, harmonize and distribute model output for plug-and-play climate analyses, such as the CMIP6 ensemble (Eyring et al., 2016), and (ii) to run experiments using these models, such as the Global Land-Atmosphere Coupling Experiment-Coupled Model Intercomparison Project phase 5 (GLACE-CMIP5) (Seneviratne et al., 2013), generating valuable model output to study land-atmosphere interactions and (iii) to validate these model findings and pinpoint weaknesses necessary for model improvement.

7.3.2 Spatiotemporal variability of climate-vegetation interactions

It is important to reconcile smaller and larger spatial and temporal scales, as climate-vegetation interactions are known to vary substantially across spatiotemporal scales (Linscheid et al., 2020). More specifically, the ET and the related ELI are governed by different processes across different scales: Spatially, ranging from sub-grid scale land surface heterogeneity, irrigation practices or shallow cumulus clouds shadowing the land surface (Pedruzo-Bagazgoitia et al., 2017), to mesoscale weather systems and temporally, ranging from the diurnal cycle of radiation, approximately bi-weekly occurring mesoscale weather systems and possibly related extreme events, to intra-annual atmospheric oscillations and longer-term effects related to intrinsic ecosystem dynamics, climate change induced trends in atmospheric CO₂, energy and water availability and nutrient limitation. As such, drivers of ET also vary across spatiotemporal scales. As we focus on bi-weekly and monthly anomalies of ET and its drivers, we exclude effects of synoptic weather variability. Further, these are the time scales that ET is most sensitive to soil moisture (Boese et al., 2019; Teuling et al., 2006). Especially at the larger spatial scales used throughout this thesis small-scale variability in soil and vegetation characteristics that are relevant for estimates of ET and its drivers average out. For example, in **Chapter 5**, I use SIF as a proxy for vegetation productivity: gross primary productivity (GPP). While at large spatiotemporal scales the SIF-GPP relation appears linear (Frankenberg et al., 2011; Guanter et al., 2012; Joiner et al., 2013), it breaks down at smaller scales (He et al., 2020; Magney et al., 2020; Maguire et al., 2020; Marrs et al., 2020; Wohlfahrt et al., 2018), inducing noise in the relation. Furthermore, our findings can also be biased by the intrinsic time signature of the considered vegetation proxy; As EVI relates more to vegetation structure and SIF to physiology, the soil moisture control over EVI is stronger than over SIF, because the act on similar time scales (Turner et al., 2020) (**Chapter 5**). Further, left unconsidered in this thesis are legacy effects of soil moisture, which could be substantial (Orth and Seneviratne, 2012). Although I do not specifically address spatial- and temporal-scale related issues using only one methodology, I partially resolve this by presenting findings at different spatiotemporal scales, ranging from the in-situ to 2.0° x 2.0° spatial scale and the daily to monthly and decadal time scales. However, it

is difficult to conclude on functional spatiotemporal scales for ELI between different chapters, as different observational versus simulated data products are used.

7.3.3 Proxies for energy and water availability and vegetation functioning

The concept of the central index in this thesis, the ELI, is based on the importance of (i) energy and (ii) water availability for (iii) vegetation functioning. Throughout the thesis, I have applied different proxies, which involve several implications. In **Chapters 2, 4 and 6**, I have defined the ELI using air temperature as an energy proxy. While some studies find surface net radiation to be a more accurate energy proxy (Maes et al., 2019), I find generally similar estimates between radiation- versus temperature-based ELI. However, noteworthy are differences in the strength of energy limitation over the tropics, reflected by stronger correlations of terrestrial evaporation with surface net radiation versus air temperature anomalies as an energy proxy, because the tropical multi-layer canopy competes for light resources (Nemani et al., 2003). In boreal regions, ecosystems are likely more temperature limited, but as I exclude cold temperatures (monthly temperature < 10 °C) from the analyses, I partly exclude by construction a stronger temperature limitation in those regions.

Ideally, matric potential would be used as a water proxy as it reflects plant available water irrespective of soil texture. However, large-scale estimates of matric potential involve large uncertainties as the relationship between soil moisture and matric potential is non-linear (Genuchten, 1987). Root-zone soil moisture can also be used as a water proxy, which unfortunately is only available at the desired global coverage from Earth system models. Although observation-based estimates are available from satellites (Dorigo et al., 2017; Entekhabi et al., 2010), the drawback of such observations is that they only represent the soil moisture dynamics in the surface layer (Ulaby, 1982). Other than showing acceptable agreement between seasonally averaged soil moisture between the surface layer and the root-zone in **Chapter 2**, the relevance of surface versus root-zone soil moisture for ELI is still to be studied. Analyses trying to extract a root-zone signature from surface satellite soil moisture observations using data assimilation (Martens et al., 2017; Tian et al., 2019; Tobin et al., 2019) and increasing lengths of satellite data products that estimate root-zone soil moisture (Reichle et al., 2017) could lead to better estimates of water availability and a more accurate representation of water limitation in the near future.

Vegetation indices can be used as a proxy for ET, as the carbon and water cycles are coupled through stomatal conductance (Gentine et al., 2019; Humphrey et al., 2021), although indices can have different characteristics and their quality might deteriorate under specific conditions; Throughout this thesis, terrestrial evaporation (ET), plant transpiration and vegetation indices (GPP, NDVI, EVI and SIF) are used interchangeably as proxies for ecosystem functioning. In **Chapter 2 and 4**, I apply a number of different proxies for vegetation functioning, which generally yield similar CSMs and also generally similar drivers of vegetation productivity during extremes, albeit with stronger water limitation on EVI than on SIF, related to their respective

intrinsic temporal variabilities. Using plant transpiration instead of ET in **Chapter 4** reveals increasing water limitation for ET, whereas plant transpiration does not become increasingly dependent on soil moisture, in line with Berg and McColl (2021), who report no projected dryland expansion. Such details are important to consider, as they might crucially change the take-away message of such research articles. These proxies correlate well on the coarser spatial and temporal scales used in this thesis. However, these correlations might deteriorate approaching higher resolutions (He et al., 2020; Magney et al., 2020; Maguire et al., 2020; Marrs et al., 2020; Wohlfahrt et al., 2018), vouching for analysis ET and vegetation indices and their respective drivers on smaller scales.

7.3.4 Causal inference

Correlation does not imply causality. However, correlative methods are used in every chapter in this thesis to indicate relations between eco-climate variables. In wording, I try to refrain from using terms such as "control" and "drivers" that imply causation. Even if such terms are used, I emphasize that they do not prove causality. Further, confounding effects between the variables involved in the computation of the ELI act on different time scales: These variables might be correlated, simply because they are subjected to similar seasonal cycles and/or trends. Such confounding effects are excluded by detrending and removal of the seasonal cycle by computing anomalies. On longer time scales, co-linearities could exist between the variables that confound long-term ELI trends. To address this, the attribution analysis in **Chapter 4** tries through all combinations of predictors, thereby excluding predictors that carry similar information. Confounding effects can also occur on shorter time scales: Per example, in energy limitation, one would not expect soil moisture to affect terrestrial evaporation in any way. However, as a wet soil moisture anomaly arises from a precipitation event and associated clouds preventing radiation from reaching the land surface, the correlation between soil moisture and terrestrial evaporation could be negative. To assure that the correlations on which our findings are based are meaningful, several steps are taken to (i) avoid spurious relations between variables and (ii) to exclude confounding effects on relations between eco-climate variables. In **Chapter 2**, I exclude the confounding effect of soil moisture on the correlation between air temperature and terrestrial evaporation, as well as the confounding effect of air temperature on the correlation between soil moisture and terrestrial evaporation. Using these individual partial correlations to compute ELI, I retrieve similar CSMs, reflecting limited importance of confounding effects in that analysis. This approach was also used using CMIP6 model data from 1980 - 2100, which revealed a more consistent confounding effect of air temperature on the correlation between soil moisture and terrestrial evaporation than of soil moisture on the correlation between air temperature and terrestrial evaporation, reflecting a globally steady increase in air temperature as opposed to the ambiguity of root-zone soil moisture trends (**Chapter 4**). In **Chapter 5**, spurious correlations between vegetation productivity and hydrometeorological drivers are excluded by filtering negative and insignificant correlations. Further, an additional analysis using only

non-anomalous vegetation productivity yields similar results to Li et al. (2021b), who use a methodology that more robustly excludes confounding effects between hydrometeorological drivers. Finally, in **Chapter 5**, I find similar results based on two approaches, underlining the robustness of the findings. Despite these efforts, correlative methods are still deemed incapable of accurately reflecting causal relation (Krich et al., 2020), which calls for other methods to validate the correlation-based findings and derive the directionality of interactions between eco-climate variables such as the application of causal networks and/or sensitivity experiments with physical models.

7.4 Outlook

In this section, I propose a series of interesting avenues that emerged from the discussion or as an extension of the results presented in the chapters of the thesis.

7.4.1 Determining the functional spatiotemporal scales for ELI and its drivers

The functional drivers behind ELI, ET and related vegetation proxies differ between scales (Linscheid et al., 2020). Although plenty of research is dedicated to determining drivers for specific vegetation indices at specific spatiotemporal scales (Li et al., 2021b; Maes et al., 2019; Zhu et al., 2016) (**Chapter 5**), there is no universal agreement with respect to the most relevant drivers for the diverse range of readily available proxies for vegetation functioning across scales. As such, this calls for a comprehensive analysis of these interactions spanning spatiotemporal scales. Temporal variability can be twofold: Firstly, it is important to consider at what temporal resolution to compute the anomalies necessary for the ELI computation, which can be varied from (sub-)daily to monthly time scales. Secondly, the period over which the ELI is computed could be varied from 5 years to 30, depending on the length of the data records. Spatial resolution could be varied from the highest resolution available to $2.0^\circ \times 2.0^\circ$ grid cell resolution. Satellite-observed proxies for vegetation productivity could include high-resolution SIF from the TROPOMI and EVI from the Advanced Very High Resolution Radiometer (AVHRR) (Zhu et al., 2013). Additionally, longer data records are guaranteed from reanalysis runs, for example from ERA5 and ERA5-Land (Hersbach et al., 2020; Muñoz-Sabater et al., 2021). As air temperature and surface net radiation are well-constrained variables, these could be extracted from such reanalyses. High-resolution satellite observations of surface and root-zone soil moisture are available from the SMAP mission (Entekhabi et al., 2010). At the high-resolution, the soil texture heterogeneity could be resolved (Hengl et al., 2017), such that the matric potential could be computed similar to Fu et al. (2022a), which more closely reflects plant available water. To reveal the causal links between between these eco-climate variables that underly ELI estimates, random forest methods in combination with Shapley Additive Explanations (SHAP) values could be used, similar to Li et al. (2021b). Such analyses could reconcile ongoing debates on the importance of

energy and water availability of different proxies for vegetation productivity (Green et al., 2019; Humphrey et al., 2021; Humphrey et al., 2018; Jung et al., 2010; Jung et al., 2017).

Within this context, another methodological issue remains which might introduce noise in the derivation of ELI. In the supplementary material of **Chapter 4**, I show the derivation of the ELI based on monthly and $2.0^\circ \times 2.0^\circ$ CMIP6 data. More specifically, I use linear detrending over the decade within which ELI is computed, to avoid spurious aliasing of the anomalies. Whereas decadal trends in energy availability are consistent, respective trends of soil moisture and terrestrial evaporation are not, such that resulting decadal trends could be substantially affected when the time frame over which they are considered is shifted by a year. This directly affects the anomaly computation and consequently, the magnitude and/or the sign of the resulting ELI. Different detrending strategies, such as high-pass filters, could prevent such spurious aliasing and might provide more robust ELI estimates.

7.4.2 Changing heat extreme characteristics in response to increasing ecosystem water limitation under climate change

In **Chapter 6**, heat extremes are described only by their intensity, since the used monthly output only includes the hottest day per month. However, climate change will also involve changes in frequency and duration of such events (Seneviratne et al., 2021). In addition to monthly output, many models from the CMIP6 ensemble also have daily output, which allows to assess frequency and the duration alongside the intensity of heat extremes. Moreover, the focus in **Chapter 6** is on the yearly daily temperature maximum, while the role of the land surface in general and the ELI in particular could be even more prominent for rarer heat extremes with longer return periods and amplified impacts (Davin et al., 2014). The daily maximum temperature can be retrieved from the CMIP6 ensemble output, from which heat extreme intensity, frequency and duration can be obtained in combination with a threshold-based method. In the concurrent season, the ELI and related reductions in evaporative cooling can be computed and trends can be computed similar to **Chapter 6**. Further, in addition to temperature, the focus can be shifted to more impact-relevant metrics, as for heat stress concurrent wind speed and humidity during heat extremes are also important (Buzan and Huber, 2020; Matthews, 2018), as reduced humidity during such extremes might even decrease human mortality (Wouters et al., 2022). These analyses could complement the findings presented in **Chapter 6**.

7.4.3 A global gridded dataset from exploiting weather balloon soundings using machine learning

Atmospheric measurements, such as balloon soundings used in **Chapter 3**, provide valuable vertical profiles of pressure, temperature, dewpoint (can be converted to relative humidity), geopotential height and horizontal displacement (wind speed and -direction), which can be used in near-real time to inform Numerical Weather Prediction (NWP) and to constrain Earth system

model simulations (Helbig et al., 2020). Millions of these balloon sounding measurements are collected in the Integrated Global Radiosonde Archive (IGRA) data set (Durre et al., 2006), starting from as early as 1905 to near-real time. At many stations morning and afternoon soundings are available, which effectively contain two snapshots of the ABL, from which the diurnal evolution of the ABL can be estimated using mixed-layer models, such as CLASS4GL (Wouters et al., 2019). Unfortunately, they are sparsely distributed, as these labour-intensive soundings are most often performed over the USA, Europe and Australia. Next to balloon soundings, atmospheric measurements are available from Global Navigation Satellite System (GNSS) radio occultation (RO) data from FORMOSAT-3/COSMIC, however only over the last fourteen years at the daily time scale. Although invaluable for NWP, these data are subject to large errors over regions with large vertical moisture gradients and have limited retrieval in the lower troposphere, or the ABL (Ho et al., 2020). Part of these issues can be resolved with the launch of FORMOSAT-7/COSMIC-2 in 2019. However, these GNSS RO data cannot compete with the length of the balloon sounding records, the accuracy in the ABL and availability of multiple vertical profiles a day.

Similar to other machine-learning based initiatives that exploit in-situ measurements and upscale these to a global gridded data products (Ghiggi et al., 2019; Jung et al., 2019; O and Orth, 2021), the IGRA balloon sounding data set can be further exploited to derive such a gridded data set. In that direction, a deep hybrid model that has been tested against balloon soundings over the US (Grover et al., 2015), yielding promising results. Other machine-learning extensions based on high-resolution climate model output have shown the potential to represent small-scale processes occurring ABL, such as moist convection (Gentine et al., 2018; Rasp et al., 2018). However, such a purely observation-based data set with global coverage is not delivered. Such a data set would comprise of all the target variables measured by balloon soundings (pressure, temperature, dewpoints, geopotential height and horizontal displacement) at the standard pressure heights as stated by the World Meteorological Organization (WMO), that presumably are within the ABL: (1000,) 925, 850 and 700 hPa. Predictors could include observation-based surface soil moisture, temperature, relative humidity, horizontal displacement, precipitation, radiative components, vegetation indices (SIF, EVI, leaf area index (LAI)) and potentially others, if available at the hourly time scale in the same $0.5^\circ \times 0.5^\circ$ as the balloon sounding site. If this method is validated in a satisfactory way, an observation-based global gridded data set of morning and afternoon vertical profiles of all the target variables could be derived. This data set could be used to, for the first time, use an observation-based atmospheric data set to study the diurnal evolution of the ABL on a global scale. A similar methodology as in **Chapter 3** could be used to estimate surface heat fluxes. Next to that, such a data set could be used to quantify the contribution of advection to heat accumulation in the ABL, if the validated machine-learning algorithm would include two versions: one which learns only from predictors locally and one which is allowed to learn from predictors both locally and upwind.

References

- Akbar, R., D. J. S. Gianotti, K. A. McColl, E. Haghghi, G. D. Salvucci, and D. Entekhabi (2018). “Estimation of Landscape Soil Water Losses from Satellite Observations of Soil Moisture”. *Journal of Hydrometeorology* 19.5, 871–889.
- Albergel, C., W. Dorigo, G. Balsamo, J. Muñoz-Sabater, P. de Rosnay, L. Isaksen, L. Brocca, R. de Jeu, and W. Wagner (2013a). “Monitoring multi-decadal satellite earth observation of soil moisture products through land surface reanalyses”. *Remote Sensing of Environment* 138, 77–89.
- Albergel, C., W. Dorigo, R. H. Reichle, G. Balsamo, P. d. Rosnay, J. Muñoz-Sabater, L. Isaksen, R. d. Jeu, and W. Wagner (2013b). “Skill and Global Trend Analysis of Soil Moisture from Reanalyses and Microwave Remote Sensing”. *Journal of Hydrometeorology* 14.4, 1259–1277.
- Anderegg, W. R. L., J. M. Kane, and L. D. L. Anderegg (2013). “Consequences of widespread tree mortality triggered by drought and temperature stress”. *Nature Climate Change* 3.1, 30–36.
- Andreotti, B., A. Fourrière, F. Ould-Kaddour, B. Murray, and P. Claudin (2009). “Giant aeolian dune size determined by the average depth of the atmospheric boundary layer”. *Nature* 457.7233, 1120–1123.
- Arellano, J. V.-G. de, B. Gioli, F. Miglietta, H. J. J. Jonker, H. K. Baltink, R. W. A. Hutjes, and A. A. M. Holtslag (2004). “Entrainment process of carbon dioxide in the atmospheric boundary layer”. *Journal of Geophysical Research: Atmospheres* 109.D18.
- Arora, V. (2002). “Modeling Vegetation as a Dynamic Component in Soil-Vegetation-Atmosphere Transfer Schemes and Hydrological Models”. *Reviews of Geophysics* 40.2, 3–1–3–26.
- Barton, K. (2018). *MuMIn: multi-model inference. R package version 1.40.4*. Accessed on the internet at <https://CRAN.R-project.org/package=MuMIn> on 3 June 2021.
- Beck, H. E., M. Pan, D. G. Miralles, R. H. Reichle, W. A. Dorigo, S. Hahn, J. Sheffield, L. Karthikeyan, G. Balsamo, R. M. Parinussa, A. I. J. M. van Dijk, J. Du, J. S. Kimball, N. Vergopolan, and E. F. Wood (2021). “Evaluation of 18 satellite- and model-based soil moisture products using in situ measurements from 826 sensors”. *Hydrology and Earth System Sciences* 25.1, 17–40.

- Beer, C., M. Reichstein, E. Tomelleri, P. Ciais, M. Jung, N. Carvalhais, C. Rödenbeck, M. A. Arain, D. Baldocchi, G. B. Bonan, A. Bondeau, A. Cescatti, G. Lasslop, A. Lindroth, M. Lomas, S. Luysaert, H. Margolis, K. W. Oleson, O. Roupsard, E. Veenendaal, N. Viovy, C. Williams, F. I. Woodward, and D. Papale (2010). “Terrestrial Gross Carbon Dioxide Uptake: Global Distribution and Covariation with Climate”. *Science* 329.5993, 834–838.
- Berg, A., K. Findell, B. Lintner, A. Giannini, S. I. Seneviratne, B. van den Hurk, R. Lorenz, A. Pitman, S. Hagemann, A. Meier, F. Cheruy, A. Ducharne, S. Malyshev, and P. C. D. Milly (2016). “Land–atmosphere feedbacks amplify aridity increase over land under global warming”. *Nature Climate Change* 6.9, 869–874.
- Berg, A. and K. A. McColl (2021). “No projected global drylands expansion under greenhouse warming”. *Nature Climate Change* 11.4, 331–337.
- Berg, A. and J. Sheffield (2018). “Climate Change and Drought: the Soil Moisture Perspective”. *Current Climate Change Reports* 4.2, 180–191.
- (2019a). “Evapotranspiration Partitioning in CMIP5 Models: Uncertainties and Future Projections”. *Journal of Climate* 32.10, 2653–2671.
- (2019b). “Historic and Projected Changes in Coupling Between Soil Moisture and Evapotranspiration (ET) in CMIP5 Models Confounded by the Role of Different ET Components”. *Journal of Geophysical Research: Atmospheres* 124.11, 5791–5806.
- Berg, A., J. Sheffield, and P. C. D. Milly (2017). “Divergent surface and total soil moisture projections under global warming”. *Geophysical Research Letters* 44.1, 236–244.
- Best, M. J., G. Abramowitz, H. R. Johnson, A. J. Pitman, G. Balsamo, A. Boone, M. Cuntz, B. Decharme, P. A. Dirmeyer, J. Dong, M. Ek, Z. Guo, V. Haverd, B. J. J. v. d. Hurk, G. S. Nearing, B. Pak, C. Peters-Lidard, J. A. Santanello, L. Stevens, and N. Vuichard (2015). “The Plumbing of Land Surface Models: Benchmarking Model Performance”. *Journal of Hydrometeorology* 16.3, 1425–1442.
- Bivand, R., N. Lewin-Koh, E. Pebesma, E. Archer, A. Baddeley, N. Bearman, H.-J. Bibiko, S. Brey, J. Callahan, G. Carrillo, S. Dray, D. Forrest, M. Friendly, P. Giraudoux, D. Golicher, V. G. Rubio, P. Hausmann, K. O. Hufthammer, T. Jagger, K. Johnson, M. Lewis, S. Luque, D. MacQueen, A. Niccolai, E. Pebesma, O. P. Lamigueiro, E. Plunkett, E. Rubak, T. Short, G. Snow, B. Stabler, M. Stokely, and R. Turner (2022). *maptools: Tools for Handling Spatial Objects*.
- Boese, S., M. Jung, N. Carvalhais, A. J. Teuling, and M. Reichstein (2019). “Carbon–water flux coupling under progressive drought”. *Biogeosciences* 16.13, 2557–2572.
- Bogdanovich, E., L. Guenther, M. Reichstein, D. Frank, G. Ruhrmann, A. Brenning, J. M. C. Denissen, and R. Orth (2022). “Societal attention to heat waves can indicate public health impacts.” *Environmental Research Letters*, in review.

- Böhnisch, A., M. Mittermeier, M. Leduc, and R. Ludwig (2021). “Hot Spots and Climate Trends of Meteorological Droughts in Europe—Assessing the Percent of Normal Index in a Single-Model Initial-Condition Large Ensemble”. *Frontiers in Water* 3.
- Bou-Zeid, E., C. Meneveau, and M. B. Parlange (2004). “Large-eddy simulation of neutral atmospheric boundary layer flow over heterogeneous surfaces: Blending height and effective surface roughness”. *Water Resources Research* 40.2.
- Brodribb, T. J., J. Powers, H. Cochard, and B. Choat (2020). “Hanging by a thread? Forests and drought”. *Science* 368.6488, 261–266.
- Brown, A. R., R. T. Cederwall, A. Chlond, P. G. Duynkerke, J.-C. Golaz, M. Khairoutdinov, D. C. Lewellen, A. P. Lock, M. K. MacVean, C.-H. Moeng, R. a. J. Neggers, A. P. Siebesma, and B. Stevens (2002). “Large-eddy simulation of the diurnal cycle of shallow cumulus convection over land”. *Quarterly Journal of the Royal Meteorological Society* 128.582, 1075–1093.
- Brum, M., M. A. Vadeboncoeur, V. Ivanov, H. Asbjornsen, S. Saleska, L. F. Alves, D. Penha, J. D. Dias, L. E. O. C. Aragão, F. Barros, P. Bittencourt, L. Pereira, and R. S. Oliveira (2019). “Hydrological niche segregation defines forest structure and drought tolerance strategies in a seasonal Amazon forest”. *Journal of Ecology* 107.1, 318–333.
- Budyko, M. I. (1974). *Climate and life*. Academic Press.
- Buitink, J., L. A. Melsen, and A. J. Teuling (2021). “Seasonal discharge response to temperature-driven changes in evaporation and snow processes in the Rhine Basin”. *Earth System Dynamics* 12.2, 387–400.
- Burden, R. L., D. J. Faires, and A. M. Burden (2016). “Numerical Analysis 10th Edition”. *Cengage Learning, Boston*.
- Burnham, K. P. and D. R. Anderson (2004). “Multimodel Inference: Understanding AIC and BIC in Model Selection”. *Sociological Methods & Research* 33.2, 261–304.
- Busch, F. A. and R. F. Sage (2017). “The sensitivity of photosynthesis to O₂ and CO₂ concentration identifies strong Rubisco control above the thermal optimum”. *New Phytologist* 213.3, 1036–1051.
- Buzan, J. R. and M. Huber (2020). “Moist Heat Stress on a Hotter Earth”. *Annual Review of Earth and Planetary Sciences* 48.1, 623–655.
- Canadell, J., R. B. Jackson, J. B. Ehleringer, H. A. Mooney, O. E. Sala, and E.-D. Schulze (1996). “Maximum rooting depth of vegetation types at the global scale”. *Oecologia* 108.4, 583–595.
- Cassou, C., L. Terray, and A. S. Phillips (2005). “Tropical Atlantic Influence on European Heat Waves”. *Journal of Climate* 18.15, 2805–2811.
- Cherchi, A., P. G. Fogli, T. Lovato, D. Peano, D. Iovino, S. Gualdi, S. Masina, E. Scoccimarro, S. Materia, A. Bellucci, and A. Navarra (2019). “Global Mean Climate and Main Patterns of Variability in the CMCC-CM2 Coupled Model”. *Journal of Advances in Modeling Earth Systems* 11.1, 185–209.

- Ciais, P., M. Reichstein, N. Viovy, A. Granier, J. Ogee, V. Allard, M. Aubinet, N. Buchmann, C. Bernhofer, A. Carrara, F. Chevallier, N. De Noblet, A. D. Friend, P. Friedlingstein, T. Grünwald, B. Heinesch, P. Keronen, A. Knohl, G. Krinner, D. Loustau, G. Manca, G. Matteucci, F. Miglietta, J. M. Ourcival, D. Papale, K. Pilegaard, S. Rambal, G. Seufert, J. F. Soussana, M. J. Sanz, E. D. Schulze, T. Vesala, and R. Valentini (2005). “Europe-wide reduction in primary productivity caused by the heat and drought in 2003”. *Nature* 437.7058, 529–533.
- Clapp, R. B. and G. M. Hornberger (1978). “Empirical equations for some soil hydraulic properties”. *Water Resources Research* 14.4, 601–604.
- Collins, M., R. Knutti, J. Arblaster, J.-L. Dufresne, T. Fichefet, P. Friedlingstein, X. Gao, W. J. Gutowski, T. Johns, T. Krinner, G. Krinner, M. Shongwe, C. Tebaldi, A. J. Weaver, and M. Wehner (2013). *Long-term Climate Change: Projections, Commitments and Irreversibility*. In: *Climate Change 2013: The Physical Science Basis. Contribution of Working Group I to the Fifth Assessment Report of the Intergovernmental Panel on Climate Change* [Stocker, T.F., D. Qin, G.-K. Plattner, M. Tignor, S.K. Allen, J. Boschung, A. Nauels, Y. Xia, V. Bex and P.M. Midgley (eds.)]. Cambridge University Press, Cambridge, United Kingdom and New York, NY, USA.
- Consortium (EC-Earth), E.-E. (2019). “EC-Earth-Consortium EC-Earth3-Veg model output prepared for CMIP6 ScenarioMIP”.
- (2020). “EC-Earth-Consortium EC-Earth3-Veg-LR model output prepared for CMIP6 CMIP historical”.
- Conzemius, R. J. and E. Fedorovich (2006). “Dynamics of Sheared Convective Boundary Layer Entrainment. Part I: Methodological Background and Large-Eddy Simulations”. *Journal of the Atmospheric Sciences* 63.4, 1151–1178.
- Cowan, I. R. (1977). “Stomatal function in relation to leaf metabolism and environment”. *Symp. Soc. Exp. Biol* 31, 471–505.
- Danabasoglu, G., J.-F. Lamarque, J. Bacmeister, D. A. Bailey, A. K. DuVivier, J. Edwards, L. K. Emmons, J. Fasullo, R. Garcia, A. Gettelman, C. Hannay, M. M. Holland, W. G. Large, P. H. Lauritzen, D. M. Lawrence, J. T. M. Lenaerts, K. Lindsay, W. H. Lipscomb, M. J. Mills, R. Neale, K. W. Oleson, B. Otto-Bliesner, A. S. Phillips, W. Sacks, S. Tilmes, L. van Kampenhout, M. Vertenstein, A. Bertini, J. Dennis, C. Deser, C. Fischer, B. Fox-Kemper, J. E. Kay, D. Kinnison, P. J. Kushner, V. E. Larson, M. C. Long, S. Mickelson, J. K. Moore, E. Nienhouse, L. Polvani, P. J. Rasch, and W. G. Strand (2020). “The Community Earth System Model Version 2 (CESM2)”. *Journal of Advances in Modeling Earth Systems* 12.2, e2019MS001916.
- Danabasoglu, G. (2019a). “NCAR CESM2 model output prepared for CMIP6 CMIP historical”.
- (2019b). “NCAR CESM2 model output prepared for CMIP6 ScenarioMIP ssp585”.
- Davin, E. L., S. I. Seneviratne, P. Ciais, A. Olioso, and T. Wang (2014). “Preferential cooling of hot extremes from cropland albedo management”. *Proceedings of the National Academy of Sciences* 111.27, 9757–9761.

- Dee, D. P., S. M. Uppala, A. J. Simmons, P. Berrisford, P. Poli, S. Kobayashi, U. Andrae, M. A. Balmaseda, G. Balsamo, P. Bauer, P. Bechtold, A. C. M. Beljaars, L. van de Berg, J. Bidlot, N. Bormann, C. Delsol, R. Dragani, M. Fuentes, A. J. Geer, L. Haimberger, S. B. Healy, H. Hersbach, E. V. Hólm, L. Isaksen, P. Kållberg, M. Köhler, M. Matricardi, A. P. McNally, B. M. Monge-Sanz, J.-J. Morcrette, B.-K. Park, C. Peubey, P. de Rosnay, C. Tavolato, J.-N. Thépaut, and F. Vitart (2011). “The ERA-Interim reanalysis: configuration and performance of the data assimilation system”. *Quarterly Journal of the Royal Meteorological Society* 137.656, 553–597.
- Denissen, J. M. C., R. Orth, H. Wouters, D. G. Miralles, C. C. van Heerwaarden, J. Vilà-Guerau de Arellano, and A. J. Teuling (2021). “Soil moisture signature in global weather balloon soundings”. *npj Climate and Atmospheric Science* 4.1, 1–8.
- Denissen, J. M. C., A. J. Teuling, G. Balsamo, X. Yu, M. M. Vogel, S. I. Seneviratne, and R. Orth (2022a). “Increasing ecosystem water limitation fuels future heat extremes”. *Global Change Biology*, in review.
- Denissen, J. M. C., A. J. Teuling, A. J. Pitman, S. Koirala, M. Migliavacca, W. Li, M. Reichstein, A. J. Winkler, C. Zhan, and R. Orth (2022b). “Widespread shift from ecosystem energy to water limitation with climate change”. *Nature Climate Change*, accepted.
- Denissen, J. M. C., A. J. Teuling, M. Reichstein, and R. Orth (2020). “Critical Soil Moisture Derived From Satellite Observations Over Europe”. *Journal of Geophysical Research: Atmospheres* 125.6, e2019JD031672.
- Didan, K. (2015). *MOD13C1 MODIS/Terra Vegetation Indices 16-Day L3 Global 0.05Deg CMG V006*.
- Dirmeyer, P. A. (2011). “The terrestrial segment of soil moisture–climate coupling”. *Geophysical Research Letters* 38.16.
- Dirmeyer, P. A., G. Balsamo, E. M. Blyth, R. Morrison, and H. M. Cooper (2021). “Land–Atmosphere Interactions Exacerbated the Drought and Heatwave Over Northern Europe During Summer 2018”. *AGU Advances* 2.2, e2020AV000283.
- Dirmeyer, P. A., L. Chen, J. Wu, C.-S. Shin, B. Huang, B. A. Cash, M. G. Bosilovich, S. Mahanama, R. D. Koster, J. A. Santanello, M. B. Ek, G. Balsamo, E. Dutra, and D. M. Lawrence (2018). “Verification of Land–Atmosphere Coupling in Forecast Models, Reanalyses, and Land Surface Models Using Flux Site Observations”. *Journal of Hydrometeorology* 19.2, 375–392.
- Dirmeyer, P. A., R. D. Koster, and Z. Guo (2006). “Do Global Models Properly Represent the Feedback between Land and Atmosphere?” *Journal of Hydrometeorology* 7.6, 1177–1198.
- Donat, M. G., A. J. Pitman, and S. I. Seneviratne (2017). “Regional warming of hot extremes accelerated by surface energy fluxes”. *Geophysical Research Letters* 44.13, 7011–7019.

- Donohue, R. J., M. L. Roderick, T. R. McVicar, and G. D. Farquhar (2013). “Impact of CO₂ fertilization on maximum foliage cover across the globe’s warm, arid environments”. *Geophysical Research Letters* 40.12, 3031–3035.
- Dorigo, W., I. Himmelbauer, D. Aberer, L. Schremmer, I. Petrakovic, L. Zappa, W. Preimesberger, A. Xaver, F. Annor, J. Ardö, D. Baldocchi, M. Bitelli, G. Blöschl, H. Bogena, L. Brocca, J.-C. Calvet, J. J. Camarero, G. Capello, M. Choi, M. C. Cosh, N. van de Giesen, I. Hajdu, J. Ikonen, K. H. Jensen, K. D. Kanniah, I. de Kat, G. Kirchengast, P. Kumar Rai, J. Kyrouac, K. Larson, S. Liu, A. Loew, M. Moghaddam, J. Martínez Fernández, C. Mattar Bader, R. Morbidelli, J. P. Musial, E. Osenga, M. A. Palecki, T. Pellarin, G. P. Petropoulos, I. Pfeil, J. Powers, A. Robock, C. Rüdiger, U. Rummel, M. Strobel, Z. Su, R. Sullivan, T. Tagesson, A. Varlagin, M. Vreugdenhil, J. Walker, J. Wen, F. Wenger, J. P. Wigneron, M. Woods, K. Yang, Y. Zeng, X. Zhang, M. Zreda, S. Dietrich, A. Gruber, P. van Oevelen, W. Wagner, K. Scipal, M. Drusch, and R. Sabia (2021). “The International Soil Moisture Network: serving Earth system science for over a decade”. *Hydrology and Earth System Sciences* 25.11, 5749–5804.
- Dorigo, W., R. de Jeu, D. Chung, R. Parinussa, Y. Liu, W. Wagner, and D. Fernández-Prieto (2012). “Evaluating global trends (1988–2010) in harmonized multi-satellite surface soil moisture”. *Geophysical Research Letters* 39.18.
- Dorigo, W., W. Wagner, C. Albergel, F. Albrecht, G. Balsamo, L. Brocca, D. Chung, M. Ertl, M. Forkel, A. Gruber, E. Haas, P. D. Hamer, M. Hirschi, J. Ikonen, R. de Jeu, R. Kidd, W. Lahoz, Y. Y. Liu, D. Miralles, T. Mistelbauer, N. Nicolai-Shaw, R. Parinussa, C. Pratola, C. Reimer, R. van der Schalie, S. I. Seneviratne, T. Smolander, and P. Lecomte (2017). “ESA CCI Soil Moisture for improved Earth system understanding: State-of-the art and future directions”. *Remote Sensing of Environment* 203, 185–215.
- Döscher, R., M. Acosta, A. Alessandri, P. Anthoni, A. Arneth, T. Arsouze, T. Bergmann, R. Bernadello, S. Bousetta, L.-P. Caron, G. Carver, M. Castrillo, F. Catalano, I. Cvijanovic, P. Davini, E. Dekker, F. J. Doblas-Reyes, D. Docquier, P. Echevarria, U. Fladrich, R. Fuentes-Franco, M. Gröger, J. v. Hardenberg, J. Hieronymus, M. P. Karami, J.-P. Keskinen, T. Koenigk, R. Makkonen, F. Massonnet, M. Ménégoz, P. A. Miller, E. Moreno-Chamarro, L. Nieradzik, T. van Noije, P. Nolan, D. O’Donnell, P. Ollinaho, G. van den Oord, P. Ortega, O. T. Prims, A. Ramos, T. Reerink, C. Rousset, Y. Ruprich-Robert, P. Le Sager, T. Schmith, R. Schrödner, F. Serva, V. Sicardi, M. Sloth Madsen, B. Smith, T. Tian, E. Tourigny, P. Uotila, M. Vancoppenolle, S. Wang, D. Wårlind, U. Willén, K. Wyser, S. Yang, X. Yepes-Arbós, and Q. Zhang (2021). “The EC-Earth3 Earth System Model for the Climate Model Intercomparison Project 6”. *Geoscientific Model Development Discussions*, 1–90.
- Durre, I., R. S. Vose, and D. B. Wuertz (2006). “Overview of the Integrated Global Radiosonde Archive”. *Journal of Climate* 19.1, 53–68.
- Ek, M. B. and A. a. M. Holtslag (2004). “Influence of Soil Moisture on Boundary Layer Cloud Development”. *Journal of Hydrometeorology* 5.1, 86–99.

- Ekblad, A., B. Boström, A. Holm, and D. Comstedt (2005). “Forest soil respiration rate and $\delta^{13}\text{C}$ is regulated by recent above ground weather conditions”. *Oecologia* 143.1, 136–142.
- Entekhabi, D., E. G. Njoku, P. E. O’Neill, K. H. Kellogg, W. T. Crow, W. N. Edelstein, J. K. Entin, S. D. Goodman, T. J. Jackson, J. Johnson, J. Kimball, J. R. Piepmeier, R. D. Koster, N. Martin, K. C. McDonald, M. Moghaddam, S. Moran, R. Reichle, J. C. Shi, M. W. Spencer, S. W. Thurman, L. Tsang, and J. Van Zyl (2010). “The Soil Moisture Active Passive (SMAP) Mission”. *Proceedings of the IEEE* 98.5, 704–716.
- EUMETSAT (2017). *Extending the working lifetime of the Metop-A weather satellite — EUMETSAT*.
- Eyring, V., S. Bony, G. A. Meehl, C. A. Senior, B. Stevens, R. J. Stouffer, and K. E. Taylor (2016). “Overview of the Coupled Model Intercomparison Project Phase 6 (CMIP6) experimental design and organization”. *Geoscientific Model Development* 9.5, 1937–1958.
- Fan, Y., G. Miguez-Macho, E. G. Jobbágy, R. B. Jackson, and C. Otero-Casal (2017). “Hydrologic regulation of plant rooting depth”. *Proceedings of the National Academy of Sciences* 114.40, 10572–10577.
- Feldman, A. F., D. J. Short Gianotti, I. F. Trigo, G. D. Salvucci, and D. Entekhabi (2019). “Satellite-Based Assessment of Land Surface Energy Partitioning–Soil Moisture Relationships and Effects of Confounding Variables”. *Water Resources Research* 55.12, 10657–10677.
- Feng, H. and M. Zhang (2015). “Global land moisture trends: drier in dry and wetter in wet over land”. *Scientific Reports* 5.1, 18018.
- Feng, S. and Q. Fu (2013). “Expansion of global drylands under a warming climate”. *Atmospheric Chemistry and Physics* 13.19, 10081–10094.
- Fernández-Martínez, M., J. Sardans, T. Musavi, M. Migliavacca, M. Iturrate-Garcia, R. J. Scholes, J. Peñuelas, and I. A. Janssens (2020). “The role of climate, foliar stoichiometry and plant diversity on ecosystem carbon balance”. *Global Change Biology* 26.12, 7067–7078.
- Findell, K. L., P. Gentine, B. R. Lintner, and B. P. Guillod (2015). “Data Length Requirements for Observational Estimates of Land–Atmosphere Coupling Strength”. *Journal of Hydrometeorology* 16.4, 1615–1635.
- Findell, K. L., P. Gentine, B. R. Lintner, and C. Kerr (2011). “Probability of afternoon precipitation in eastern United States and Mexico enhanced by high evaporation”. *Nature Geoscience* 4.7, 434–439.
- Fischer, E. M., S. I. Seneviratne, D. Lüthi, and C. Schär (2007). “Contribution of land-atmosphere coupling to recent European summer heat waves”. *Geophysical Research Letters* 34.6.
- Flach, M., S. Sippel, F. Gans, A. Bastos, A. Brenning, M. Reichstein, and M. D. Mahecha (2018). “Contrasting biosphere responses to hydrometeorological extremes: revisiting the 2010 western Russian heatwave”. *Biogeosciences* 15.20, 6067–6085.
- Ford, T. W., E. Harris, and S. M. Quiring (2014). “Estimating root zone soil moisture using near-surface observations from SMOS”. *Hydrology and Earth System Sciences* 18.1, 139–154.

- Frankenberg, C., J. B. Fisher, J. Worden, G. Badgley, S. S. Saatchi, J.-E. Lee, G. C. Toon, A. Butz, M. Jung, A. Kuze, and T. Yokota (2011). “New global observations of the terrestrial carbon cycle from GOSAT: Patterns of plant fluorescence with gross primary productivity”. *Geophysical Research Letters* 38.17.
- Freedman, J. M., D. R. Fitzjarrald, K. E. Moore, and R. K. Sakai (2001). “Boundary Layer Clouds and Vegetation–Atmosphere Feedbacks”. *Journal of Climate* 14.2, 180–197.
- Friedl, M. A., D. Sulla-Menashe, B. Tan, A. Schneider, N. Ramankutty, A. Sibley, and X. Huang (2010). “MODIS Collection 5 global land cover: Algorithm refinements and characterization of new datasets”. *Remote Sensing of Environment* 114.1, 168–182.
- Fu, Z., P. Ciais, D. Makowski, A. Bastos, P. C. Stoy, A. Ibrom, A. Knohl, M. Migliavacca, M. Cuntz, L. Šigut, M. Peichl, D. Loustau, T. S. El-Madany, N. Buchmann, M. Gharun, I. Janssens, C. Markwitz, T. Grünwald, C. Rebmann, M. Mölder, A. Varlagin, I. Mammarella, P. Kolari, C. Bernhofer, M. Heliasz, C. Vincke, A. Pitacco, E. Cremonese, L. Foltýnová, and J.-P. Wigneron (2022a). “Uncovering the critical soil moisture thresholds of plant water stress for European ecosystems”. *Global Change Biology* 28.6, 2111–2123.
- Fu, Z., P. Ciais, I. C. Prentice, P. Gentine, D. Makowski, A. Bastos, X. Luo, J. K. Green, P. C. Stoy, H. Yang, and T. Hajima (2022b). “Atmospheric dryness reduces photosynthesis along a large range of soil water deficits”. *Nature Communications* 13.1, 989.
- Gampe, D., J. Zscheischler, M. Reichstein, M. O’Sullivan, W. K. Smith, S. Sitch, and W. Buermann (2021). “Increasing impact of warm droughts on northern ecosystem productivity over recent decades”. *Nature Climate Change* 11.9, 772–779.
- Gentine, P., A. Chhang, A. Rigden, and G. Salvucci (2016). “Evaporation estimates using weather station data and boundary layer theory”. *Geophysical Research Letters* 43.22, 11, 661–11, 670.
- Gentine, P., M. Pritchard, S. Rasp, G. Reinaudi, and G. Yacalis (2018). “Could Machine Learning Break the Convection Parameterization Deadlock?” *Geophysical Research Letters* 45.11, 5742–5751.
- Gentine, P., J. K. Green, M. Guérin, V. Humphrey, S. I. Seneviratne, Y. Zhang, and S. Zhou (2019). “Coupling between the terrestrial carbon and water cycles—a review”. *Environmental Research Letters* 14.8, 083003.
- Genuchten, M. T. van (1987). “A Numerical Model for Water and Solute Movement in and Below the Root Zone.”
- Ghiggi, G., V. Humphrey, S. I. Seneviratne, and L. Gudmundsson (2019). “GRUN: an observation-based global gridded runoff dataset from 1902 to 2014”. *Earth System Science Data* 11.4, 1655–1674.
- Good, P., A. Sellar, Y. Tang, S. Rumbold, R. Ellis, D. Kelley, T. Kuhlbrodt, and J. Walton (2019). “MOHC UKESM1.0-LL model output prepared for CMIP6 ScenarioMIP”.

- Good, S. P., D. Noone, and G. Bowen (2015). “Hydrologic connectivity constrains partitioning of global terrestrial water fluxes”. *Science* 349.6244, 175–177.
- Goulart, H. M. D., K. van der Wiel, C. Folberth, J. Balkovic, and B. van den Hurk (2021). “Storylines of weather-induced crop failure events under climate change”. *Earth System Dynamics* 12.4, 1503–1527.
- Green, J. K., J. Berry, P. Ciais, Y. Zhang, and P. Gentine (2020). “Amazon rainforest photosynthesis increases in response to atmospheric dryness”. *Science Advances* 6.47, eabb7232.
- Green, J. K., S. I. Seneviratne, A. M. Berg, K. L. Findell, S. Hagemann, D. M. Lawrence, and P. Gentine (2019). “Large influence of soil moisture on long-term terrestrial carbon uptake”. *Nature* 565.7740, 476–479.
- Greve, P., M. L. Roderick, A. M. Ukkola, and Y. Wada (2019). “The aridity Index under global warming”. *Environmental Research Letters* 14.12, 124006.
- Greve, P., B. Orlowsky, B. Mueller, J. Sheffield, M. Reichstein, and S. I. Seneviratne (2014). “Global assessment of trends in wetting and drying over land”. *Nature Geoscience* 7.10, 716–721.
- Greve, P., M. L. Roderick, and S. I. Seneviratne (2017). “Simulated changes in aridity from the last glacial maximum to 4xCO₂”. *Environmental Research Letters* 12.11, 114021.
- Groemping, U. (2007). “Relative Importance for Linear Regression in R: The Package relaimpo”. *Journal of Statistical Software* 17, 1–27.
- Grover, A., A. Kapoor, and E. Horvitz (2015). “A Deep Hybrid Model for Weather Forecasting”. In: *Proceedings of the 21th ACM SIGKDD International Conference on Knowledge Discovery and Data Mining*. New York, NY, USA: Association for Computing Machinery, 379–386.
- Gruber, A., W. A. Dorigo, W. Crow, and W. Wagner (2017). “Triple Collocation-Based Merging of Satellite Soil Moisture Retrievals”. *IEEE Transactions on Geoscience and Remote Sensing* 55.12, 6780–6792.
- Guanter, L., C. Frankenberg, A. Dudhia, P. E. Lewis, J. Gómez-Dans, A. Kuze, H. Suto, and R. G. Grainger (2012). “Retrieval and global assessment of terrestrial chlorophyll fluorescence from GOSAT space measurements”. *Remote Sensing of Environment* 121, 236–251.
- Guillod, B. P., E. L. Davin, C. Kündig, G. Smiatek, and S. I. Seneviratne (2013). “Impact of soil map specifications for European climate simulations”. *Climate Dynamics* 40.1, 123–141.
- Guillod, B. P., B. Orlowsky, D. G. Miralles, A. J. Teuling, and S. I. Seneviratne (2015). “Reconciling spatial and temporal soil moisture effects on afternoon rainfall”. *Nature Communications* 6.1, 6443.
- Guo, H., J. G. John, C. Blanton, C. McHugh, S. Nikonov, A. Radhakrishnan, K. Rand, N. T. Zadeh, V. Balaji, J. Durachta, C. Dupuis, R. Menzel, T. Robinson, S. Underwood, H. Vahlenkamp, M. Bushuk, K. A. Dunne, R. Dussin, P. P. Gauthier, P. Ginoux, S. M. Griffies, R. Hallberg, M. Harrison, W. Hurlin, P. Lin, S. Malyshev, V. Naik, F. Paulot, D. J. Paynter, J. Ploshay, B. G. Reichl, D. M. Schwarzkopf, C. J. Seman, A. Shao, L. Silvers, B. Wyman, X.

- Yan, Y. Zeng, A. Adcroft, J. P. Dunne, I. M. Held, J. P. Krasting, L. W. Horowitz, P. C. D. Milly, E. Shevliakova, M. Winton, M. Zhao, and R. Zhang (2018a). “NOAA-GFDL GFDL-CM4 model output historical”.
- Guo, H., J. G. John, C. Blanton, C. McHugh, S. Nikonov, A. Radhakrishnan, K. Rand, N. T. Zadeh, V. Balaji, J. Durachta, C. Dupuis, R. Menzel, T. Robinson, S. Underwood, H. Vahlenkamp, K. A. Dunne, P. P. Gauthier, P. Ginoux, S. M. Griffies, R. Hallberg, M. Harrison, W. Hurlin, P. Lin, S. Malyshev, V. Naik, F. Paulot, D. J. Paynter, J. Ploshay, D. M. Schwarzkopf, C. J. Seman, A. Shao, L. Silvers, B. Wyman, X. Yan, Y. Zeng, A. Adcroft, J. P. Dunne, I. M. Held, J. P. Krasting, L. W. Horowitz, C. Milly, E. Shevliakova, M. Winton, M. Zhao, and R. Zhang (2018b). “NOAA-GFDL GFDL-CM4 model output prepared for CMIP6 ScenarioMIP”.
- Guo, Z. and P. A. Dirmeyer (2013). “Interannual Variability of Land–Atmosphere Coupling Strength”. *Journal of Hydrometeorology* 14.5, 1636–1646.
- Haghighi, E., D. J. Short Gianotti, R. Akbar, G. D. Salvucci, and D. Entekhabi (2018). “Soil and Atmospheric Controls on the Land Surface Energy Balance: A Generalized Framework for Distinguishing Moisture-Limited and Energy-Limited Evaporation Regimes”. *Water Resources Research* 54.3, 1831–1851.
- Hansen, M. and X.-P. Song (2018). *Vegetation Continuous Fields (VCF) Yearly Global 0.05 Deg.*
- Harman, I. N. (2012). “The Role of Roughness Sublayer Dynamics Within Surface Exchange Schemes”. *Boundary-Layer Meteorology* 142.1, 1–20.
- Harrington, L. J., F. E. L. Otto, T. Cowan, and G. C. Hegerl (2019). “Circulation analogues and uncertainty in the time-evolution of extreme event probabilities: evidence from the 1947 Central European heatwave”. *Climate Dynamics* 53.3, 2229–2247.
- Hauser, M., R. Orth, and S. I. Seneviratne (2016). “Role of soil moisture versus recent climate change for the 2010 heat wave in western Russia”. *Geophysical Research Letters* 43.6, 2819–2826.
- Haylock, M. R., N. Hofstra, A. M. G. Klein Tank, E. J. Klok, P. D. Jones, and M. New (2008). “A European daily high-resolution gridded data set of surface temperature and precipitation for 1950–2006”. *Journal of Geophysical Research: Atmospheres* 113.D20.
- He, L., T. Magney, D. Dutta, Y. Yin, P. Köhler, K. Grossmann, J. Stutz, C. Dold, J. Hatfield, K. Guan, B. Peng, and C. Frankenberg (2020). “From the Ground to Space: Using Solar-Induced Chlorophyll Fluorescence to Estimate Crop Productivity”. *Geophysical Research Letters* 47.7, e2020GL087474.
- Heerwaarden, C. C. van and A. J. Teuling (2014). “Disentangling the response of forest and grassland energy exchange to heatwaves under idealized land–atmosphere coupling”. *Biogeosciences* 11.21, 6159–6171.

- Heerwaarden, C. C. v. van and J. V. G. d. Arellano (2008). “Relative Humidity as an Indicator for Cloud Formation over Heterogeneous Land Surfaces”. *Journal of the Atmospheric Sciences* 65.10, 3263–3277.
- Heerwaarden, C. C. v. van, J. V.-G. d. Arellano, A. Gounou, F. Guichard, and F. Couvreux (2010). “Understanding the Daily Cycle of Evapotranspiration: A Method to Quantify the Influence of Forcings and Feedbacks”. *Journal of Hydrometeorology* 11.6, 1405–1422.
- Heerwaarden, C. C. van, J. Vilà-Guerau de Arellano, A. F. Moene, and A. A. M. Holtslag (2009). “Interactions between dry-air entrainment, surface evaporation and convective boundary-layer development”. *Quarterly Journal of the Royal Meteorological Society* 135.642, 1277–1291.
- Heijden, G. M. van der, S. A. Schnitzer, J. S. Powers, and O. L. Phillips (2013). “Liana Impacts on Carbon Cycling, Storage and Sequestration in Tropical Forests”. *Biotropica* 45.6, 682–692.
- Helbig, M., T. Gerken, E. Beamesderfer, D. Baldocchi, T. Banerjee, S. Biraud, N. Brunzell, S. Butterworth, W. Chan, A. Desai, J. Fuentes, D. Hollinger, N. Klijun, M. Mauder, K. Novick, J. Perkins, C. Rey-Sanchez, R. Scott, B. Seyednasrollah, P. Stoy, R. Sullivan, J. V.-G. d. Arellano, S. Wharton, C. Yi, and A. Richardson (2020). “Whitepaper: Understanding land-atmosphere interactions through tower-based flux and continuous atmospheric boundary layer measurements”. *Libraries*.
- Held, I. M., H. Guo, A. Adcroft, J. P. Dunne, L. W. Horowitz, J. Krasting, E. Shevliakova, M. Winton, M. Zhao, M. Bushuk, A. T. Wittenberg, B. Wyman, B. Xiang, R. Zhang, W. Anderson, V. Balaji, L. Donner, K. Dunne, J. Durachta, P. P. G. Gauthier, P. Ginoux, J.-C. Golaz, S. M. Griffies, R. Hallberg, L. Harris, M. Harrison, W. Hurlin, J. John, P. Lin, S.-J. Lin, S. Malyshev, R. Menzel, P. C. D. Milly, Y. Ming, V. Naik, D. Paynter, F. Paulot, V. Rammiaswamy, B. Reichl, T. Robinson, A. Rosati, C. Seman, L. G. Silvers, S. Underwood, and N. Zadeh (2019). “Structure and Performance of GFDL’s CM4.0 Climate Model”. *Journal of Advances in Modeling Earth Systems* 11.11, 3691–3727.
- Hengl, T., J. M. d. Jesus, G. B. M. Heuvelink, M. R. Gonzalez, M. Kilibarda, A. Blagotić, W. Shangquan, M. N. Wright, X. Geng, B. Bauer-Marschallinger, M. A. Guevara, R. Vargas, R. A. MacMillan, N. H. Batjes, J. G. B. Leenaars, E. Ribeiro, I. Wheeler, S. Mantel, and B. Kempen (2017). “SoilGrids250m: Global gridded soil information based on machine learning”. *PLOS ONE* 12.2, e0169748.
- Hersbach, H., B. Bell, P. Berrisford, G. Biavati, A. Horanyi, J. Muñoz Sabater, J. Nicolas, C. Peubey, R. Radu, I. Rozum, D. Schepers, A. Simmons, C. Soci, D. Dee, and J.-N. Thépaut (2019). *ERA5 monthly averaged data on single levels from 1979 to present*.
- Hersbach, H., B. Bell, P. Berrisford, S. Hirahara, A. Horányi, J. Muñoz-Sabater, J. Nicolas, C. Peubey, R. Radu, D. Schepers, A. Simmons, C. Soci, S. Abdalla, X. Abellan, G. Balsamo, P. Bechtold, G. Biavati, J. Bidlot, M. Bonavita, G. De Chiara, P. Dahlgren, D. Dee, M. Diamantakis, R. Dragani, J. Flemming, R. Forbes, M. Fuentes, A. Geer, L. Haimberger, S. Healy, R. J. Hogan, E. Hólm, M. Janisková, S. Keeley, P. Laloyaux, P. Lopez, C. Lupu, G. Radnoti, P. de Rosnay, I. Rozum, F. Vamborg, S. Villaume, and J.-N. Thépaut (2020). “The

- ERA5 global reanalysis”. *Quarterly Journal of the Royal Meteorological Society* 146.730, 1999–2049.
- Hirschi, M., B. Mueller, W. Dorigo, and S. I. Seneviratne (2014). “Using remotely sensed soil moisture for land–atmosphere coupling diagnostics: The role of surface vs. root-zone soil moisture variability”. *Remote Sensing of Environment* 154, 246–252.
- Hirschi, M., S. I. Seneviratne, V. Alexandrov, F. Boberg, C. Boroneant, O. B. Christensen, H. Formayer, B. Orłowsky, and P. Stepanek (2011). “Observational evidence for soil-moisture impact on hot extremes in southeastern Europe”. *Nature Geoscience* 4.1, 17–21.
- Ho, S.-p., R. A. Anthes, C. O. Ao, S. Healy, A. Horanyi, D. Hunt, A. J. Mannucci, N. Pedatella, W. J. Randel, A. Simmons, A. Steiner, F. Xie, X. Yue, and Z. Zeng (2020). “The COSMIC/FORMOSAT-3 Radio Occultation Mission after 12 Years: Accomplishments, Remaining Challenges, and Potential Impacts of COSMIC-2”. *Bulletin of the American Meteorological Society* 101.7, E1107–E1136.
- Homaee, M., R. A. Feddes, and C. Dirksen (2002). “Simulation of root water uptake: II. Non-uniform transient water stress using different reduction functions”. *Agricultural Water Management* 57.2, 111–126.
- Hong, X., M. J. Leach, and S. Raman (1995). “A Sensitivity Study of Convective Cloud Formation by Vegetation Forcing with Different Atmospheric Conditions”. *Journal of Applied Meteorology and Climatology* 34.9, 2008–2028.
- Huang, J., H. Yu, X. Guan, G. Wang, and R. Guo (2016). “Accelerated dryland expansion under climate change”. *Nature Climate Change* 6.2, 166–171.
- Humphrey, V., A. Berg, P. Ciais, P. Gentine, M. Jung, M. Reichstein, S. I. Seneviratne, and C. Frankenberg (2021). “Soil moisture–atmosphere feedback dominates land carbon uptake variability”. *Nature* 592.7852, 65–69.
- Humphrey, V., J. Zscheischler, P. Ciais, L. Gudmundsson, S. Sitch, and S. I. Seneviratne (2018). “Sensitivity of atmospheric CO₂ growth rate to observed changes in terrestrial water storage”. *Nature* 560.7720, 628–631.
- IPCC (2021). *Summary for Policymakers. In: Climate Change 2021: The Physical Science Basis. Contribution of Working Group I to the Sixth Assessment Report of the Intergovernmental Panel on Climate Change.* [Masson-Delmotte, V., P. Zhai, A. Pirani, S.L. Connors, C. Péan, S. Berger, N. Caud, Y. Chen, L. Goldfarb, M.I. Gomis, M. Huang, K. Leitzell, E. Lonnoy, J.B.R. Matthews, T.K. Maycock, T. Waterfield, O. Yelekçi, R. Yu, and B. Zhou (eds.)]. Cambridge University Press. In Press.
- Jackson, R. B., J. Canadell, J. R. Ehleringer, H. A. Mooney, O. E. Sala, and E. D. Schulze (1996). “A global analysis of root distributions for terrestrial biomes”. *Oecologia* 108.3, 389–411.
- Jézéquel, A., J. Cattiaux, P. Naveau, S. Radanovics, A. Ribes, R. Vautard, M. Vrac, and P. Yiou (2018). “Trends of atmospheric circulation during singular hot days in Europe”. *Environmental Research Letters* 13.5, 054007.

- Jiao, W., L. Wang, W. K. Smith, Q. Chang, H. Wang, and P. D'Odorico (2021). "Observed increasing water constraint on vegetation growth over the last three decades". *Nature Communications* 12.1, 3777.
- Joiner, J., L. Guanter, R. Lindstrot, M. Voigt, A. P. Vasilkov, E. M. Middleton, K. F. Huemmrich, Y. Yoshida, and C. Frankenberg (2013). "Global monitoring of terrestrial chlorophyll fluorescence from moderate-spectral-resolution near-infrared satellite measurements: methodology, simulations, and application to GOME-2". *Atmospheric Measurement Techniques* 6.10, 2803–2823.
- Jonard, F., S. De Cannière, N. Brüggemann, P. Gentine, D. J. Short Gianotti, G. Lobet, D. G. Miralles, C. Montzka, B. R. Pagán, U. Rascher, and H. Vereecken (2020). "Value of sun-induced chlorophyll fluorescence for quantifying hydrological states and fluxes: Current status and challenges". *Agricultural and Forest Meteorology* 291, 108088.
- Jung, M., S. Koirala, U. Weber, K. Ichii, F. Gans, G. Camps-Valls, D. Papale, C. Schwalm, G. Tramontana, and M. Reichstein (2019). "The FLUXCOM ensemble of global land-atmosphere energy fluxes". *Scientific Data* 6.1, 74.
- Jung, M., M. Reichstein, P. Ciais, S. I. Seneviratne, J. Sheffield, M. L. Goulden, G. Bonan, A. Cescatti, J. Chen, R. de Jeu, A. J. Dolman, W. Eugster, D. Gerten, D. Gianelle, N. Gobron, J. Heinke, J. Kimball, B. E. Law, L. Montagnani, Q. Mu, B. Mueller, K. Oleson, D. Papale, A. D. Richardson, O. Roupsard, S. Running, E. Tomelleri, N. Viovy, U. Weber, C. Williams, E. Wood, S. Zaehle, and K. Zhang (2010). "Recent decline in the global land evapotranspiration trend due to limited moisture supply". *Nature* 467.7318, 951–954.
- Jung, M., M. Reichstein, C. R. Schwalm, C. Huntingford, S. Sitch, A. Ahlström, A. Arneth, G. Camps-Valls, P. Ciais, P. Friedlingstein, F. Gans, K. Ichii, A. K. Jain, E. Kato, D. Papale, B. Poulter, B. Raduly, C. Rödenbeck, G. Tramontana, N. Viovy, Y.-P. Wang, U. Weber, S. Zaehle, and N. Zeng (2017). "Compensatory water effects link yearly global land CO₂ sink changes to temperature". *Nature* 541.7638, 516–520.
- Jung, M., C. Schwalm, M. Migliavacca, S. Walther, G. Camps-Valls, S. Koirala, P. Anthoni, S. Besnard, P. Bodesheim, N. Carvalhais, F. Chevallier, F. Gans, D. S. Goll, V. Haverd, P. Köhler, K. Ichii, A. K. Jain, J. Liu, D. Lombardozzi, J. E. M. S. Nabel, J. A. Nelson, M. O'Sullivan, M. Pallandt, D. Papale, W. Peters, J. Pongratz, C. Rödenbeck, S. Sitch, G. Tramontana, A. Walker, U. Weber, and M. Reichstein (2020). "Scaling carbon fluxes from eddy covariance sites to globe: synthesis and evaluation of the FLUXCOM approach". *Biogeosciences* 17.5, 1343–1365.
- Keenan, T. F., J. Gray, M. A. Friedl, M. Toomey, G. Bohrer, D. Y. Hollinger, J. W. Munger, J. O'Keefe, H. P. Schmid, I. S. Wing, B. Yang, and A. D. Richardson (2014). "Net carbon uptake has increased through warming-induced changes in temperate forest phenology". *Nature Climate Change* 4.7, 598–604.

- Köhler, P., L. Guanter, and J. Joiner (2015). “A linear method for the retrieval of sun-induced chlorophyll fluorescence from GOME-2 and SCIAMACHY data”. *Atmospheric Measurement Techniques* 8.6, 2589–2608.
- Köhler, P., C. Frankenberg, T. S. Magney, L. Guanter, J. Joiner, and J. Landgraf (2018). “Global Retrievals of Solar-Induced Chlorophyll Fluorescence With TROPOMI: First Results and Intersensor Comparison to OCO-2”. *Geophysical Research Letters* 45.19, 10, 456–10, 463.
- Kolby Smith, W., S. C. Reed, C. C. Cleveland, A. P. Ballantyne, W. R. L. Anderegg, W. R. Wieder, Y. Y. Liu, and S. W. Running (2016). “Large divergence of satellite and Earth system model estimates of global terrestrial CO₂ fertilization”. *Nature Climate Change* 6.3, 306–310.
- Koster, R. D., S. D. Schubert, and M. J. Suarez (2009). “Analyzing the Concurrence of Meteorological Droughts and Warm Periods, with Implications for the Determination of Evaporative Regime”. *Journal of Climate* 22.12, 3331–3341.
- Koster, R. D., Y. Chang, H. Wang, and S. D. Schubert (2016). “Impacts of Local Soil Moisture Anomalies on the Atmospheric Circulation and on Remote Surface Meteorological Fields during Boreal Summer: A Comprehensive Analysis over North America”. *Journal of Climate* 29.20, 7345–7364.
- Koster, R. D., P. A. Dirmeyer, Z. Guo, G. Bonan, E. Chan, P. Cox, C. T. Gordon, S. Kanae, E. Kowalczyk, D. Lawrence, P. Liu, C.-H. Lu, S. Malyshev, B. McAvaney, K. Mitchell, D. Mocko, T. Oki, K. Oleson, A. Pitman, Y. C. Sud, C. M. Taylor, D. Verseghy, R. Vasic, Y. Xue, and T. Yamada (2004). “Regions of Strong Coupling Between Soil Moisture and Precipitation”. *Science* 305.5687, 1138–1140.
- Koster, R. D., Y. C. Sud, Z. Guo, P. A. Dirmeyer, G. Bonan, K. W. Oleson, E. Chan, D. Verseghy, P. Cox, H. Davies, E. Kowalczyk, C. T. Gordon, S. Kanae, D. Lawrence, P. Liu, D. Mocko, C.-H. Lu, K. Mitchell, S. Malyshev, B. McAvaney, T. Oki, T. Yamada, A. Pitman, C. M. Taylor, R. Vasic, and Y. Xue (2006). “GLACE: The Global Land–Atmosphere Coupling Experiment. Part I: Overview”. *Journal of Hydrometeorology* 7.4, 590–610.
- Krich, C., J. Runge, D. G. Miralles, M. Migliavacca, O. Perez-Priego, T. El-Madany, A. Carrara, and M. D. Mahecha (2020). “Estimating causal networks in biosphere–atmosphere interaction with the PCMCI approach”. *Biogeosciences* 17.4, 1033–1061.
- Kroll*, J., J. M. C. Denissen*, M. Migliavacca, W. Li, A. Hildebrandt, and R. Orth (2022). “Spatially varying relevance of hydrometeorological hazards for vegetation productivity extremes”. *Biogeosciences* 19.2, 477–489, [*These authors contributed equally to this work].
- Lasslop, G., M. Reichstein, D. Papale, A. D. Richardson, A. Arneeth, A. Barr, P. Stoy, and G. Wohlfahrt (2010). “Separation of net ecosystem exchange into assimilation and respiration using a light response curve approach: critical issues and global evaluation”. *Global Change Biology* 16.1, 187–208.
- Lawrence, D. M., P. E. Thornton, K. W. Oleson, and G. B. Bonan (2007). “The Partitioning of Evapotranspiration into Transpiration, Soil Evaporation, and Canopy Evaporation in a GCM: Impacts on Land–Atmosphere Interaction”. *Journal of Hydrometeorology* 8.4, 862–880.

- Lee, W.-L. and H.-C. Liang (2019). “AS-RCEC TaiESM1.0 model output prepared for CMIP6 CMIP”.
- (2020). “AS-RCEC TaiESM1.0 model output prepared for CMIP6 CMIP historical”.
- Lee, W.-L., Y.-C. Wang, C.-J. Shiu, I.-c. Tsai, C.-Y. Tu, Y.-Y. Lan, J.-P. Chen, H.-L. Pan, and H.-H. Hsu (2020). “Taiwan Earth System Model Version 1: description and evaluation of mean state”. *Geoscientific Model Development* 13.9, 3887–3904.
- Lemordant, L. and P. Gentine (2019). “Vegetation Response to Rising CO₂ Impacts Extreme Temperatures”. *Geophysical Research Letters* 46.3, 1383–1392.
- Li, J., C.-Y. Tam, A. P. K. Tai, and N.-C. Lau (2021a). “Vegetation-heatwave correlations and contrasting energy exchange responses of different vegetation types to summer heatwaves in the Northern Hemisphere during the 1982–2011 period”. *Agricultural and Forest Meteorology* 296, 108208.
- Li, W., M. Migliavacca, M. Forkel, S. Walther, M. Reichstein, and R. Orth (2021b). “Revisiting Global Vegetation Controls Using Multi-Layer Soil Moisture”. *Geophysical Research Letters* 48.11, e2021GL092856.
- Li, Z., J. Guo, A. Ding, H. Liao, J. Liu, Y. Sun, T. Wang, H. Xue, H. Zhang, and B. Zhu (2017). “Aerosol and boundary-layer interactions and impact on air quality”. *National Science Review* 4.6, 810–833.
- Lian, X., S. Piao, A. Chen, C. Huntingford, B. Fu, L. Z. X. Li, J. Huang, J. Sheffield, A. M. Berg, T. F. Keenan, T. R. McVicar, Y. Wada, X. Wang, T. Wang, Y. Yang, and M. L. Roderick (2021). “Multifaceted characteristics of dryland aridity changes in a warming world”. *Nature Reviews Earth & Environment* 2.4, 232–250.
- Lilly, D. K. (1968). “Models of cloud-topped mixed layers under a strong inversion”. *Quarterly Journal of the Royal Meteorological Society* 94.401, 292–309.
- Linscheid, N., L. M. Estupinan-Suarez, A. Brenning, N. Carvalhais, F. Cremer, F. Gans, A. Ram-mig, M. Reichstein, C. A. Sierra, and M. D. Mahecha (2020). “Towards a global understanding of vegetation–climate dynamics at multiple timescales”. *Biogeosciences* 17.4, 945–962.
- Liu, Y. Y., W. A. Dorigo, R. M. Parinussa, R. A. M. de Jeu, W. Wagner, M. F. McCabe, J. P. Evans, and A. I. J. M. van Dijk (2012). “Trend-preserving blending of passive and active microwave soil moisture retrievals”. *Remote Sensing of Environment* 123, 280–297.
- Lobell, D. B. and G. P. Asner (2002). “Moisture Effects on Soil Reflectance”. *Soil Science Society of America Journal* 66.3, 722–727.
- Lofgren, B. M., T. S. Hunter, and J. Wilbarger (2011). “Effects of using air temperature as a proxy for potential evapotranspiration in climate change scenarios of Great Lakes basin hydrology”. *Journal of Great Lakes Research* 37.4, 744–752.
- Lorenz, R., D. Argüeso, M. G. Donat, A. J. Pitman, B. van den Hurk, A. Berg, D. M. Lawrence, F. Chéruy, A. Ducharne, S. Hagemann, A. Meier, P. C. D. Milly, and S. I. Seneviratne (2016).

- “Influence of land-atmosphere feedbacks on temperature and precipitation extremes in the GLACE-CMIP5 ensemble”. *Journal of Geophysical Research: Atmospheres* 121.2, 607–623.
- Lovato, T. and D. Peano (2020a). “CMCC CMCC-CM2-SR5 model output prepared for CMIP6 CMIP historical”.
- (2020b). “CMCC CMCC-CM2-SR5 model output prepared for CMIP6 ScenarioMIP”.
- Madani, N., J. S. Kimball, L. A. Jones, N. C. Parazoo, and K. Guan (2017). “Global Analysis of Bioclimatic Controls on Ecosystem Productivity Using Satellite Observations of Solar-Induced Chlorophyll Fluorescence”. *Remote Sensing* 9.6, 530.
- Maes, W. H., P. Gentine, N. E. C. Verhoest, and D. G. Miralles (2019). “Potential evaporation at eddy-covariance sites across the globe”. *Hydrology and Earth System Sciences* 23.2, 925–948.
- Maes, W. H., B. R. Pagán, B. Martens, P. Gentine, L. Guanter, K. Steppe, N. E. C. Verhoest, W. Dorigo, X. Li, J. Xiao, and D. G. Miralles (2020). “Sun-induced fluorescence closely linked to ecosystem transpiration as evidenced by satellite data and radiative transfer models”. *Remote Sensing of Environment* 249, 112030.
- Magney, T. S., M. L. Barnes, and X. Yang (2020). “On the Covariation of Chlorophyll Fluorescence and Photosynthesis Across Scales”. *Geophysical Research Letters* 47.23, e2020GL091098.
- Maguire, A. J., J. U. H. Eitel, K. L. Griffin, T. S. Magney, R. A. Long, L. A. Vierling, S. C. Schmiege, J. S. Jennewein, W. A. Weygint, N. T. Boelman, and S. G. Bruner (2020). “On the Functional Relationship Between Fluorescence and Photochemical Yields in Complex Evergreen Needleleaf Canopies”. *Geophysical Research Letters* 47.9, e2020GL087858.
- Mahrt, L. (1991). “Boundary-layer moisture regimes”. *Quarterly Journal of the Royal Meteorological Society* 117.497, 151–176.
- Marrs, J. K., J. S. Reblin, B. A. Logan, D. W. Allen, A. B. Reinmann, D. M. Bombard, D. Tabachnik, and L. R. Hutya (2020). “Solar-Induced Fluorescence Does Not Track Photosynthetic Carbon Assimilation Following Induced Stomatal Closure”. *Geophysical Research Letters* 47.15, e2020GL087956.
- Martens, B., D. G. Miralles, H. Lievens, R. van der Schalie, R. A. M. de Jeu, D. Fernández-Prieto, H. E. Beck, W. A. Dorigo, and N. E. C. Verhoest (2017). “GLEAM v3: satellite-based land evaporation and root-zone soil moisture”. *Geoscientific Model Development* 10.5, 1903–1925.
- Matthews, T. (2018). “Humid heat and climate change”. *Progress in Physical Geography: Earth and Environment* 42.3, 391–405.
- McDowell, N. G. and C. D. Allen (2015). “Darcy’s law predicts widespread forest mortality under climate warming”. *Nature Climate Change* 5.7, 669–672.
- Mekonnen, M. M. and A. Y. Hoekstra (2016). “Four billion people facing severe water scarcity”. *Science Advances* 2.2, e1500323.

- Menne, M. J., I. Durre, R. S. Vose, B. E. Gleason, and T. G. Houston (2012). “An Overview of the Global Historical Climatology Network-Daily Database”. *Journal of Atmospheric and Oceanic Technology* 29.7, 897–910.
- Milly, P. C. D. and K. A. Dunne (2016). “Potential evapotranspiration and continental drying”. *Nature Climate Change* 6.10, 946–949.
- Miralles, D. G., M. J. van den Berg, A. J. Teuling, and R. a. M. de Jeu (2012). “Soil moisture-temperature coupling: A multiscale observational analysis”. *Geophysical Research Letters* 39.21.
- Miralles, D. G., W. Brutsaert, A. J. Dolman, and J. H. Gash (2020). “On the Use of the Term “Evapotranspiration””. *Water Resources Research* 56.11, e2020WR028055.
- Miralles, D. G., M. J. van den Berg, J. H. Gash, R. M. Parinussa, R. A. M. de Jeu, H. E. Beck, T. R. H. Holmes, C. Jiménez, N. E. C. Verhoest, W. A. Dorigo, A. J. Teuling, and A. Johannes Dolman (2014a). “El Niño–La Niña cycle and recent trends in continental evaporation”. *Nature Climate Change* 4.2, 122–126.
- Miralles, D. G., A. J. Teuling, C. C. van Heerwaarden, and J. Vilà-Guerau de Arellano (2014b). “Mega-heatwave temperatures due to combined soil desiccation and atmospheric heat accumulation”. *Nature Geoscience* 7.5, 345–349.
- Mueller, B., M. Hirschi, C. Jimenez, P. Ciais, P. A. Dirmeyer, A. J. Dolman, J. B. Fisher, M. Jung, F. Ludwig, F. Maignan, D. G. Miralles, M. F. McCabe, M. Reichstein, J. Sheffield, K. Wang, E. F. Wood, Y. Zhang, and S. I. Seneviratne (2013). “Benchmark products for land evapotranspiration: LandFlux-EVAL multi-data set synthesis”. *Hydrology and Earth System Sciences* 17.10, 3707–3720.
- Muñoz Sabater, J. (2019). *ERA5-Land monthly averaged data from 2001 to present*.
- Muñoz-Sabater, J., E. Dutra, A. Agustí-Panareda, C. Albergel, G. Arduini, G. Balsamo, S. Boussetta, M. Choulga, S. Harrigan, H. Hersbach, B. Martens, D. G. Miralles, M. Piles, N. J. Rodríguez-Fernández, E. Zsoter, C. Buontempo, and J.-N. Thépaut (2021). “ERA5-Land: a state-of-the-art global reanalysis dataset for land applications”. *Earth System Science Data* 13.9, 4349–4383.
- Naumann, G., L. Alfieri, K. Wyser, L. Mentaschi, R. A. Betts, H. Carrao, J. Spinoni, J. Vogt, and L. Feyen (2018). “Global Changes in Drought Conditions Under Different Levels of Warming”. *Geophysical Research Letters* 45.7, 3285–3296.
- Nemani, R. R., C. D. Keeling, H. Hashimoto, W. M. Jolly, S. C. Piper, C. J. Tucker, R. B. Myneni, and S. W. Running (2003). “Climate-Driven Increases in Global Terrestrial Net Primary Production from 1982 to 1999”. *Science* 300.5625, 1560–1563.
- Novák, V. and J. Havrila (2006). “Method to estimate the critical soil water content of limited availability for plants”. *Biologia* 61.19, S289–S293.
- Novick, K. A., D. L. Ficklin, P. C. Stoy, C. A. Williams, G. Bohrer, A. C. Oishi, S. A. Papuga, P. D. Blanken, A. Noormets, B. N. Sulman, R. L. Scott, L. Wang, and R. P. Phillips (2016).

- “The increasing importance of atmospheric demand for ecosystem water and carbon fluxes”. *Nature Climate Change* 6.11, 1023–1027.
- O, S., E. Dutra, and R. Orth (2020a). “Robustness of Process-Based versus Data-Driven Modeling in Changing Climatic Conditions”. *Journal of Hydrometeorology* 21.9, 1929–1944.
- O, S., X. Hou, and R. Orth (2020b). “Observational evidence of wildfire-promoting soil moisture anomalies”. *Scientific Reports* 10.1, 11008.
- O, S. and R. Orth (2021). “Global soil moisture data derived through machine learning trained with in-situ measurements”. *Scientific Data* 8.1, 170.
- O’Neill, B. C., C. Tebaldi, D. P. van Vuuren, V. Eyring, P. Friedlingstein, G. Hurtt, R. Knutti, E. Kriegler, J.-F. Lamarque, J. Lowe, G. A. Meehl, R. Moss, K. Riahi, and B. M. Sanderson (2016). “The Scenario Model Intercomparison Project (ScenarioMIP) for CMIP6”. *Geoscientific Model Development* 9.9, 3461–3482.
- Oren, R., J. S. Sperry, G. G. Katul, D. E. Pataki, B. E. Ewers, N. Phillips, and K. V. R. Schäfer (1999). “Survey and synthesis of intra- and interspecific variation in stomatal sensitivity to vapour pressure deficit”. *Plant, Cell & Environment* 22.12, 1515–1526.
- Orth, R. and S. I. Seneviratne (2012). “Analysis of soil moisture memory from observations in Europe”. *Journal of Geophysical Research: Atmospheres* 117.D15.
- Orth, R. (2021). “When the Land Surface Shifts Gears”. *AGU Advances* 2.2, e2021AV000414.
- Orth, R., G. Destouni, M. Jung, and M. Reichstein (2020). “Large-scale biospheric drought response intensifies linearly with drought duration in arid regions”. *Biogeosciences* 17.9, 2647–2656.
- Orth, R., S. O, J. Zscheischler, M. D. Mahecha, and M. Reichstein (2022). “Contrasting biophysical and societal impacts of hydro-meteorological extremes”. *Environmental Research Letters* 17.1, 014044.
- Orth, R., J. Zscheischler, and S. I. Seneviratne (2016). “Record dry summer in 2015 challenges precipitation projections in Central Europe”. *Scientific Reports* 6.1, 28334.
- Otu-Larbi, F., C. G. Bolas, V. Ferracci, Z. Staniaszek, R. L. Jones, Y. Malhi, N. R. P. Harris, O. Wild, and K. Ashworth (2020). “Modelling the effect of the 2018 summer heatwave and drought on isoprene emissions in a UK woodland”. *Global Change Biology* 26.4, 2320–2335.
- Pal, S., I. Xueref-Remy, L. Ammoura, P. Chazette, F. Gibert, P. Royer, E. Dieudonné, J. .-.C. Dupont, M. Haeffelin, C. Lac, M. Lopez, Y. Morille, and F. Ravetta (2012). “Spatio-temporal variability of the atmospheric boundary layer depth over the Paris agglomeration: An assessment of the impact of the urban heat island intensity”. *Atmospheric Environment* 63, 261–275.
- Palmer, W. C. (1965). *Meteorological Drought*. U.S. Department of Commerce, Weather Bureau.
- Panwar, A., A. Kleidon, and M. Renner (2019). “Do Surface and Air Temperatures Contain Similar Imprints of Evaporative Conditions?” *Geophysical Research Letters* 46.7, 3802–3809.

- Pastorello, G., C. Trotta, E. Canfora, H. Chu, D. Christianson, Y.-W. Cheah, C. Poindexter, J. Chen, A. Elbashandy, M. Humphrey, P. Isaac, D. Polidori, M. Reichstein, et al. (2020). “The FLUXNET2015 dataset and the ONEFlux processing pipeline for eddy covariance data”. *Scientific Data* 7.1, 225.
- Pedruzo-Bagazgoitia, X., H. G. Ouwersloot, M. Sikma, C. C. v. Heerwaarden, C. M. J. Jacobs, and J. V.-G. d. Arellano (2017). “Direct and Diffuse Radiation in the Shallow Cumulus–Vegetation System: Enhanced and Decreased Evapotranspiration Regimes”. *Journal of Hydrometeorology* 18.6, 1731–1748.
- Peñuelas, J., P. Ciais, J. G. Canadell, I. A. Janssens, M. Fernández-Martínez, J. Carnicer, M. Obersteiner, S. Piao, R. Vautard, and J. Sardans (2017). “Shifting from a fertilization-dominated to a warming-dominated period”. *Nature Ecology & Evolution* 1.10, 1438–1445.
- Peñuelas, J., B. Poulter, J. Sardans, P. Ciais, M. van der Velde, L. Bopp, O. Boucher, Y. Godderis, P. Hinsinger, J. Llusia, E. Nardin, S. Vicca, M. Obersteiner, and I. A. Janssens (2013). “Human-induced nitrogen–phosphorus imbalances alter natural and managed ecosystems across the globe”. *Nature Communications* 4.1, 2934.
- Perdomo, J. A., S. Capó-Bauçà, E. Carmo-Silva, and J. Galmés (2017). “Rubisco and Rubisco Activase Play an Important Role in the Biochemical Limitations of Photosynthesis in Rice, Wheat, and Maize under High Temperature and Water Deficit”. *Frontiers in Plant Science* 8.
- Piao, S., P. Ciais, Y. Huang, Z. Shen, S. Peng, J. Li, L. Zhou, H. Liu, Y. Ma, Y. Ding, P. Friedlingstein, C. Liu, K. Tan, Y. Yu, T. Zhang, and J. Fang (2010). “The impacts of climate change on water resources and agriculture in China”. *Nature* 467.7311, 43–51.
- Piao, S., X. Wang, T. Park, C. Chen, X. Lian, Y. He, J. W. Bjerke, A. Chen, P. Ciais, H. Tømmervik, R. R. Nemani, and R. B. Myneni (2020). “Characteristics, drivers and feedbacks of global greening”. *Nature Reviews Earth & Environment* 1.1, 14–27.
- Pielke, R. A., J. Adegoke, A. Beltraán-Przekurat, C. A. Hiemstra, J. Lin, U. S. Nair, D. Niyogi, and T. E. Nobis (2007). “An overview of regional land-use and land-cover impacts on rainfall”. *Tellus B: Chemical and Physical Meteorology* 59.3, 587–601.
- Pitman, A. J. (2003). “The evolution of, and revolution in, land surface schemes designed for climate models”. *International Journal of Climatology* 23.5, 479–510.
- Prein, A. F. and A. J. Heymsfield (2020). “Increased melting level height impacts surface precipitation phase and intensity”. *Nature Climate Change* 10.8, 771–776.
- Qiu, B., J. Ge, W. Guo, A. J. Pitman, and M. Mu (2020). “Responses of Australian Dryland Vegetation to the 2019 Heat Wave at a Subdaily Scale”. *Geophysical Research Letters* 47.4, e2019GL086569.
- Qiu, J., W. T. Crow, and G. S. Nearing (2016). “The Impact of Vertical Measurement Depth on the Information Content of Soil Moisture for Latent Heat Flux Estimation”. *Journal of Hydrometeorology* 17.9, 2419–2430.

- Qiu, J., W. T. Crow, G. S. Nearing, X. Mo, and S. Liu (2014). “The impact of vertical measurement depth on the information content of soil moisture times series data”. *Geophysical Research Letters* 41.14, 4997–5004.
- Quesada, B., R. Vautard, P. Yiou, M. Hirschi, and S. I. Seneviratne (2012). “Asymmetric European summer heat predictability from wet and dry southern winters and springs”. *Nature Climate Change* 2.10, 736–741.
- Rasmijn, L. M., G. van der Schrier, R. Bintanja, J. Barkmeijer, A. Sterl, and W. Hazeleger (2018). “Future equivalent of 2010 Russian heatwave intensified by weakening soil moisture constraints”. *Nature Climate Change* 8.5, 381–385.
- Rasp, S., M. S. Pritchard, and P. Gentine (2018). “Deep learning to represent subgrid processes in climate models”. *Proceedings of the National Academy of Sciences* 115.39, 9684–9689.
- Reichle, R. H., G. J. M. D. Lannoy, Q. Liu, J. V. Ardizzone, A. Colliander, A. Conaty, W. Crow, T. J. Jackson, L. A. Jones, J. S. Kimball, R. D. Koster, S. P. Mahanama, E. B. Smith, A. Berg, S. Bircher, D. Bosch, T. G. Caldwell, M. Cosh, Á. González-Zamora, C. D. H. Collins, K. H. Jensen, S. Livingston, E. Lopez-Baeza, J. Martínez-Fernández, H. McNairn, M. Moghaddam, A. Pacheco, T. Pellarin, J. Prueger, T. Rowlandson, M. Seyfried, P. Starks, Z. Su, M. Thibeault, R. v. d. Velde, J. Walker, X. Wu, and Y. Zeng (2017). “Assessment of the SMAP Level-4 Surface and Root-Zone Soil Moisture Product Using In Situ Measurements”. *Journal of Hydrometeorology* 18.10, 2621–2645.
- Reichstein, M., M. Bahn, P. Ciais, D. Frank, M. D. Mahecha, S. I. Seneviratne, J. Zscheischler, C. Beer, N. Buchmann, D. C. Frank, D. Papale, A. Rammig, P. Smith, K. Thonicke, M. van der Velde, S. Vicca, A. Walz, and M. Wattenbach (2013). “Climate extremes and the carbon cycle”. *Nature* 500.7462, 287–295.
- Rieck, M., C. Hohenegger, and C. C. v. Heerwaarden (2014). “The Influence of Land Surface Heterogeneities on Cloud Size Development”. *Monthly Weather Review* 142.10, 3830–3846.
- Robinson, F. J., S. C. Sherwood, and Y. Li (2008). “Resonant Response of Deep Convection to Surface Hot Spots”. *Journal of the Atmospheric Sciences* 65.1, 276–286.
- Rockström, J., M. Falkenmark, L. Karlberg, H. Hoff, S. Rost, and D. Gerten (2009). “Future water availability for global food production: The potential of green water for increasing resilience to global change”. *Water Resources Research* 45.7.
- Rong, X. (2019a). “CAM5 CAMS_CSM1.0 model output prepared for CMIP6 CMIP historical”. – (2019b). “CAM5 CAMS-CSM1.0 model output prepared for CMIP6 ScenarioMIP”.
- Rong, X.-Y., J. Li, H.-M. Chen, Y.-F. Xin, J.-Z. Su, L.-J. Hua, and Z.-Q. Zhang (2019). “Introduction of CAM5-CSM model and its participation in CMIP6”. *Advances in Climate Change Research* 15.5, 540.
- Ruffault, J., T. Curt, V. Moron, R. M. Trigo, F. Mouillot, N. Koutsias, F. Pimont, N. Martin-StPaul, R. Barbero, J.-L. Dupuy, A. Russo, and C. Belhadj-Khedher (2020). “Increased likelihood of heat-induced large wildfires in the Mediterranean Basin”. *Scientific Reports* 10.1, 13790.

- Salvucci, G. D. and P. Gentine (2013). “Emergent relation between surface vapor conductance and relative humidity profiles yields evaporation rates from weather data”. *Proceedings of the National Academy of Sciences* 110.16, 6287–6291.
- Santanello, J. A. and T. N. Carlson (2001). “Mesoscale Simulation of Rapid Soil Drying and Its Implications for Predicting Daytime Temperature”. *Journal of Hydrometeorology* 2.1, 71–88.
- Santanello, J. A., P. A. Dirmeyer, C. R. Ferguson, K. L. Findell, A. B. Tawfik, A. Berg, M. Ek, P. Gentine, B. P. Guillod, C. v. Heerwaarden, J. Roundy, and V. Wulfmeyer (2018). “Land–Atmosphere Interactions: The LoCo Perspective”. *Bulletin of the American Meteorological Society* 99.6, 1253–1272.
- Santanello, J. A., M. A. Friedl, and M. B. Ek (2007). “Convective Planetary Boundary Layer Interactions with the Land Surface at Diurnal Time Scales: Diagnostics and Feedbacks”. *Journal of Hydrometeorology* 8.5, 1082–1097.
- Santanello, J. A., M. A. Friedl, and W. P. Kustas (2005). “An Empirical Investigation of Convective Planetary Boundary Layer Evolution and Its Relationship with the Land Surface”. *Journal of Applied Meteorology and Climatology* 44.6, 917–932.
- Santanello, J. A., C. D. Peters-Lidard, S. V. Kumar, C. Alonge, and W.-K. Tao (2009). “A Modeling and Observational Framework for Diagnosing Local Land–Atmosphere Coupling on Diurnal Time Scales”. *Journal of Hydrometeorology* 10.3, 577–599.
- Scheff, J., J. S. Mankin, S. Coats, and H. Liu (2021). “CO₂-plant effects do not account for the gap between dryness indices and projected dryness impacts in CMIP6 or CMIP5”. *Environmental Research Letters* 16.3, 034018.
- Scheff, J., R. Seager, H. Liu, and S. Coats (2017). “Are Glacials Dry? Consequences for Paleoclimatology and for Greenhouse Warming”. *Journal of Climate* 30.17, 6593–6609.
- Schlesinger, W. H. and S. Jasechko (2014). “Transpiration in the global water cycle”. *Agricultural and Forest Meteorology* 189-190, 115–117.
- Schumacher, D. L., J. Keune, C. C. van Heerwaarden, J. Vilà-Guerau de Arellano, A. J. Teuling, and D. G. Miralles (2019). “Amplification of mega-heatwaves through heat torrents fuelled by upwind drought”. *Nature Geoscience* 12.9, 712–717.
- Schwaab, J., R. Meier, G. Mussetti, S. Seneviratne, C. Bürgi, and E. L. Davin (2021). “The role of urban trees in reducing land surface temperatures in European cities”. *Nature Communications* 12.1, 6763.
- Schwingshackl, C., M. Hirschi, and S. I. Seneviratne (2017). “Quantifying Spatiotemporal Variations of Soil Moisture Control on Surface Energy Balance and Near-Surface Air Temperature”. *Journal of Climate* 30.18, 7105–7124.
- (2018). “A theoretical approach to assess soil moisture–climate coupling across CMIP5 and GLACE-CMIP5 experiments”. *Earth System Dynamics* 9.4, 1217–1234.
- Seddon, A. W. R., M. Macias-Fauria, P. R. Long, D. Benz, and K. J. Willis (2016). “Sensitivity of global terrestrial ecosystems to climate variability”. *Nature* 531.7593, 229–232.

- Seferian, R. (2018). “CNRM-CERFACS CNRM-ESM2-1 model output prepared for CMIP6 CMIP historical”.
- Séférian, R., P. Nabat, M. Michou, D. Saint-Martin, A. Voldoire, J. Colin, B. Decharme, C. Delire, S. Berthet, M. Chevallier, S. Sénési, L. Franchisteguy, J. Vial, M. Mallet, E. Joetzjer, O. Geoffroy, J.-F. Guérémy, M.-P. Moine, R. Msadek, A. Ribes, M. Rocher, R. Roebrig, D. Salas-y-Méllia, E. Sanchez, L. Terray, S. Valcke, R. Waldman, O. Aumont, L. Bopp, J. Deshayes, C. Éthé, and G. Madec (2019). “Evaluation of CNRM Earth System Model, CNRM-ESM2-1: Role of Earth System Processes in Present-Day and Future Climate”. *Journal of Advances in Modeling Earth Systems* 11.12, 4182–4227.
- Sellar, A. A., C. G. Jones, J. P. Mulcahy, Y. Tang, A. Yool, A. Wiltshire, F. M. O’Connor, M. Stringer, R. Hill, J. Palmieri, S. Woodward, L. de Mora, T. Kuhlbrodt, S. T. Rumbold, D. I. Kelley, R. Ellis, C. E. Johnson, J. Walton, N. L. Abraham, M. B. Andrews, T. Andrews, A. T. Archibald, S. Berthou, E. Burke, E. Blockley, K. Carslaw, M. Dalvi, J. Edwards, G. A. Folberth, N. Gedney, P. T. Griffiths, A. B. Harper, M. A. Hendry, A. J. Hewitt, B. Johnson, A. Jones, C. D. Jones, J. Keeble, S. Liddicoat, O. Morgenstern, R. J. Parker, V. Predoi, E. Robertson, A. Siahann, R. S. Smith, R. Swaminathan, M. T. Woodhouse, G. Zeng, and M. Zerroukat (2019). “UKESM1: Description and Evaluation of the U.K. Earth System Model”. *Journal of Advances in Modeling Earth Systems* 11.12, 4513–4558.
- Sellers, P. J., R. E. Dickinson, D. A. Randall, A. K. Betts, F. G. Hall, J. A. Berry, G. J. Collatz, A. S. Denning, H. A. Mooney, C. A. Nobre, N. Sato, C. B. Field, and A. Henderson-Sellers (1997). “Modeling the Exchanges of Energy, Water, and Carbon Between Continents and the Atmosphere”. *Science* 275.5299, 502–509.
- Sellers, P. J., F. G. Hall, G. Asrar, D. E. Strebel, and R. E. Murphy (1992). “An overview of the First International Satellite Land Surface Climatology Project (ISLSCP) Field Experiment (FIFE)”. *Journal of Geophysical Research: Atmospheres* 97.D17, 18345–18371.
- Sen, P. K. (1968). “Estimates of the Regression Coefficient Based on Kendall’s Tau”. *Journal of the American Statistical Association* 63.324, 1379–1389.
- Seneviratne, S. I., X. Zhang, M. Adnan, W. Badi, C. Dereczynski, A. Di Luco, S. Ghosh, I. Iskandar, J. Kossin, S. Lewis, F. Otto, I. Pinto, M. Satoh, S. Vicente-Serrano, M. Wehner, and B. Zhou (2021). *Climate Change 2021: The Physical Science Basis. Contribution of Working Group I to the Sixth Assessment Report of the Intergovernmental Panel on Climate Change*. [Masson-Delmotte, V., P. Zhai, A. Pirani, S.L. Connors, C. Péan, S. Berger, N. Caud, Y. Chen, L. Goldfarb, M.I. Gomis, M. Huang, K. Leitzell, E. Lonnoy, J.B.R. Matthews, T.K. Maycock, T. Waterfield, O. Yelekçi, R. Yu, and B. Zhou (eds.)]. Cambridge University Press. In Press.
- Seneviratne, S. I., T. Corti, E. L. Davin, M. Hirschi, E. B. Jaeger, I. Lehner, B. Orlowsky, and A. J. Teuling (2010). “Investigating soil moisture–climate interactions in a changing climate: A review”. *Earth-Science Reviews* 99.3, 125–161.
- Seneviratne, S. I., M. G. Donat, B. Mueller, and L. V. Alexander (2014). “No pause in the increase of hot temperature extremes”. *Nature Climate Change* 4.3, 161–163.

- Seneviratne, S. I., D. Lüthi, M. Litschi, and C. Schär (2006). “Land–atmosphere coupling and climate change in Europe”. *Nature* 443.7108, 205–209.
- Seneviratne, S. I., M. Wilhelm, T. Stanelle, B. van den Hurk, S. Hagemann, A. Berg, F. Cheruy, M. E. Higgins, A. Meier, V. Brovkin, M. Claussen, A. Ducharne, J.-L. Dufresne, K. L. Findell, J. Ghattas, D. M. Lawrence, S. Malyshev, M. Rummukainen, and B. Smith (2013). “Impact of soil moisture-climate feedbacks on CMIP5 projections: First results from the GLACE-CMIP5 experiment”. *Geophysical Research Letters* 40.19, 5212–5217.
- Sherwood, S. and Q. Fu (2014). “A Drier Future?” *Science* 343.6172, 737–739.
- Shuttleworth, W. J., R. J. Gurney, A. Y. Hsu, and J. P. Ormsby (1989). “FIFE: The variation in energy partition at surface flux sites”. *IAHS Publ* 186.6, 523–534.
- Sillmann, J., T. Thorarinsdottir, N. Keenlyside, N. Schaller, L. V. Alexander, G. Hegerl, S. I. Seneviratne, R. Vautard, X. Zhang, and F. W. Zwiers (2017). “Understanding, modeling and predicting weather and climate extremes: Challenges and opportunities”. *Weather and Climate Extremes* 18, 65–74.
- Sippel, S., J. Zscheischler, M. D. Mahecha, R. Orth, M. Reichstein, M. Vogel, and S. I. Seneviratne (2017). “Refining multi-model projections of temperature extremes by evaluation against land–atmosphere coupling diagnostics”. *Earth System Dynamics* 8.2, 387–403.
- Smith, M. D. (2011). “An ecological perspective on extreme climatic events: a synthetic definition and framework to guide future research”. *Journal of Ecology* 99.3, 656–663.
- Smith-Martin, C. M., X. Xu, D. Medvigy, S. A. Schnitzer, and J. S. Powers (2020). “Allometric scaling laws linking biomass and rooting depth vary across ontogeny and functional groups in tropical dry forest lianas and trees”. *New Phytologist* 226.3, 714–726.
- Stegehuis, A. I., M. M. Vogel, R. Vautard, P. Ciais, A. J. Teuling, and S. I. Seneviratne (2021). “Early Summer Soil Moisture Contribution to Western European Summer Warming”. *Journal of Geophysical Research: Atmospheres* 126.17, e2021JD034646.
- Sun, Y., R. Fu, R. Dickinson, J. Joiner, C. Frankenberg, L. Gu, Y. Xia, and N. Fernando (2015). “Drought onset mechanisms revealed by satellite solar-induced chlorophyll fluorescence: Insights from two contrasting extreme events”. *Journal of Geophysical Research: Biogeosciences* 120.11, 2427–2440.
- Tang, Y., S. Rumbold, R. Ellis, D. Kelley, J. Mulcahy, A. Sellar, J. Walton, and C. Jones (2019). “MOHC UKESM1.0-LL model output prepared for CMIP6 CMIP historical”.
- Taylor, C. M., A. Gounou, F. Guichard, P. P. Harris, R. J. Ellis, F. Couvreur, and M. De Kauwe (2011). “Frequency of Sahelian storm initiation enhanced over mesoscale soil-moisture patterns”. *Nature Geoscience* 4.7, 430–433.
- Taylor, C. M., R. A. M. de Jeu, F. Guichard, P. P. Harris, and W. A. Dorigo (2012). “Afternoon rain more likely over drier soils”. *Nature* 489.7416, 423–426.
- Tennekes, H. (1973). “A Model for the Dynamics of the Inversion Above a Convective Boundary Layer”. *Journal of the Atmospheric Sciences* 30.4, 558–567.

- Tennekes, H. and A. G. M. Driedonks (1981). “Basic entrainment equations for the atmospheric boundary layer”. *Boundary-Layer Meteorology* 20.4, 515–531.
- Teuling, A. J., M. Hirschi, A. Ohmura, M. Wild, M. Reichstein, P. Ciais, N. Buchmann, C. Ammann, L. Montagnani, A. D. Richardson, G. Wohlfahrt, and S. I. Seneviratne (2009a). “A regional perspective on trends in continental evaporation”. *Geophysical Research Letters* 36.2.
- Teuling, A. J., S. I. Seneviratne, C. Williams, and P. A. Troch (2006). “Observed timescales of evapotranspiration response to soil moisture”. *Geophysical Research Letters* 33.23.
- Teuling, A. J. (2018). “A hot future for European droughts”. *Nature Climate Change* 8.5, 364–365.
- Teuling, A. J., S. I. Seneviratne, R. Stöckli, M. Reichstein, E. Moors, P. Ciais, S. Luysaert, B. van den Hurk, C. Ammann, C. Bernhofer, E. Dellwik, D. Gianelle, B. Gielen, T. Grünwald, K. Klumpp, L. Montagnani, C. Moureaux, M. Sottocornola, and G. Wohlfahrt (2010). “Contrasting response of European forest and grassland energy exchange to heatwaves”. *Nature Geoscience* 3.10, 722–727.
- Teuling, A. J., R. Uijlenhoet, B. v. d. Hurk, and S. I. Seneviratne (2009b). “Parameter Sensitivity in LSMs: An Analysis Using Stochastic Soil Moisture Models and ELDAS Soil Parameters”. *Journal of Hydrometeorology* 10.3, 751–765.
- Theil, H. (1992). “A Rank-Invariant Method of Linear and Polynomial Regression Analysis”. In: *Henri Theil’s Contributions to Economics and Econometrics: Econometric Theory and Methodology*. Dordrecht: Springer Netherlands, 345–381.
- Thorarinsdottir, T. L., J. Sillmann, M. Haugen, N. Gissibl, and M. Sandstad (2020). “Evaluation of CMIP5 and CMIP6 simulations of historical surface air temperature extremes using proper evaluation methods”. *Environmental Research Letters* 15.12, 124041.
- Tian, S., L. J. Renzullo, A. I. J. M. van Dijk, P. Tregoning, and J. P. Walker (2019). “Global joint assimilation of GRACE and SMOS for improved estimation of root-zone soil moisture and vegetation response”. *Hydrology and Earth System Sciences* 23.2, 1067–1081.
- Tobin, K. J., W. T. Crow, J. Dong, and M. E. Bennett (2019). “Validation of a New Root-Zone Soil Moisture Product: Soil MERGE”. *IEEE Journal of Selected Topics in Applied Earth Observations and Remote Sensing* 12.9, 3351–3365.
- Tollerud, H. J., J. F. Brown, and T. R. Loveland (2020). “Investigating the Effects of Land Use and Land Cover on the Relationship between Moisture and Reflectance Using Landsat Time Series”. *Remote Sensing* 12.12, 1919.
- Tramontana, G., M. Jung, C. R. Schwalm, K. Ichii, G. Camps-Valls, B. Ráduly, M. Reichstein, M. A. Arain, A. Cescatti, G. Kiely, L. Merbold, P. Serrano-Ortiz, S. Sickert, S. Wolf, and D. Papale (2016). “Predicting carbon dioxide and energy fluxes across global FLUXNET sites with regression algorithms”. *Biogeosciences* 13.14, 4291–4313.
- Transeau, E. N. (1905). “Forest Centers of Eastern America”. *The American Naturalist* 39.468, 875–889.

- Trenberth, K. E., J. T. Fasullo, and T. G. Shepherd (2015). “Attribution of climate extreme events”. *Nature Climate Change* 5.8, 725–730.
- Turner, A. J., P. Köhler, T. S. Magney, C. Frankenberg, I. Fung, and R. C. Cohen (2020). “A double peak in the seasonality of California’s photosynthesis as observed from space”. *Biogeosciences* 17.2, 405–422.
- Ukkola, A. M., A. J. Pitman, M. G. Donat, M. G. De Kauwe, and O. Angélil (2018). “Evaluating the Contribution of Land-Atmosphere Coupling to Heat Extremes in CMIP5 Models”. *Geophysical Research Letters* 45.17, 9003–9012.
- Ukkola, A. M., I. C. Prentice, T. F. Keenan, A. I. J. M. van Dijk, N. R. Viney, R. B. Myneni, and J. Bi (2016). “Reduced streamflow in water-stressed climates consistent with CO₂ effects on vegetation”. *Nature Climate Change* 6.1, 75–78.
- Ulaby, F. T. (1982). “Microwave remote sensing active and passive”. *Radar remote sensing and surface scattering and emission theory II*, 848–902.
- Van Looy, K., J. Bouma, M. Herbst, J. Koestel, B. Minasny, U. Mishra, C. Montzka, A. Nemes, Y. A. Pachepsky, J. Padarian, M. G. Schaap, B. Tóth, A. Verhoef, J. Vanderborght, M. J. van der Ploeg, L. Weihermüller, S. Zacharias, Y. Zhang, and H. Vereecken (2017). “Pedotransfer Functions in Earth System Science: Challenges and Perspectives”. *Reviews of Geophysics* 55.4, 1199–1256.
- Vicente-Serrano, S. M., S. Beguería, and J. I. López-Moreno (2010). “A Multiscalar Drought Index Sensitive to Global Warming: The Standardized Precipitation Evapotranspiration Index”. *Journal of Climate* 23.7, 1696–1718.
- Vilà-Guerau de Arellano, J., C. C. van Heerwaarden, B. J. H. van Stratum, and K. van den Dries (2015). *Atmospheric Boundary Layer: Integrating Air Chemistry and Land Interactions*. Cambridge: Cambridge University Press.
- Vogel, M. M., R. Orth, F. Cheruy, S. Hagemann, R. Lorenz, B. J. J. M. van den Hurk, and S. I. Seneviratne (2017). “Regional amplification of projected changes in extreme temperatures strongly controlled by soil moisture-temperature feedbacks”. *Geophysical Research Letters* 44.3, 1511–1519.
- Vogel, M. M., M. Hauser, and S. I. Seneviratne (2020). “Projected changes in hot, dry and wet extreme events’ clusters in CMIP6 multi-model ensemble”. *Environmental Research Letters* 15.9, 094021.
- Vogel, M. M., J. Zscheischler, and S. I. Seneviratne (2018). “Varying soil moisture-atmosphere feedbacks explain divergent temperature extremes and precipitation projections in central Europe”. *Earth System Dynamics* 9.3, 1107–1125.
- Voltaire, A. (2019). “CNRM-CERFACS CNRM-ESM2-1 model output prepared for CMIP6 ScenarioMIP ssp585”.
- Volodin, E. M., E. V. Mortikov, S. V. Kostykin, V. Y. Galin, V. N. Lykossov, A. S. Gritsun, N. A. Diansky, A. V. Gusev, N. G. Iakovlev, A. A. Shestakova, and S. V. Emelina (2018).

- “Simulation of the modern climate using the INM-CM48 climate model”. *Russian Journal of Numerical Analysis and Mathematical Modelling* 33.6, 367–374.
- Volodin, E., E. Mortikov, A. Gritsun, V. Lykossov, V. Galin, N. Diansky, A. Gusev, S. Kostrykin, N. Iakovlev, A. Shestakova, and S. Emelina (2019a). “INM INM-CM4-8 model output prepared for CMIP6 CMIP historical”.
- (2019b). “INM INM-CM4-8 model output prepared for CMIP6 ScenarioMIP”.
- Wang, X., B. Qiu, W. Li, and Q. Zhang (2019). “Impacts of drought and heatwave on the terrestrial ecosystem in China as revealed by satellite solar-induced chlorophyll fluorescence”. *Science of The Total Environment* 693, 133627.
- Wei, Z., K. Yoshimura, L. Wang, D. G. Miralles, S. Jasechko, and X. Lee (2017). “Revisiting the contribution of transpiration to global terrestrial evapotranspiration”. *Geophysical Research Letters* 44.6, 2792–2801.
- Wickham, H., W. Chang, L. Henry, T. L. Pedersen, K. Takahashi, C. Wilke, K. Woo, H. Yutani, D. Dunnington, and RStudio (2022). *ggplot2: Create Elegant Data Visualisations Using the Grammar of Graphics*.
- Wiel, K. van der and R. Bintanja (2021). “Contribution of climatic changes in mean and variability to monthly temperature and precipitation extremes”. *Communications Earth & Environment* 2.1, 1–11.
- Wiel, K. van der, G. Lenderink, and H. de Vries (2021). “Physical storylines of future European drought events like 2018 based on ensemble climate modelling”. *Weather and Climate Extremes* 33, 100350.
- Williams, C. A., M. Reichstein, N. Buchmann, D. Baldocchi, C. Beer, C. Schwalm, G. Wohlfahrt, N. Hasler, C. Bernhofer, T. Foken, D. Papale, S. Schymanski, and K. Schaefer (2012). “Climate and vegetation controls on the surface water balance: Synthesis of evapotranspiration measured across a global network of flux towers”. *Water Resources Research* 48.6.
- Williams, I. N. and M. S. Torn (2015). “Vegetation controls on surface heat flux partitioning, and land-atmosphere coupling”. *Geophysical Research Letters* 42.21, 9416–9424.
- Wilson, K., A. Goldstein, E. Falge, M. Aubinet, D. Baldocchi, P. Berbigier, C. Bernhofer, R. Ceulemans, H. Dolman, C. Field, A. Grelle, A. Ibrom, B. E. Law, A. Kowalski, T. Meyers, J. Moncrieff, R. Monson, W. Oechel, J. Tenhunen, R. Valentini, and S. Verma (2002). “Energy balance closure at FLUXNET sites”. *Agricultural and Forest Meteorology* 113.1, 223–243.
- Winkler, A. J., R. B. Myneni, A. Hannart, S. Sitch, V. Haverd, D. Lombardozzi, V. K. Arora, J. Pongratz, J. E. M. S. Nabel, D. S. Goll, E. Kato, H. Tian, A. Arneth, P. Friedlingstein, A. K. Jain, S. Zaehle, and V. Brovkin (2021). “Slowdown of the greening trend in natural vegetation with further rise in atmospheric CO₂”. *Biogeosciences* 18.17, 4985–5010.
- Wohlfahrt, G., K. Gerdel, M. Migliavacca, E. Rotenberg, F. Tatarinov, J. Müller, A. Hammerle, T. Julitta, F. M. Spielmann, and D. Yakir (2018). “Sun-induced fluorescence and gross primary productivity during a heat wave”. *Scientific Reports* 8.1, 14169.

- Wouters, H., J. Keune, I. Y. Petrova, C. C. van Heerwaarden, A. J. Teuling, J. S. Pal, J. Vilà-Guerau de Arellano, and D. G. Miralles (2022). “Soil drought can mitigate deadly heat stress thanks to a reduction of air humidity”. *Science Advances* 8.1, eabe6653.
- Wouters, H., I. Y. Petrova, C. C. van Heerwaarden, J. Vilà-Guerau de Arellano, A. J. Teuling, V. Meulenbergh, J. A. Santanello, and D. G. Miralles (2019). “Atmospheric boundary layer dynamics from balloon soundings worldwide: CLASS4GL v1.0”. *Geoscientific Model Development* 12.5, 2139–2153.
- Wu, T., M. Chu, M. Dong, Y. Fang, W. Jie, J. Li, W. Li, Q. Liu, X. Shi, X. Xin, J. Yan, F. Zhang, J. Zhang, L. Zhang, and Y. Zhang (2018). “BCC BCC-CSM2MR model output prepared for CMIP6 CMIP historical”.
- Wu, T., Y. Lu, Y. Fang, X. Xin, L. Li, W. Li, W. Jie, J. Zhang, Y. Liu, L. Zhang, F. Zhang, Y. Zhang, F. Wu, J. Li, M. Chu, Z. Wang, X. Shi, X. Liu, M. Wei, A. Huang, Y. Zhang, and X. Liu (2019). “The Beijing Climate Center Climate System Model (BCC-CSM): the main progress from CMIP5 to CMIP6”. *Geoscientific Model Development* 12.4, 1573–1600.
- Xin, X., T. Wu, X. Shi, F. Zhang, J. Li, M. Chu, Q. Liu, J. Yan, Q. Ma, and M. Wei (2019). “BCC BCC-CSM2MR model output prepared for CMIP6 ScenarioMIP ssp370”.
- Yuan, W., Y. Zheng, S. Piao, P. Ciais, D. Lombardozzi, Y. Wang, Y. Ryu, G. Chen, W. Dong, Z. Hu, A. K. Jain, C. Jiang, E. Kato, S. Li, S. Lienert, S. Liu, J. E. Nabel, Z. Qin, T. Quine, S. Sitch, W. K. Smith, F. Wang, C. Wu, Z. Xiao, and S. Yang (2019). “Increased atmospheric vapor pressure deficit reduces global vegetation growth”. *Science Advances* 5.8, eaax1396.
- Zhang, L., N. Qiao, C. Huang, and S. Wang (2019). “Monitoring Drought Effects on Vegetation Productivity Using Satellite Solar-Induced Chlorophyll Fluorescence”. *Remote Sensing* 11.4, 378.
- Zhang, Y., Z. Gao, D. Li, Y. Li, N. Zhang, X. Zhao, and J. Chen (2014). “On the computation of planetary boundary-layer height using the bulk Richardson number method”. *Geoscientific Model Development* 7.6, 2599–2611.
- Zhang, Y., J. L. Peña-Arancibia, T. R. McVicar, F. H. S. Chiew, J. Vaze, C. Liu, X. Lu, H. Zheng, Y. Wang, Y. Y. Liu, D. G. Miralles, and M. Pan (2016). “Multi-decadal trends in global terrestrial evapotranspiration and its components”. *Scientific Reports* 6.1, 19124.
- Zhao, M. and S. W. Running (2010). “Drought-Induced Reduction in Global Terrestrial Net Primary Production from 2000 Through 2009”. *Science* 329.5994, 940–943.
- Zhao, T. and A. Dai (2017). “Uncertainties in historical changes and future projections of drought. Part II: model-simulated historical and future drought changes”. *Climatic Change* 144.3, 535–548.
- Zhou, S., A. P. Williams, B. R. Lintner, A. M. Berg, Y. Zhang, T. F. Keenan, B. I. Cook, S. Hagemann, S. I. Seneviratne, and P. Gentile (2021). “Soil moisture–atmosphere feedbacks mitigate declining water availability in drylands”. *Nature Climate Change* 11.1, 38–44.

- Zhou, S., Y. Zhang, A. Park Williams, and P. Gentine (2019). “Projected increases in intensity, frequency, and terrestrial carbon costs of compound drought and aridity events”. *Science Advances* 5.1, eaau5740.
- Zhu, Z., J. Bi, Y. Pan, S. Ganguly, A. Anav, L. Xu, A. Samanta, S. Piao, R. R. Nemani, and R. B. Myneni (2013). “Global Data Sets of Vegetation Leaf Area Index (LAI)3g and Fraction of Photosynthetically Active Radiation (FPAR)3g Derived from Global Inventory Modeling and Mapping Studies (GIMMS) Normalized Difference Vegetation Index (NDVI3g) for the Period 1981 to 2011”. *Remote Sensing* 5.2, 927–948.
- Zhu, Z., S. Piao, R. B. Myneni, M. Huang, Z. Zeng, J. G. Canadell, P. Ciais, S. Sitch, P. Friedlingstein, A. Arneeth, C. Cao, L. Cheng, E. Kato, C. Koven, Y. Li, X. Lian, Y. Liu, R. Liu, J. Mao, Y. Pan, S. Peng, J. Peñuelas, B. Poulter, T. A. M. Pugh, B. D. Stocker, N. Viovy, X. Wang, Y. Wang, Z. Xiao, H. Yang, S. Zaehle, and N. Zeng (2016). “Greening of the Earth and its drivers”. *Nature Climate Change* 6.8, 791–795.
- Ziehn, T., M. A. Chamberlain, R. M. Law, A. Lenton, R. W. Bodman, M. Dix, L. Stevens, Y.-P. Wang, J. Srbinovsky, T. Ziehn, M. A. Chamberlain, R. M. Law, A. Lenton, R. W. Bodman, M. Dix, L. Stevens, Y.-P. Wang, and J. Srbinovsky (2020). “The Australian Earth System Model: ACCESS-ESM1.5”. *Journal of Southern Hemisphere Earth Systems Science* 70.1, 193–214.
- Ziehn, T., M. Chamberlain, A. Lenton, R. Law, R. Bodman, M. Dix, Y. Wang, P. Dobrohotoff, J. Srbinovsky, L. Stevens, P. Vohralik, C. Mackallah, A. Sullivan, S. O’Farrell, and K. Druken (2019a). “CSIRO ACCESS-ESM1.5 model output prepared for CMIP6 CMIP historical”.
- (2019b). “CSIRO ACCESS-ESM1.5 model output prepared for CMIP6 ScenarioMIP ssp585”.
- Zscheischler, J., M. Reichstein, S. Harmeling, A. Rammig, E. Tomelleri, and M. D. Mahecha (2014a). “Extreme events in gross primary production: a characterization across continents”. *Biogeosciences* 11.11, 2909–2924.
- Zscheischler, J., M. D. Mahecha, J. v. Buttlar, S. Harmeling, M. Jung, A. Rammig, J. T. Randerson, B. Schölkopf, S. I. Seneviratne, E. Tomelleri, S. Zaehle, and M. Reichstein (2014b). “A few extreme events dominate global interannual variability in gross primary production”. *Environmental Research Letters* 9.3, 035001.
- Zscheischler, J., M. D. Mahecha, S. Harmeling, and M. Reichstein (2013). “Detection and attribution of large spatiotemporal extreme events in Earth observation data”. *Ecological Informatics* 15, 66–73.
- Zscheischler, J., R. Orth, and S. I. Seneviratne (2015). “A submonthly database for detecting changes in vegetation-atmosphere coupling”. *Geophysical Research Letters* 42.22, 9816–9824.

Statement of authorship contributions

The introduction (Chapter 1) and the synthesis (Chapter 7) have been written solely by Jasper M.C. Denissen. An overview of (co-)authorship and other contributions to the remainder of the chapters is summarized below.

AH = Anke Hildebrandt (UFZ, FSU)

AP = Andrew J. Pitman (ARC-CECE, CCRC)

AT = Adriaan J. Teuling (WUR))

AW = Alexander J. Winkler (MPI-BGC)

CH = Chiel C. van Heerwaarden (WUR)

CZ = Chunhui Zhan (MPI-BGC)

DM = Diego Miralles (UGhent)

GB = Gianpaolo Balsamo (ECMWF)

HW = Hendrik Wouters (UGhent, VITO)

JD = Jasper Denissen (MPI-BGC, WUR)

JK = Josephin Kroll (MPI-BGC)

JV = Jordi Vilá-Guerau de Arellano (WUR)

MM = Mirco Migliavacca (JRC)

MR = Markus Reichstein (MPI-BGC)

MV = Martha M. Vogel (UNESCO)

RO = René Orth (MPI-BGC)

SK = Sujan Koirala (MPI-BGC)

UW = Ulrich Weber (MPI-BGC)

WL = Wantong Li (MPI-BGC)

XY = Xin Yu (MPI-BGC)

Chapter 2

Design of the work:

JD, RO

Data collection:

JD, UW

Data analysis and interpretation:

JD in consultation with AT, MR, RO

Drafting the article:

JD

Critical revision of the article:

JD, AT, MR, RO

Approval of the version to be published:

JD, AT, MR, RO

Chapter 3

Design of the work:

JD, AT, DM, HW, RO

Data collection:

JD, DM, HW

Data analysis and interpretation:

JD in consultation with AT, CH, DM, HW, JV, RO

Drafting the article:

JD

Critical revision of the article:

JD, AT, CH, DM, HW, JV, RO

Approval of the version to be published:

JD, AT, CH, DM, HW, JV, RO

Chapter 4

Design of the work:	JD, RO
Data collection:	JD, SK
Data analysis and interpretation:	JD in consultation with AP, AT, AW, CZ, MM, MR, RO, SK, WL
Drafting the article:	JD,
Critical revision of the article:	JD, AP, AT, AW, MM, RO, SK, WL
Approval of the version to be published:	JD, AP, AT, RO

Chapter 5

Design of the work:	JK, JD, RO
Data collection:	JK, JD, UW
Data analysis and interpretation:	JK in consultation with AH, JD, MM, RO, WL
Drafting the article:	JK, JD
Critical revision of the article:	JK, AH, JD, MM, RO, WL
Approval of the version to be published:	JK, AH, JD, MM, RO, WL

Chapter 6

Design of the work:	JD, RO
Data collection:	JD, SK
Data analysis and interpretation:	JD in consultation with AT, GB, MR, MV, RO, XY
Drafting the article:	JD
Critical revision of the article:	JD, AT, MV, RO
Approval of the version to be published:	JD, AT, MV, RO

Acknowledgements

It has been just over four years that I started my PhD project at the Max-Planck Institute for Biogeochemistry in Jena. During this time, I have met a great deal of people that have made my professional and personal life much more interesting and fun. Further, many friendships have persevered the 6-hour car ride distance from the Netherlands. Also, spending time away from the Netherlands, especially during these recent uncertain times, has made me value my family even more. Here, I want to take the opportunity to say some special thanks to the people that have particularly contributed positively throughout these times. For sure I have forgotten to include someone in these acknowledgements. All I can do is offer you a beverage of your choice to soften the blow, if you feel rightfully inclined.

In the first place, I'd like to thank René for giving me the opportunity to pursue a career in science and for accepting me as his first PhD student in Jena. We came a long way from having group meetings with just the two of us to a group of >10 people. I am very happy to have had such a unique position at the start of what is now a productive and inclusive research group and really appreciated to see you grow into your group leader position as well. I thoroughly enjoyed your candidness during our discussions. I greatly appreciated that our meetings were never just science, but we also took the chance to discuss other things, such as the state of football or biking. I very much enjoyed the many BBQs and watching football in your garden. Let me know when you plan another visit to the Signal Iduna Park, hopefully not against a Dutch team, so that we can both cheer for BVB ;).

I also want to thank Ryan; from other PhD students at the MPI-BGC, I didn't really know what I could expect from an external supervisor. But from the first time I stepped in your office in Wageningen and noticed you already had put up a picture of your new favorite PhD student (I believe this was a picture of some waterfall from the Iceland excursion, taken over my shoulder), I knew it was going to be all right. But jokes aside, I really appreciated your directness and your honesty. From the start you have been pushing to be included more in the research projects here, which resulted in a lot of scientific output of a high quality and frankly, a lot more than I thought I would be able to do. I hold in very high regard the opportunity to do a research stay in Wageningen and working on my favorite topic of boundary layer processes & land-atmosphere interactions with colleagues both from HWM and MAQ.

Thanks to all the opponents from close and afar that took the time to (critically) read the thesis and make the trip to Wageningen to attend the defense.

Ik wil graag ook mijn familie bedanken en dan in het bijzonder: ons pa en ons moeder, Dennis, Nort, Mieke, Daniëlle en, last but not least, ons oma. Jullie bezoeken hier in Jena en de weekenden thuis waren altijd iets om naar uit te kijken. De deuren in Moergestel, Nijmegen en Vught staat altijd open en als ik er ben is er altijd volop drank en spijs. Dat is natuurlijk niet de eerste reden dat ik thuis kom, maar ik zou liegen als ik zou zeggen dat het geen rol speelt. Jullie waren altijd geïnteresseerd in mijn werk; pa kent nu zelfs de wisselwerking van verdamping en het opwarmen van de lucht boven het aardoppervlak aan de hand van veranderingen in bodemvocht! Ik ben erg blij dat ik jullie familie mag noemen.

Thanks to Tina for being the best office mate I could have wished for and more than that. Thanks for enjoying coffee together with me and, by now, sharing my newly developed passion for Sudoku. The thought of not sharing an office with you in the future is both weird and sad. But to end on a high note, thanks for laughing for 2 hours straight, when I was learning cross-country skiing. And also, thanks for helping me through the painful process of writing the thesis: it was difficult, but it helped to think that you were there every day to struggle together with me. Also, thanks Jake and Tiana for being the most hospitable people I know in Jena. Thanks for the many crazy nights, where we drank 1-10 drinks too many. I'm very happy to have included you inside my Corona bubble during the heights of the pandemic. Thanks for all the game nights we had together and for going on a skiing trip with me. I love you guys.

Thanks to all my flatmates of at the Camsdorfer Straße 10, Martin, Lennart, Vanessa, Sophie, Julius and Claas, for making it a joy to come home everyday back when coming home from work was still a thing and making it a joy to be locked up with you guys during the heights of the pandemic. Without you, I would have probably gone crazy. Thanks for being patient with me and listening to me during all the times I was going on and on about troubles with programming and publishing papers. Thanks for all the times we cooked together, brewed cocktails with random bottles of liquor that were in the kitchen since God knows how long and played a round of Regenwormen. I especially enjoyed our beerpong tournament, which we repeated again the day after the beerpong tournament.

Thanks aan de Creeperzzz en co, Dennis en Mieke, Puck en Elke, Sander en Karlijn, Joris en Raphael. Er zijn tijden dat ik jullie vaker zie en tijden dat het minder is, maar ik weet dat jullie er altijd voor me zijn en dat gevoel bestaat zeker ook andersom.

I want to thank Markus for welcoming me in the department and his essential feedback that advanced the science. Thanks to the Hydrosphere-Biosphere-Climate interactions group for the fruitful discussions and the valuable feedback, more than I wanted sometimes but always of high quality. Thanks to the department for the fruitful discussions after department seminars. Thanks to all the co-authors for your contributions big and small; I have enjoyed immensely the discussions we've had, both in person and online, and learned a great deal from them.

A special thanks to Uli and Sujan: What for you might be one day of work, saved me weeks. I greatly appreciate your help and also your friendship. A special thanks also to Josephin, with whom I co-authored Chapter 5 of this thesis. I always looked forward to discuss with you, which made working with you truly a pleasure. Thanks, Steffi, for streamlining the organization of my PhD and for being a friend. Thanks to Linda, Alice and Sarah for all the help from the BGI office. Thank you, Sinikka, for providing excellent graphics that have elevated the introduction of my thesis. Thanks to everyone contributing their coding knowledge to Stackoverflow; I would have been lost without others having similar problems as I did. I have enjoyed playing football with many colleagues from other Max-Planck Institutes from Jena; Pretending we were a research group from the Max-Planck Institute for Human History that recently moved to Leipzig, we even managed to win the Max-Planck cup in Leipzig, under strong guidance of our passionate Italian Coachimo! I have also had many fun times playing with the guys of FC Thüringen Jena III, where I got to know the local dialect very fast. Thanks for joining me on my (crazy) bike rides, Bernie, Santiago, Caglar, Mappi, and others. Thanks Matthijs en Marion, dat jullie mij voor 3 maanden in huis hebben genomen toen ik mijn research stay in Wageningen deed. Het was een mooie tijd, waarin ik jullie nog beter leerde kennen en jullie mij ook. Zulke gastvrijheid zal ik niet snel vergeten. Ik wil ook mijn paranymphen, Dennis en Matthijs, bedanken. Uiteraard niet alleen voor het paranymph zijn, maar jullie weten dat jullie dat zijn omdat jullie zo veel meer voor mij betekenen. Last but definitely not least, I want to thank the Quarantine Club and other peripheral members, Tina, Jake and Tiana, Richard and Silvia, Shane and Amber, Jeff and Dora, Bernie and Nora, Basil and Elena, Santiago and Carolina, Caglar and Xece, Franzi, Max, Sujan, Millie, Javier, for organizing so many on- and offline gatherings that made the worst of times during the pandemic into something that I looked forward to and enjoyed. We have built such a strong friendship over the years and you have been the basis for all my social activities for so long that it is going to be difficult to do it without you guys. I can't thank you all enough. I hope to stay in touch with you; Come visit me in Bonn!

Curriculum Vitae



Jasper Denissen

Curriculum Vitae

I come up with structured approaches and I am assertive, direct in communication and disciplined. This makes me an ambitious, persevering and resourceful team player.

Employment

- Feb. 2018–
Jul. 2022 **PhD researcher**, *Max Planck Institute for Biogeochemistry*, Jena, Germany.
Project: "Mapping terrestrial evaporation regimes – A data-driven analysis of land-atmosphere interactions under climate change." Keywords: Land-atmosphere interactions, soil moisture, energy and water limitation & boundary layer processes. Advisors: Dr. René Orth. (Daily advisor; Max-Planck Institute for Biogeochemistry) and Dr.ir. Ryan Teuling (External advisor; Wageningen University)
- **PhD representative:** serve the interests of PhD researchers in the Biogeochemical Integration Department, by voicing concerns from PhD researchers to the directorate and vice-versa.
 - **Organize the Earth System PhD Conference 2019:** Chairing meetings and co-organizing session "Natural Processes" (imprs-gbgc.de/esp2019/).
 - **Supervising:** a MSc and BSc thesis for the FSU University, Jena.

Education

- Jan. 2015–
Aug. 2017 **MSc Earth & Environment**, *Wageningen University*, Wageningen, Netherlands.
Understanding of physical, biological and chemical processes through field work and modelling; Specialization: Meteorology.
- **MSc. thesis:** *The effect cloud-core area fraction on convective transport by cumulus convection in EMAC* at Max-Planck-Institute for Chemistry, Mainz, Germany. Supervisors: Prof. dr. Maarten Krol & Dr. ir. Huug Ouwersloot. **Graded: 8.5/10**
 - **MSc. internship:** *Developing a tool for lightning forecasting based on ECMWF's Integrated Forecasting System (IFS) data* at Joint Meteorological Group, Royal Netherlands Air Force, Woensdrecht, Netherlands. Supervisor: Dr. ir. Chiel C. van Heerwaarden. **Graded: 8/10**
 - **Erasmus MSc Atmospheric Sciences** at Leopold-Franzens-University, Innsbruck, Austria.
- Sept. 2010–
Dec. 2014 **BSc Soil, Water, Atmosphere**, *Wageningen University*, Wageningen, Netherlands.
Biogeochemical processes and anthropological effects on system Earth.

Experience

Extracurricular

- Sept. 2011–
Jul. 2013 **Secretary**, *Lustrum Committee of Wageningen Student Association Ceres (W.S.V. Ceres)*.
Fulltime: Sep. 2012–Jul. 2013. Budget: €280.000. Organize different festive activities related to the 135 year existence of the W.S.V. Ceres. I supervised several committees, was responsible for contact with all the current- and old members, maintained the administration of tasks and updated the membership file, which was severely outdated. Workload: ± 60h/week.

Camsdorfer Str. 10, Wohnung 05 – 07749, Jena, Germany
☎ +49 175 5377 093 • ✉ jasper.denissen@bgc-jena.mpg.de

Computer skills

Models	Weather- Research and Forecast (WRF) Model ECHAM/MESSy Atmospheric Chemistry (EMAC) Model Chemistry Land-surface Atmosphere Soil Slab model for Global Studies (CLASS4GL)
Text editors	\LaTeX <i>expert</i> Microsoft Office (incl. MS Power BI) <i>expert</i>
Programming	FORTRAN 90/95 <i>expert</i> R <i>expert</i> PYTHON <i>intermediate</i>

Languages

Dutch	Mothertongue
English	Fluent
German	Fluent

Interests

Sports	Football (also watching), biking (also longer holiday trips) & running
Music	Playing drums & going to festivals
Acting	

Peer-reviewed Journal Publications

- Bogdanovich, E., L. Guenther, M. Reichstein, D. Frank, G. Ruhrmann, A. Brenning, J. M. C. Denissen, and R. Orth (2022). “Societal attention to heat waves can indicate public health impacts.” *Environmental Research Letters*, *in review*.
- Denissen, J. M. C., R. Orth, H. Wouters, D. G. Miralles, C. C. van Heerwaarden, J. Vilà-Guerau de Arellano, and A. J. Teuling (2021c). “Soil moisture signature in global weather balloon soundings”. *npj Climate and Atmospheric Science* 4.1, 1–8.
- Denissen, J. M. C., A. J. Teuling, G. Balsamo, X. Yu, M. M. Vogel, S. I. Seneviratne, and R. Orth (2022b). “Increasing ecosystem water limitation fuels future heat extremes”. *Global Change Biology*, *in review*.
- Denissen, J. M. C., A. J. Teuling, A. J. Pitman, S. Koirala, M. Migliavacca, W. Li, M. Reichstein, A. J. Winkler, C. Zhan, and R. Orth (2022c). “Widespread shift from ecosystem energy to water limitation with climate change”. *Nature Climate Change*, *accepted*.
- Denissen, J. M. C., A. J. Teuling, M. Reichstein, and R. Orth (2020a). “Critical Soil Moisture Derived From Satellite Observations Over Europe”. *Journal of Geophysical Research: Atmospheres* 125.6, e2019JD031672.
- Kroll*, J., J. M. C. Denissen*, M. Migliavacca, W. Li, A. Hildebrandt, and R. Orth (2022). “Spatially varying relevance of hydrometeorological hazards for vegetation productivity extremes”. *Biogeosciences* 19.2, 477–489, [*These authors contributed equally to this work].
- Li, W., M. Migliavacca, M. Forkel, J. M. C. Denissen, M. Reichstein, H. Yang, G. Duveiller, U. Weber, and R. Orth (2022). “Global vegetation getting more sensitive to short-term soil moisture variability.” *Nature Communications*, *in revision*.
- O, S., A. Bastos, M. Reichstein, W. Li, J. M. C. Denissen, H. Graefen, and R. Orth (2022). “The role of climate and vegetation in regulating drought-heat extremes.” *Journal of Climate*, *accepted*.

Other Scientific Publications

- Denissen, J. M. C. (2020). *What soil moisture can teach us about heat waves*. Deutsches Klima-Konsortium, <https://www.deutsches-klima-konsortium.de/de/ueber-uns/positionen/kolumne-zur-sache.html?expand=5591&cHash=ea7d441410129e1547dacf9a5d2064d8>.
- Denissen, J. M. C., R. Orth, M. Reichstein, and A. J. Teuling (2019a). *Characteristic soil moisture range transitioning between energy and water limitation of the biosphere*. EGU General Assembly 2019, Vienna, Austria, 7-12 Apr, 2019.

- Denissen, J. M. C., R. Orth, H. Wouters, D. G. Miralles, C. C. van Heerwaarden, J. Vilà-Guerau de Arellano, and A. J. Teuling (2021a). *Soil moisture control on the atmospheric boundary layer*. Nederlands Aardwetenschappelijk Congres (NACGEO) 2021, online, 8-9 April 2021.
- (2021b). *Soil moisture signature in global weather balloon soundings*. Land-Atmosphere Interactions workshop, online, 10-11 June 2021.
- Denissen, J. M. C., A. J. Teuling, G. Balsamo, M. Reichstein, and R. Orth (2022a). *Shift towards ecosystem water limitation exacerbates hot temperature extremes*. EGU General Assembly 2022, Vienna, 23-27 May 2022,
- Denissen, J. M. C., A. J. Teuling, W. Li, M. Reichstein, A. J. Pitman, and R. Orth (2021d). *Future trends in global water vs. energy-controlled evaporative regimes*. EGU General Assembly 2021, online, 19-30 Apr 2021,
- Denissen, J. M. C., A. J. Teuling, A. J. Pitman, S. Koirala, M. Migliavacca, W. Li, M. Reichstein, A. J. Winkler, C. Zhan, and R. Orth (2021e). *Increase in global ecosystem water limitation with warming temperatures*. AGU Fall Meeting 2021, hybrid, 13-17 Dec 2021.
- Denissen, J. M. C., A. J. Teuling, M. Reichstein, and R. Orth (2019b). *Characteristic soil moisture range transitioning between energy and water limitation of the biosphere*. Earth System PhD Conference 2019, Jena, Germany, 13-15 March 2019.
- Denissen, J. M. C., H. Wouters, R. Orth, D. G. Miralles, and A. J. Teuling (2020b). *What balloon soundings can tell about surface heat flux partitioning*. EGU General Assembly 2020, online, 4-8 May 2020,
- Teuling, A. J. and J. M. C. Denissen (2021). *Soil moisture conditions reflected in observations from weather balloons*. drought.NL, <https://drought.nl/research/soil-moisture-conditions-reflected-in-observations-from-weather-balloons/>.
- Wouters, H. and J. M. C. Denissen (2021). *We can measure soil moisture with weather balloons!* CLASS4GL, <https://class4gl.eu/?p=1022>.

IMPRS certificate

Certificate

This is to certify that
Mr. Jasper Denissen
born on 11th May 1992
in Tilburg, The Netherlands

has undertaken and fully completed the graduate training programme offered at the International Max Planck Research School for Global Biogeochemical Cycles in Jena.

Title of thesis:

Mapping terrestrial evaporation regimes - A data-driven analysis of land-atmosphere interactions under climate change

PhD thesis advisory committee:

Prof. Dr. R. Teuling (Wageningen University & Research)
Dr. R. Orth (Max Planck Institute for Biogeochemistry)
Prof. Dr. M. Reichstein (Max Planck Institute for Biogeochemistry)

Other members of the doctoral committee:

Prof. Dr. M. Scheffer (Wageningen University & Research)
Prof. Dr. P. A. Dirmeyer (George Mason University)
Prof. Dr. P. Gentine (Columbia University)
Dr. K. van der Wiel (Royal Netherlands Meteorological Institute)

PhD start: 1st February 2018
Thesis submission: 18th March 2022
PhD defense: 1st July 2022

AP.S. 22

apl. Prof. Dr. Gerd Gleixner

Spokesperson of the IMPRS-gBGC



SENSE certificate



*Netherlands Research School for the
Socio-Economic and Natural Sciences of the Environment*

D I P L O M A

for specialised PhD training

The Netherlands research school for the
Socio-Economic and Natural Sciences of the Environment
(SENSE) declares that

Jasper Marinus Cornelis Denissen

born on 11th May 1992 in Tilburg, The Netherlands

has successfully fulfilled all requirements of the
educational PhD programme of SENSE.

Wageningen, 1st July 2022

Chair of the SENSE board

Prof. dr. Martin Wassen

The SENSE Director

Prof. Philipp Pattberg

The SENSE Research School has been accredited by the Royal Netherlands Academy of Arts and Sciences (KNAW)



K O N I N K L I J K E N E D E R L A N D S E
A K A D E M I E V A N W E T E N S C H A P P E N



The SENSE Research School declares that **Jasper Marinus Cornelis Denissen** has successfully fulfilled all requirements of the educational PhD programme of SENSE with a work load of 40.9 EC, including the following activities:

SENSE PhD Courses

- o Environmental research in context (2018)
- o Research in context activity: 'Co-organize discussion on climate communication in Earth System PhD Conference2019' (Year)

Selection of Other PhD and Advanced MSc Courses

- o Biogeochemical cycles in the Earth System, IMPRS, Jena (2018)
- o Thermodynamics, IMPRS, Jena (2018)
- o Swiss Climate Summer School, ETH Zürich, Ascona, Switzerland (2019)
- o Terrestrial Biosphere, IMPRS, Jena, (2020)
- o R course: advanced modules, IMPRS, Jena (2018)
- o Earth Observation Techniques , IMPRS, Jena (2018)
- o Data visualization, IMPRS, Jena (2018)
- o Good Scientific Practice, IMPRS, Jena (2019)
- o Climate science communication, SENSE, Wageningen (2019)
- o Applied Statistics & Data Analysis, IMPRS, Jena (2020)
- o Applied Statistics & Data Analysis – Advanced, IMPRS, Jena, (2020)
- o Grant Proposal Writing, IMPRS, Jena (2021)

Management and Didactic Skills Training

- o Organizer of the Earth System PhD Conference 2019, Jena.
- o PhD representative of the Biogeochemical Integration Department (2019)
- o Supervising one MSc student (2019) and one BSc student (2021) with thesis
- o Teaching in the B/MSc course 'Climate Change' (2018)

Selection of Oral Presentations

- o *Characteristic soil moisture range transitioning between energy and water limitation of the biosphere.* EGU, 7-12 April 2019, Vienna, Austria
- o *The critical soil moisture (CSM) from different perspectives.* Seminar Ghent University, 13 December2019, Ghent, Belgium
- o *Soil moisture control on the atmospheric boundary layer.* NACGEO, 8-9 April 2021, online
- o *Increase in global ecosystem water limitation with warming.* AGU, 13-17 December 2021, online

SENSE coordinator PhD education

Dr. ir. Peter Vermeulen

This research received funding from the Emmy Noether Program (Grant number 391059971)

Cover design by Puck van Iersel, in consultation with Jasper M.C. and Dennis A.M. Denissen.
The cover represents terrestrial evaporation regimes, with contoured leaves of banana plants symbolizing energy-limited conditions on the front and contoured cracks in clay symbolizing water-limited conditions on the back.